



INSTITUTO POTOSINO DE INVESTIGACIÓN CIENTÍFICA Y TECNOLÓGICA, A.C.

DIVISIÓN DE CIENCIAS AMBIENTALES

Immobilization of bimetallic oxyhydroxides on graphitic matrices to remove arsenate and fluorides from water

Tesis que presenta:

Esmeralda Vences Alvarez

Para obtener el grado de

Doctor en Ciencias Aplicadas

en la opción de

Ciencias Ambientales

Director de tesis:

Dr. José René Rangel Méndez

San Luis Potosí, S.L.P., junio 2022



Constancia de aprobación de la tesis

La tesis “Inmovilización de oxihidróxidos bimetálicos sobre matrices gráficas para remover arseniato y fluoruros del agua” presentada para obtener el Grado de Doctor en Ciencias Aplicadas en la opción de Ciencias Ambientales fue elaborada por Esmeralda Vences Alvarez y aprobada el 01 de junio de 2022 por los suscritos, designados por el Colegio de Profesores de la División de Ciencias Ambientales del Instituto Potosino de Investigación Científica y Tecnológica, A.C.

Dr. José René Rangel Méndez

(Director de la tesis)

Dr. Luis Felipe Cházaro Ruiz

(Miembro del Comité Tutorial)

Dr. Horacio Flores Zúñiga

(Miembro del Comité Tutorial)

Dr. Alejandro López Valdivieso

(Miembro del Comité Tutorial)

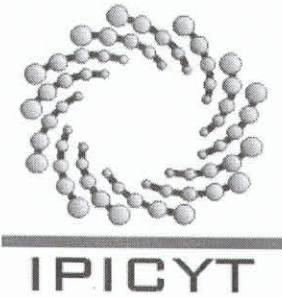


Créditos Institucionales

Esta tesis fue elaborada en la División de Ingeniería Ambiental del Instituto Potosino de Investigación Científica y Tecnológica, A.C., bajo la dirección del Dr. José René Rangel Méndez.

Durante la realización del trabajo el autor recibió una beca académica del Consejo Nacional de Ciencia y Tecnología (209008) y del Instituto Potosino de Investigación Científica y Tecnológica, A. C.

La investigación de esta tesis fue financiada por los proyectos CONACYT-Fondos Sectoriales-SEP-CB_2014-01-237118 del Fondo sectorial Ciencia Básica, y FORDECYT-2018-8-297525. Estos proyectos fueron asignados al Dr. José René Rangel Méndez. La autora de esta tesis recibió recursos financieros por parte de la División de Ciencias Ambientales del Instituto Potosino de Investigación Científica y Tecnológica, A.C., para la divulgación de los resultados de esta investigación en congresos internacionales.



Instituto Potosino de Investigación Científica y Tecnológica, A.C.

Acta de Examen de Grado

La Secretaría Académica del Instituto Potosino de Investigación Científica y Tecnológica, A.C., certifica que en el Acta 033 del Libro Primero de Actas de Exámenes de Grado del Programa de Doctorado en Ciencias Ambientales está asentado lo siguiente:

En la ciudad de San Luis Potosí a los 28 días del mes de junio del año 2022, se reunió a las 10:00 horas en las instalaciones del Instituto Potosino de Investigación Científica y Tecnológica, A.C., el Jurado integrado por:

Dr. Alejandro López Valdivieso	Presidente	UASLP
Dr. Horacio Flores Zúñiga	Secretario	IPICYT
Dr. José René Rangel Méndez	Sinodal	IPICYT
Dr. Luis Felipe Cházaro Ruiz	Sinodal	IPICYT

a fin de efectuar el examen, que para obtener el Grado de:

DOCTORA EN CIENCIAS AMBIENTALES

sustentó la C.

Esmeralda Vences Alvarez

sobre la Tesis intitulada:

Immobilization of bimetallic oxyhydroxides on graphitic matrices to remove arsenate and fluorides from water

que se desarrolló bajo la dirección de


Dr. José René Rangel Méndez

El Jurado, después de deliberar, determinó

APROBARLA

Dándose por terminado el acto a las 12:50 horas, procediendo a la firma del Acta los integrantes del Jurado. Dando fe la Secretaría Académica del Instituto.

A petición de la interesada y para los fines que a la misma convengan, se extiende el presente documento en la ciudad de San Luis Potosí, S.L.P., México, a los 28 días del mes de junio de 2022.


Dra. Lina Raquel Riego Ruiz
Secretaría Académica


Mtra. Ivonne Lizette Cuevas Vélez
Jefa del Departamento del Posgrado

Dedicatorias

*Dedico esta tesis de doctorado en primer lugar a **Díos** por guiarme día a día en este largo camino; dándome la sabiduría y paciencia necesaria para alcanzar una meta más en mi vida.*

*Al **Dr. José René Rangel Méndez**, por su paciencia, enseñanzas y grandes consejos que me ayudaron a realizar un trabajo de calidad y que deja un impacto en la investigación. Gracias por todos los conocimientos que me transmitió durante toda esta ardua trayectoria.*

*A mis padres, **Ysabel** y **Enrique** por impulsarme siempre a seguir mis sueños y apoyarme incondicionalmente en casa una de las decisiones que tomo. Gracias por enseñarme a ser emprendedora y perseverante con cada cosa que realizo; por los consejos, regaños, apapachos, pero sobre todo por el amor y la confianza que me brindan día con día. Gracias por confiar en mí y ser siempre parte de los grandes proyectos que me forjan a ser un mejor ser humano y profesionista.*

*A mi hermano **Eduardo**, que siempre tiene las palabras de aliento precisas que me ayudan a seguir esforzándome para lograr mis objetivos. Gracias por creer que puedo lograr grandes cosas y brindarme la fortaleza para seguir creciendo en mil formas.*

*A mis sobrinas **Amairaní** y **Vanía** y a mi sobrino **Ian**, por ser el motor que me impulsa a continuar esforzándome para ser un gran ejemplo para seguir como su única tía paterna.*

A José quien con su amor incondicional me apoyo y alentó durante este recorrido tan largo y un tanto difícil. Gracias por todas esas palabras de aliento y amor que me brindaste en esta gran trayectoria. Por nunca dudar de mis capacidades y mi talento. Por recordarme constantemente las cosas positivas que poseo.

Agradecimientos

A Dios por ser la luz que ilumina mi camino para lograr mis objetivos y alcanzar cada una de mis metas propuestas. Por darme la fortaleza necesaria para soportar las adversidades y darme la humildad para compartir con mis compañeros mis conocimientos.

A el Dr. René Rangel Méndez por aceptarme en su grupo de trabajo, compartirme de sus conocimientos, creer en mi desempeño y por todos sus consejos que me facilitaron la comprensión del trabajo de tesis. Principalmente agradezco la confianza que deposito en mi durante mi estancia doctoral y el apoyo para realizar mi estancia en Alicante, España, así como a todos los congresos a los cuales asistí para presentar mi trabajo de doctorado. Por enseñarme que un excelente investigador, no es aquel que sabe más que los demás, sino es aquel que con humildad está dispuesto a continuar aprendiendo de sus compañeros de trabajo mediante colaboraciones, de otros investigadores y de sus propios alumnos.

A mis padres y hermano por su fortaleza, su comprensión, su apoyo y su amor incondicional

Al Instituto Potosino de Investigación Científica y Tecnológica (IPICYT), en especial a la División de Ciencias Ambientales (DCA) por la infraestructura facilitada para la realización el presente trabajo de investigación.

A mis asesores de tesis: Dr, Luis Felipe Chazaro, Dr. Alejandro Valdivieso y Dr. Horacio Flores

A el Dr. Cesar Nieto, por su apoyo en la comprensión sobre aspectos químicos. Por su siempre amable disposición a ayudarme a entender conceptos y reacciones.

A mis amigos: Iván Bueno, Carlos Chaparro (Charly), Kardia Ramírez, Diana Alejo, Rigoberto Santoyo, Ivonne Torres, Andrea Susana González, Carmelita Medina y Guadalupe Arriaga que con su entusiasmo siempre me han impulsado a seguir mis metas, pero sobre todo a creer que puedo lograr grandes cosas. Les agradezco su amistad incondicional y dejarme ser parte de su vida.

A mis compañeros de generación del IPICYT: Irma, Rigoberto y Jack Por sus consejos, ánimos y por todos esos momentos llenos de risas y angustias.

A mis compañeros del grupo de adsorción: Rigo, Joel, Jessica, Andrea, Mercedes, David, Eduardo, Miguel, Aries, y Paola por compartirme de sus conocimientos y por sus valiosos comentarios que me ayudaron durante el desarrollo de la tesis.

A los técnicos de las divisiones de Ciencias Ambientales y Materiales Avanzados: Ma. Carmen Rocha, Elizabeth Isaacs, Guillermo Vidriales, Beatriz Rivera, Ana Iris Peña, Héctor Gabriel Silva que siempre me apoyaron con disponibilidad y paciencia.

A el Dr. Diego Cazorla, Dra. Emilia Morallon y Dr. David Salinas de la Universidad de Alicante España. Por su apoyo en mi trabajo de investigación durante mi estancia doctoral en sus instalaciones. Por todos los conocimientos compartidos y su paciencia. ¡Muchas gracias!

A todos los mencionados ¡Muchas Gracias!

Contents

Constancia de aprobación de la tesis.....	ii
Créditos Institucionales	iii
Acta de EXAMEN	iv
Dedicatorias.....	v
Agradecimientos.....	vii
List of Figures	xx
Resumen	xxviii
Abstract	xxx
Structure of this thesis	xxxii

CHAPTER I

Introduction.....	1
1.1. Water contamination by Arsenic and Fluorides in Mexico and in the world	3
1.2. Chemistry and Toxicity of Arsenic and Fluoride	6
1.3. Methods to remove arsenic(V) and fluorides from water.....	9
1.4. Adsorption process.....	10
1.4.1. Fundamentals of adsorption.....	10
1.4.1.1. Nature of physisorption forces.....	13
1.4.1.1.1. External sphere complexes.....	14
1.4.1.2. Chemisorption	15
1.4.1.2.1. Inner sphere complex	16
1.4.2. Solid-liquid interface models	17
1.4.2.1. Electric double and triple layer model.....	18

1.4.3.	Adsorption equilibrium.....	21
1.4.3.1.	Langmuir model.....	22
1.4.3.2.	Freundlich model.....	23
1.4.4.	Adsorption kinetics.....	24
1.5.	Adsorbent materials used in the removal of arsenic (V) and fluorides.....	25
1.5.1.	Activated carbon.....	26
1.5.1.1.	Textural and chemical properties.....	26
1.5.2.	Metal Oxyhydroxides.....	29
1.5.3.	Bimetallic oxides.....	30
1.5.4.	Modified activated carbon with metal oxides.....	31
1.5.4.1.	Methods to modifying activated carbon with bimetallic oxyhydroxides.....	33
1.5.4.1.1.	Hydrothermal synthesis.....	36
1.5.4.1.1.1.	Hydrothermal synthesis assisted by microwave.....	39
1.6.	Motivation for this research.....	40
1.7.	Hypothesis.....	41
1.8.	Objectives.....	41
1.8.1.	General objective.....	41
1.8.2.	Specific objectives.....	42

CHAPTER II

Enhanced arsenic removal from water by a bimetallic material ZrO_x-FeO_x with high OH density

Abstract.....	43
2.1. Introduction.....	44
2.2. Experimental.....	45
2.2.1. Materials and chemical.....	45

2.2.2.	Synthesis of Bimetallic Oxyhydroxides	45
2.2.3.	Physicochemical Characterization	46
2.2.3.1.	Surface charge and pK _a 's distributions.....	46
2.2.3.2.	FTIR spectroscopy studies	46
2.2.3.3.	XRD spectroscopy studies	47
2.2.3.4	Transmission Electron Microscopy (TEM).....	47
2.2.4.	Adsorption Experiments	47
2.2.4.1.	Adsorption Isotherms.....	47
2.2.4.2.	Adsorption Kinetics.....	48
2.2.4.3.	Effect of anions on adsorption capacity.....	49
2.3.	Results and discussion.....	49
2.3.1.	Physicochemical Characterization	49
2.3.1.1.	Textural Properties	49
2.3.1.2.	Surface charge and pK _a 's distributions.....	50
2.3.1.3.	FTIR spectroscopy studies	52
2.3.1.4.	XRD spectroscopy studies	53
2.3.1.6.	Transmission Electron Microscopy.....	55
2.3.2.	Assembly Mechanism of Bimetallic Oxide.	57
2.3.3.	Adsorption Experiments	59
2.3.3.1.	Adsorption Isotherm	59
2.3.3.2.	Effect of pH on the Arsenic Adsorption Capacity of the ZrOx-FeOx.....	61
2.3.3.3.	Effect of Co-adsorbing anions	62
2.3.3.4.	Adsorption Kinetics.....	63
2.4.	Conclusions.....	65

CHAPTER III

New bimetallic adsorbent material based on cerium-iron nanoparticles highly selective and affine for arsenic(V)

Abstract	66
3.1. Introduction.....	67
3.2. Methods and Materials	69
3.2.1. Chemical materials.....	69
3.2.2. Experimental design and synthesis of adsorbent materials	69
3.2.2. Physiochemical characterization.....	70
3.2.3. Arsenic (V) adsorption test.....	71
3.3. Results and discussion.....	73
3.3.1. Experiments design.....	73
3.3.2. Materials characterization	76
3.3.2.1. Surface area and pore volume distribution.....	76
3.3.2.2. Structure and morphology studies of synthesized materials	77
3.3.2.3. Surface charge distribution studies.	79
3.3.2.4. FTIR, XRD and XPS studies.	81
3.3.3. Synthesis mechanism of Ce:Fe-P's	86
3.3.4. Arsenic adsorption test.....	89
3.3.4.1. Effect of pH and co-existing anions on the arsenic adsorption capacity ...	94
3.3.5. Arsenic adsorption mechanism onto Ce:Fe-P's	95
3.4. Conclusions.....	98

CHAPTER IV

Immobilization of metallic oxyhydroxides Ce^{3+} and Fe^{2+} on graphitic matrices to remove arsenate from water

Abstract	95
4.1. Introduction.....	96
4.2. Experimental	98
4.2.1. Materials and chemicals.....	98
4.2.2. Synthesis and characterization of adsorbent material	98
4.2.3. Adsorption experiments	99
4.3. Results and discussion.....	100
4.3.1. Effect of the cerium and iron concentration on the activated carbon surface in the arsenic removal.	100
4.3.2. Adsorbent material characterization.....	101
4.3.2.1. Physical properties	101
4.3.3. Chemical properties.	104
Anchorage mechanism of Ce-Fe in activated carbon.....	111
4.4. Adsorption experiments.....	113
4.4.1. Effect of solution pH and co-anion presents in the solution on the arsenic adsorption capacity.....	116
4.5. Conclusions.....	118

CHAPTER V

Modification of activated carbon with Ce³⁺ and Mn²⁺ ions in hydrolysis solution by hydrothermal synthesis to remove fluoride from aqueous solutions

Abstract	119
5.1. Introduction	120
5.2. Experimental	122
5.2.1. Synthesis of adsorbent materials	122
5.2.2. Characterization of adsorbent material.	122
5.2.3. Adsorption Experiments	123
5.3. Results and discussion.....	123
5.3.1. Effect of manganese and cerium concentration in activated carbon to remove fluoride.	123
5.3.2. Physicochemical Characterization	127
5.3.2.1. Textural proprieties of activate carbon unmodified and modified.	127
5.3.2.2. Activated carbon modified morphology by Scanning Electron Microscopy (SEM).	129
5.3.2.3. Surface charge and pK _a distribution	131
5.3.3. Mechanisms for anchoring metal oxides.....	136
5.3.4. Adsorption experiments.	140
5.3.4.1. Adsorption isotherms and kinetic of gAC-Ce and gAC-Ce:Mn.....	140
5.3.4.2. Effect of solution pH about the fluoride adsorption capacity.....	145
5.3.5. Fluoride adsorption mechanisms onto gAC-Ce:Mn.	146
5.3.5.1. Determination of the point of zero charge (PZC) and pK _a 's distribution of the gAC-Ce and gAC-Ce:Mn loaded with fluorides.	146
5.4. Conclusions.....	148

CHAPTER VI

Bimetallic oxyhydroxides anchored on graphitic matrices for their application in the removal of arsenic and fluorides from water.

Abstract	150
6.1. Introduction.....	151
6.2. Experimental	152
6.2.1. Synthesis of bimetallic oxyhydroxides	152
6.2.2. Physicochemical characterization of hybrid adsorbents materials	152
6.2.3. Adsorption Experiments	153
6.3. Results and discussion.....	154
6.3.1. Evaluation of the adsorption capacity of different carbon-based adsorbent materials.....	154
6.3.1.1. Surface charge and pK_a 's distribution of adsorbents materials	157
6.3.2. Characterization physicochemical of Ac-LaZr	160
6.3.3. Adsorption experiments	164
6.4. Conclusions.....	167

CHAPTER VII

General Discussion

7.1. Final Remarks	168
--------------------------	-----

CHAPTER VIII

Final Conclusions, perspectives, and scientific products

8.1.	Final Conclusions	178
8.2.	Perspectives.....	180
8.3.	Scientific Products.....	181
8.3.1.	List of publications.....	181
8.3.2.	Attendance to conferences	182
	References	184
	Annexes.....	235

List of Tables

CHAPTER I

Table 1.1.	Average arsenic and fluoride concentration in water for human use and consumption in Mexico.	5
Table 1.2.	Factors that affect the physisorption process	12
Table 1.3.	Bimetallic oxides and their ability to adsorb arsenic and fluorides.	31

CHAPTER II

Table 2.1.	Surface area and pore volume of studied materials.	50
Table 2.2.	Langmuir and Freundlich parameters for the arsenic adsorption onto FeO _x , ZrO _x and ZrO _x -FeO _x .	61

CHAPTER III

Table 3.1.	Solutions used to synthesize the bimetallic oxyhydroxides adsorbents	69
Table 3.2.	Surface area, pore volume and average pore diameter of studied materials.	76
Table 3.3.	Langmuir and Freundlich isotherm parameters for arsenic adsorption onto Fe-P's, Ce-P's and Ce:Fe-P's.	90
Table 3.4.	Comparison of As(V) adsorption capacities between Ce-Fe-P's and other reported adsorbents.	91
Table 3.5.	Kinetic constants for As(V) adsorption onto Fe-P's, Fe-P's and Ce:Fe-P's.	93

CHAPTER IV

Table 4.1.	Physicochemical Characterization of nonmodified and modified activated carbon.	104
Table 4.2.	Langmuir and Freundlich parameters for the As(V) adsorption onto AC, AC-Fe, AC-Ce and AC-Ce:Fe.	113

CHAPTER V

Table 5.1.	Percentage of Ce and Mn anchored in the gAC and its adsorption capacity.	127
Table 5.2.	Specific area and pore size distribution of granular activated carbon unmodified (gAC) and modified (gAC-Mn, gAC-Ce and gAC-Ce:Mn).	128
Table 5.3.	Langmuir and Freundlich parameters for the fluoride adsorption on activated carbon unmodified (gAC) and modified (gAC-Ce:Mn).	141
Table 5.4.	Langmuir parameters for the arsenic and fluoride adsorption in the gAC-Ce:Mn and gAC-Ce.	145

CHAPTER VI

Table 6.1.	Langmuir and Freundlich parameters of modified carbons in the fluoride adsorption.	155
Table 6.2.	Langmuir and Freundlich parameters of modified carbons in the arsenic adsorption.	155

Table 6.3.	Physicochemical Characterization of nonmodified and modified activated carbon.	163
-------------------	--	-----

CHAPTER VII

Table 7.1.	Ce-Fe and Zr-Fe bimetallic oxides for the removal of Arsenic	173
-------------------	--	-----

List of Figures

CHAPTER I

Figure 1.1.	Diagram of arsenic and fluoride contamination in the world and in Mexico.	6
Figure 1.2.	(a) Arsenic species diagram and (b) arsenic toxicity.	7
Figure 1.3.	(a) Fluoride species diagram and (b) fluoride toxicity.	8
Figure 1.4.	Schematic representation of the (a) adsorption process and its classification: (b) physisorption and (c) chemisorption.	11
Figure 1.5.	Forces of attraction: (a) dipole, (b) dipole-dipole, (c) London dispersion and (d) hydrogen bridge.	14
Figure 1.6.	(a) Solvation of the ion and (b) external sphere complex on the hydroxylated surface.	15
Figure 1.7.	Monodentate and bidentate internal sphere complexes.	17
Figure 1.8.	Hydration Mechanism of metallic oxide (modified from Dzombak & Morel, 1987).	18
Figure 1.9.	Representation of EDL according to the (a) Helmholtz model, (b) the Gouy-Chapman model and (c) the Gouy-Chapman-Stern model (Modified from Burt et al., 2014).	19
Figure 1.10.	Representation of the ETL Stern-Graham model.	20
Figure 1.11.	(a) Adsorption equilibrium, the same number of molecules adsorbed onto adsorbent and in the solution. (b) Langmuir and Freundlich isotherms.	22
Figure 1.12.	Langmuir model where the surface is perfectly smooth and homogeneous, and the adsorbate form a monolayer formation on surface (modified from Soares et al., 2016 [1]).	23
Figure 1.13.	Freundlich isotherm, the equilibrium on heterogeneous surfaces through multilayers.	24
Figure 1.14.	Stages of the adsorption process on activated carbon: (a) particle diffusion, (b) interparticle diffusion and (c) adsorption.	25

Figure 1.15.	Structure of activated carbon, (a) Schematic representation of the Norit model; (b) formation of pores of different size (potato chip model); (c) solute transport through macropores to micropores (Branched tree model) and (d) pore size.	27
Figure 1.16.	Chemical structure of activated carbon and the different groups on its surface (Modified from Cárdenas-López, et al., 2007 [2]).	28
Figure 1.17.	Possible interactions between oxygenated groups and oxides aquo-complexes.	32
Figure 1.18.	Temperature-Pressure Diagram for various synthesis techniques for ceramic materials.	38
Figure 1.19.	Schematic representation of the modification of granular activated carbon (CAG) with bimetallic oxyhydroxides.	41

CHAPTER II

Figure 2.1.	The nitrogen adsorption isotherms	50
Figure 2.2.	Point of zero charge (A) and pK_a 's distribution (B) of FeOx, ZrOx, and ZrOx-FeOx.	51
Figure 2.3.	FT-IR spectra of a) ZrOx, b) FeOx, and c) ZrOx-FeOx.	53
Figure 2.4.	XRD patterns of ZrOx, FeOx and ZrOx-FeOx with a step of 0.02° 2θ at 10 s per step. The symbols show the crystalline phase of each oxide.	54
Figure 2.5	HAADF image (A and C) for ZrOx-FeOx and EDS analysis (B and D) .	56
Figure 2.6.	HRTEM images of morphologies of ZrOx-FeOx and its Fourier transforms (insets).	56
Figure 2.7.	Micrograph, EDX and profiles of different points of a ZrOx-FeOx particle.	57
Figure 2.8.	Illustration of bimetallic oxyhydroxide (ZrOx-FeOx).	58
Figure 2.9.	(a) Punctual defects in crystalline structures: vacancies and interstitials. (b) Proposed schematic representation of the crystalline structure of iron and zirconium when forming a	

	bimetallic oxide (Modified figure from University of Cambridge, 2019).	59
Figure 2.10.	Adsorption isotherms of As(V) of FeOx, ZrOx and ZrOx-FeOx at pH 7 and 25 °C.	60
Figure 2.11.	Relationship between the Point of Zero Charge and pH on the As(V) adsorption capacity of ZrOx-FeOx.	62
Figure 2.12.	Effect of the presence of adsorbing anions on the arsenic adsorption capacity: mixture of 1, 5, 10, 30 y 50 mg L ⁻¹ of each anion (F^- , Cl^- , SO_4^{2-} , NO_3^- , PO_4^{2-} and bicarbonates (HCO_3^{2-} and $H_2CO_3^{2-}$)) in the presence of 2 mg L ⁻¹ of As(V) at pH 7(±0.2) and 25 °C.	63
Figure 2.13.	Adsorption kinetics of FeOx, ZrOx and ZrOx-FeOx oxyhydroxides at pH 7, 25 °C and As(V) initial concentration of 2 mg L ⁻¹ .	64

CHAPTER III

Figure 3.1.	(a) Effect of cerium and iron concentrations in the synthesis of hybrid materials and in their arsenic adsorption capacity when using an initial concentration of 5.6 mg L ⁻¹ of contaminant. (b) Arsenic adsorption capacity and (c) Ce and Fe content of three replicas of bimetallic oxyhydroxides Ce:Fe-P's (2:3) to demonstrate the synthesis reproducibility.	74
Figure 3.2.	FTIR of synthesized materials at different molar ratios of Ce:Fe.	75
Figure 3.3.	(a) Pore size distribution from N ₂ adsorption with BJH model and (b) N ₂ adsorption isotherms for Ce-P's, Fe-P's and Ce:Fe-P's.	77
Figure 3.4.	SEM images of (a) Ce-P's, (b) Fe-P's and (c) Ce:Fe-P's , and their respective EDS analysis.	78
Figure 3.5	Elementary mapping of bimetallic oxyhydroxides (Ce:Fe-P's).	78
Figure 3.6.	The particle size of the Ce:Fe-P's by laser diffraction using a zettameter NANOTRAC WAVE II Microtrac.	79
Figure 3.7.	(a) Surface charge distribution and (b) pK _a 's distribution for each material. (c) FT-IR of Fe-P's, Ce-P's and Ce:Fe-P's.	80

Figure 3.8.	XRD patterns of Ce-P's, Fe-P's and Ce:Fe-P's with a step of 0.02 ° 2θ at 10 s per step. The symbols show the crystalline phase of each oxide.	83
Figure 3.9.	The complete XPS spectra in the C 1s region referenced at 284.6 eV.	84
Figure 3.10.	XPS spectra in the C 1s region referenced at 284.5 eV for: (a) Fe 2p, (b) Ce 3d, (c) O 1s and (c) S 2p of Ce:Fe-P's.	85
Figure 3.11.	Mechanism of condensation reactions given by two steps called (a) initiation and (b) propagation and condensation [4].	87
Figure 3.12.	(a) Arsenic adsorption isotherm for metal oxyhydroxides Fe-P's, Ce-P's and bimetallic Ce:Fe-P's at pH 7 and 25 °C. (b) Arsenic adsorption isotherm for Ce:Fe-P's at low concentrations at pH 7 and 25 °C. The solid lines represent the Langmuir model and the dotted line the Freundlich model. (c) Adsorption kinetics of Fe-P's, Ce-P's and Ce:Fe-P's at pH 7, 25 °C and initial As concentration of 5 mg L ⁻¹ . (d) Relationship between the surface charge distribution and arsenic adsorption capacity of Ce:Fe-P's at different pH values.	92
Figure 3.13.	Effect of co-existing anions chloride (Cl^-), sulfate (SO_4^{2-}), nitrate (NO_3^-), phosphate (PO_4^{2-}) and carbonate (CO_3^{2-}) in the arsenic adsorption capacity of Ce:Fe-P's when using 5 mg L ⁻¹ of arsenic at pH 7 and 25 °C.	95
Figure 3.14.	(a) Surface charge distribution, (b) pK _a 's distribution and (c) FT-IR of Ce:Fe-P's before and after arsenic adsorption.	97
Figure 3.15.	Proposed arsenic adsorption mechanism on Ce:Fe-P's.	97

CHAPTER IV

Figure 4.1.	Effect of the cerium and iron concentration during the AC modification and consequently its arsenic adsorption capacity (q , $mg\ g^{-1}$).	101
Figure 4.2.	SEM images of the surface of (a) AC-Fe, (b) AC-Ce y (c) AC-Ce:Fe and their respective EDS.	102

Figure 4.3.	(a) N ₂ adsorption isotherms at 75 K and (b) pore distribution of modified carbons.	103
Figure 4.4.	(a) Content of cerium and iron in modified activated carbon and unmodified. (b) Surface charge distribution and (c) pK _a 's distribution of pristine activated carbon and modified activated carbon, using 0.1M NaCl as electrolytic support. (d) FT-IR of AC, AC-Fe, AC-Ce and AC-Ce:Fe.	105
Figure 4.5	XRD patterns of GAC, GAC-Ce, GAC-Fe and GAC-Ce-Fe with a step of 0.02 ° 2θ at 10 s per step. The letters show the crystalline phase of each material.	108
Figure 4.6.	XPS full spectra referenced to C 1s level at 284.6 eV for AC-Ce:Fe.	109
Figure 4.7.	XPS spectra (a) in the C 1s region referenced at 284.6 eV, (b) O 1s, (c) S 2p and (d) Fe 2p for AC-CeFe.	110
Figure 4.8.	(a) Dissociation of Activated Carbon and (b) Nucleophilic attack of the surface oxygenated groups of activated carbon on the metal aquo-complex (Fe and Ce).	112
Figure 4.9.	(a) Arsenic adsorption Isotherms at pH 7 and 25 °C. The solid line corresponds to the Langmuir model and the dotted line to the Freundlich model. (b) Adsorption kinetics of GAC, GAC-Fe, GAC-Ce and GAC-Ce-Fe at pH 7, 25 °C and As(V) initial concentration of 2 mg L ⁻¹ .	114
Figure 4.10.	(a) Effect of pH on the As(V) adsorption capacity of GAC-Ce:Fe at arsenic initial concentration. (b) Iron species diagram. (c) The effect of co-existing anions such as, chloride (Cl ⁻), sulfate (SO ₄ ²⁻), nitrate (NO ₃ ⁻), phosphate (PO ₄ ²⁻) and carbonate (CO ₃ ²⁻), in the arsenic adsorption capacity on the Ce-Fe (C ₀ = 0, 1, 5, 10, 30 and 50 mg L ⁻¹ of each anion in the presence of 2 mg L ⁻¹ of arsenic at pH 7 and 25 °C). (d) Phosphates adsorption capacity on the GAC-Ce:Ce.	117

CHAPTER V

-
- Figure 5.1.** Effect of Ce^{3+} and Mn^{2+} concentration on the adsorption capacity (q), **(a)** of nanoparticles in the presence of gAC, **(b)** of modified gAC with Ce:Mn and **(c)** Fluoride adsorption capacity of gAC-Ce:Mn (2:1), gAC-Ce, gAC-Mn and GAC. Adsorption experiments were carried out in batch with an initial fluoride concentration of 20 mg L^{-1} at pH 7 and $25 \text{ }^{\circ}\text{C}$. Adsorbent dose was 30 mg and solution volume 30 mL 125
- Figure 5.2.** **(a)** N_2 adsorption-desorption isotherms and **(b)** size pore distribution from the granular activated carbon (gAC) unmodified and modifies with manganese (gAC-Mn), cerium (gAC-Ce) and Ce:Mn (gAC-Ce:Mn). 128
- Figure 5.3.** **(a)** SEM and EDS images of the gAG-Mn, **(b)** SEM and EDS images of the gAG-Ce and, **(c)** SEM and EDS images of the gAG-Ce:Mn 130
- Figure 5.4.** **Figure 5.4. a)** Charge distribution (PZC) and **(b)** distribution of pK_a for the gAC, gAC.Mn, gAC-Ce and gAC-Ce: Mn. 132
- Figure 5.5** **Figure 5.5. (a)** Fourier Transform Infrared (FTIR) and **(b)** X-ray diffraction (XRD) of gAC unmodified and modified. The symbols show the crystalline phase of graphite, goethite, hematite and cerium oxide, in a step size of $0.02 \text{ }^{\circ} 2\theta$ in 10s per step. 134
- Figure 5.6.** XPS spectra in the **(a)** C 1s region referenced at 284.5 eV for: **(b)** Ce 3d, **(c)** O 1s, **(d)** S 2p, of gAC-Ce:Mn. 136
- Figure 5.7.** **(a)** gAC surface oxygenated groups in acidic and basic medium. **(b)** Adsorption and stabilization of the surface charge by anions. **(c)** Crystal growth and $M(OH)_2^0$ adsorption. **(d)** and **(e)** Metal ion partial charge. 138
- Figure 5.8.** **(a)** Electrostatic attraction and repulsion between manganese hydroxy complexes and cerium oxide in the propagation process (modified from Gutiérrez Martínez et al, 2016). Anchoring mechanism of: **(b)** Ce:Mn and **(c)** removal of manganese from the particles surface. 139

Figure 5.9	Anchoring mechanism of Ce(III) onto surface oxygenated groups of gAC.	140
Figure 5.10.	(a) Fluoride adsorption isotherms on gAC, gAC-Mn, gAC-Ce and gAC-Ce: Mn, at pH 7 (± 0.2) and 25 ° C. The solid line indicates the Langmuir model. (b) Fluoride adsorption kinetics at fluoride initial concentration (C_0) of 20mg L ⁻¹ , pH 7 and 25 ° C. Adsorption isotherms of (c) fluoride and (d) arsenic on CAG-Ce:Mn and GAC-Ce in the presence of both contaminants at pH 7 (± 0.2) and 25 ° C. The solid line indicates the Langmuir model.	142
Figure 5.11.	Surface charge distributions of the materials studied at 25 ° C (dotted (gAC-Ce:Mn) and solid (gAC-Ce) line) and effect of pH on the fluoride adsorption capacity (square (gAC-Ce:Mn) and circle (gAC-Ce) symbols).	146
Figure 5.12.	(a) Load distribution (PZC) and distribution of pKa for GAC-Ce: Mn (b) and GAC-Ce (c) before and after the fluoride ion adsorption process. (d) Fluoride adsorption mechanism on the material modified with Ce (III).	147

CHAPTER VI

Figure 6.1.	(a) Fluoride and (b) arsenic adsorption isotherms on Ac-CeZr, Ac-LaZr, Ac-CeFe and Ac-CeMn, at pH _i 7 (± 0.2) and 25 °C. The solid line indicates the Langmuir model.	156
Figure 6.2.	(a) Fluorides and (b) arsenic adsorption kinetics of the adsorbent materials at pH 7, 25 °C and fluorides and arsenic initial concentration of 10 and 25 mg L ⁻¹ , respectively.	157
Figure 6.3.	(a) Point of zero charge (pH _{PZC}) and (b) surface distribution (pKa's) of unmodified and modified carbons.	158
Figure 6.4.	Schematics represent of electrostatic attraction and repulsion onto adsorbent material with high OH group density.	160
Figure 6.5	(a) SEM and (b) EDS micrograph of LaZr-modified Ac.	161

Figure 6.6.	(a) N ₂ adsorption isotherms at 75 °K and pore distribution of (b) micropores, mesopores, (c) super-micropores and ultra-micropores of modified carbons.	162
Figure 6.7.	(a) FTIR and (b) XRD of the Ac and LaZr-modified Ac.	163
Figure 6.8.	Effect of arsenic and fluoride on the adsorption capacity of GAC-LaZr. Adsorption kinetics at pH 7 and 25 ° C. Initial concentration of (a) fluorides and (b) arsenic of 5 and 0.5 mg g ⁻¹ , respectively, of GAC-LaZr.	165
Figure 6.9.	(a) Breakdown curves for arsenic and fluorides in a packed bed column at pH 7 and EBCT for 10 min. (b) Breakdown curves for arsenic.	166

Resumen

Inmovilización de oxihidróxidos bimetálicos sobre matrices gráficas para remover arseniato y fluoruros del agua

El exceso de arsénico y fluoruro en el agua ha dado lugar a graves problemas de salud, por lo que son considerados contaminantes prioritario para ser eliminado del agua potable por la Organización Mundial de la Salud (OMS). Varias investigaciones han demostrado que los óxidos cerámicos han demostrado ser excelentes materiales adsorbentes para varios aniones en soluciones acuosas. Además, la combinación de estos óxidos ha mostrado tener un efecto sinérgico en cuanto a la capacidad de adsorción de arsénico y fluoruro. Esto es debido a que los óxidos bimetálicos creados heredan las propiedades de los óxidos prístinos que lo conforman, como la elevada densidad de grupos OH. Por lo anterior, en esta investigación se sintetizaron óxidos bimetálicos de Zr-Fe y Ce-Fe por un método hidrotermal asistido por microondas. Mediante el mismo método se modificó carbón activado (F400) con una solución bimetálica de Ce-Fe, Ce-Mn y La-Zr. Se caracterizaron los materiales sintetizados mediante FTIR, distribución de carga y pK_a 's, XRD y XPS además, se estudió la capacidad y cinética de adsorción de los materiales.

Los resultados mostraron que el método hidrotermal fue bastante eficiente para formar óxidos bimetálicos con una alta capacidad de adsorción. La capacidad de adsorción de arsénico de los oxihidróxidos bimetálicos sintetizados en este trabajo fue de hasta 179.8 mg g⁻¹. La excelente capacidad de adsorción del Ce:Fe-P's y ZrOx-FeOx se atribuyó en gran medida a la alta densidad de grupos OH en su superficie y a la excelente afinidad de estos materiales por el arsénico. La morfología del bimetal Ce:Fe-P's fue de jerarquía tridimensional en forma de flores, lo cual resultó en una mayor exposición de los grupos activos del oxihidróxido bimetálico dando como resultado una alta capacidad de adsorción de arsénico. Además que el pH_{PZC} y el pH de la solución no tienen un efecto negativo en la

capacidad de adsorción de Ce:Fe-P's y ZrOx-FeOx, debido a que la adsorción de arsénico se lleva a cabo principalmente por intercambio de ligandos con los grupos OH del material adsorbente.

Por otro lado, la presencia de carbón activado inhibe la formación de óxidos bimetálicos, ya que solo uno de los óxidos que se encuentra en solución se ancla en la superficie del carbón activado. Por ejemplo, cuando se tiene en solución Fe y Ce el metal que se ancla sobre la superficie del carbón activado es el Fe. En este caso, se observó que el cerio tiene un efecto en el tamaño de partícula de los óxidos de Fe, por lo tanto, actúa como un agente complejante. La morfología, el pH_{PZC} y pH de la solución influyen en la capacidad de adsorción de arsénico de los óxidos bimetálicos anclados sobre el carbón activado. Los carbones modificados con las soluciones metálicas mostraron capacidades de adsorción de arsénico y fluoruros de hasta 8.2 and 11 $mg\ g^{-1}$, respectivamente. La caracterización mostro que los grupos carboxílicos y fenólicos juegan un papel importante en el anclaje de los óxidos metálicos en la superficie del carbón activado, debido a que los cationes metálicos (Ce o Fe, por ejemplo) se anclan a estos grupos funcionales mediante un desplazamiento de un H^+ .

Finalmente, los resultados presentados en esta tesis doctoral demuestran el gran potencial que tienen los óxidos metálicos cuando estos forman oxihidróxidos bimetálicos y posteriormente la modificación de carbón activado con soluciones bimetálicas, para la remoción de arsénico y fluoruros de soluciones acuosas. Esta investigación logró un importante avance en el desarrollo de materiales adsorbentes basados en oxihidróxidos bimetálicos para la remoción de contaminantes prioritarios en agua. Debido a lo anterior se obtuvo la patente: "Compuestos bimetálicos basado en Cerio y Fierro y composito polimérico para la remoción de contaminantes del agua. IPICYT", MX/a/2019/010551.

Palabras clave: Óxidos bimetálicos, Carbón activado, Zirconio, Hierro, Cerio, Manganeso, Lantano, Arsénico, Fluoruros.

Abstract

Immobilization of bimetallic oxyhydroxides on graphitic matrices to remove arsenate and fluorides from water

The excess of arsenic and fluoride in the water has led to serious health problems, which is why they are considered a priority pollutant to be eliminated from drinking water by the World Health Organization (WHO). Various investigations have shown that ceramic oxides have proven to be excellent adsorbent materials for various anions in aqueous solutions. Furthermore, the combination of these oxides has been shown to have a synergistic effect regarding the arsenic and fluoride adsorption capacity. This is because the bimetallic oxides created inherit the properties of the pristine oxides that make it up, such as the high density of OH groups. Therefore, in this research bimetallic oxides of Zr-Fe and Ce-Fe were synthesized by a microwave-assisted hydrothermal method. Activated carbon (F400) was modified by the same method with a bimetallic solution of Ce-Fe, Ce-Mn and La-Zr. The synthesized materials were characterized by FTIR, charge distribution and pK_a 's, XRD and XPS, in addition, the adsorption capacity and kinetics of the materials were studied.

The results showed that the hydrothermal method was quite efficient to form bimetallic oxyhydroxides with a high adsorption capacity. The arsenic adsorption capacity of the bimetallic oxyhydroxides synthesized in this work was up to 179.8 mg g^{-1} . The excellent adsorption capacity of Ce: Fe-P's and ZrOx-FeOx was largely attributed to the high density of OH groups on their surface and the excellent affinity of these materials for arsenic. The morphology of the Ce: Fe-P's bimetal was of a three-dimensional hierarchy in the shape of flowers, which resulted in a greater exposure of the active groups of bimetallic oxyhydroxide,

resulting in a high arsenic adsorption capacity. In addition, the pH_{PZC} and the solution pH do not have a negative effect on the adsorption capacity of Ce: Fe-P's and ZrOx-FeOx

On the other hand, the presence of activated carbon inhibits the formation of bimetallic oxides, since only one of the oxides is anchored on the activated carbon surface. For example, when Fe and Ce are in solution, the metal that is anchored on the activated carbon surface is Fe. In this case, it was observed that cerium cannot be anchored in the activated carbon has an effect on the particle size of the anchored Fe oxides, therefore, it acts as a complexing agent. The morphology, pH_{PZC} and solution pH influence the arsenic adsorption capacity of the bimetallic oxyhydroxides anchored onto activated carbon. The carbons modified with the metallic solutions showed arsenic and fluoride adsorption capacities of up to 8.2 and 11 mg g^{-1} , respectively. The characterization showed that the carboxylic and phenolic groups play an important role in the anchoring of metal oxides on the activated carbon surface.

Finally, the results presented in this doctoral thesis demonstrate the great potential of the functionalization of two metal oxides to form bimetallic oxyhydroxides and the modification of activated carbon with nanoparticles of metal oxyhydroxides, for the removal of arsenic and fluorides from aqueous solutions. This research achieved an important advance in the development of adsorbent materials based on bimetallic oxyhydroxides for the removal of priority contaminants in water. Due to the above, the patent was obtained: "Bimetallic compounds based on Cerium and Iron and polymeric composition for the removal of contaminants from water. IPICYT", MX/a/ 2019/010551.

Key words: Bimetallic oxides, Activated carbon, Zirconium, Iron, Cerium, Manganese, Lanthanum, Arsenic, Fluorides.

Structure of this thesis

Chapter I presents an overview of the problematic of arsenic and fluoride, priority pollutants of water. Methodologies to control pollution, emphasizing on the adsorption process. The physical and chemical characteristics of activated carbon are also presented in this chapter, and the importance of tailoring this adsorbent to increase its affinity for anions arsenic and fluoride. The methodologies to modify it with metallic oxyhydroxides.

Chapter II reports the synthesis of bimetallic oxyhydroxide, ZrOx-FeOX with high arsenic adsorption capacity. Besides, the analytic techniques helped to elucidate the way that those pristine metal ions interact with each other to form a bimetal oxyhydroxide with high OH group density.

Chapter III reports the functionalization of cerium and iron to create a new bimetal oxyhydroxide with a morphology of three-dimensional hierarchy. Besides, the analytic techniques helped to elucidate the mechanism of formation of bimetal oxyhydroxide. Finally, de adsorption studies show the high arsenic adsorption capacity of Ce:Fe-P's, due on its high OH groups density.

Chapter IV discusses the Immobilization of metallic oxyhydroxides Ce^{3+} and Fe^{2+} on graphitic matrices of activated carbon. Arsenic and fluoride adsorption capacity was studied in this chapter with emphasis arsenic adsorption. The effect of the presence of two metallic ions and activated carbon in the synthesis was discussed.

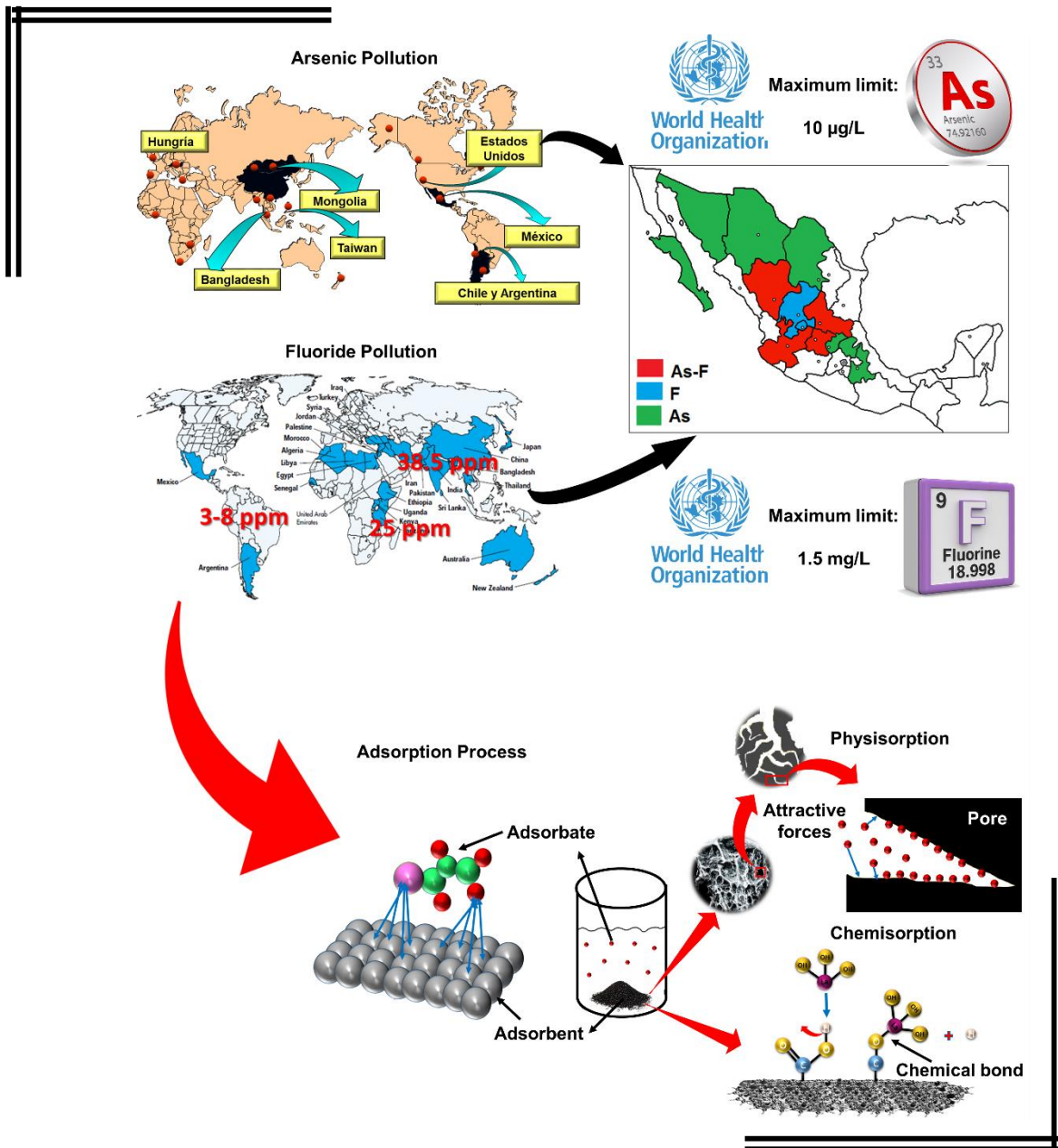
Chapter V present the modification of activated carbon with Ce^{3+} and Mn^{2+} ions in hydrolysis solution by hydrothermal synthesis. Fluoride adsorption capacity was evaluated and effect of pH on adsorption capacity. In this chapter was discussed the anchoring mechanism of metallic ions and effect of Mn^{2+} on the morphology of cerium oxyhydroxide.

Chapter VI presents a comparison in terms of arsenic and fluoride adsorption capacity of modified activated carbon with various bimetallic solutions (Ce-Fe, Ce-Mn, La-Zr and Ce-Zr). Continuous adsorption study using La-Zr modified activated carbon packed bed column is shown in the present chapter.

Finally, the general remarks and conclusions of this research are presented in *Chapter VII* and *Chapter VIII*, respectively.

CHAPTER I

Introduction



CHAPTER I

Introduction

Currently, there is a serious problem in terms of pollution and water quality due to the presence of heavy metals and toxic metalloids, which have adverse effects on the environment and living organisms at low concentrations. Sometimes the contamination has a non-anthropogenic origin that makes the problem much more difficult to identify and solve, as is the case with arsenic and fluorine. Arsenic (As) is the twentieth most abundant element in nature, and its mobilization is due to a combination of natural processes such as weathering reactions, biological activity and volcanic emissions, as well as through a series of anthropogenic activities, such as the use of pesticides, herbicides and preservatives for wood [5–7]. Arsenic consumption in concentrations greater than $50 \mu\text{g L}^{-1}$ can cause skin changes, damage to the main organs of the body, arsenicosis and some types of cancer [6].

On the other hand, the water contamination by fluorides (F^-) is mainly due to the water-geological material interaction. It has been determined that the source of F^- is found in the fractured volcanic rocks, so that when the groundwater circulates through the fractures it interacts with the vitreous matrix and with minerals such as topaz, as a consequence the F^- quickly passes to the solution. Consuming water with high fluoride levels for long periods of time represents a health risk. It is known that fluoride is an essential element for the dental health of the population, but in high concentrations ($> 1 \text{ ppm}$) it causes dental and skeletal fluorosis [8].

It is well documented that the presence of arsenic and fluoride in groundwater intended for human consumption is a problem that affects millions of people around the world. High

As and F⁻ concentrations have been found in natural underground sources that provide drinking water for millions of inhabitants in countries such as: Bangladesh, West Bengal, Argentina, China, Mexico, USA, Thailand, Ethiopia, Kenya, South Africa, Tanzania, Chile and Japan [9]. Consequently, the World Health Organization (WHO) has established a maximum allowable limit for arsenic and fluoride in drinking water of 10 g μL^{-1} (in 1993) and 1.5 mg L^{-1} (WHO, 1991), respectively. However, complying with regulations can be critical in many parts of the world, mainly in developing countries [10]. In addition, it should be noted that the maximum permissible limits in water for these two contaminants will decrease to not detectable for arsenic and to 0.7 mg L^{-1} for fluorine in the coming years (US EPA; NOM-041-SSA1-1993).

Due to the above, it is necessary to invest in the development of new materials and more efficient technology for the removal of priority pollutants. There are several methodologies available for the arsenic and fluorides removal, such as: coagulation-flocculation [11,12], ion exchange [13], membrane filtration, reverse osmosis, precipitation [14] and adsorption [15,16]. However, its effectiveness depends on the characteristics of the test water, the volume to be treated and the target concentrations. Among the technologies available for the control of arsenic and fluoride contamination, adsorption is considered a promising process for the removal of these priority contaminants. Numerous studies have reported the benefits of the adsorption process in the As and F⁻ removal from aqueous solutions [7,17–19]; the success of this process depends on the physicochemical properties of the adsorbent materials, among which are organic and inorganic materials. In this sense, carbon-based adsorbents (nanotubes, fibers, graphene, and granular activated carbons) modified with metal oxyhydroxides have received a great deal of attention in recent years due to their acceptable adsorption capacity and selectivity. However, there are still

challenges to overcome to develop more efficient materials, for example capable of removing more than 1.5 mg g^{-1} of fluorides at concentrations less than 5 mg L^{-1} and more than 1 mg g^{-1} of arsenic at a concentration less than $50 \text{ } \mu\text{g L}^{-1}$ [20,21].

In the last three years there has been a special interest in the use of powdered bimetallic oxides (e.g. Fe-Ti, Al-Ce, Fe-Mn, Ce-Zr) for the As (V) and F^- removal from solutions. aqueous, since they exhibit better adsorption performance due to their high specific area and higher hydroxyl groups concentration compared to individual metal oxides [22–24]; of these the Zr-Fe, Ce-Fe and Ce-Mn mixture has shown promising results. However, the nanometric size of powdered bimetallic oxides limits their application in continuous systems, which is why there is a need to support these bimetallic compounds in a matrix. Activated carbon is a very versatile commercial material that is used in large-scale water treatment, in addition, it has the great advantage that its surface can be modified to make it a more related and selective material for various pollutants. For this reason, the objective of this work is to take advantage of the qualities of activated carbon to anchor bimetallic oxides of Ce:Fe and Ce:Mn on its surface, in order to produce a hybrid adsorbent material with high As(V) and F^- adsorption capacity.

1.1. Water contamination by Arsenic and Fluorides in Mexico and in the world

The main sources of arsenic and/or fluoride exposure for the human population are food, water, soil, and air. The arsenic presence in water can be attributed to different sources and dispersal processes. Among the main natural sources of arsenic emission to the environment are volcanic eruptions (WHO, 2001), and the composition of the rocks that are

part of the aquifers [25]. Anthropogenic sources of arsenic emission include industrial mining, metal smelting, pesticides, wood preservatives and waste disposal (WHO, 2001).

On the other hand, the fluorides concentration in the water of an aquifer depends on several factors, among which the fluorine concentration in the mineral, decomposition, dissociation, dissolution, residence time and chemical reactions kinetics stand out. Some studies indicate that the fluorine solubility in water differs according to the rock type [26]. The most common fluorine mineral in the earth's crust is fluorspar, which contains fluorite or calcium fluoride, cryolite, and apatite; it is generally a compound of calcium, fluoride, carbonates, and sulfates [27].

The presence of As(III and V) and F^- in groundwater at high concentrations, has generated concern by various regulatory bodies, because the ingestion of these chemical elements are causing serious health problems throughout the world [5,28,29]. Among the countries affected by the presence of high arsenic and/or F^- concentrations in water are (Figure 1.1): Taiwan, Mongolia, China, Argentina, Chile, Bolivia, Brazil, Mexico, Germany, Hungary, USA [29], Bangladesh [30,31], India [32], Vietnam [33], and Thailand [34]. To tackle the arsenic problem, the World Health Organization (WHO) lowered the maximum allowable limit for arsenic in water from 50 to 10 $\mu g L^{-1}$ and its goal is to make it undetectable. Regarding fluoride, the WHO establishes that the maximum permissible limit should be 1.5 $mg L^{-1}$ in drinking water, but due to previous studies, this concentration will decrease to 0.7 $mg L^{-1}$ in the coming years. On the other hand, in Mexico, the presence of arsenic and/or fluorides has been recorded in the aquifers of the states of Aguascalientes, Coahuila, Chihuahua, Durango, Guanajuato, Hidalgo, Jalisco, Sonora, San Luis Potosí and Zacatecas

(Table 1.1), which exceed the maximum limit established by NOM-127-SSAI-1994 ($50 \mu\text{g L}^{-1}$ and 1.5 mg L^{-1} of As and F^{-} , respectively (CONAGUA 1999)).

Table 1.1. Average arsenic and fluoride concentration in water for human use and consumption.

State	Municipality	Fluoride concentration mg L^{-1}	Arsenic concentration mg L^{-1}
Aguascalientes			
	Aguascalientes	2.12	-
	Calvillo	1.95	-
	Jesús María	2.80	-
	Pabellon de Arteaga	1.95	-
	Rincon de Ramos	2.20	-
Chihuahua			
Camargo-Jiménez	Camargo	1.50	0.044
	Jiménez	1.70	0.103
	San francisco de Conchos	3.72	0.261
Delicias-Meoqui	Aldama	2.40	0.085
	Delicias	1.70	0.040
	Julimes	5.90	0.143
Delicias-Meoqui	La Cruz	2.70	0.800
	Meoquí	5.30	1.130
	Rosales	2.50	0.080
	Saucillo		0.470
Comarca Lagunera			
Coahuila	Francisco I. Madero	-	0.200
	Matamoros	-	0.510
	San Pedro	-	0.140
Durango			
	Tlahualilo		0.290
	Valle del Guadina	3.23	0.064
	Cd. de Durango	5.37	0.052
	Guadalupe Victoria	1.86	0.040
Hidalgo			
	Zimapán	-	0.090
Jalisco			
	Lagos de Moreno	2.40	-
	San Juan de los Lagos	1.89	-
	Teocaltiche	4.40	-

Gleason, 2010

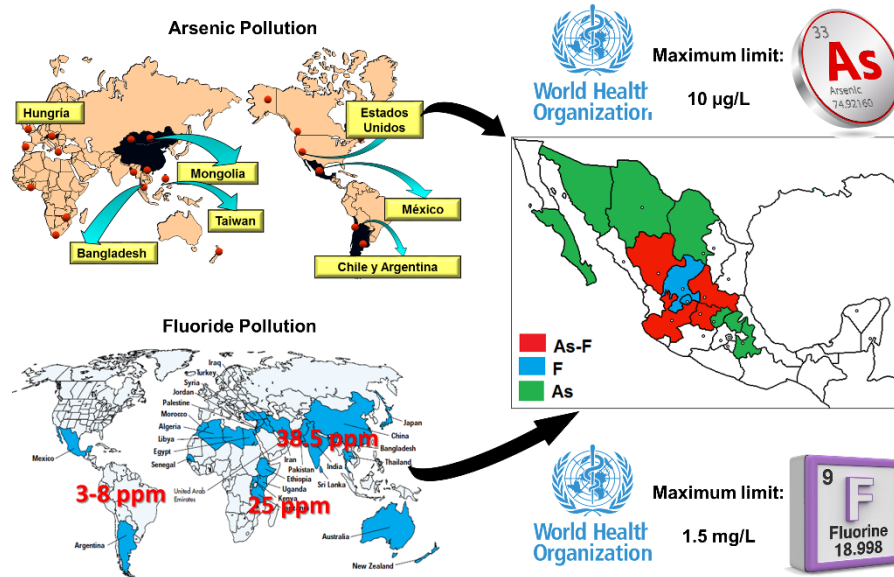


Figure 1.1. Diagram of arsenic and fluoride contamination in the world and in Mexico.

1.2. Chemistry and Toxicity of Arsenic and Fluoride

Arsenic is a metalloid that is present with different oxidation states (As^0 , As^{-3} , As^{+3} , As^{+5}) in inorganic and organic forms (Vaclavikova et al., 2007). In natural waters the inorganic forms of arsenic are generally found as dissolved species forming oxyanions. Arsenite ($As(III)$) and arsenate ($As(V)$) are the two main species found in water (Hyun and Gi, 2010; Rahman et al., 2014). The mobility and arsenic distribution depend on the interactions of geochemical factors such as pH and oxidation-reduction reactions since these control the arsenic oxidation states. Under oxidizing conditions ($pHs < 6$), $H_2AsO_4^-$ is the dominant species; while at pH greater than 6, $HAsO_4^{2-}$ predominates (Figure 1.2a). Under reductive conditions ($pHs > 9$) the dominant species is H_3AsO_3 (Vaclavikova et al., 2007).

The arsenic presence in water affects millions of people in the world since this element is highly toxic. As(III) is 50 times more toxic than As(V) because As(III) reacts with enzymes of the human respiratory system and, in turn, As(III) is 4 to 10 times more soluble in water than As(V) (Jain and Ali, 2000; Seung-Hyun and Hun-Gi, 2010). However, As(III) oxidizes instantly when in contact with the air, in such a way that As(V) is the one of interest in water treatment systems. Consumption of inorganic arsenic at low concentrations can cause various symptoms of intoxication such as: gastrointestinal upset, vomiting, shock, seizures, and coma. Chronic exposure to this pollutant, at concentrations of $50 \mu\text{g L}^{-1}$, is associated with cancer of the lung, skin, internal organs, bladder, cardiovascular and neurological diseases, complications in pregnancy (abortion and premature delivery) and death if necessary. consumed in doses greater than 60 mg L^{-1} . A well-known chronic disease due to prolonged ingestion of arsenic-contaminated water is arsenicosis (Figure 1.2b), which is characterized by hyperpigmentation and hyperkeratosis (Choong et al., 2007; Ferreccio et al., 2000; Han et al. , 2002; Hughes, 2002).

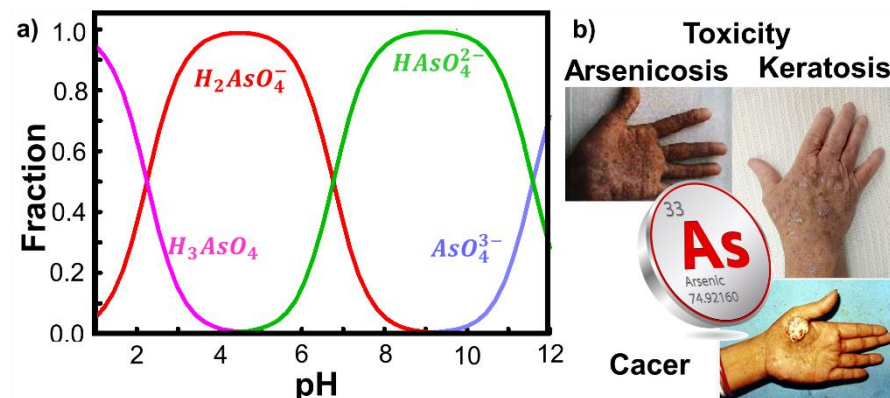


Figure 1.2. (a) Arsenic species diagram and (b) arsenic toxicity.

On the other hand, fluoride (F^-) is the reduced state of fluorine that is the most electronegative of all the elements of the periodic table (estimated standard power +2.85 V), for this reason it is rarely found in nature in an elemental state. In aqueous solution it is found as a fluoride ion, which tends to form complexes with metal ions. The most representative minerals that contain fluorine in their chemical composition are fluorite (CaF_2), fluorapatite [$Ca_5(PO_4)_3F$], cryolite (Na_3AlF_6), villiaumite (NaF), topaz [$Al_2(SiO_4)F_2$] and sellaite (MgF_2) (Nagendra, 2003). According to the speciation diagram of fluorine (Figure 1.3a), at pH values less than 5, it associates with the hydrogen ion (H^+) to form hydrogen fluoride (HF) and at pH values greater than 5 it is found as a fluoride ion (F^-). The presence of fluoride at levels from 0.5 to 1.0 $mg\ L^{-1}$ is beneficial for the production and maintenance of bones and teeth, however, an intake of water with high fluoride concentrations ($>1.5\ mg\ L^{-1}$) can cause bone fluorosis or dental (Figure 1.3b) (Fan et al., 2003). The excessive consumption of fluorides can cause various diseases such as osteoporosis, arthritis, brittle bones, cancer, infertility, brain damage, Alzheimer's syndrome, and thyroid disorder.

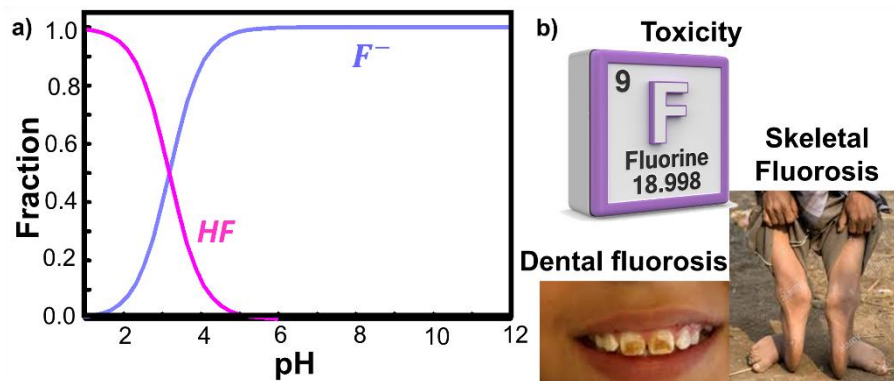


Figure 1.3. (a) Fluoride species diagram and (b) fluoride toxicity.

1.3. Methods to remove arsenic(V) and fluorides from water

Various treatment methods have been developed for the arsenic and/or fluorides removal from water, such as sorption and ion exchange [35], precipitation [36], coagulation and flocculation [37,38], reverse osmosis [39,40], membranes [41], electrodialysis [36] and biological processes [42].

Coagulation-precipitation methods involve the precipitation or co-precipitation of the contaminant using coagulating agents such as salts of lime, aluminum, calcium, and magnesium, as well as some polymers and chitin. The use of these reagents creates a colloidal suspension to promote chemical dissolution and destabilization of particles to create flocs. The resulting flocs are removed from the aqueous solution by sedimentation or filtration. However, coagulation-precipitation has some disadvantages such as residual concentrations of reagents used in the treated water and the formation of toxic sludge. These disadvantages limit its application in the removal of contaminants from water.

In membrane techniques, a high-pressure flow is passed through a microporous membrane. Depending on the type of membrane (ultrafiltration (UF), nanofiltration (NF) and reverse osmosis (RO)) it will allow particles from 10 to 1×10^{-4} μm to pass, which allows the filtration of water. MF and RO have the disadvantage of being expensive technologies for water purification, so their use is justified only when the removal of various compounds is required. In addition, electrotreatments such as electrodialysis, membrane electrolysis and electrochemical precipitation for the fluoride and metals removal have also been investigated less extensively. Although they are highly efficient in removing pollutants, they have the disadvantage of being a technique with a high operating cost caused by the price of the membranes and the high energy consumption.

Ion exchange is a technology that can be applied successfully and consists of exchanging the contaminant to be removed from the solution at the same time as it is replaced by a non-toxic compound in the resin. There are several exchange resins and they are named depending on whether the ion type to be exchanged (cationic or anionic). A polymeric resin exchanges negatively charged ions with the solution that immobilizes fluoride or arsenic [13]. The disadvantage of this technique is the high cost of ion exchangers since the problem of arsenic and fluorides ingestion continues mainly in marginalized communities. Therefore, the application of these technologies continues to be little feasible.

On the other hand, adsorption is probably the most sustainable technique that can be applied in the removal of both arsenic and fluorides in aqueous solutions [14,15]. Adsorption is characterized by the use of the adsorbent materials where arsenic or fluoride is concentrated on their surface. However, the success of the operation depends on the arsenic and fluoride concentration in the effluent, the volume of water to be treated and the adsorption capacity of the adsorbent material. Various materials have been tested to remove these contaminants and include activated carbon, metal oxides, activated alumina, fly ash, clay, minerals and soils, natural materials, among others.

1.4. Adsorption process

1.4.1. Fundamentals of adsorption

Adsorption is a mass transfer process in which one or more substances (adsorbates) present in a fluid, whether liquid or gaseous, accumulate in a solid phase (adsorbent) and are removed from the fluid (Figure 1.4a) [43]. Adsorption is considered as a physicochemical wastewater treatment process, which has gained importance due to the quality of the treated effluents, which contain low concentrations of dissolved organic compounds and even metal

ions [44]. Given the above, adsorption is considered one of the best techniques and one of the most used for the removal of organic and inorganic contaminants from water [45]. The recovery of costly toxic substances from wastewater is a further advantage of the adsorption process. With the selection of a suitable adsorbent, the adsorption process can be a promising technique for the removal of contaminants such as As and F^- [20,21,46]. This method will be inexpensive if the adsorbent material used is cheap and does not require any additional pretreatment [47].

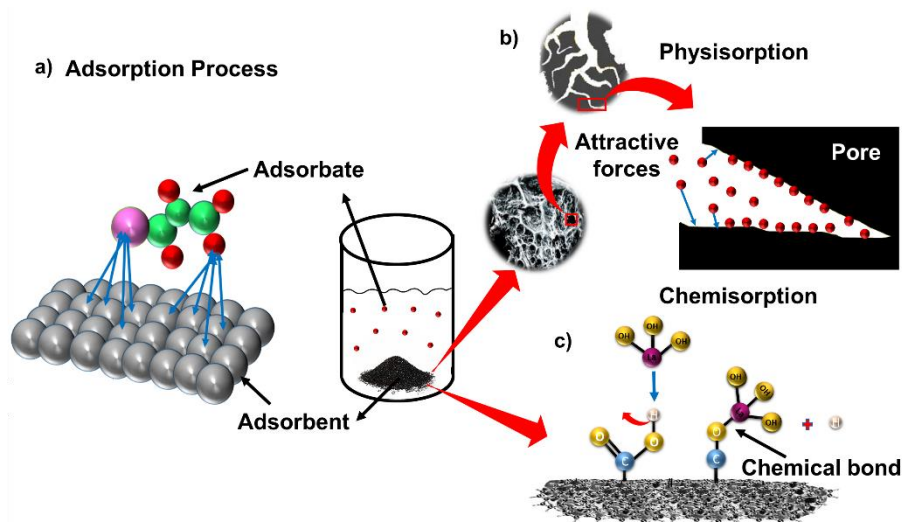


Figure 1.4. Schematic representation of the **(a)** adsorption process and its classification: **(b)** physisorption and **(c)** chemisorption.

Adsorption can be classified into physisorption and chemisorption depending on the nature of the forces that interact between the adsorbate and the adsorbent (Figure 1.4). The attraction between the solid and the molecule by electrostatic forces is called physisorption. However, when there is the formation of a chemical bond between the adsorbate and the adsorbent, the term chemisorption is used (Bansal and Goyal, 2005). It is important to

mention that physical adsorption (physisorption) is affected by various factors such as temperature, pH, nature of the adsorbate and the adsorbent, among others (see Table 1.2).

Table 1.2. Factors that affect the physisorption process

Factor	Effect in the physisorption process
Temperature	The higher the temperature, the lower the adsorption. This is because the adsorbed molecules have a higher vibrational energy and therefore can be desorbed from the surface.
pH	Regulates the degree of ionization of the species to be adsorbed. There is a low adsorption of the solute when it is ionized (charged).
Adsorbent nature	Some inorganic compounds or ions are adsorbed to a greater or lesser extent. So, it is important to consider whether these are neutral or ionizable molecules.
Solvent nature	The solvent has an important effect since it competes for the adsorption sites of the solute.
Adsorbent specific area	The extent of adsorption is directly proportional to the specific area of the adsorbent material
Porous structure	It is important to consider the size of pores in which molecules can access them.

1.4.1.1. Nature of physisorption forces

Physisorption is carried out through an interaction between the adsorbate and the surface of the adsorbent material and they always act as attractive forces between adjacent atoms. These interactions can be Van der Waals-type forces caused by the interaction of dipoles, quadrupoles, and dispersive forces (London forces) (Figure 1.5).

Chemical dipole moment is defined as the measure of the intensity of the attractive force between two atoms (Figure 1.5a). It is the expression of the asymmetry of the electric charge in a chemical bond [48]. When two molecules with dipoles move closer to each other, they experience a repulsive or attractive force that depends on the charge on the dipole. The dipole-dipole forces are then forcing of attraction between the positive and negative sides of the molecules (Figure 1.5b). Although some molecules do not present a dipole moment, they do have a quadrupole moment in which their interaction involves symmetric molecules with atoms of different electronegativity, giving rise to dipole-quadrupole and quadrupole-quadrupole interactions.

In London scattering forces are weak intermolecular forces that arise from interactive forces between temporary multipoles in molecules without permanent multipole moment, therefore, the formation of instantaneous dipoles takes place. A dipole moment is induced when a molecule approaches another in which electrons are temporarily out of symmetry, leading to a temporary attraction of the dipole [49] (Figure 1.5c). London scattering forces is the only attractive intermolecular force at great distances, present between neutral atoms and is the main attractive force between nonpolar molecules. Without London's forces, there would be no attractive forces between the atoms of a noble gas, and they could not exist in the liquid form. Hydrogen bridging force or hydrogen bonding is the predominantly attractive

electrostatic force between an electronegative atom and a hydrogen atom covalently bonded to another electronegative atom. When hydrogen binds to an electronegative atom, the molecule becomes strongly polarized, leading to hydrogen with a positive charge that is strongly attracted to the unshared electrons of another electronegative atom [48] (Figure 1.5d).

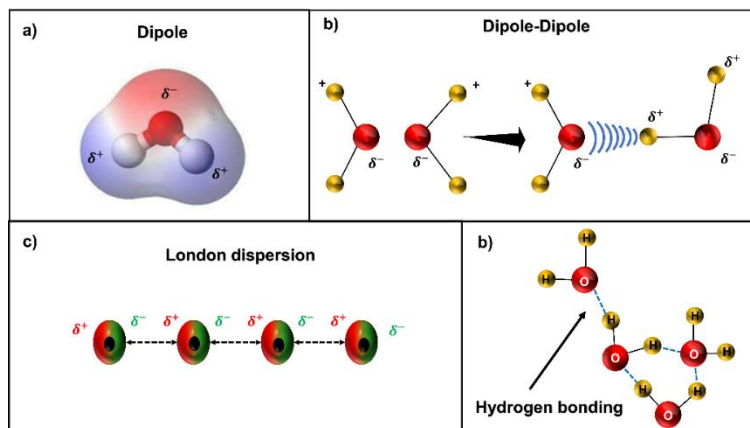


Figure 1.5. Forces of attraction: **(a)** dipole, **(b)** dipole-dipole, **(c)** London dispersion and **(d)** hydrogen bridge.

1.4.1.1.1. External sphere complexes

The ions in aqueous solution are mainly surrounded by six water molecules forming a first solvation layer (Figure 1.6a). The ions with their solvation layer are attracted by non-specific forces (electrostatic charges and preferential solvation) towards the surface. However, the solvation sphere of the adsorbed cations does not undergo changes with these types of interactions (Figure 1.6b). The solvation sphere has greater attraction for the hydroxylated surface of the solid (S-OH) than for liquid water [50]. The coordinated water molecules are gradually displaced by the ligand (L) as its concentration increases in the

solution, until the MeL_n complex is formed (n is coordination number). Depending on the charge of the complex there will be an affinity for other species that are present in the solution. When complexes are negatively charged, interaction of the anionic complex with metal ions can be expected [51].

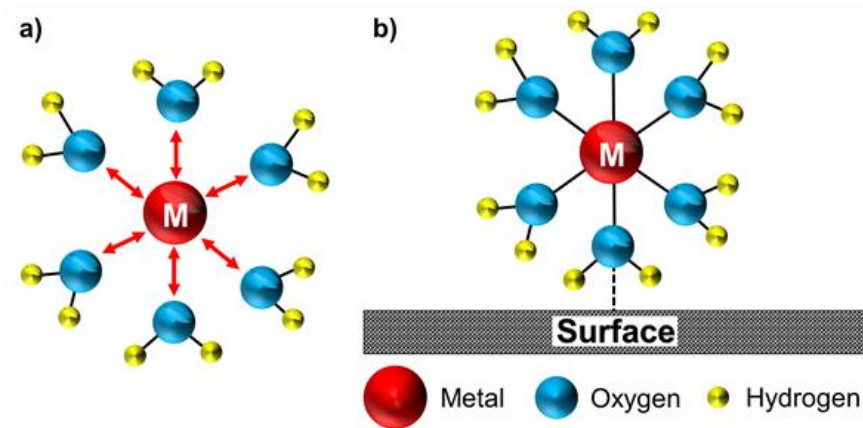


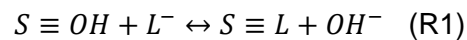
Figure 1.6. (a) Solvation of the ion and (b) external sphere complex on the hydroxylated surface.

1.4.1.2. Chemisorption

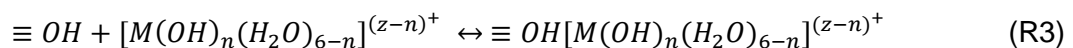
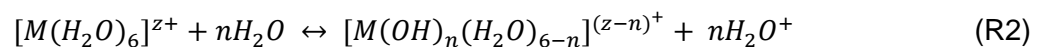
Chemisorption or chemical adsorption is carried out by a chemical reaction that involves the electrons transfer between the adsorbent and the adsorbate. Chemical adsorption is an irreversible process because the adsorbate chemically reacts with the surface through a covalent or ionic bond between the atoms, with a short bond length and high energy (200 kJ mol^{-1}). Generally, in this process a monolayer is formed. Furthermore, the binding can be specific to a particular site or functional group on the adsorbent surface [52].

1.4.1.2.1. Inner sphere complex

An internal sphere complex is formed when the first hydration layer of the adsorbate is replaced by a direct bond with the solid surface [53]. In the complexes of the internal sphere, the hydroxyl groups on the surface act as σ donor ligands, which increase the electron density of the coordinated metal ion [54]. Anions are ligands (L^-) that can act as donors of coordinated bonds because they have one or more atoms with only one pair of electrons. The ligand replaces the specific reactive group (OH) located on the surface of the adsorbent (R1), forming monodentate or bidentate internal sphere complexes (Figure 1.7).



Transition metals are easily hydrolyzed and have a strong affinity for the hydroxylated surface (S-OH). The aqueous complex is hydrolyzed forming a metallic hydroxy complex (R2), which is physisorbed on the surface of the material (R3).



On the other hand, a metal complex can bind to the adsorbent material through a proton shift (H^+) (R4) [55]. When the first solvation layer of the adsorbate is replaced and the ion forms a chemical bond with the surface of the solid, an internal sphere complex is said to have formed [50].

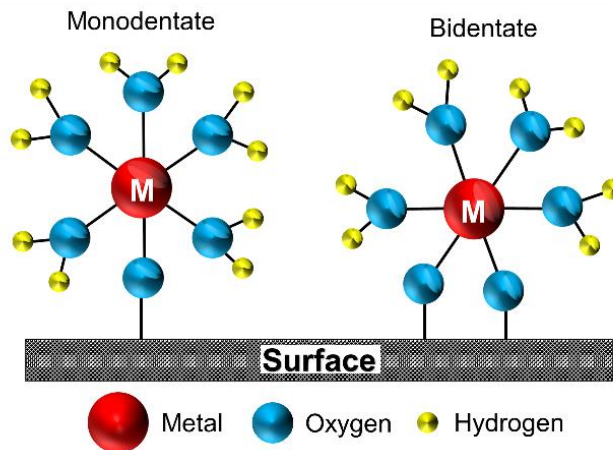
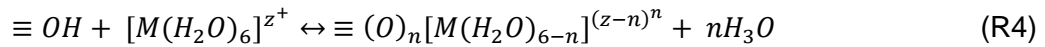


Figure 1.7. Monodentate and bidentate internal sphere complexes.

1.4.2. Solid-liquid interface models

Several models have been developed to explain the surface reaction involved during the adsorption process. These models are based on the charge of the solid when it comes into contact with an aqueous solution. Positive or negative sites (surface ions) on the material surface can occur when protons or hydroxyl ions are adsorbed on the material surface [53,55]. On the other hand, when metal oxides are put in contact with an aqueous solution, the water molecules occupy the vacant coordination sites via chemisorption (Figure 1.8a). The OH groups attached by two metal ions (doubly coordinated) are strongly polarized by cations, releasing hydrogen, and resulting in an acid character. For individually coordinated OH groups, they are basic in character because the polarization is much weaker. In this case, the OH groups can be exchangeable for other anions (Figure 1.8b).

Finally, new water molecules are physisorbed by hydroxyl groups, forming the oxide/water interface (Figure 1.8c) [50].

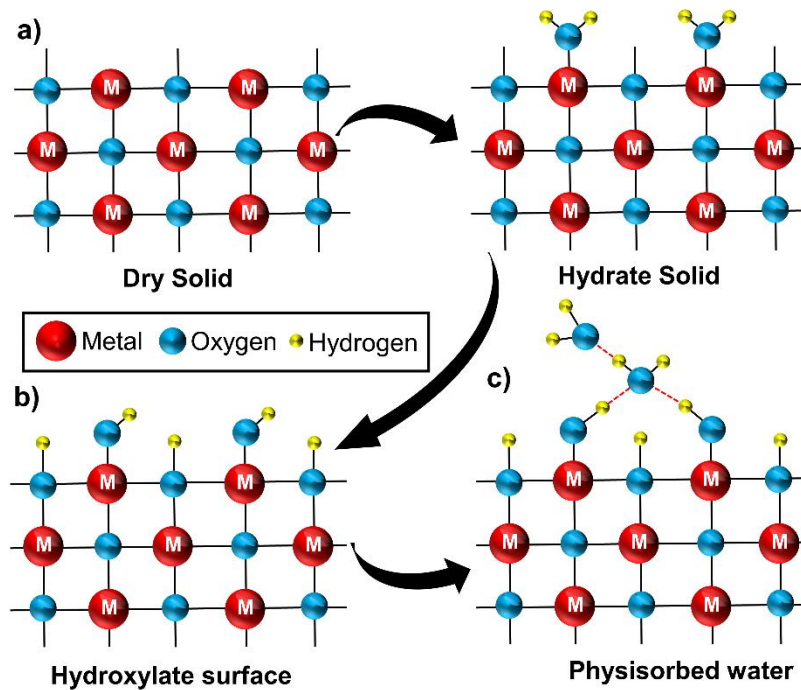


Figure 1.8. Hydration mechanism of metallic oxide (modified from Dzombak & Morel, 1987).

1.4.2.1. Electric double and triple layer model

The ionization of a hydroxylated surface generates a charge to the solid, which is balanced by a ions layer of opposite charge located in the aqueous phase. Counter ion adsorption occurs until the interfacial region is electrically neutral. The surface charge together with the counterions layer in the solution, make up the electric double layer (EDL) [53]. Von Helmholtz, was the first to describe the electric double layer model and established that two layers of opposite charge form an electrode/electrolyte interface, separated by a

small distance (H). The structure of this model is analogous to the conventional flat capacitor parallels (Figure 1.9a) [56]. However, the Helmholtz model did not consider ions to be mobile in the solvent electrolyte.

The model proposed by Helmholtz was modified by Gouy (1910) and Chapman (1913) considering the mobility of the ions in the electrolyte. Instead of the ions being very close to the surface, the Gouy-Chapman model proposes a counterions distribution in a region with a thickness much greater than H , named diffuse layer (Fig. 1.9b) [50]. Later, Stern (1924) combined both models (Helmholtz model and Gouy-Chapman model) taking into account the two regions (Helmholtz or Stern layer and the diffuse layer), in the so-called Gouy-Chapman-Stern model (Figure 1.9c) [56].

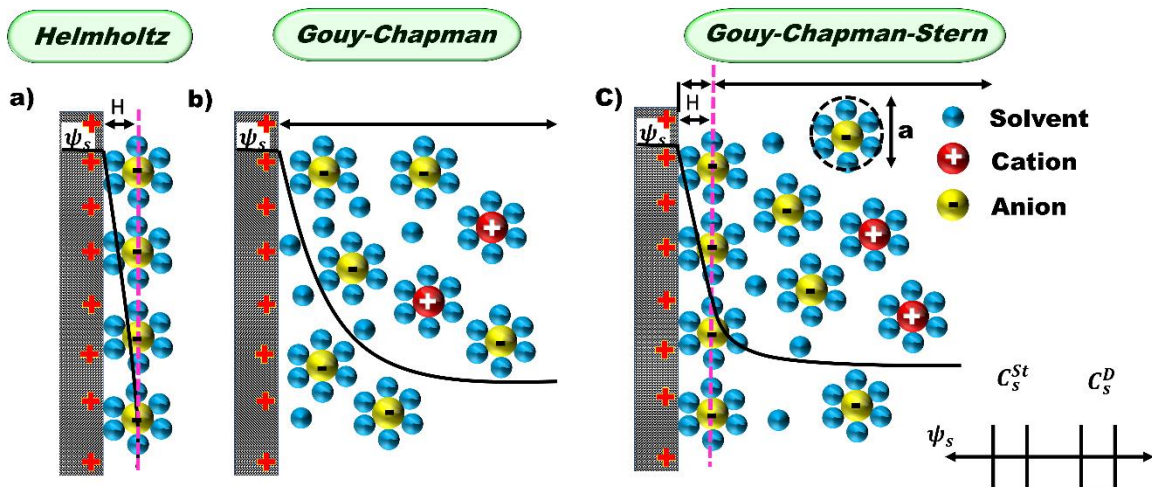


Figure 1.9. Representation of EDL according to the **(a)** Helmholtz model, **(b)** the Gouy-Chapman model and **(c)** the Gouy-Chapman-Stern model (Modified from Burt et al., 2014).

Stern and Grahame took up the original Gouy-Chapman model considering the finite size of the ions. Stern and Grahame propose that counterions can approach a certain

distance from the charged surface [50], giving rise to the concept of specific adsorption. In addition, Stern proposed that ions desolvated at the interface, forming complexes with surface groups, which can be treated as paired ions, without defining any specific bond [55]. Grahame proposed an internal region of two planes that separate the surface of the diffuse layer (Figure 1.10). The area closest to the surface is called the inner Helmholtz plane (IHP), where ion pairs are formed with surface groups. The outer zone is called the outer Helmholtz plane (OHP), being the closest approximation that the ions of the diffuse layer can have [57]. Solvated ions require a greater amount of energy to break their solvation shells, therefore they only come close to OHP while remaining active bystanders or indifferent electrolytes. On the other hand, the ions capable of penetrating up to IHP are those that do not have the first complete solvation layer and behave as specific ions [50].

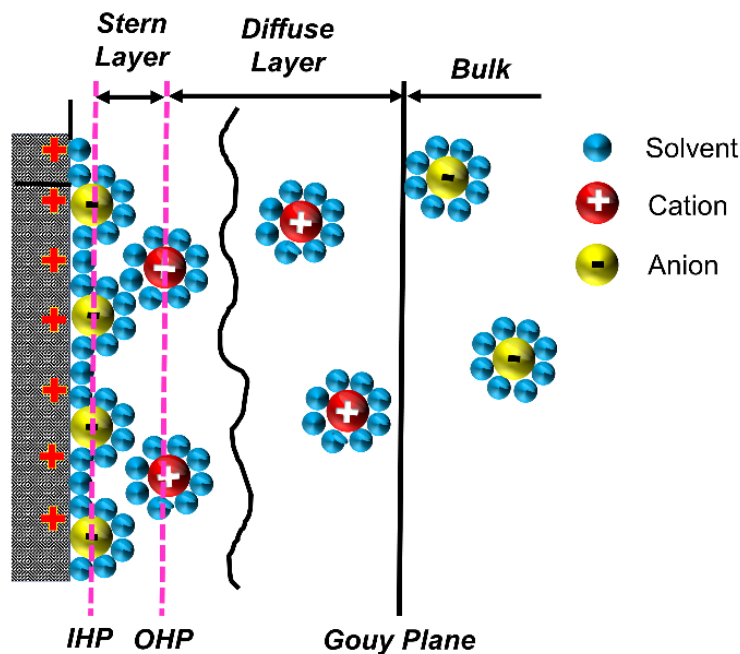


Figure 1.10. Representation of the ETL Stern-Graham model.

1.4.3. Adsorption equilibrium

During the adsorption process, solute molecules begin to adsorb onto the solid surface at a certain rate while other molecules already adsorbed can desorb. As time increases, the adsorption rate decreases, and the desorption rate increases until an equilibrium is reached between both (Figure 1.11a). Equilibrium is known as the adsorption isotherm when temperature and pH remain constant in a system [58]. Experimentally adsorption isotherms are carried out by contacting a known mass of the solid with a solution containing a set adsorbate concentration, once the concentration in solution is constant, it indicates that equilibrium has been reached. Therefore, the concentration in the aqueous phase of the adsorbate is measured and the adsorption capacity is calculated using the following mass balance (Eq 1.1):

$$q_e = \frac{V(C_0 - C_e)}{m} \quad (\text{Eq 1.1})$$

Where q_e is the adsorption capacity of the solute (mg g^{-1}), C_0 is the initial concentration of the adsorbate (mg L^{-1}), C_e is the concentration at equilibrium (mg L^{-1}), m is the mass of the adsorbent (g) and V is the volume of the solution (L).

To describe the adsorption capacity at equilibrium, different mathematical models have been developed, with which the experimental data obtained can be adjusted. Among the most common are the Langmuir and Freundlich models (Figure 1.11b) [43].

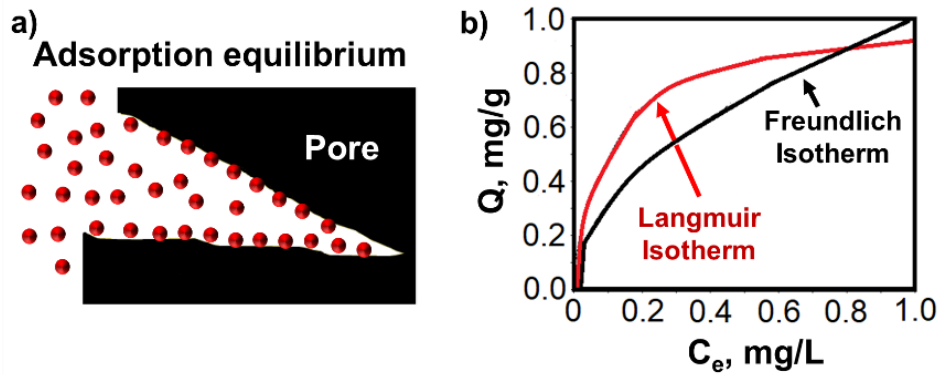


Figure 1.11. (a) Adsorption equilibrium, the same number of molecules adsorbed onto adsorbent and in the solution. (b) Langmuir and Freundlich isotherms.

1.4.3.1. Langmuir model

The Langmuir isotherm equation is the first theoretically developed adsorption isotherm. Langmuir derives his equation using some assumptions [58] such as that adsorbed entities (atoms or molecules or ions) are bound to the surface at defined sites. Each site has capacity for only one adsorbed entity. The energy state of each adsorbed entity is the same at all sites on the surface independent of the presence or absence of other adsorbed entities at neighboring sites. Therefore, the Langmuir model assumes that the surface is perfectly smooth and homogeneous (monolayer formation) and that the lateral interactions between the adsorbed entities are negligible (Figure 1.12). The Langmuir isotherm is represented by the following formula:

$$q_e = \frac{q_m b C_e}{1 + b C_e} \quad (\text{Eq 1.2})$$

Where: q_e is the adsorption capacity of the solute ($\text{mg}_{\text{adsorbate}}/\text{g}_{\text{adsorbent}}$ (mg g^{-1})), b is the Langmuir adsorption constant (L mg^{-1}), q_m is the maximum adsorption capacity (mg g^{-1}) and C_e is the equilibrium concentration (mg L^{-1}) [43].

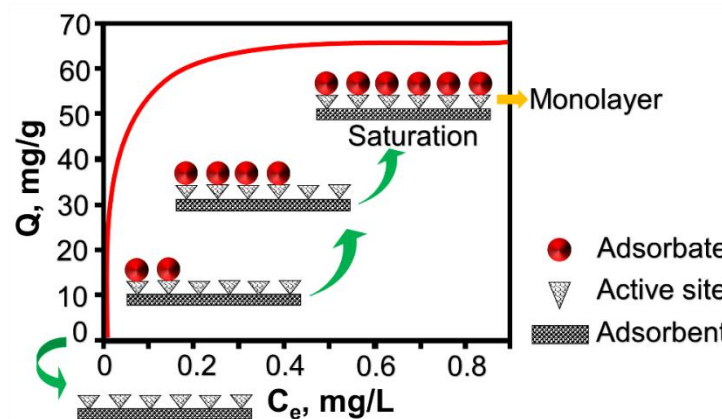


Figure 1.12. Langmuir model where the surface is perfectly smooth and homogeneous, and the adsorbate form a monolayer formation on surface (modified from Soares et al., 2016 [1]).

1.4.3.2. Freundlich model

The Freundlich isotherm describes the equilibrium on heterogeneous surfaces and does not assume that the adsorption occurs in a monolayer but through multilayers since there are interactions between adjacent adsorbed molecules (Figure 1.13). It can be represented as:

$$q_e = K_F C_e^{1/n} \quad (\text{Eq 1.3})$$

Where: q_e is the solute adsorption capacity ($\text{mg}_{\text{adsorbate}}/\text{g}_{\text{adsorbent}}$ (mg g^{-1})), C_e is the concentration at equilibrium (mg L^{-1}), K_F and n are the Freundlich constants for the adsorption capacity and adsorption intensity, respectively [43].

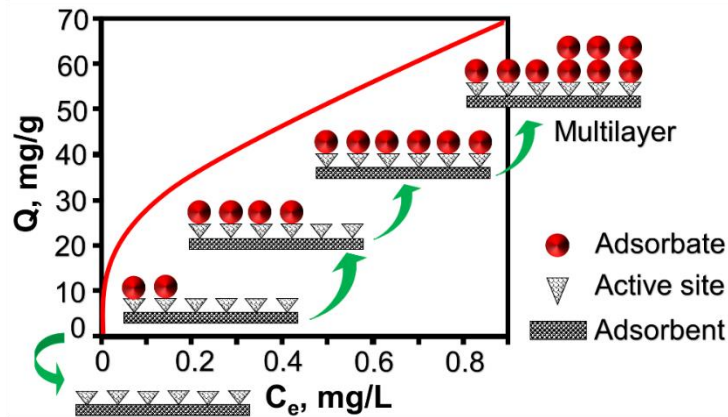


Figure 1.13. Freundlich isotherm, the equilibrium on heterogeneous surfaces through multilayers.

1.4.4. Adsorption kinetics

For the adsorption equipment design, it is necessary to know not only the equilibrium of the process, but it is also important to know the speed with which that equilibrium is reached, that is, adsorption kinetics. Kinetics, in most adsorption processes on porous solids, is usually determined by the diffusivity of the adsorbate molecules in the porous system [59]. Every adsorption process in adsorbents can be described by a mechanism of three consecutive stages that determine the adsorption kinetics as shown in Figure 1.14. In the first stage, external mass transfer (particle diffusion) of solute is carried out from bulk solution through the limiting layer to the surface of the adsorbent (Figure 1.14a). In the second stage, the solute diffusion through the adsorbent solid matrix (intraparticle diffusion) is carried out, associated with the interparticle mass transfer (diffusion through the pore volume or surface diffusion, Figure 1.14b). In the third stage, the solute molecules are adsorbed on the active sites (Figure 1.14c) [60].

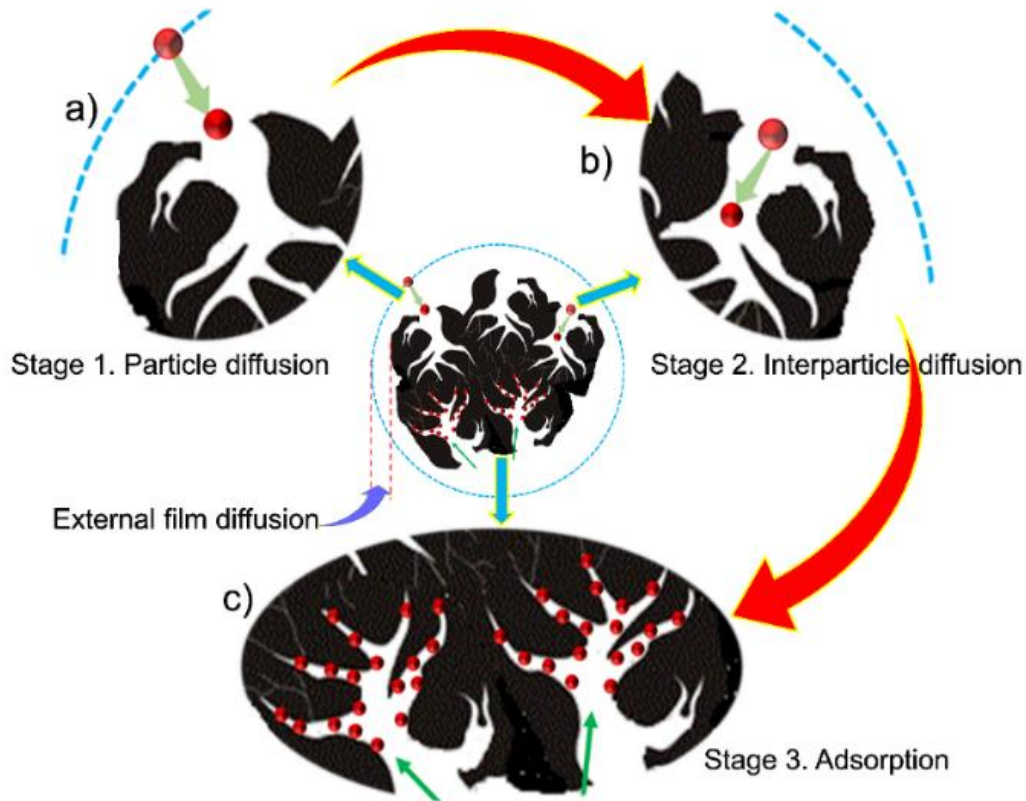


Figure 1.14. Stages of the adsorption process on activated carbon: **(a)** particle diffusion, **(b)** interparticle diffusion and **(c)** adsorption.

1.5. Adsorbent materials used in the removal of arsenic (V) and fluorides

In general, the adsorbent materials commonly used for the removal of these contaminants are activated carbons, zeolites, polymer resins, biosorbents and nanotubes. In addition, metal oxides are also used in the removal of arsenic and fluorides, mainly iron oxides [61,62], zirconium [63,64], lanthanum [65,66], cerium and manganese [67–69]. Activated carbon and carbon nanotubes have been modified with metallic oxides [20,70] in order to increase their adsorption capacity, and recently, powdered bimetallic oxides have shown excellent removals of As (V) and F⁻ [71,72].

1.5.1. Activated carbon

Activated carbon (AC) is known as one of the best adsorbents due to its large specific area, chemical stability, and various chemical functionalities, making it an ideal material for the adsorption of polar and non-polar compounds in the liquid and gas phase. Activated carbon consists of several disordered graphite layers, with multiple structural defects that give it porosity [58,73]. Carbon atoms at the edges of graphitic layers are normally linked with heteroatoms forming reactive groups (or active sites). These active sites are associated with higher densities of unpaired electrons and, therefore, show a strong tendency to chemisorb other heteroatoms [74]. To produce activated carbon there are natural and/or synthetic precursors. As natural precursors are wood, coal, peat, coconut husk, rice husk, etc.; while synthetic precursors are manufactured from various polymeric materials such as nylon, cellulose, phenolic resins, rayon, etc. [60].

1.5.1.1. Textural and chemical properties

The porous structure of activated carbon is very complex, so many models have been developed to explain the details of this structure. Norit model indicates that carbon is made up of misaligned graphite layers (Figure 1.15a), some of these are removed by physical activation processes that lead to the formation of pores of different sizes in activated carbon. The Potato-Chip model (Figure 1.15b) describes the porous structure and activated carbon surface area, roughly indicating how the shape of the spaces between the chips (pores) depend on the shape and potatoes size (micro-deformed graphite layers). Because two potatoes chips are not the same shape and size, each pore will have different sizes. It can also be seen in this model that if another brand of potato chips (of different shapes and

sizes) is used, the porous characteristics would change and a different microporous carbon would be created [73].

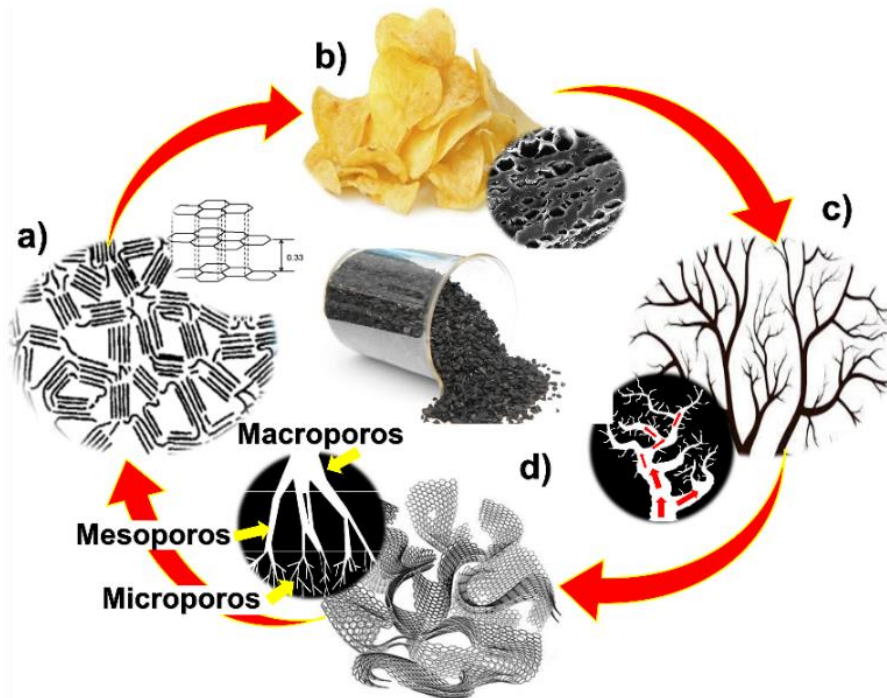


Figure 1.15. Structure of activated carbon, **(a)** Schematic representation of the Norit model; **(b)** formation of pores of different size (potato chip model); **(c)** solute transport through macropores to micropores (Branched tree model) and **(d)** pore size.

The Branched tree model (Figure 1.15c) shows the various pore sizes that can exist within a porous carbon, which can range from micro to macropores. The model suggests the transport of solute (adsorbate) through the macropores (the trunk) towards the narrower pores (branches) [73]. Activated carbon pores are classified into micropores (<2nm), mesopores (2 to 50nm) and macropores (> 50nm) which are represented in Figure 1.15d (IUPAC) [75,76]. The adsorption energy depends on the type of pores in which the process

is carried out. In micropores the adsorption is greater than in mesopores due to the superposition of adsorption forces from the opposite walls of the micropores.

The adsorption capacity of an activated carbon depends not only on the textural properties but also on the surface chemistry. Carbon atoms at the edges of graphite layers are normally linked with heteroatoms that form reactive groups. Those reactive groups located in the carbon layers together with the π system of the graphite basal plane are responsible for the active sites in activated carbon [74]. Figure 1.16 shows the surface groups present in activated carbon. The oxygen-containing groups (carboxyl, carbonyl, lactone, hydroxyl, etc.) give acidic properties that allow the cations adsorption; while the basic groups that are associated with chromene-type structures or pyrone-type structures can be used as adsorption sites for anionic species [58].

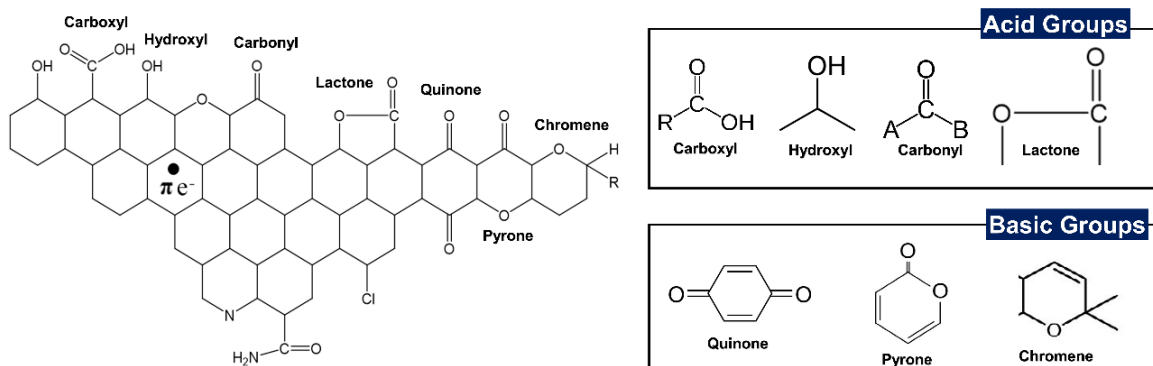


Figure 1.16. Chemical structure of activated carbon and the different groups on its surface

(Modified from Cárdenas-López, et al., 2007 [2]).

Activated carbon has several advantages in the removal of various pollutants, however, it presents limitations for the removal of arsenic and fluorides from water. For the As(V) and F⁻ removal, its main disadvantage is the low selectivity and adsorption capacity. The versatility of the chemical surface of activated carbon not only has a great impact on its adsorption properties, but also allows it to be adapted to specific applications. In addition to the oxidation of the carbon, other chemical modifications are carried out to increase the adsorption properties of the activated carbons. The active sites on activated carbon allow its surface to be modified with a great diversity of metal oxides, which allows obtaining hybrid adsorbent materials with greater selectivity and adsorption capacity [20,21].

1.5.2. Metal Oxyhydroxides

Metallic oxides are considered ceramic materials, which are made up of metallic and non-metallic elements [77,78]. In aqueous medium, the metal oxides surface forms hydroxyl groups that act as coordination sites for dissolved cations [79]. The OH groups formed on the metal oxide surface give it the property of adsorbing anions by exchange of ligands. Due to this, the anions adsorption on metallic oxides in aqueous medium has gained interest by researchers due to their high capacities. The main characteristics of metallic oxides are their surface chemistry (high OH groups density), the presence of one or more phases, high specific area, and the presence of defects in their structure (vitreous or amorphous structure) [78].

The metallic oxides studied for the arsenic and fluorides removal are La³⁺, Zr⁴⁺, Fe³⁺, Ce³⁺, Mn⁴⁺, Al³⁺, among others, which have shown excellent adsorption capacities [20,70,72,80,81]. The most studied oxides for the arsenic and fluoride removal are iron and aluminum, due to their low cost, availability, and chemical stability [53]. On the other hand,

rare earths have been shown to be more efficient in removing pollutants. However, the high costs of rare earths have led to the search for other alternatives such as incorporating them in other less expensive metallic structures such as iron or manganese [82–85]. Incorporation of a rare earth oxide into the structure of another metal oxide results in a bimetallic oxide.

1.5.3. Bimetallic oxides

In the last three years, there has been a special interest in applying bimetallic oxides to remove fluorides and arsenic from water. This is due to the fact that not only the oxides that make up the hybrid adsorbent inherit the advantages of pristine oxides (considerable high specific area, adsorption capacity and selectivity), but they also show a synergistic effect: greater specific area and active groups concentration, which results in a higher adsorption capacity. Powdered bimetallic oxides such as Fe-Ce, Fe-Mn, Fe-Zr, Al-Ce, Al-Mn, Mn-Ce and Fe-Al, have been used in the removal of As and/or F⁻ showing a high adsorption capacity. Table 1.3 shows a list of the bimetallic oxides used in the removal of As and F⁻, as well as the adsorption capacities, pH, and temperature.

Therefore, if bimetallic oxides can be anchored in activated carbon, hybrid adsorbents with high adsorption capacities in continuous systems could be obtained. However, it is important to consider that the magnitude of the increase in the reactive properties of activated carbons modified with metallic oxides depends on a large number of variables, such as: the size and type of metallic species in solution, modification processes, surface chemistry and textural properties of activated carbons, etc. Due to this, the methodology applied to modify carbon materials has to be evaluated from different points of view.

Table 1.3. Bimetallic oxides and their ability to adsorb arsenic and fluorides.

Adsorbent	q (mg g ⁻¹)			C _e mg L ⁻¹	pH	T °C	Ref.
	As(III)	As(V)	F ⁻				
Fe ₂ O ₃ /TiO ₂	77.76	99.5	---	60	6-7	---	[86]
Fe ₃ O ₄ -MnO ₂	2.1	1,4	---	0.8	7	25	[87]
Fe-Cu	122.3	82.7	---	35	7	25	[88]
Fe-Ce	2.42	2.11	---	---	7	25	[89]
CeO ₂ -ZrO ₂	110.7	145.35	---	35	6-7	---	[90]
Mn-Al	142.2	99.7	---	55	7	25	[91]
Fe-Zr	120	46.1	---	35	7	25	[92]
Ce-Ti	---	46	---	5	6	25	[93]
Zr-Ti	---	25	---	5	6	25	[94]
La-Ti	---	45	---	5	6	25	[94]
Li-Al	---	---	42.43	20	7	40	[95]
Ce-Fe	---	---	60.97	100	--	20	[96]
Ce(IV)-Zr(IV)	---	---	12.4	1.5	5.8	30	[97]
Mn-Ce	---	---	79.5	10	6	25	[98]
Fe ₂ O ₃ /Al(OH) ₃	---	---	88.49	60	6.5	25	[99]
Al- Ce	---	---	62	10	6	25	[85]
Fe(III)-Zr(IV)	---	---	7.51	---	6.8	20	[101]
Al-Mn	---	---	2.852	25	4-7	30	[81]

1.5.4. Modified activated carbon with metal oxides

The metal ions are classified into three classes A, B and Border line. Class A metal ions refer to “strong acids” and Class B metal ions refer to “weak acids”. Ce, Zr is among

the metals of class A, therefore, in aqueous solution they have an affinity for forming bonds in the following preferential sequence with the ligands: $F^- > Cl^- > Br^- > I^-$. The functional groups that class A metal ions seek to form complexes are carboxyl, phenolic and carbonyl. This is because class A metal ions seek oxygen to form binding sites, while class B ions prefer to bind nitrogen and/or sulfur (Nieboer and Richardson, 1980). Fe and Mn are within the Border line class; however, among the borderline metal ions, class B character increases in the order $Mn^{2+} < Zn^{2+} < Ni^{2+} < Fe^{2+}$. However, studies have shown that Fe, Ce, and Zr tend to form complexes with the acid groups of the activated carbon (Figure 1.17).

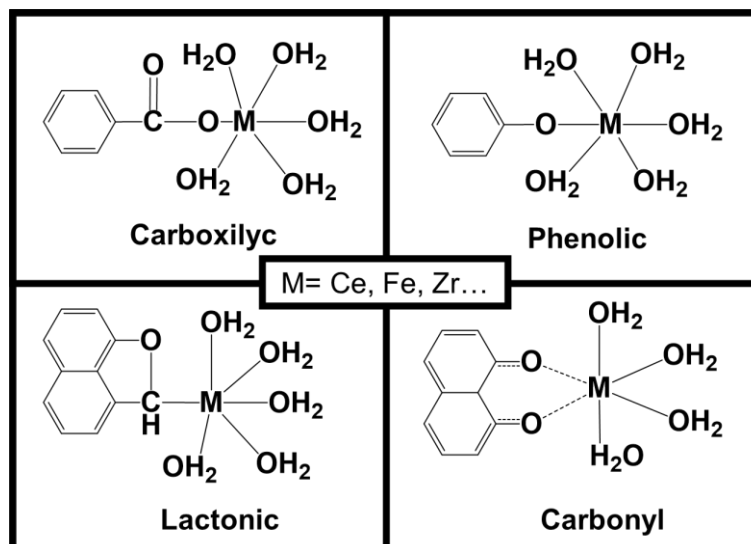


Figure 1.17. Possible interactions between oxygenated groups and oxides aquo-complexes.

Recent studies have shown that arsenic (V) can be removed from water by hybrid adsorbents such as CA impregnated with iron oxyhydroxide nanoparticles [20,70,102,103], this due to its high selectivity and considerable arsenic adsorption capacity. Additionally, several metal oxide nanoparticles have shown promising arsenic adsorption properties [79].

For example, zirconium dioxide, titanium dioxide and manganese oxide can be used to create new hybrid materials capable of removing arsenic from aqueous solutions [104]. On the other hand, the removal of fluorides from water with activated carbon modified with zirconium, cerium, manganese, iron and aluminum oxyhydroxides has been studied [21,105,106]. These hybrid adsorbents (activated carbon-metallic oxides) have been shown to have considerable selectivity and adsorption capacity for fluoride ions.

Several studies have reported the modification of activated carbon with metal oxides for the removal of As and F⁻ in aqueous solutions, however, no studies have been found that indicate the immobilization or anchoring of bimetallic oxides on the surface of activated carbons for the removal of these contaminants.

1.5.4.1. Methods to modifying activated carbon with bimetallic oxyhydroxides

Various methodologies have been used for the modification of activated carbon with metallic oxyhydroxides. Studies have shown that the characteristics of the material such as morphology, particle size and crystalline phase are highly dependent on the oxyhydroxides incorporation method on the carbon surface. The methods that have been used for the metal oxides incorporation into activated carbon are impregnation, precipitation, evaporation, and hydrothermal synthesis.

The metals impregnation on the internal activated carbon surface has emerged as an alternative to remove of priority contaminants that are not very related to the activated carbon surface chemistry [107]. Metal oxides are used to modify activated carbon taking

advantage of its capacity to attract dissolved species such as metal anions and cations, as well as neutral species and polymers [108]. The impregnation of activated carbon using metal ions salts in solution is the most frequent method to dope activated carbon [109], where the surface oxygenated groups act as nucleation centers for the oxyhydroxides anchorage [110]. Velazquez-Jimenez impregnated activated carbon with zirconium and oxalic acid to remove fluorides from the water. In the first instance, the CA was contacted with a zirconium solution (0.1 to 15% of Zr) for 2 days. Subsequently, the material was contacted with oxalic acid for 1 day. Modified carbon increased its fluoride adsorption capacity 4.5 times compared to pristine activated carbon [21]. Huang and Vane, 1989, reported that impregnation with different iron salts can increase the arsenic adsorption capacity of activated carbon by 10 times [111].

The use of precipitation to modify activated carbon with oxyhydroxides consists of contacting the AC with a metal salt and gradually increasing the pH until the metal ions precipitate on the surface of the AC. The particles obtained on the support depend to a great extent on the precipitating agent and the synthesis conditions. Various works have used NaOH as a precipitating agent until reaching a pH higher than 8.0, then the solution is heated for a certain time [112–114]. However, other works use another type of precipitating agent such as $(\text{NH}_4)_2\text{CO}_3$. Deliyanni and Bandosz, 2011, modified activated carbon with iron by precipitation [109]. Modified samples were prepared by contacting activated carbon with an aqueous solution of iron (III) nitrate. The precipitating agent (ammonium carbonate) was added dropwise to the solution until a pH of 8 was obtained by vigorous mechanical stirring.

Evaporation consists of the activated carbon impregnation with a metal salt (iron, zirconium, cerium, platinum, etc.) followed by the complete evaporation of the solution. Generally, the water is removed with the help of a rotary evaporator or a glass reactor and under a N₂ atmosphere to promote dehydration. In some cases, the solution can be heated in a temperature range of 50 to 350 °C depending on the quality of particle distribution on the carbon surface that is desired [113,115].

Forced hydrolysis has been used for the metallic oxyhydroxides synthesis; however, there are few studies reporting its use for the activated carbons modification. Fierro et al., 2009 and Arcibar et al., 2014, used this method to modify activated carbon with iron oxides. The authors contacted the AC with a FeCl₃ solution, the mixture was subjected to heating at a temperature in a range of 80 to 110 °C for 1 to 72 h [20,110]. The advantage of this methodology is that when high temperatures and metal ion concentrations are used, small nanoparticles of oxyhydroxides can be anchored on the surface. The resulting material has high adsorbent properties and excellent chemical stability, in addition, the percentage by weight of the oxide that is on the carbon surface is low compared to the adsorbents modified with other methodologies.

Many of these methodologies have the great disadvantage of the use of external agents (precipitating agents) and therefore the formation of agglomerates on the carbon surface. In addition, supplying energy to sources that are not uniform and can extend their reaction time to more than 24 hours as in the case of forced hydrolysis. On the other hand, hydrothermal techniques assisted by microwave have emerged as one of the most important

tools for the processing of advanced materials, especially due to the formation of highly homogeneous and monodisperse nanoparticles [116].

1.5.4.1.1. Hydrothermal synthesis

Ceramic materials acquire their properties after a heat treatment that can range from approximately 100 to 3000 °C. The formation of ceramic bimetallic oxides has generated great interest, because it is possible to obtain materials with specific areas and active groups concentration much higher than the individual oxides, these ceramics being more reactive. Techniques that are increasingly efficient in energy terms have been implemented in oxide synthesis processes as shown in Figure 1.18, which require equal or shorter treatment times at relatively low temperatures for ceramic processes (between 100 and 200 °C). Within these techniques is hydrothermal synthesis [117], which consists of carrying out a homogeneous or heterogeneous chemical reaction in the presence of a solvent (aqueous or non-aqueous) above room temperature and at a higher pressure at 1 atm in a closed system [118].

The hydrothermal technique has several advantages such as: greater reaction kinetics with a small increase in temperature, new meta-stable products are formed, production of highly crystalline particles and with better control over their size [119]. The hydrothermal pathway is very versatile for the materials synthesis and has been well established, carrying out experiments below the supercritical temperature of water, that is, below 374 °C [120]. A great variety of ceramic powders have been synthesized by hydrothermal methods. The most common are oxide-type materials (ZrO_2 , CeO_2 , TiO_2 , SiO_2 , ZnO , FeO_3 , Al_2O_3 , SnO_2 , etc.) and the crystalline products prepared by this method can have a variety of shapes such

as equiaxed (cubes, spheres), elongated (fibers, filaments, nanobridges and nanotubes), plates, nanoribbons and core-shell-type particles (CdS/ZnO) [121]. Also, flower-like structures, hollow spheres and sea urchins can be obtained using a nucleating molecule such as glycerol.

In recent years, there has been great interest in synthesizing and studying bimetallic oxyhydroxides mixtures as nano-adsorbents, which individually were already known as good materials for adsorbing contaminants in water, such as arsenic and fluorides. In addition, it has been shown that there is a synergistic effect between bimetallic oxyhydroxides that allows them to form nanostructures with a three-dimensional hierarchy, which have networks that form meso and macropores, which avoids adsorbate diffusion problems, and also have a specific area up to three times more larger than individual metal oxyhydroxide nanoparticles. These characteristics of bimetallic oxyhydroxides provide a higher concentration of active hydroxyl groups that result in a high arsenic and fluoride adsorption capacity [24].

On the other hand, cerium and zirconium are highly reactive rare earth metal oxides, which have been widely studied for their applications in catalysts, fuel cells, and gas sensors [122]. Recently, it has been found that the incorporation of cerium or zirconium oxide in other metallic adsorbents (Fe and Mn) significantly improves the arsenic and fluoride adsorption capacity due to the fact that they present an increase in the specific area and hydroxyl groups concentration. Cerium and zirconium in aqueous solutions can form tetranuclear or octanuclear species, which have abundant hydroxyl groups that are involved in replacement of ligands with arsenic species [123]. Xu et al., 2013 and Chen et al., 2016 have shown that

Ce-Zr bimetallic nano-oxides are an ideal candidate to remove arsenic and fluoride, since that it was achieved an adsorption capacity of up to 137 and 145 mg g⁻¹ of As(V) and F⁻, respectively [24,124]. However, the colloidal form of these bimetallic hybrid adsorbents limits their application in continuous treatment systems as mentioned above. Other studies show that Ce-Fe and Ce-Mn are a promising adsorbent material to removal arsenic and fluoride from water.

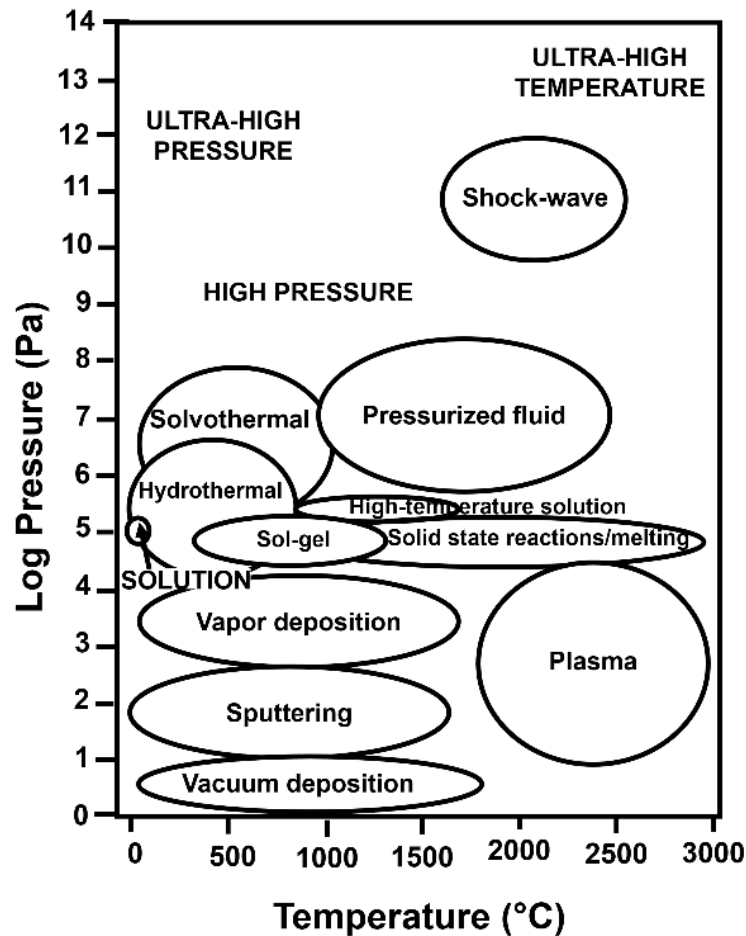


Figure 1.18. Temperature-Pressure Diagram for various synthesis techniques for ceramic materials.

1.5.4.1.1.1. Hydrothermal synthesis assisted by microwave.

The use of microwaves under hydrothermal conditions (M-H) has been used for the synthesis of inorganic materials, with controlled physical and chemical characteristics [125]. The main advantages of this method are rapid heating, reaction kinetics two orders of magnitude lower, phase purity, higher yield and higher reproducibility [126]. Yürüm et al., 2014, modified activated carbon with iron oxides by microwave oven (MH). In the first 6 and 9 minutes of synthesis was observed the formation of FeOOH and Fe₂O₃, respectively. The physicochemical characterization of the adsorbent material revealed an anchoring 20 %w of iron distributed homogeneously on the activated carbon surface, with a particle size of 55 nm [127]. To obtain a highly efficient adsorbent material, one must have greater interest in reflecting a true synergy between porous matrix and oxyhydroxides. For this, the textural and chemical properties, such as specific area, pore size distribution and high OH groups density, must be preserved. With these characteristics, the adsorbent material will have a high efficiency in removing contaminants from water, such as arsenic and/or fluorides from water. Due to all these advantages shown by the microwave oven-assisted hydrothermal method, the motivation arises to synthesize a variety of bimetallic oxides with and without the presence of activated carbon by this method. From the materials obtained, evaluate their textural and chemical properties, adsorption capacity and kinetics, among other effects (pH and anions).

1.6. Motivation for this research

The high arsenic and fluoride concentrations in groundwater intended for human consumption represent a serious problem worldwide due to its high toxicity. The great need to comply with the maximum permissible limits for government organizations, gives a guide to the search for new efficient adsorbent materials for the remove As and F⁻ from water. In recent years there has been great interest in synthesizing and studying nano-adsorbents composed of bimetallic oxyhydroxides, which individually, that is, as metal oxyhydroxides, were already known as good materials to adsorb arsenate and fluorides. Cerium, zirconium, iron and manganese as metal oxyhydroxides have shown an acceptable adsorption capacity for arsenic and/or fluorides, which increases when both oxides are mixed to form bimetallic oxyhydroxides (Ce-Fe, Zr-Fe and Ce-Mn). The disadvantage of the use of bimetallic oxyhydroxides for the removal of contaminants, is that these have been synthesized mainly as nano-adsorbents in powder or colloids, so their direct application in water treatment systems is not feasible, since granular adsorbent materials with good mechanical properties are required that allow their application in continuous systems in packed beds. On the other hand, the wide activated carbon properties such as its high specific area, chemical diversity, and its ability to be modified, allow us to propose new alternatives for the application of bimetallic oxyhydroxide nanoparticles. It is worth mentioning that no report has been found in the literature on the use of activated carbon modified with bimetallic oxyhydroxides nanoparticles to remove As(V) and/or F⁻ from water. Therefore, this research work proposes to anchor bimetallic nano-oxyhydroxides in the graphitic sheets of granular activated carbons. This with the aim of obtaining hybrid adsorbent materials with a high hydroxyl sites concentration where it will be feasible to adsorb high arsenic (V) and fluoride concentrations from water.

1.7. Hypothesis

The anchoring of basic bimetallic nano-oxyhydroxides with a three-dimensional hierarchy in granular activated carbon will raise the point of zero charge and will increase the active area and the hydroxyl sites concentration of the hybrid adsorbent, thereby promoting more hydrogen bonding interactions and exchange of ligands with toxic anions such as arsenic and fluoride. In addition, these adsorbents can be used in continuous treatment systems due to their size, chemical and mechanical stability.

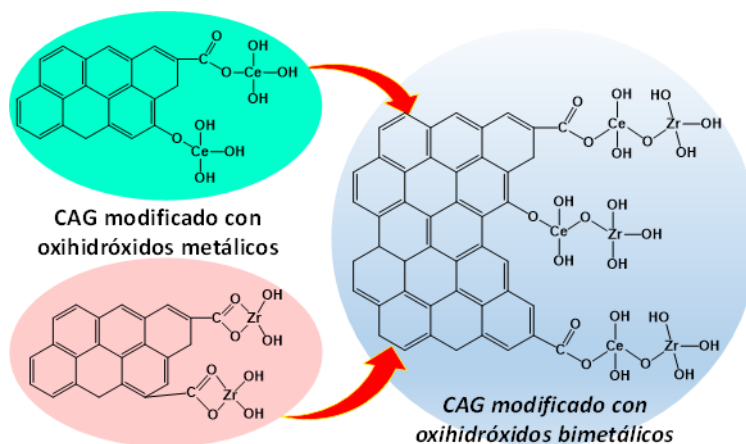


Figure 1.19. Schematic representation of the modification of granular activated carbon (CAG) with bimetallic oxyhydroxides.

1.8. Objectives

1.8.1. General objective

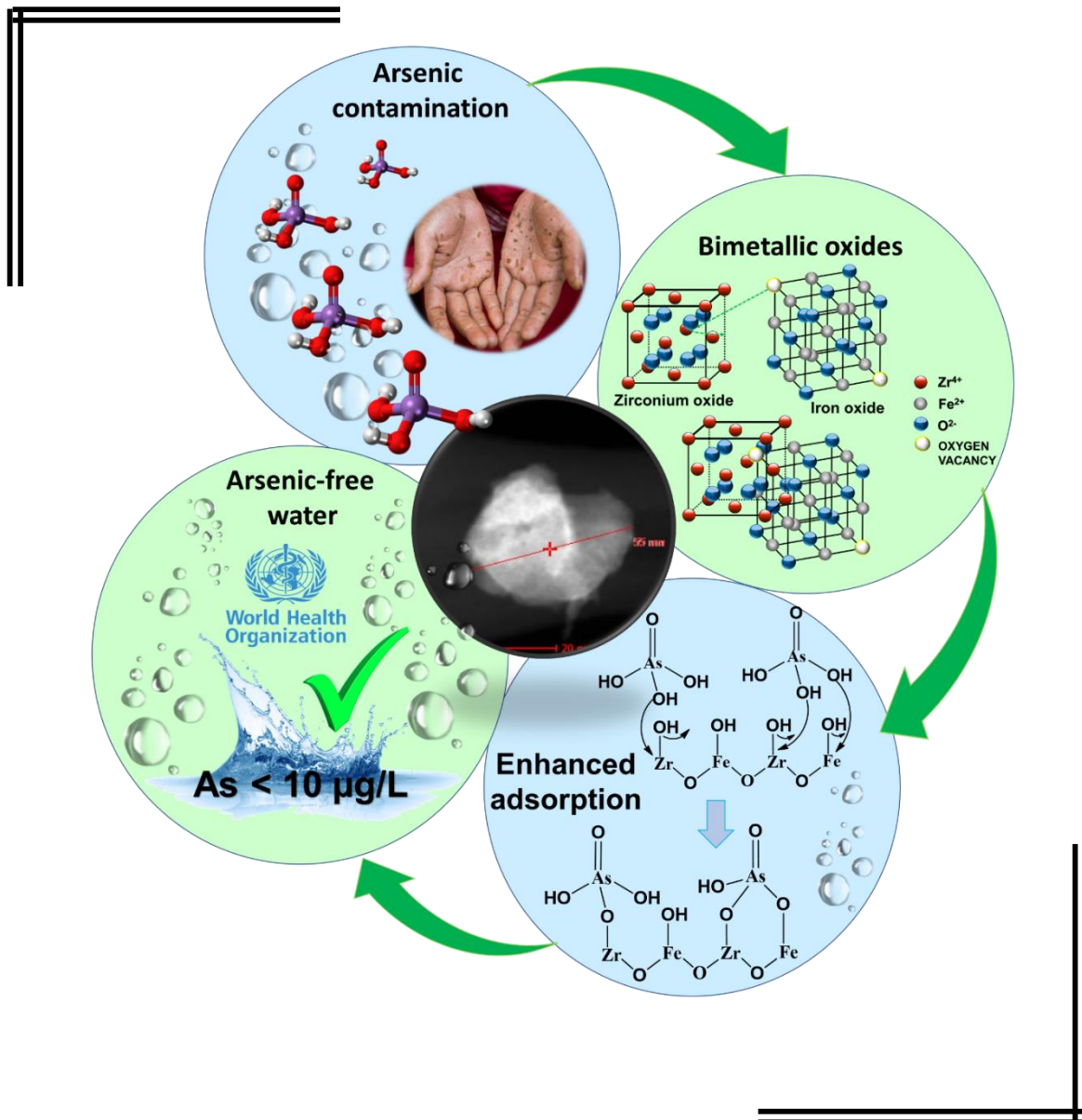
Synthesize and anchor bimetallic oxyhydroxides with a three-dimensional hierarchy on granular activated carbon and study the adsorption processes of As(V) and F⁻ on the modified materials.

1.8.2. Specific objectives

- Determine the hydrothermal synthesis conditions of bimetallic oxyhydroxides to anchor them on the activated carbon surface and thus improve the As (V) and F⁻ adsorption capacity.
- Determine the chemical composition and distribution of inorganic elements in bimetallic oxyhydroxides by means of energy dispersive X-ray microscopy (EDX) and elemental mapping.
- Determine the physicochemical characteristics of modified and unmodified activated carbons to know their specific area, pore volume, surface charge, active groups and crystalline phases using various characterization techniques.
- Elucidate the anchoring mechanism of bimetallic oxyhydroxides by characterizing the modified and unmodified material, which will allow the production of highly selective adsorbent materials.
- Study the adsorption process and kinetics of arsenic (V) and fluorides in water. The above considering variables such as concentration, pH, presence of other ions.
- Elucidate the adsorption mechanism of As (V) and F⁻ on materials modified with bimetallic oxyhydroxides, through the physical and chemical characterization of the materials and the adsorption process.

CHAPTER II

Microwave-hydrothermal synthesis of a bimetallic material ZrO_x-FeO_x with high OH density for enhance arsenic removal from water.



CHAPTER II

Enhanced arsenic removal from water by a bimetallic material ZrOx-FeOx with high OH density

Abstract

Arsenic in groundwater for human consumption has negative effects on human's health worldwide. Due to the above, it is essential to invest in the development of new materials and more efficient technology for the elimination of such priority contaminants as arsenic. Therefore, in the present work, it was synthesized an amorphous hybrid material ZrOx-FeOx with a high density of OH groups, to improve the arsenic adsorption capacity of iron (FeOx) and zirconium (ZrOx) that makes up the bimetallic oxyhydroxide. The spectra of FT-IR and pKa's distribution suggest that in the synthesized binary oxides a new union between the two metallic elements is formed by means of an oxygen (metal-O-metal). In addition, TEM profiles suggest that there are chemical interactions between both metals since no individual particles of iron oxide and zirconium oxide were found. According to the results the adsorption capacity of the ZrOx-FeOx material increases 4.5 and 1.4 times with respect to FeOx and ZrOx, respectively. At pH 6, the maximum adsorption capacity was 27 mg g⁻¹, but at pH greater than 7, the arsenic adsorption capacity onto ZrOx-FeOx decreased 66%.

Key words: *Bimetal oxides, zirconium, iron, adsorption, arsenic, assembly mechanism*

2.1. Introduction

Arsenic (As) is highly dangerous, due to its toxic and carcinogenic properties [128] that have affected the health of human beings around the world. Sometimes the pollution has a non-anthropogenic origin that makes the problem more difficult to identify and solve, such as the case of arsenic. This element is found mainly in clayey rocks [129,130] and in some geological formations [131]. However, water contamination by arsenic is primarily due to the arsenic compounds desorbed from iron oxyhydroxides from natural rocks [132]. In addition, the contamination of underground water by arsenic is also associated to the extraction of values in mines, volcanic activities and geothermal streams [133]. High arsenic concentrations ($>50 \mu\text{g L}^{-1}$) have been found in water in various countries around the world, including Mexico, due to the excessive exploitation of their aquifers [134,135]. Consumption of inorganic arsenic at low concentrations can cause gastrointestinal discomfort, vomiting, shock, seizures, and coma. A chronic disease well known for the prolonged intake of water contaminated with arsenic ($50 \mu\text{g L}^{-1}$) is Arsenicosis, which is characterized by hyperpigmentation and hyperkeratosis [136–139]. Therefore, the World Health Organization (WHO) and Environmental Protection Agency (EPA) have suggested $10 \mu\text{g L}^{-1}$ of arsenic in drinking water as the maximum permissible limit. [140]. However, this concentration will decrease to undetectable in the coming years. Due to the above, it is essential to invest in the elaboration of new materials and to offer more effective technology for the remove priority pollutants. The technologies used in the removal of arsenic from water are: filtration with membranes, electrodialysis, ion exchange with resin, alumina precipitation, and adsorption [141]. However, adsorption has been considered as a widely efficient technology due to its advantages in terms of costs and design. On the other hand, among the various adsorbents that have been used to uptake various contaminants are metal oxides, bimetallic oxyhydroxides and activated carbon [142]. However, it is important to consider that an adsorbent must exhibit good mechanical strength and not be soluble in water, and must not

cause harm to the human being [143]. Several studies have shown that iron oxides are quite efficient for arsenic removal in aqueous solutions [144]. Moreover, zirconium oxide is considered as a potential adsorbent due to its properties such as: virtually no thermal conductivity, high resistance to acidic or basic solutions, as well as to oxidizing and reducing agents [143,145–147]. Recently, the bimetallic oxides synthesis has taken a special interest, because the synthesized compound can inherit the properties of the pristine metallic oxides. Iron oxide has been synthesized with various oxides (tin, titanium, cerium, zirconium, copper and manganese) by precipitation in order to form bimetallic oxides and improve their adsorption performance [148–150]. The objective of this research was to synthesize ZrOx-FeOx oxyhydroxides by the hydrothermal method assisted by a microwave. This method produced a nanometric material with a more uniform morphology and particle size, to increase the OH groups density of pristine oxides and hence the arsenic adsorption capacity. In addition, a physicochemical characterization to analyze the morphology, crystalline structure, pK_a 's and charge distribution of the metallic and bimetallic oxides was conducted.

2.2. Experimental

2.2.1. Materials and chemical

Reagents with purity greater than 99% were used in experiments. Zirconium oxynitrate hydrate ($ZrO(NO_3)_2 \cdot xH_2O$), ferrous sulfate heptahydrate ($FeSO_4 \cdot 7H_2O$), Arsenic salt ($Na_2HAsO_4 \cdot 7H_2O$), sodium hydroxide (NaOH) and hydrochloric acid (HCl) were used.

2.2.2. Synthesis of Bimetallic Oxyhydroxides

The synthesis of the metal oxides was carried out as follows: To synthesize iron oxyhydroxide, 2.8 g of $FeSO_4 \cdot 7H_2O$ was dissolved in 20 mL of deionized water to obtain a

0.5 M iron solution. The iron aqueous solution was immediately introduced to the microwave oven in a G30 vessel. Then, for the synthesis of the zirconium oxyhydroxides, a stock solution of 0.5 M zirconium was prepared. Subsequently, 20 mL of the stock solution was poured into a G30 vessel and introduced into the microwave oven. The bimetallic oxides, 2.8 g of $\text{FeSO}_4 \cdot 7\text{H}_2\text{O}$ were mixed with 20 mL of the zirconium stock solution and the mixture was introduced into the microwave oven. The synthetic products were rinsed with pure ethyl alcohol for three times and dried at 80 °C in an oven for 12 hours.

The synthesis was carried out in an Anton Paar Monowave 400 microwave oven at 110 °C for 30 min for FeOx and ZrOx-FeOx and at 150 °C for 3 h for ZrOx.

2.2.3. Physicochemical Characterization

2.2.3.1. Surface charge and pK_a 's distributions

Potentiometric titrations were performed in an automatic titrator (Mettler-Toledo T70), to determine the pH_{PZC} and distribution of pK_a 's of the adsorbent materials. The pK_a distribution was obtained by using the program SAEIUS-pK-Dist © (1994) [151].

2.2.3.2. FTIR spectroscopy studies

To perform the infrared analyzes, the ZrOx-FeOx oxyhydroxides were dried for 12 h. Subsequently, 0.03 g of oxyhydroxides were analyzed through ATR technique, subtracting the presence of water and CO_2 . For this analysis, an infrared Thermo-Nicolet, Nexus 470 FT-IR E.S.P was used.

2.2.3.3. XRD spectroscopy studies

Diffraction analyzes were carried out using a Bruker D8 Advance diffractometer, with a time and step size of 2 s and 0.01° , respectively, and a blank support to identify the crystalline phases of the ZrOx, FeOx and ZrOx-FeOx oxyhydroxides. X-ray diffractograms were analyzed using the Hannawalt method.

2.2.3.4 Transmission Electron Microscopy (TEM)

TEM analyzes were achieved using a FEI Tecnai F30 microscope at 300 kV. The samples were supported on a copper grid. In addition, EDS analysis (EDAX system) and scanning electron microscopy (STEM) were performed in dark field. The high-resolution transmission electron microscopy (HRTEM) technique was used to obtain high resolution images.

2.2.4. Adsorption Experiments

2.2.4.1. Adsorption Isotherms

To perform the adsorption isotherms, 2 mg of metal and bimetallic oxyhydroxides were contacted with 0.03 L of As(V) solution with an initial concentration of 0.025 to 10 mg L^{-1} in polypropylene conical tubes at pH 7 and 25°C . The aqueous solution was analyzed at a wavelength of 188.98 nm by ICP-OES (vary 730-ES) to determine the arsenic concentration. The adsorption capacity was determined by the mass balance (Eq. 1).

$$q_e = \frac{V(C_0 - C_e)}{m} \quad \text{Eq 1}$$

where q (mg g^{-1}) is the adsorption capacity, V (L) is the volume, C_0 (mg L^{-1}) is the initial concentration, C_e (mg L^{-1}) equilibrium concentration and m (g) is the mass of the adsorbent.

The experimental adsorption data obtained were adjusted to the Langmuir (Eq. 2) and Freundlich (Eq. 3) models, based on the correlation coefficient (R^2).

$$q_e = \frac{q_m * b * C_e}{1 + b * C_e} \quad \text{Eq. 2}$$

$$q_e = K_F C_e^{1/n} \quad \text{Eq. 3}$$

In the Eq 2 and Eq 3 the adsorption capacity at equilibrium (mg g^{-1}), and the maximum adsorption capacity to form a complete monolayer on the surface (mg g^{-1}) are represented with the following symbology: q_e , C_e and q_m respectively. b (L mg^{-1}) is the Langmuir constant. K_F and $1/n$ are the Freundlich model constants.

2.2.4.2. Adsorption Kinetics

A standard As(V) solution of 2 mg L^{-1} at pH 7 was prepared. Then, 30 mL of the stock solution was added to 13 polypropylene tubes of 50 mL that contained 2 mg of the adsorbent material and placed at $25 \text{ }^\circ\text{C}$ and 120-130 rev/min in an incubator. About 10 mL aliquot was withdrawn of each sample at different times, namely, 0.5, 1, 5, 10, 20, 40, 60, 90, 120, 180, 240 and 300 minutes and the pH variation was recorded all time. An ICP-OES was used to determine the As concentration in the water samples as described above.

2.2.4.3. Effect of anions on adsorption capacity

Effect of anions such as fluorides (F^-), chloride (Cl^-), sulfate (SO_4^{2-}), nitrate (NO_3^-), phosphate (PO_4^{2-}) and carbonate (CO_3^{2-}), that are normally found in groundwater, on the adsorption capacity of arsenic in bimetallic oxyhydroxides was determined. Synthetic water was prepared containing a concentration of 1, 5, 10 and 30 mg L⁻¹ of each anion (F^- , Cl^- , SO_4^{2-} , NO_3^- , PO_4^{2-} y CO_3^{2-}), in the presence of 2 mg L⁻¹ of As(V). Co-adsorbing anions effect experiments were carried out in batch systems.

2.3. Results and discussion

2.3.1. Physicochemical Characterization

2.3.1.1. Textural Properties

The textural properties of ZrOx, FeOx and ZrOx-FeOx are shown in Table 2.1. The pore size and surface area of the materials were calculated from N₂ adsorption-desorption isotherms at 77 K (Micrometrics ASAP 2020). Surface area was estimated from the BET isotherms, and the pore size distribution was obtained by using the density functional theory (DFT). Zirconium and iron oxyhydroxides have a surface area of 181 and 21 m² g⁻¹, respectively, while that of ZrOx-FeOx was 49 m² g⁻¹, 88 % less than that of ZrOx, with less than 20 % of micropores, 36 % of mesopores and 57 % macropores. Accordingly, it can be suggested that ZrOx acted as a support, while FeOx penetrates into its pores and anchors on its hydroxyl groups, forming the bimetal ZrOx-FeOx. The nitrogen adsorption isotherms (Figure 2.1) are type IV and showed a hysteresis loop similar to H1, which is characteristic of mesoporous materials [152].

Table 2.1. Surface area and pore volume of studied materials.

Sample	m ² g ⁻¹		cm ³ g ⁻¹		nm
	S _{BET}	V _{mic}	V _{mes}	V _{mac}	Average pore diameter
ZrOx	181	0.036	0.212	0.004	5.89
FeOx	21	0.001	0.050	0.018	11.78
ZrOx-FeOx	49	0.007	0.077	0.002	8.04

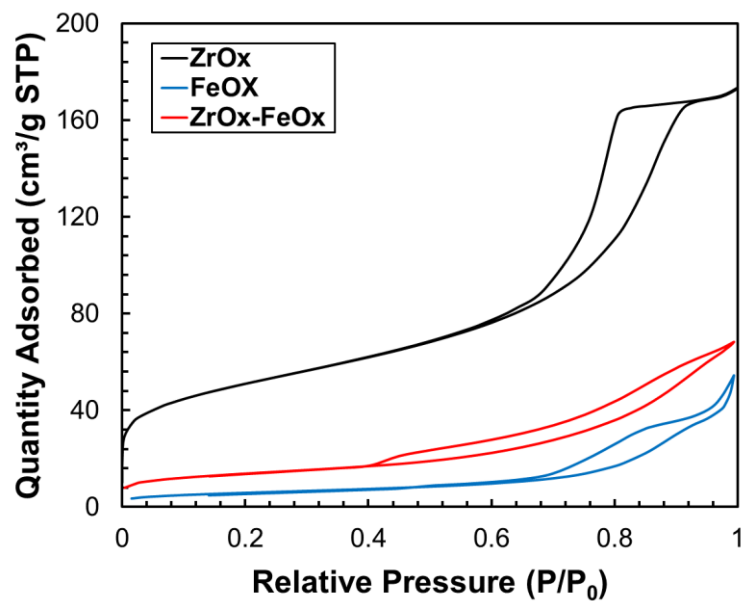


Figure. 2.1. The nitrogen adsorption isotherms

2.3.1.2. Surface charge and pK_a's distributions

Point of zero charge (PZC) specifies the total surface electric charge of metal oxyhydroxides. As known the PZC is located at the pH at which the positive and negative electric charges of a material are balanced, i.e. the electric charge is neutral. The adsorbent

has a positive surface charge when the pH is below the pH_{PZC} , attracting anions like arsenic species. In contrast, the material will have a negative charge, when the pH solution is greater than the pH_{PZC} attracting cationic species. The distribution of the surface charge of ZrOx, FeOx and ZrOx-FeOx oxyhydroxides is shown in Figure 2.2a. The pH_{PZC} of the FeOx and ZrOx is 7.2 and 7.8, respectively, indicating that at the working pH of 7 the material possesses an almost neutral charge. On the other hand, bimetallic oxyhydroxides showed a pH_{PZC} of 7.2, which is similar to the pH_{PZC} of the pristine metal oxides with which the bimetallic oxyhydroxide was formed. However, its surface charge density is much higher as will be explained below. The pH_{PZC} of iron oxides can be between 7.5 and 9.5 for goethite and hematite, between 6.0 and 7.1 for magnetite [153] and 6.5 for amorphous zirconium oxide [154]: these differences can be related to the OH groups concentration, which is also associated to the synthesis method, for example iron oxides can be synthesized by precipitation with either sodium hydroxide or potassium hydroxide. Also, in the present study, the presence of goethite was favored depending on the synthesis parameters, as observed in the XRD results (Figure 2.4).

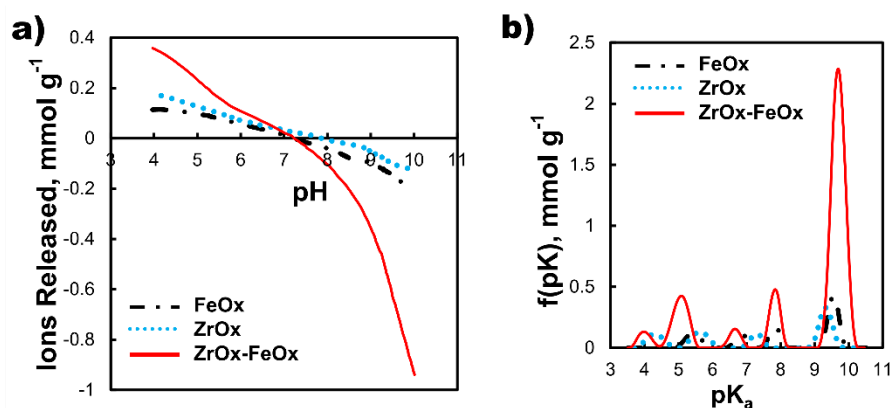


Figure 2.2. Point of zero charge **(a)** and pK_a 's distribution **(b)** of FeOx, ZrOx, and ZrOx-FeOx.

Figure 2.2b shows the intensity and pK_a 's distribution, which illustrates the chemical changes on the surface of ZrOx, FeOx and ZrOx-FeOx as a function of pH. The peaks that are observed in $8 \leq pK_a \leq 11$ and $3 \leq pK_a \leq 7$ can be attributed to OH groups and the metal species, respectively. The presence of OH groups is associated with hydrolysis of iron and zirconium where iron species such as: $Fe(OH)_3$, Fe^{2+} and $Fe(OH)_4^-$ have a pK_a of 6, 5.5 and 11.9, respectively [155,156]. In the case of zirconium the peaks at pK_a 5.1 and 9.7 are associated to the presence of $Zr(OH)_3^+$ and $Zr(OH)_4^-$, respectively. When the bimetallic oxyhydroxide is formed it can be seen that the peaks in the pK_a 's between 3.5 and 8 underwent a shift and an increase in the intensity of the peaks at pK_a 5 and ~8, indicating interaction between the two pristine metals. In addition, it can be seen that the intensity of the peak attributed to the OH groups increase ($9 \leq pK_a \leq 11$), indicating an increase on these groups on the surface of the ZrOx-FeOx. Accordingly, these adsorbents will have a higher adsorption capacity for arsenic species.

2.3.1.3. FTIR spectroscopy studies

The vibrational frequencies of iron (Fe) bonds to zirconium (Zr) were analyzed in order to elucidate the interaction between both metal ions. The FT-IR spectra of FeOx, ZrOx and ZrOx-FeOx are shown in Figure 2.3. The Fe spectrum showed bands at 582 and 664 cm^{-1} that are characteristic of goethite and arise due to the vibration of bending γ and δ -OH. The symmetrical Fe-O stretching is indicated by a band at 613 cm^{-1} [157]. The band in 810 cm^{-1} is attributed to the vibration of O-H [153], and the doublet at 1150 cm^{-1} and the band at 1050 cm^{-1} correspond to O-H flexion vibrations and to Fe-O stretching, respectively [153]. The ZrOx spectrum showed a band at 830 cm^{-1} related to symmetric (OZrO) and asymmetric (OZrO) vibrations of ZrO_2 , which according to the literature is present in the region between 800 and 850 cm^{-1} [158]. The vibration of Zr-OH is attributed to the presence of band 1348

cm^{-1} [159]. The FT-IR spectrum of ZrOx-FeOx showed a wide band in 3608 cm^{-1} which is associated to OH groups [142]. Broadband and weak band at 580 cm^{-1} and 615 cm^{-1} , respectively, are attributed to the bond-forming between Fe and OH groups of Zr (Zr-O-Fe) [160,161]. Besides, the band at 1100 cm^{-1} is attributed to the flexion vibrations of hydroxyl groups in metal oxides (Zr-OH, Fe-OH). This anion can drive the spatial arrangement of the $[\text{FeO}_3(\text{OH})_3]$ octahedra double chains common in FeOOH [153].

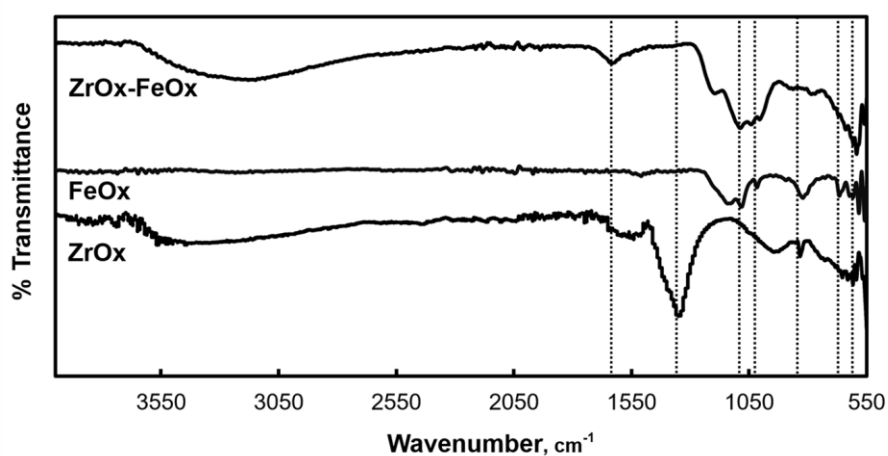


Fig 2.3. FT-IR spectra of ZrOx , FeOx , and ZrOx-FeOx .

2.3.1.4. XRD spectroscopy studies

The polymorphic phases of ZrOx , FeOx and ZrOx-FeOx were identified by XRD studies. Figure 2.4 shows the XRD patterns for ZrOx , where the peaks 17.54, 24.38, 28.31, 31.22, 34.2, 41.48 and 49.9 at 2θ angles can be attributed to the monoclinic structure of zirconium dioxide (ZrO_2). While the peaks 17.54, 24.38, 28.31, 34.2, 45.38, 49.9, 61.41 and 65.24 at 2θ angles correspond to the monoclinic zirconium oxide ($\text{Zr}_{0.932}\text{O}_2$). For both compounds the associated pattern was verified by the cards # 01-078-0047 and # 01-081-1315, respectively. In addition, the shape of the ZrO_2 diffractogram indicates that it is a highly amorphous material. On the other hand, FeOx showed the presence of monoclinic

$\text{Fe}(\text{SO}_4)(\text{H}_2\text{O})$ (iron sulphate hydrate) with the highest peak and orthorhombic FeOOH (Goethite). Their patterns were found in the cards # 01-081-0019 and # 01-076-7156, respectively. Finally, XRD patterns for the bimetallic oxide ZrOx-FeOx are show in Figure 2.4, where the peaks in 17.58, 24.45, 28.61, 32.69 and 50.89 at 2θ angles correspond to ZrO_2 . On the other hand, the same sample showed compounds of $\text{FeO}(\text{OH})$ and $\text{Fe}(\text{SO}_4)(\text{H}_2\text{O})$ at 2θ angles of 17.58, 21.59, 32.86, 36.69, 43.39, 50.41 and 26.37, 29.11, 45.71, respectively.

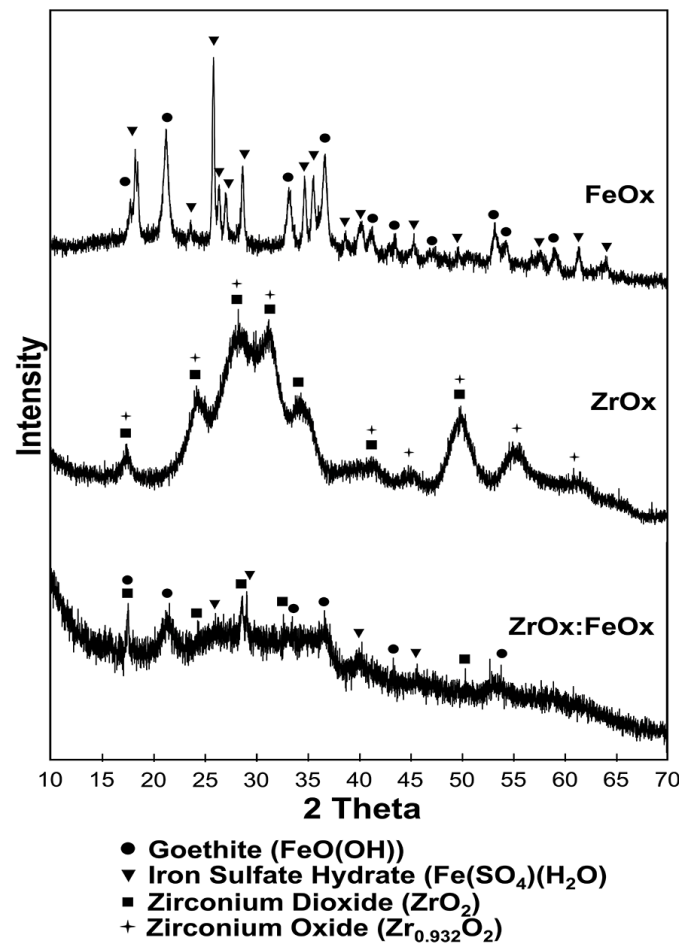


Figure 2.4. XRD patterns of ZrOx , FeOx and ZrOx-FeOx with a step of 0.02° 2θ at 10 s per step. The symbols show the crystalline phase of each oxide.

2.3.1.6. Transmission Electron Microscopy

Figure 2.5 shows the HAADF images of ZrOx-FeOx with its EDS spectrum. ZrOx-FeOx shows agglomerated particles and flat cube shapes (Figure 2.5a and 2.5c). EDS analysis (Figure 2.5b and d), marked with a square on the most amorphous area of the sample, shows the elemental composition of sulfur, oxygen, zirconium, and iron. The presence of sulfur can be attributed to the precursor of iron oxides (FeSO₄). Figure 2.5c shows in a rectangle the most solid zone of the ZrOx-FeOx sample in which the EDS analysis (Figure 2.5d) was performed showing a higher iron and zirconium oxides concentration than in the more amorphous zone. This can be attributed to an agglomeration of iron and zirconium species. When a high-resolution transmission electron microscopy was performed on the ZrOx-FeOx morphologies, a short-length crystalline arrangement that is characteristic of the nanostructured materials was observed. The high-resolution image of ZrOx-FeOx in two areas of the same sample is shown in Figure 2.6, where the lattices in the ZrOx-FeOx are observed. FTIR analysis showed a characteristic ring pattern of polycrystalline materials with a crystal size less than 10 nm [151]. Therefore, the bimetallic oxide is expected to have better surface interactions compared to materials with larger crystals that would have less grain boundaries.

Figure 2.7 shows the HAADF image of ZrOx-FeOx and its respective EDX spectrum and profile at different points of the bimetallic oxide particle. It was observed in the ZrOx-FeOx EDX that in the whole region of the particle the presence of both metals existed, which suggests the formation of bimetallic oxides. However, the profiles show that it is not an alloy because the profiles of both elements do not follow the same pattern, which suggests that between both metals there are chemical interactions, since no individual particles of zirconium and iron oxides were found in sample ZrOx-FeOx.

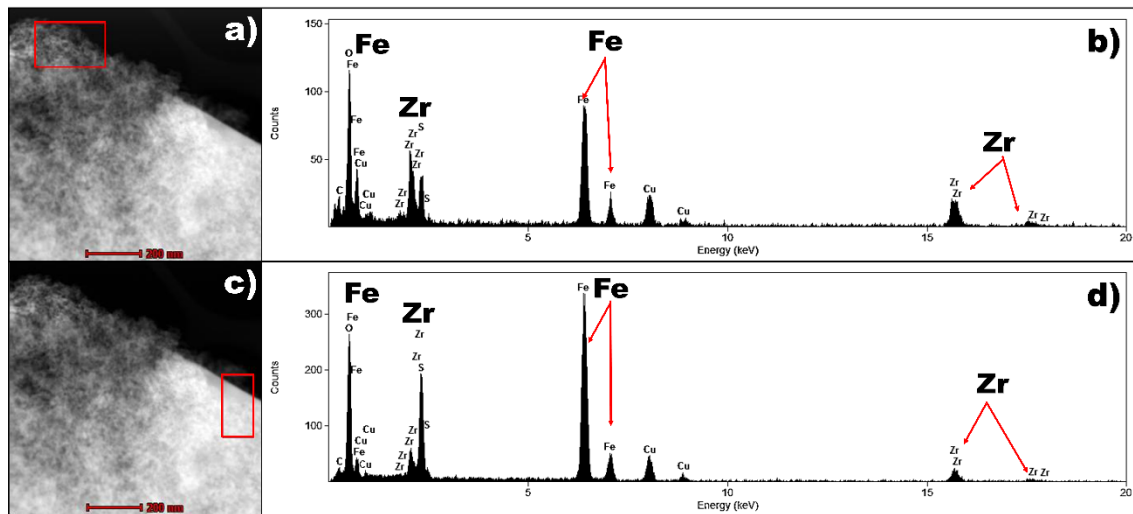


Figure 2.5. HAADF image (a and c) for ZrO_x-FeO_x and EDS analysis (b and d).

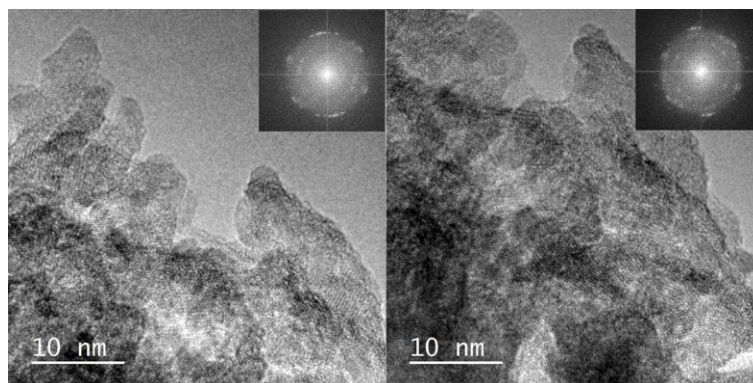


Figure 2.6. HRTEM images of morphologies of ZrO_x-FeO_x and its Fourier transforms (insets).

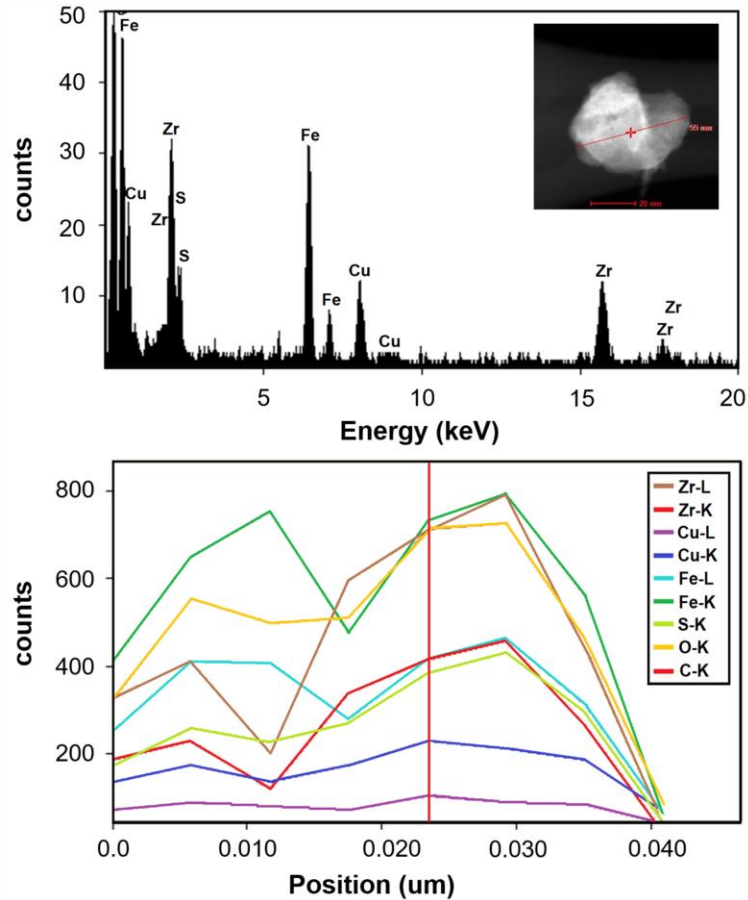


Figure 2.7. Micrograph, EDX and profiles of different points of a ZrO_x-FeO_x particle.

2.3.2. Assembly Mechanism of Bimetallic Oxide.

It is suggested that the increase in the amount of the hydroxyl group on the surface of binary oxides is due to the formation of a new bond between zirconium and iron through an oxygen atom as shown in Figure 2.8. This M-O-M bond (M=metal) would increase the arsenic adsorption capacity, due to an increase of polarity of these mixed oxides [143].

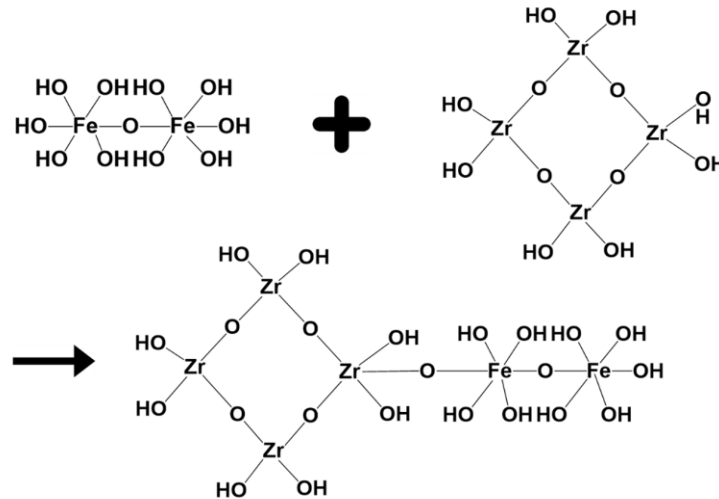


Figure 2.8. Illustration of bimetallic oxyhydroxide (ZrOx-FeOx).

To elucidate both the formation of bimetallic oxyhydroxide and its high arsenic adsorption capacity, it is essential to comprehend how the crystalline structure of both metals is modified. Zirconium has three main crystalline phases: monoclinic, tetragonal, and cubic. XRD analysis indicated a zirconium oxide monoclinic structure and an orthorhombic structure for FeOOH. However, it should be considered that the crystalline structures of different materials can have linear, punctual, interfacial and volume defects, especially when they come from non-pure materials. Punctual defects (see Figure 2.9a) play a key role in the development of bimetal oxides because vacancies (lack of an atom) can occur in the crystal lattice of the metal oxides that make it up. Therefore, one atom of the same material (autointerstitial atom) or another (interstitial atom) will fill the vacancy or the interstices of the lattice, forming the bimetallic oxide. According to Chaudhry et al., (2017), crystalline defects are generated due to the replacement of Zr^{4+} ions in FeOx and therefore cause a reduction in the degree of crystallization compared to pure Fe_2O_3 . Therefore, it is considered that the presence of Zr^{4+} in the FeOOH crystal lattice generates a quite amorphous bimetallic oxyhydroxide, due to the deformation of the crystalline phases, with a high density of

available OH groups, which can increase the arsenic adsorption by ligand exchange with these groups (Gupta et al., 2009; Chaudhry et al., 2017). The schematic representation of the proposed crystalline structure of iron and zirconium when forming a bimetallic oxide is shown in Figure 2.9b.

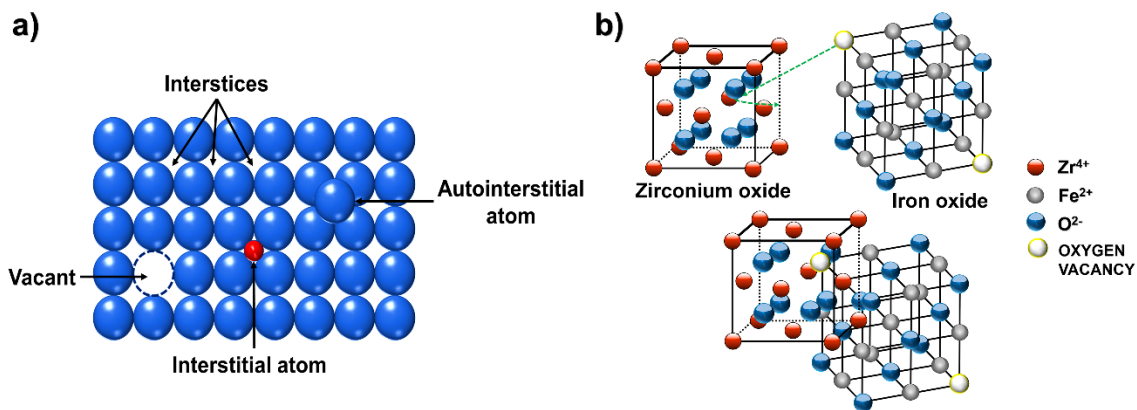


Figure 2.9. (a) Punctual defects in crystalline structures: vacancies and interstitials. **(b)** Proposed schematic representation of the crystalline structure of iron and zirconium when forming a bimetallic oxide (Modified figure from [3]).

2.3.3. Adsorption Experiments

2.3.3.1. Adsorption Isotherm

It can be observed in Figure 2.10 that the equilibrium adsorption capacity (q_e) increases significantly with the increase in arsenic concentration in the equilibrium (C_e) in the initial stage where more active sites are available, then as the materials get saturated, the isotherms slope becomes lower and finally nearly reach equilibrium. The arsenic adsorption isotherm of bimetal oxide was compared with the isotherms of the pristine oxides that make it up (FeO_x and ZrO_x). In the case of FeO_x and ZrO_x , it is observed that q_e

remains constant and/or without significant changes at a C_e greater than 1 and 2 mg L⁻¹, respectively. On the other hand, the arsenic adsorption capacity of ZrOx-FeOx increases even at C_e higher than 2 mg L⁻¹, which indicates that this material has a high affinity for arsenic and therefore, a high adsorption capacity.

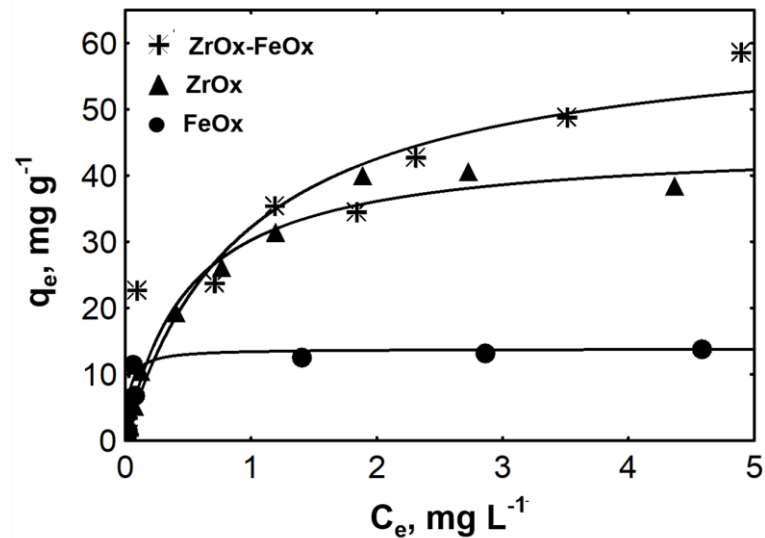


Figure 2.10. Adsorption isotherms of As(V) of FeOx, ZrOx and ZrOx-FeOx at pH 7 and 25 °C.

The arsenic adsorption isotherms of FeOx, ZrOx and ZrOx-FeOx (Fig 9) were adjusted to the Langmuir and Freundlich models, and their respective computed parameters are reported in Table 2.2. The adsorption intensity (n) values less than 2, suggest a high affinity of arsenic for the adsorbents [159]. Moreover, the experimental data were best fitted with the Langmuir model according to the correlation coefficient R^2 .

The maximum adsorption capacity (q_{max}) of FeOx and ZrOx was 13.8 and 44.8 mg g⁻¹, respectively, according to the Langmuir model (Fig 9). The above suggests that adsorption

forms a monolayer. The bimetallic oxyhydroxides ZrOx-FeOx have a maximum arsenic adsorption capacity of 62.7 mg g⁻¹, being 4.5 and 1.4 times greater with respect to FeOx and ZrOx, respectively. The adsorbent capacity of the hybrid adsorbent presented in this work was superior to that reported by Ren et al., (2011) [162] ($q_{\max} = 46.1 \text{ mg g}^{-1}$), who prepared Zr-Fe bimetallic oxides by precipitation and found the presence of ferrihydrite, but not the crystalline phase of zirconium, in their XRD results. This suggests that the synthesis method influences the physicochemical characteristics of the hybrid material having a favorable impact on the adsorption capacity of arsenic. On the other hand, it is important to mention that the Freundlich and Langmuir models are used only to compare the performance between adsorbent, however, they cannot be used to describe the contaminant adsorption mechanism [159].

Table 2.2. Langmuir and Freundlich parameters for the arsenic adsorption onto FeOx, ZrOx and ZrOx-FeOx.

Sample	Langmuir			Freundlich		
	$q_{\max} \text{ (mg g}^{-1}\text{)}$	$b \text{ (L mg}^{-1}\text{)}$	R^2	K	n	R^2
FeOx	13.8	31.7	0.89	10.9	0.18	0.89
ZrOx	44.8	2.08	0.99	25.4	0.34	0.94
ZrOx-FeOx	62.7	1.05	0.93	30.9	0.38	0.97

2.3.3.2. Effect of pH on the Arsenic Adsorption Capacity of the ZrOx-FeOx

The arsenic uptake was determinate at different pH. Adsorption experiments were performed at pH 5 to 9 to study the effect of pH on the arsenic adsorption capacity onto ZrOx-FeOx oxyhydroxide. These pH values were selected since they include the natural and

industrial waters. The results show that at pH 5 and 6 the highest adsorption capacity (27.3 mg g⁻¹, in both cases) is obtained, which decreases as the pH increases (Fig 2.11). The above is related to the pHPZC of the material, which is 7.2 (see Fig 1A), therefore at pH 5 and 6 the ZrOx-FeOx is positively charged and consequently attracts the arsenic anions. Moreover, at pH 8 and 9 a low adsorption capacity is observed. This is because at pH > 7 the surface of the material is negative charge and therefore increases the electrostatic repulsions between arsenic and ZrOx-FeOx.

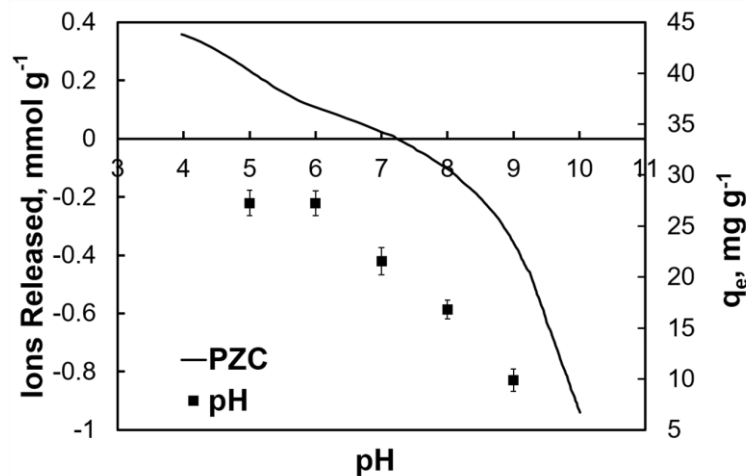


Figure 2.11. Relationship between the Point of Zero Charge and pH on the As(V) adsorption capacity of ZrOx-FeOx.

2.3.3.3. Effect of Co-adsorbing anions

The effect of anions such as fluorides (F^-), nitrate (NO_3^-), chloride (Cl^-), phosphate (PO_4^{2-}), sulfate (SO_4^{2-}) and carbonate (CO_3^{2-}), normally found in groundwater, on the arsenic adsorption capacity in ZrOx-FeOx is shown in Figure 2.12. The results indicated that 1 mg L⁻¹ of competing anions F^- , Cl^- , SO_4^{2-} , NO_3^- , PO_4^{2-} and CO_3^{2-} reduced the As(V) adsorption capacity 16.5%. Moreover, the As(V) adsorption decreases 52, 71 and 81% when increasing

the anions concentration at 10, 30 and 50 mg L⁻¹, respectively. According to Ren et al., (2011), phosphate causes the greatest reduction in the arsenic uptake: the molecular size and structure of phosphate and arsenic is very similar. For example, considering that the groundwater of some wells of the city of San Luis Potosí, Mexico, have an average concentration of 15.2, 25.6 and 1 mg L⁻¹ of Cl⁻, SO₄²⁻, and CO₃²⁻, respectively [163], the arsenic adsorption of ZrOx-FeOx will be 5.9 mg g⁻¹, at 2 mg L⁻¹ of initial concentration, which is very considerably and similar to that reported by other works that did not contemplated the presence of anions.

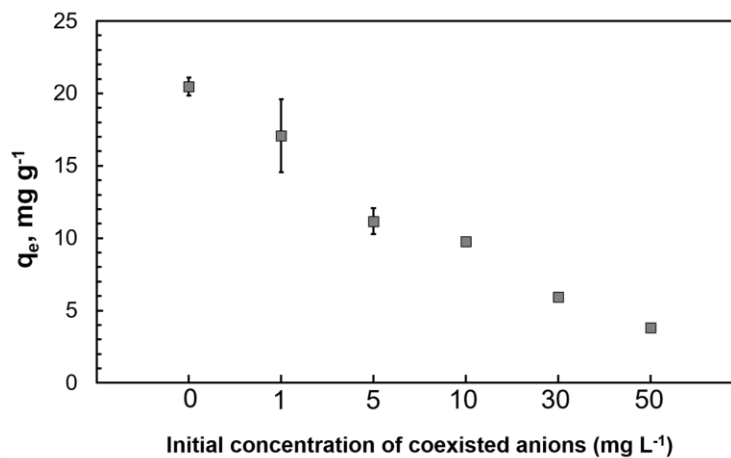


Figure 2.12. Effect of the presence of adsorbing anions on the arsenic adsorption capacity: mixture of 1, 5, 10, 30 y 50 mg L⁻¹ of each anion (F⁻, Cl⁻, SO₄²⁻, NO₃⁻, PO₄²⁻ and bicarbonates (HCO₃²⁻ and H₂CO₃²⁻)) in the presence of 2 mg L⁻¹ of As(V) at pH 7(±0.2) and 25 °C.

2.3.3.4. Adsorption Kinetics

Adsorption kinetics were performed to study the arsenic adsorption rate on ZrOx, FeOx and ZrOx-FeOx, as well as the time required to reach equilibrium (Figure 2.13). The adsorption process is carried out in the first instance on the most accessible places, i.e.

external surface and macropores. At this rapid stage, ZrOx-FeOx removed about 47% of the maximum capacity in the first 5 min. ZrOx and FeOx removed 18 and 61% of the maximum capacity at the same time, respectively. In the next stage dominates the intraparticle diffusion, therefore, the process becomes slower. FeOx and ZrOx-FeOx require about 40 min to reach equilibrium that could be considered fast, whereas ZrOx requires more than 90 min, which could be associated with the morphology and/or structure of the material. ZrOx requires more than 90 minutes to reach the equilibrium, because it has the highest surface area ($181 \text{ m}^2 \text{ g}^{-1}$) attributed to more micropores (see Table 2.1), therefore it requires more time for As(V) to diffuse within the porous structure and reach the active sites. Meanwhile, FeOx and ZrOx-FeOx require less time because these are more mesoporous (see Table 2.1) and their surface area is much smaller (21 and $49 \text{ m}^2 \text{ g}^{-1}$), therefore, the diffusion restrictions are lessened and the active sites are reached faster than in ZrOx. As known, the adsorption processes is carried out in seconds, when only exist electrostatic interactions [164], however, the arsenic adsorption process onto the adsorbents studied in this research takes minutes to reach equilibrium, which indicates that the adsorption takes place in particular sites [162].

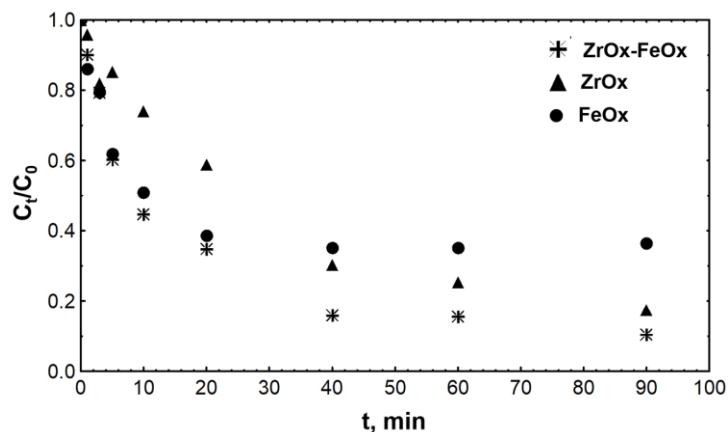


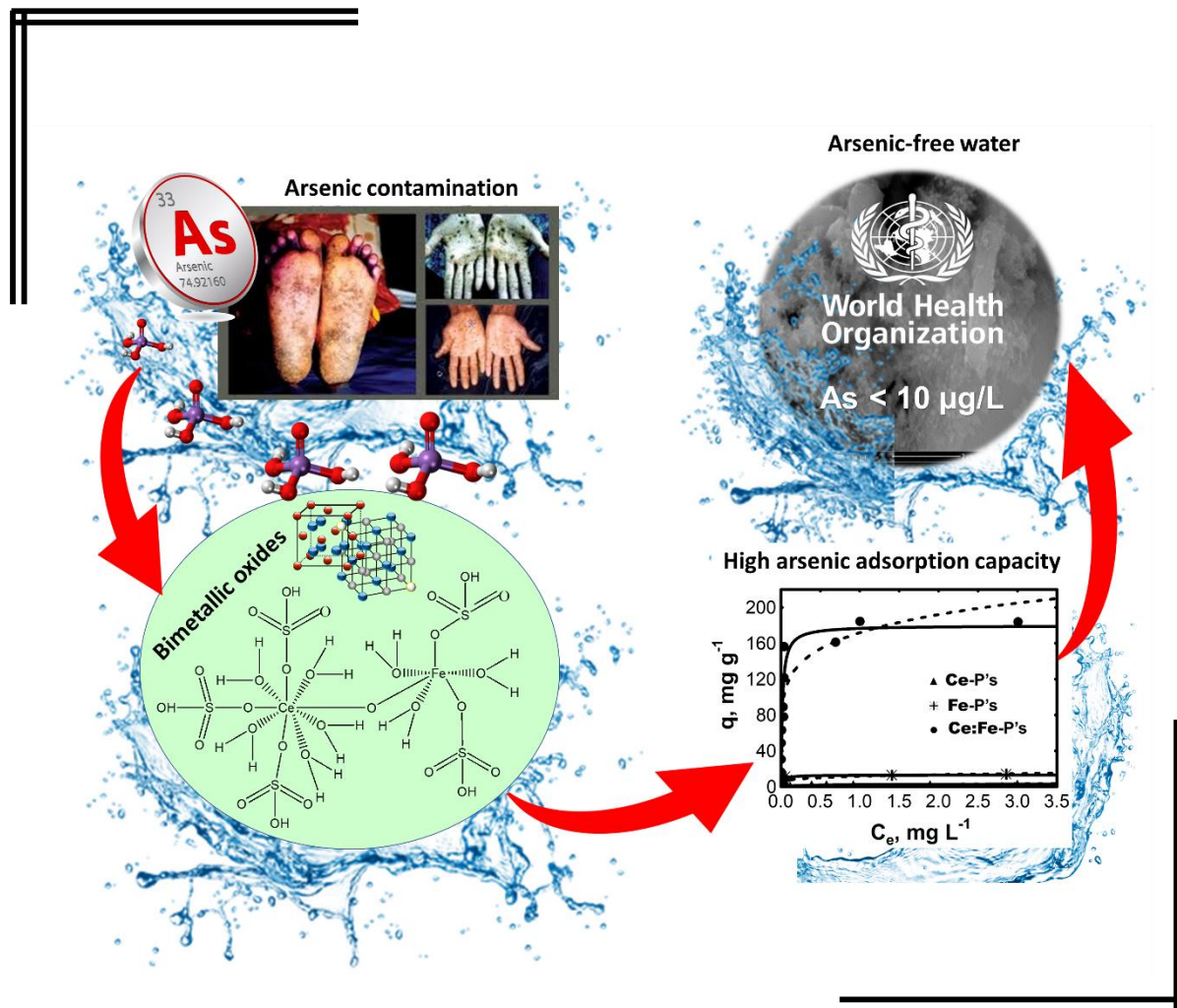
Figure 2.13. Adsorption kinetics of FeOx, ZrOx and ZrOx-FeOx oxyhydroxides at pH 7, 25 °C and As(V) initial concentration of 2 mg L^{-1} .

2.4. Conclusions

The results showed that the bimetallic oxides synthesized through the hydrothermal synthesis process, assisted by a microwave oven, are very efficient materials to remove arsenic from water. This methodology allows obtaining much smaller, homogeneous, and amorphous particles with a high density of OH groups in a short synthesis time. The spectra of FT-IR and the distribution of pKa's suggest that in the binary oxides (ZrOx-FeOx) a new union between the two metallic elements is formed by means of an oxygen (metal-O-metal). In addition, the substitution of the zirconium(IV) ion in the FeOx could induce defects in the crystals, thus increasing the surface area and the concentration of the hydroxyl groups. Due to the above, the bimetallic oxide of ZrOx-FeOx has a high arsenic adsorption capacity of up to 62.72 mg g⁻¹. In addition, the particles of ZrOx-FeOx have a nanometric size, therefore, the active sites are much more accessible, thus achieving 40% removal of the initial concentration of arsenic in the first 5 minutes. On the other hand, the adsorbent material ZrOx-FeOx can remove arsenic (27.3 to 10 mg g⁻¹) even when there are variations in the solution pH from 5 to 9, in addition, an adsorption capacity of about 20 mg g⁻¹ is maintain even in the presence of 1 mg L⁻¹ of coexisting anions such as F⁻, Cl⁻, SO₄²⁻, NO₃⁻, PO₄²⁻ and bicarbonates (HCO₃²⁻ and H₂CO₃²⁻).

CHAPTER III

New bimetallic adsorbent material based on cerium-iron nanoparticles highly selective and affine for arsenic(V)



CHAPTER III

New bimetallic adsorbent material based on cerium-iron nanoparticles highly selective and affine for arsenic(V)

Abstract

Bimetallic oxides have shown great interest in pollutant adsorption processes. Bimetallic oxides, in addition to inheriting the oxides properties that make them up, have a high OH groups density, which makes them highly promising adsorbents. In this work, a bimetallic oxide of cerium and iron (Ce: Fe-P's) was synthesized for the arsenic removal from water. The Ce: Fe-P's were characterized by various techniques (SEM, FTIR, XRD and XPS) and the adsorption capacity and kinetics as well as the effect of pH and the presence of coexisting anions were determined. The results showed that Ce: Fe-P's has an excellent adsorption capacity (179.8 mg g^{-1} at $\text{Ce} = 1 \text{ mg L}^{-1}$) even at low concentrations (120 mg g^{-1} at $\text{Ce} = 37 \text{ } \mu\text{g L}^{-1}$). Adsorption kinetics reached equilibrium in the first minute with an adsorption rate of $0.123 \text{ mg min}^{-1}$ (that is, in the first minute Ce: Fe-P's removed 80% of As initial concentration). Regarding the effect of pH, the arsenic adsorption capacity decreased up to 19% at pH above 7, attributed to the material's pHPZC, which is 6.8. On the other hand, the arsenic adsorption capacity of Ce:Fe-P's decreased 21% in the presence of 10 mg L^{-1} of each of the following anions F^{-} , Cl^{-} , SO_4^{2-} , NO_3^{-} , PO_4^{2-} and CO_3^{2-} . Ce:Fe-P's has been shown to be an excellent adsorbent material with low pH interference and coexisting anions, for which it has the patent number MX/a/2019/010551.

Key words: *Bimetal oxides, cerium, iron, adsorption, arsenic*

3.1. Introduction

The extraordinary increase of anthropogenic activities has created a great demand for natural resource, specialty water. Therefore, it is necessary to dig deeper wells to supply this vital liquid, which ends in the dissociation of various minerals, resulting in naturally occurring water contamination. Among the priority pollutants is arsenic, due to its very high toxicity [165]: this is found mainly in clay rocks [166,167] and in some geological formations [168]. Moreover, the arsenic contamination in groundwater is mainly due the desorption of arsenic compounds from natural rocks [169]. High arsenic concentrations have been reported in water mainly in Mexico, United States, China, Pakistan, India and Bangladesh, Argentina, Poland, Canada, Hungary, Japan and Korea, due to excessive exploitation of their aquifers [170,171]. On the other hand, developing countries tend to have a growing number of industrial factories, which unfortunately damage the environment. Arsenic is used mainly as an insecticide and herbicide or preservative for wood [172], in addition to being used in medicine, electronics and industrial manufacturing [173,174]. In the environment, arsenic and its compounds are mobile since they can dissolve in rain and contaminate lakes, rivers, and groundwater. Arsenic contamination in groundwater is a great danger to public health in various countries of the world [173,175,176]. The long-term ingestion of arsenic-contaminated water ($50 \mu\text{g L}^{-1}$) can cause arsenicosis, which is characterized by hyperpigmentation and hyperkeratosis [177–180]. Therefore, the World Health Organization (WHO), Environmental Protection Agency (EPA) and other health-related regulatory agencies have recommended an arsenic concentration of $10 \mu\text{g L}^{-1}$ as the maximum permissible limit in drinking water [181]. Due to the above, it is necessary to invest in the development of new and more efficient materials to remove priority pollutants such as arsenic from water. Among the various technologies for the arsenic removal from water, adsorption has emerged as the most promising technology due to the low costs and the simplicity of design. On the other hand, among the various adsorbent materials used for the

removal of numerous contaminants are activated carbon, colloidal oxides and bimetallic oxyhydroxides [182]. Various studies have shown that iron oxide is an efficient adsorbent for arsenic in water [183]. In addition, cerium is one of the most abundant and least expensive rare earths. Among the advantages that cerium oxide present are its low solubility in acid solutions and the null dissolution during the elimination of contaminants from water [184]. Thus, cerium oxide has been considered as one of the most promising alternative adsorbents for anions removal, such as: fluoride [185], dichromate [186] and arsenate [187,188]. Recently, the synthesis of mixed metallic oxides as adsorbents has gained more attention, since the result compound can inherit the advantages of the original materials. Iron oxide has been synthesized in combination with various oxides (i.e. cerium, copper, manganese, titanium, zirconium and tin) in order to form bimetallic oxides and improve their adsorption performance of contaminants [189–191]. In recent studies the bimetallic oxides of Ce-Fe have been studied giving good arsenic adsorption capacities, even higher than 90 mg g⁻¹ [192–196]. Generally, these bimetallic oxides have been synthesized by precipitation and solvothermal processes, giving good results. However, methods of synthesis that allow a better control, such as the hydrothermal method assisted by a microwave oven, have proven to obtain not only mixes of bimetallic oxides but also bimetallic oxides with superior adsorption capacities. Due to the above, the objective of this research is to find the optimum synthesis conditions to develop bimetallic oxyhydroxides of iron and cerium (CeOx-FeOx) with three-dimensional hierarchy of nanometric size with an elevated OH density to improve the ligands exchange between anionic species of As(V) and the hybrid adsorbent and the adsorption kinetics.

3.2. Methods and Materials

3.2.1. Chemical materials

The reagents for the oxides and bimetallic oxides synthesis were cerium nitrate hexahydrate ($\text{Ce}(\text{NO}_3)_3 \cdot 6\text{H}_2\text{O}$) and ferrous sulfate heptahydrate ($\text{FeSO}_4 \cdot 7\text{H}_2\text{O}$). Sodium arsenate ($\text{Na}_2\text{HAsO}_4 \cdot 7\text{H}_2\text{O}$) was used for the preparation of arsenic solution, hydrochloric acid 0.1 M (HCl) and sodium hydroxide 0.1 M (NaOH) were used to adjust the solutions pH, all of which were of analytical grade with a purity higher than 99% from Sigma-Aldrich (USA). The solutions were prepared with desionized water (18 M Ω /cm).

3.2.2. Experimental design and synthesis of adsorbent materials

The molar ration of cerium, lanthanum and/or iron was varied in the G30 vials used in a microwave oven (Monowave 400, Anton Paar) to synthesize bimetallic oxyhydroxides, as shown in Table 3.1.

Table 3.1. Solutions used to synthesize the bimetallic oxyhydroxides adsorbents

Design	Molar Ration (MR)														
Ce:Fe	1:0	1:1	1:2	1:3	1:4	2:1	2:3	2:4	3:1	3:2	3:4	4:1	4:2	4:3	0:1

The microwave oven was programmed to start at room temperature and then increase it up to 110 °C within 5 min, then this was kept isothermal for 30 min. After the synthesis process ended, the supernatant was decanted, and the solids obtained were washed with deionized water to eliminate the remaining solution, and then these were rinsed three times with ethanol to ensure a better drying of the oxyhydroxides. Finally, these were dried for 12 h at 80 °C in an oven.

3.2.2. Physiochemical characterization

The surface charge distribution and the point of zero charge (pH_{PZC}) of each adsorbent were obtained by means of an automatic titrator (Mettler-Toledo T70). 100 mg of sample were dispersed in 50 ml of a 0.1 M NaCl aqueous solution as electrolyte and stirred for 12 h to ensure that the equilibrium was reached. Subsequently, the solution pH was adjusted to 3 with 0.1 M HCl. Then, a titration was carried out with 0.1 M NaOH under a nitrogen atmosphere to avoid CO_2 interferences. The pK_a values, from the surface charge distribution, were obtained with the program SAEIUS-pK-Dist © (1994).

The surface area, pore volume and pore-size distribution of Ce-P's, Fe-P's and Ce:fe-P's were determined by N_2 adsorption-desorption isotherms at 77 K in a Micrometrics Accelerated Surface Area and Porosimetry Analyzer 2020. The surface area was calculated using the BET equation and the pore size distribution was determined by using the density functional theory (DFT), protocol established in this equipment.

For infrared analysis, a Thermo-Nicolet device, Nexus 470 FT-IR E.S.P., was used. The atmospheric water and CO_2 were always subtracted.

The morphological and structural characteristics of samples were studied by scanning electron microscopy (SEM) by an ESEM FEI-QUANTA 200, and X-ray Diffraction (XRD) by a Bruker D8 Advance diffractometer. The diffractograms analysis was carried out by using the Hannawalt method.

X-Ray photoelectron spectroscopy (XPS) was performed in a VG-Microtech Multilab 3000 spectrometer using an Al K α radiation (1253.6 eV). The deconvolution of the XPS peaks for C1s, O2p, Fe2p, Ce3d and S2p was done by least squares fitting using Gaussian-Lorentzian curves, while a Shirley line was used for the background determination.

3.2.3. Arsenic (V) adsorption test

30 mL of As(V) solution at different concentrations (from 0.05 to 20 mg L⁻¹) were added in conical polypropylene tubes containing 2 mg of Ce-P's, Fe-P's or Ce:Fe-P's at pH 7 and 25 °C (pH was adjusted with 0.1 M NaOH or HCl). The concentration of arsenic in solution was determined by ICP-OES (varian 730-ES) at a wavelength of 188.98 nm. The adsorption capacity was determined by a mass balance (Eq. 1).

$$q = \frac{V(C_0 - C_e)}{w} \quad (\text{Eq. 1})$$

where **q** is the adsorption capacity in mg g⁻¹, **V** is the volume in L, **C₀** and **C_e** are the initial and in equilibrium concentrations in mg L⁻¹, respectively and **w** is the mass of the adsorbent in g.

Adsorption kinetics were performed as following: a stock solution of 5 mg L⁻¹ of As(V) was prepared at pH 7. The initial pH was adjusted with 0.1 M HCl or NaOH. Subsequently, 30 mL of the stock solution were added to 13 polypropylene falcon tubes of 50 mL containing 2 mg of the adsorbent material, which were then placed in an incubator at 25 °C and 120-130 rev/min. Test tubes were taken at different times (30 seconds, 1, 5, 10, 20, 40, 60, 90,

120, 180 and 240 minutes) and the solution was analyzed to determine the remaining As(V) concentration as explained in the previous section: the solution pH was also recorded.

To evaluate specific velocity constants, the pseudo-first and pseudo-second kinetic equations were applied [197,198]. The linear form of pseudo-first-order kinetic rate equation can be presented as follows:

$$\ln(q_e - q_t) = \ln(q_e - k_1) t \quad (\text{Eq. 2})$$

where q_t and q_e are the adsorption capacities (mg g^{-1}) at equilibrium and t time (min), respectively, and k_1 (min^{-1}) is the pseudo first-order rate constant computed from the slope of the linear plot of $\ln(q_e - q_t)$ vs. t .

The pseudo-second-order-kinetic rate equation assumes that the driving force on adsorption capacity ($q_e - q_t$), is proportional to the available fraction of active sites. The linear expression can be represented as follows:

$$\frac{t}{q_t} = \frac{1}{k_2 q_e^2} + \frac{1}{q_e} t \quad (\text{Eq. 3})$$

where k_2 is the pseudo-second-order rate constant of sorption ($\text{g} \cdot \text{mg}^{-1} \cdot \text{min}^{-1}$), q_e is the amount of analyte adsorbed at equilibrium ($\text{mg}^{-1} \cdot \text{g}^{-1}$), and q_t is the amount of analyte adsorbed ($\text{mg}^{-1} \cdot \text{g}^{-1}$) at any time t (min).

The effect of co-existing anions such as: chloride (Cl^-), sulfate (SO_4^{2-}), nitrate (NO_3^-), phosphate (PO_4^{2-}) and carbonate (CO_3^{2-}), which are normally found in groundwater, were considered on the arsenic adsorption capacity of bimetallic oxyhydroxides. To study this effect, a synthetic water was prepared with 1, 5, 10, 30 and 50 mg L⁻¹ of each anion (Cl^- , SO_4^{2-} , NO_3^- , PO_4^{2-} and CO_3^{2-}), in the presence of 5 mg L⁻¹ of As(V): these experiments were performed in batch systems.

3.3. Results and discussion.

3.3.1. Experiments design

The experimental design results showed that with an initial As concentration of 5.6 mg L⁻¹ the hybrid Ce-Fe materials with a molar ratio (MR) of 2:3 and 2:4 presented the highest arsenic adsorption capacity, 81 and 79 mg g⁻¹, accordingly, as reported in Figure 3.1a. Moreover, it was observed that the arsenic adsorption capacity of Ce:Fe-P's increases approximately 8 times with respect to the pristine oxides that make it up (7.9 and 8.9 mg g⁻¹ for Fe-P's and Ce-P's oxides, respectively). The high adsorption capacity of the Ce:Fe (2:3) and Ce:Fe (2:4) materials is mainly due to the high density of OH groups on their surface. The density of OH sites is very low in the case of Ce:Fe (1:1), however as the concentration of cerium and/or iron increases, so does the intensity of the broad band from 1250 to 950 cm⁻¹ in the FTIRs attributed to OH groups (Figure 3.2). However, it reaches a point where the concentration of cerium or iron is very high that these cations occupy the OH groups to form Ce-O and/or Fe-O bonds and therefore, the density of OH groups start to decrease as seen in Figure 3.2. That is why the appropriate concentrations of both metals must be sought (i.e., 2:3 and 2:4 Ce:Fe ratios) to obtain materials with a high OH groups density and hence a high adsorption capacity. Arsenic, according to the literature and as

explained in section 3.4.2, is adsorbed by means of ligand exchange with the OH groups of the adsorbent material [199].

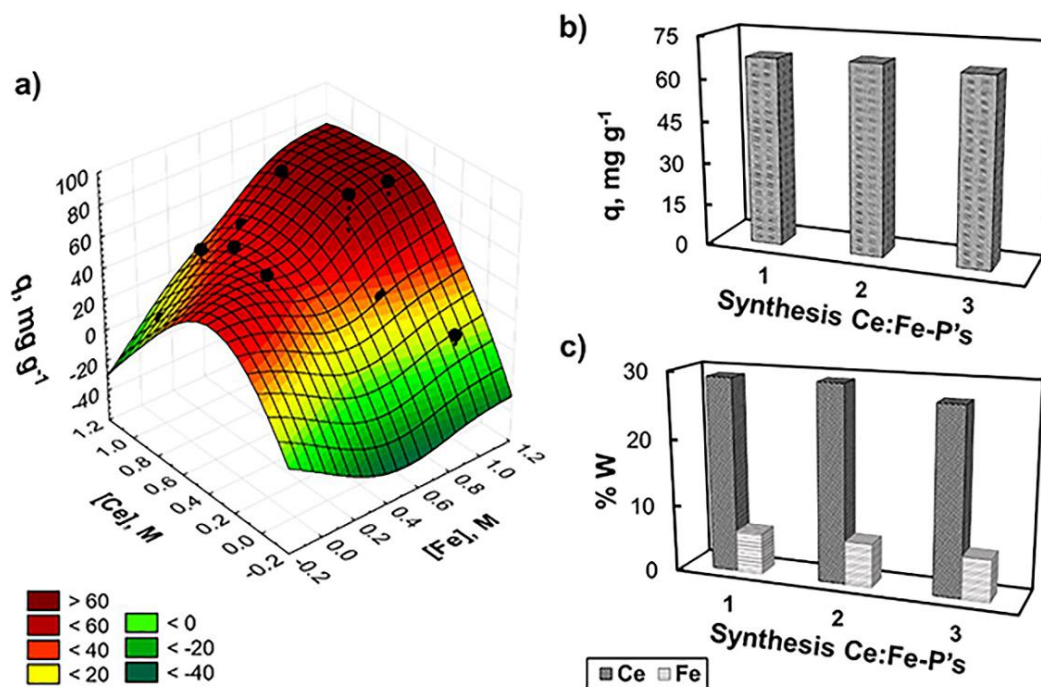


Figure 3.1. (a) Effect of cerium and iron concentrations in the synthesis of hybrid materials and in their arsenic adsorption capacity when using an initial concentration of 5.6 mg L⁻¹ of contaminant. (b) Arsenic adsorption capacity and (c) Ce and Fe content of three replicas of bimetallic oxyhydroxides Ce:Fe-P's (2:3) to demonstrate the synthesis reproducibility.

Also the synthesis and adsorption capacity of the hybrid material Ce:Fe-P's (2:3) was fully reproducible as shown in Figure 3.1b and c where the average cerium and iron content of these three replicates was 28.5 and 6.3 %W, respectively. Therefore, a high cerium content causes a synergistic effect in terms of adsorption capacity due to the higher density of OH groups, as will be discussed below. It is important to mention that from this point on, only the blanks and sample Ce:Fe-P's(2:3), called Ce:Fe-P's, were studied.

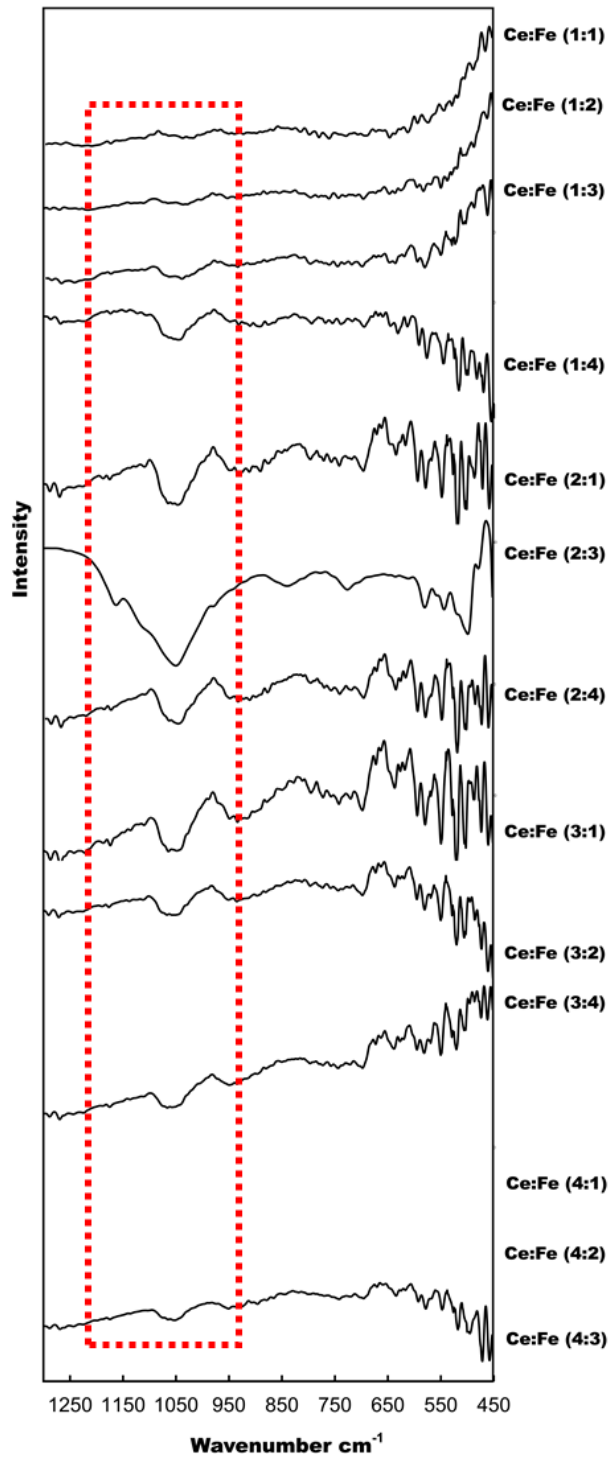


Figure 3.2. FTIR of synthesized materials at different molar ratios of Ce:Fe.

3.3.2. Materials characterization

3.3.2.1. Surface area and pore volume distribution

The BET surface area and pore volume of Ce-P's, Fe-P's and Ce:Fe-P's are reported in Table 3.2 in supplementary material. Ce-P's and Fe-P's had a surface area of 1 and 21 $\text{m}^2 \text{g}^{-1}$, respectively. However, the Ce:Fe-P's reported only 6 $\text{m}^2 \text{g}^{-1}$, 72% less than Fe-P's, which is attributed to the decrease in the volume of mesopores and macropores of 69 and 44%, respectively (Figure 3.3a). Moreover, Ce-P's are non-porous since the CeO_2 structure is highly crystalline, as will be discussed later in the XRD and SEM results. The nitrogen adsorption isotherms of the studied materials were type IV, and the hysteresis of the isotherms corresponds to type H3, characteristic of solids with laminar pores (Figure 3.3b).

Table 3.2. Surface area, pore volume and average pore diameter of studied materials.

Sample	m^2/g		cm^3/g		nm
	BET area	V_{micro}	V_{meso}	V_{macro}	Average pore diameter
Fe-P's	21	0.0011	0.0503	0.0185	11.7
Ce-P's	1	0.0004	0.0002	0.0000	2.7
Ce:Fe-P's	6	0.0000	0.0155	0.0103	3.1

On the other hand, the materials Fe-P's, Ce-P's and Ce:Fe-P's presented a pore diameter of 11.7, 2.7 and 3.1 nm, respectively. Fe-P's has a higher proportion of meso and macropores (0.0503 and 0.0185 $\text{cm}^3 \text{g}^{-1}$, respectively) than Ce-P's which only presented micro and mesopores (0.0004 and 0.0002 $\text{cm}^3 \text{g}^{-1}$, respectively), and a very small surface area due to its high crystallinity as reported by SEM and XRD analyzes. Finally, it was

observed that Ce:Fe-P's have an average pore diameter and surface area between that of Fe-P's and Ce-P's, and lack micropores.

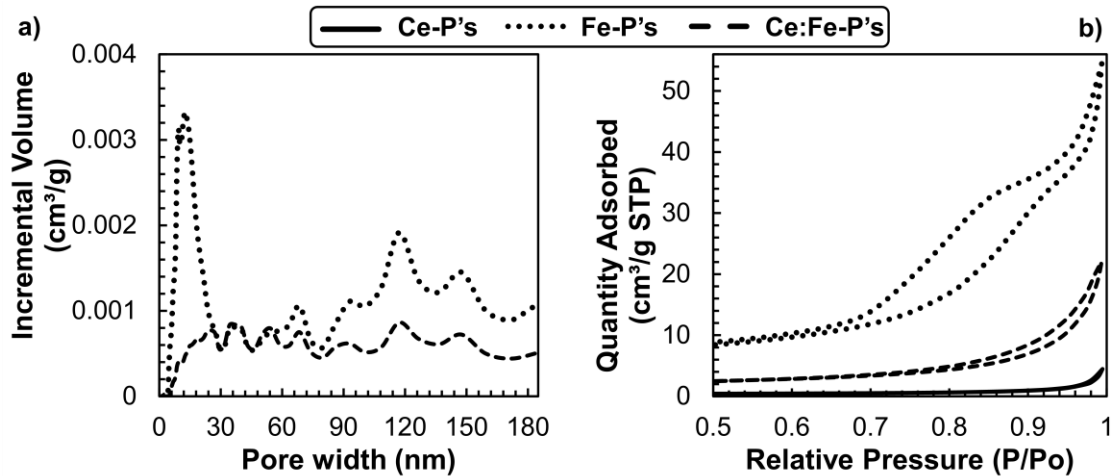


Figure 3.3. (a) Pore size distribution from N₂ adsorption with BJH model and (b) N₂ adsorption isotherms for Ce-P's, Fe-P's and Ce:Fe-P's.

3.3.2.2. Structure and morphology studies of synthesized materials

The scanning electron microscopy studies of Ce-P's, Figure 3.4a, show octahedral structures that agree with the observed morphology for pure ceria reported by Hakuta et al., 1998. Moreover, Figure 3.4b shows Fe-P's particles in form of flowers, which can be attributed to the interaction between goethite and iron sulfate [201,202], and Figure 3.4c reports Ce:Fe-P's in the form of urchins and fibrils. These last morphologies of Ce:Fe-P's were very different to those shown by the blanks, therefore they can be attributed to the interactions between cerium and iron atoms. Moreover, their respective EDS showed the presence of Ce and Fe, while Cu and Al come from the grid and pin. The elemental mapping reported 34% of Fe and 8% of Ce (Figure 3.5) in a ratio of 1:4.25, like that found by acid digestion (1:4.5). A good distribution of oxygen and sulfur was also observed, which may suggest the interaction of sulfate ions with the bimetallic oxide structure of Ce:Fe-P's as

observed in the XRD analyzes. Furthermore, the particle size of Ce:Fe-P's, determined by laser diffraction, was between 578 and 818 nm (Figure 3.6).

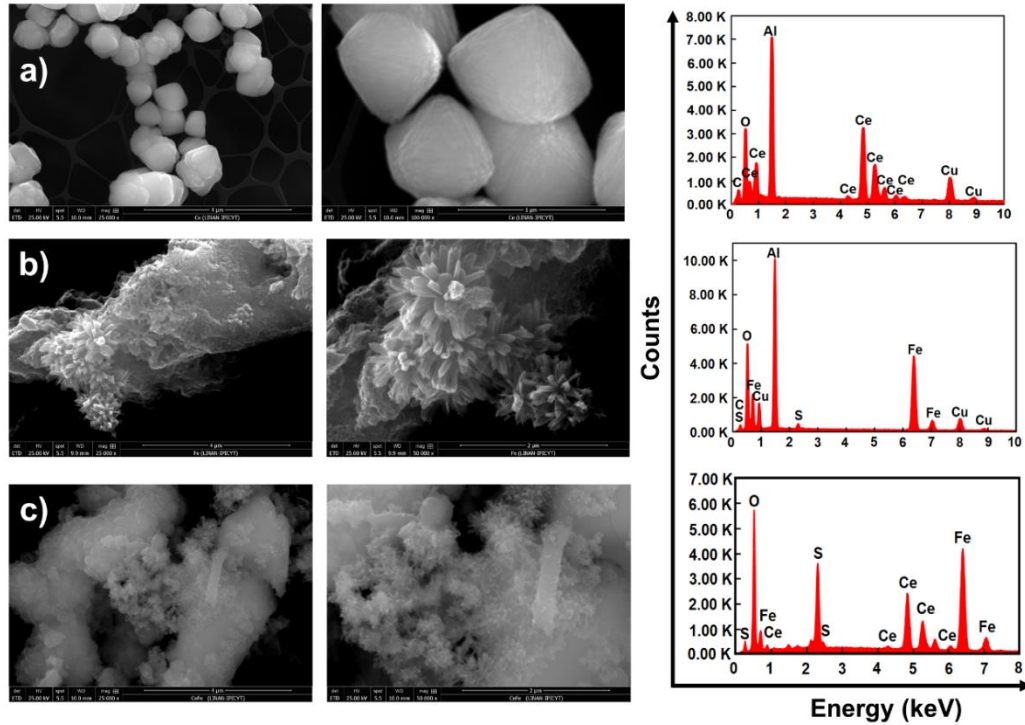


Figure 3.4. SEM images of (a) Ce-P's, (b) Fe-P's and (c) Ce:Fe-P's , and their respective EDS analysis.

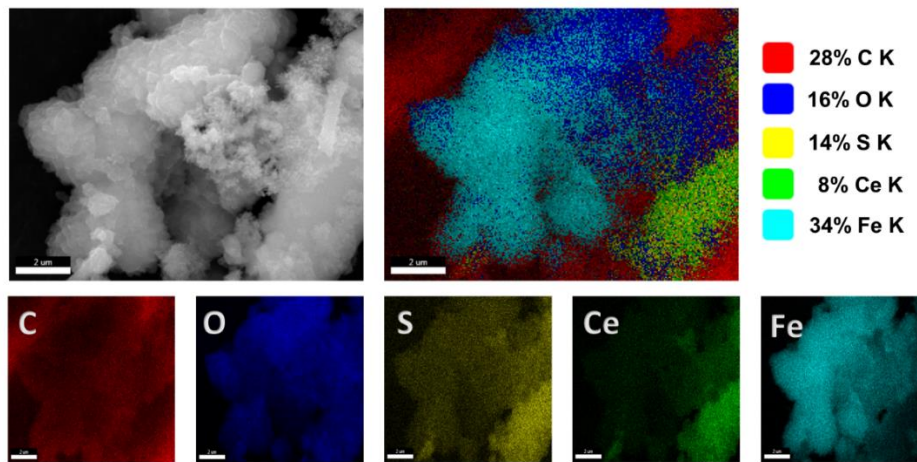


Figure 3.5. Elementary mapping of bimetallic oxyhydroxides (Ce:Fe-P's).

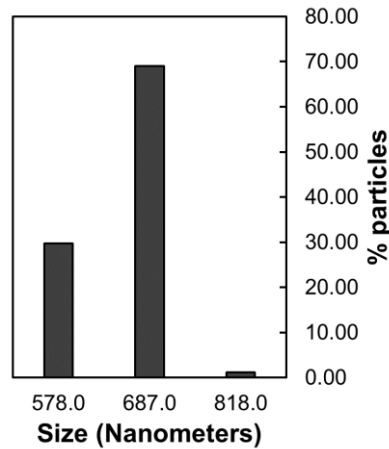


Figure 3.6. The particle size of the Ce:Fe-P's by laser diffraction using a zettameter NANOTRAC WAVE II Microtrac.

3.3.2.3. Surface charge distribution studies.

As known the point of zero charge (pH_{PZC}) is the pH at which the positive and negative charges of a material are balanced, that is, the surface charge is neutral. At pH lower than pH_{PZC} the surface of the adsorbent is positively charged; therefore, it attracts anions. On the contrary, when the pH is higher than the pH_{PZC} , the surface is negatively charged attracting cations. The pH_{PZC} of Fe-P's was 7.2 (see Figure 3.7a), which indicates that at the working pH ($\text{pH} = 7$) the charge of the material is more less neutral. According to the literature, the pH_{PZC} of iron oxides is between 5.5 to 9.0 [203], and between 7.5 to 9.2 specifically for goethite [204–206]. Therefore, the pH_{PZC} value of Fe-P's is attributed in part to the presence of goethite as shown in the XRD analyzes (Figure 3.8). On the other hand, the pH_{PZC} of Ce-P's was 8.1, which was similar to that reported in the literature by De Faria and Trasatti, 1994; Limbach et al., 2008; Speed, 2016, whom reported that the pH_{PZC} of CeO_2 in deionized water was equal to 8.0, however, Phanichphant et al., 2016, reported a pH_{PZC} of 6.95. These

differences can be explained by the presence of several components or groups on the nanoparticles surface of cerium oxides due to also to their different oxidation states, since these particles were usually obtained from different sources [211,212]. On the other hand, the hybrid Ce:Fe-P's showed a pH_{PZC} of 6.8, similar to that of pristine iron oxide. However, something to highlight is the remarkable increase of positive and negative active sites with respect to iron oxyhydroxides, which accounts on the arsenic adsorption capacity, as will be discussed later.

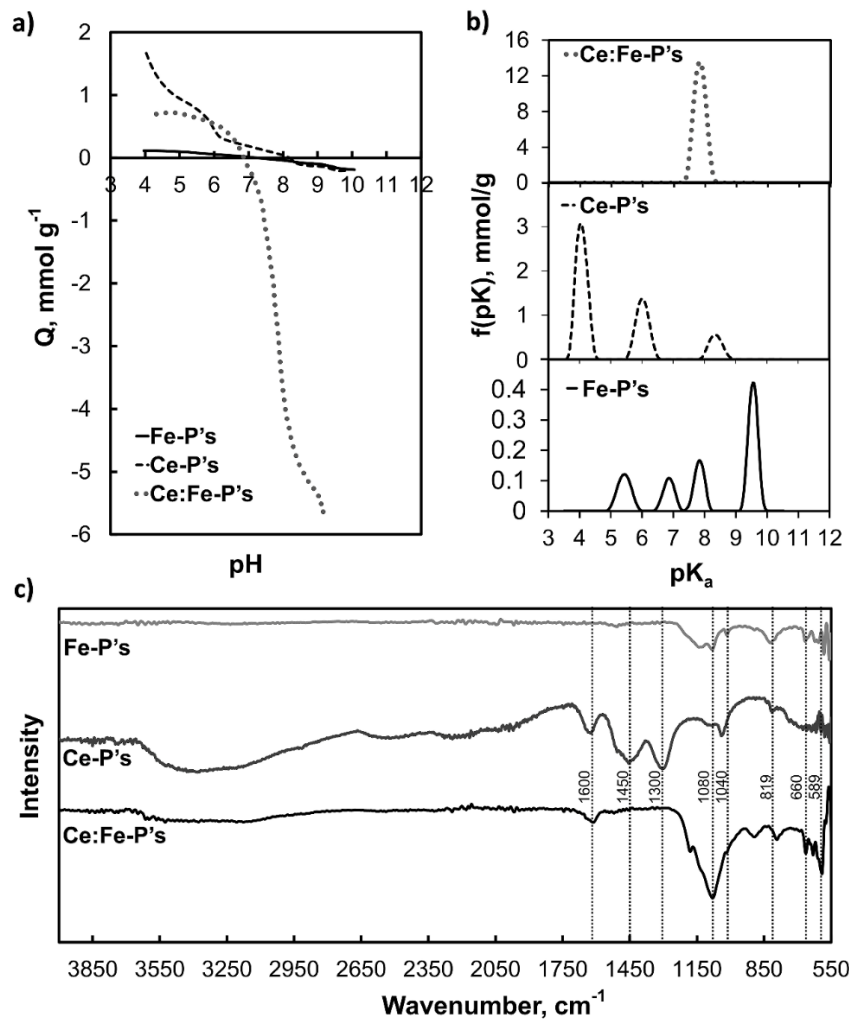


Figure 3.7. (a) Surface charge distribution and (b) pK_a 's distribution for each material. (c)

FT-IR of Fe-P's, Ce-P's and Ce:Fe-P's.

The pK_a 's distribution in Figure 3.7b, were associated with the chemical changes on the surface of pristine and bimetallic oxyhydroxides. The pK_a from 5.0 to 6.0 and 9.0 to 10.0 can be related to $Fe(OH)_3$ and $Fe(OH)_4$, respectively [213]. In the case of Ce-P's the pK_a values between 3.5-4.5, 5.5-6.5 and 8.0-9.0 can be associated to CeO_2 , Ce-OH and $Ce(OH)_2$, respectively [214]. In the case of the bimetallic oxyhydroxides (Ce:Fe-P's) the pK_a 's peaks between 3.5 and 7 decreased in intensity, while the pK_a between 7.0 and 8.5 showed a remarkable intensity rise, indicating an outstanding increase in OH groups concentration (OH-Ce-O-Fe-OH), which is expected to show a much higher As(V) adsorption capacity than the blanks (FeOx, CeOx).

3.3.2.4. FTIR, XRD and XPS studies.

To compliment the materials characterization, FT-IR studies were conducted (Figure 3.7c). The spectrum of Fe-P's showed low intensity bands at 589 and 664 cm^{-1} attributed to vibrations of the symmetric stretch of Fe-O [215–217]. The band at 810 cm^{-1} is attributed to the vibration of OH [218], whereas the doublet at 1150 cm^{-1} and 1050 cm^{-1} correspond to vibrations of OH bending and stretch of Fe-O, respectively [218]. The Ce-P's spectrum showed a band at 819 cm^{-1} which is characteristic of Ce-O vibrations [219], whereas the bands at 1040, 1300 and 1450 cm^{-1} are attributed to the characteristic peaks of CeO_2 [220,221]. In the case of Ce:Fe-P's, the FT-IR spectrum showed an adsorption band at 1600 cm^{-1} which is attributed to OH. An small band at 790 cm^{-1} and a broad band at 660 cm^{-1} are attributed to the Ce-O-Fe bond that is formed by the OH of the individual oxides (Fe-OH and Ce-OH) [101,222]. According to the pK_a distribution studies, the Ce:Fe-P's have a high density of OH groups (see Figure 3.10). These groups contribute to the formation of bimetallic oxyhydroxides (Ce-O-Fe), characteristic of the synthesized metal oxides Ce-OH and Fe-OH

observed at 1080 cm^{-1} [223]. The peak at 950 cm^{-1} was attributed to the bending vibration of Ce–OH or Fe–OH [224]. Also the band at 1030 cm^{-1} is attributed to Fe–O [218]. On the other hand, the low intensity bands at 1180 and 880 cm^{-1} are characteristic of SO_4^{2-} complexes (M– SO_4 ; M = Ce and/or Fe) [225].

Furthermore XRD studies identified the polymorphic phases of Ce-P's, Fe-P's and Ce:Fe-P's as shown in Figure 3.8. The diffraction patterns of Ce-P's showed peaks at 2θ angles of 28.21° , 33.16° , 47.54° , 56.31° , 59.02° , 69.35° , 76.53° , 79.21° , 88.57° and 95.45° that are attributed to the cubic structure of cerium dioxide (CeO_2), according to the reference standard PDF 01-081-9325. In addition, the diffractogram shape indicates that this metal oxide is crystalline [226–228]. On the other hand, Fe-P's showed two phases, the monoclinic phase of $\text{Fe}(\text{SO}_4)(\text{H}_2\text{O})$ (hydrated iron sulphate) and the orthorhombic phase of FeOOH (Goethite). Their patterns were corroborated with PDF files 01-081-0019 and 01-076-7156, respectively. Additionally, Figure 3.8 shows the XRD patterns for the hybrid Ce:Fe-P's, where most of the peaks correspond to a monoclinic structure of $\text{Ce}_2(\text{SO}_4)_3(\text{H}_2\text{O})_5$. Furthermore, the same sample showed the structure of the orthorhombic compound of $\text{Fe}(\text{SO}_4)_2\text{H}$ at 2θ angles of 27.1° , 28.48° , 39.91° , 40.24° , 45.99° , 51.42° , 56.69° , 59.04° , 61.22° and 78.57° (PDF 01-073-3970). It is important to point out that the three peaks with the highest intensity correspond to $\text{Ce}_2(\text{SO}_4)_3(\text{H}_2\text{O})_5$ at 2θ angles of 11.1° , 27.1° and 28.48° (PDF 01-089-6404), which is associated with the high concentration of cerium in the bimetallic oxyhydroxide (see Figure 3.1c).

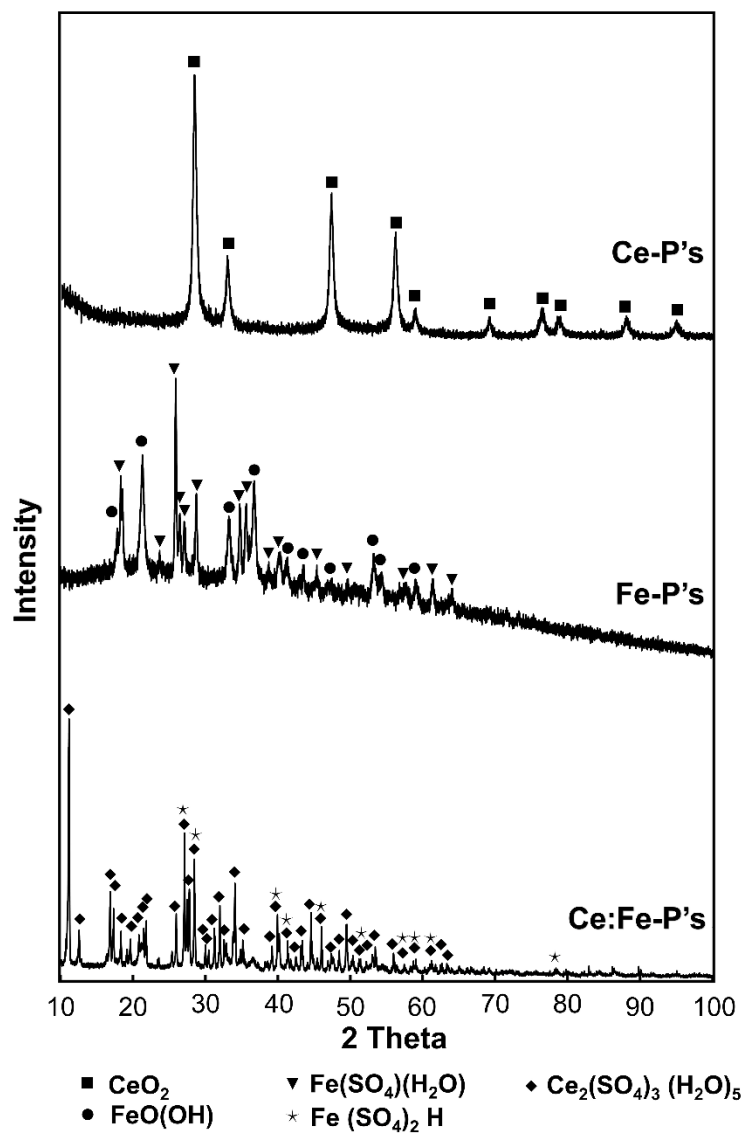


Figure 3.8. XRD patterns of Ce-P's, Fe-P's and Ce:Fe-P's with a step of $0.02^\circ 2\theta$ at 10 s per step. The symbols show the crystalline phase of each oxide.

Furthermore, XPS analyzes were performed to elucidate the possible structure of Ce:Fe-P's and to confirm the crystalline phases reported by XRD analysis. The complete XPS spectra in the C 1s region referenced at 284.6 eV was realized (see Figure 3.9).

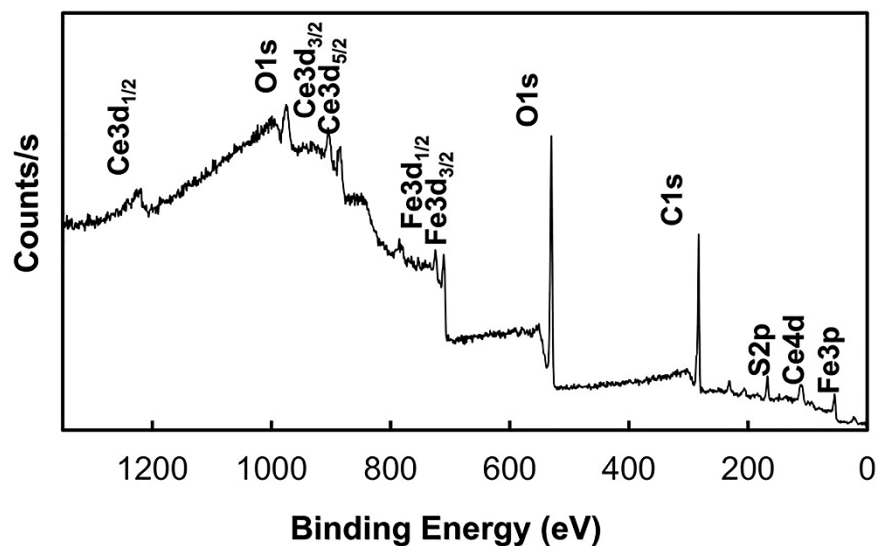


Figure 3.9. The complete XPS spectra in the C 1s region referenced at 284.6 eV.

Figure 3.10 shows the XPS spectra in the Ce 3d, Fe 2p, O 1s and S 2p, region. The XPS peaks of Fe 2p_{3/2} and Fe 2p_{1/2} for Ce:Fe-P's are shown in Figure 3.10a. The Fe 2p_{3/2} peak is narrower and has high intensity, therefore, its area is greater than Fe 2p_{1/2}, which may be associated with Fe 2p_{3/2} having four-state degeneration while Fe 2p_{1/2} has only two. A satellite peak at 719.69 eV is clearly observed, which does not overlap the Fe 2p_{3/2} and/or Fe 2p_{1/2} peaks. Fe 2p_{3/2} peaks at a binding energy (BE) of 711.4 and 713.34 eV are associated with FeOOH and FeSO₄, respectively [229–231], which were reported by the XRD analyzes (Figure 3.8). The peak at 711.4 eV binding energy of Fe 2p_{3/2} is also associated with FeSO₄ 7H₂O. This is corroborated with the oxygen spectrum (Figure 3.10c) and S 2p (Figure 3.10d), where the presence of FeSO₄ 7H₂O (168.9 eV) and FeSO₄²⁻ (169.8 eV) is also observed [229,230,232,233]. All these results are consistent with the XRD studies.

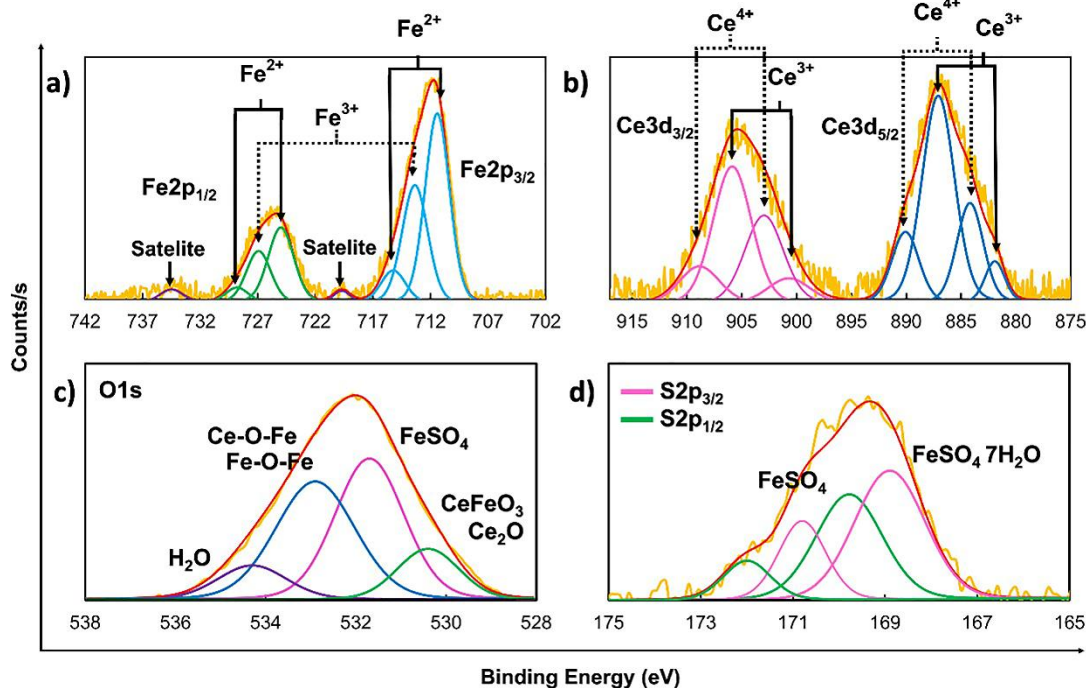


Figure 3.10. XPS spectra in the C 1s region referenced at 284.5 eV for: **(a)** Fe 2p, **(b)** Ce 3d, **(c)** O 1s and **(c)** S 2p of Ce:Fe-P's.

Moreover, the XPS of cerium is associated with Ce 3d_{5/2} and Ce 3d_{3/2} peaks at 880-893 eV and 896-915 eV, respectively (Figure 3.10b) [234]. The peaks corresponding to the levels Ce_{5/2} at a BE of 884.2 and 890.1 eV and the peaks corresponding to the levels Ce_{3/2} at a BE of 903.0 and 908.9 eV have been assigned to a mixture of the final states Ce 3d⁹ 4f² O 2p⁴ and Ce 3d⁹ 4f¹ O 2p⁵ for Ce(IV). On the other hand, the peaks corresponding to the Ce_{5/2} levels at a binding energy of 881.9 and 887.1 eV and the Ce_{3/2} levels at a BE of 900.7 and 905.9 eV are assigned to Ce 3d⁹ 4f² O 2p⁵ and Ce 3d⁹ 4f¹ O 2p⁶ for Ce(III) [235,236]. Therefore, the XPS of Ce:Fe-P's indicates the existence of both oxidation states of cerium (Ce⁴⁺ and Ce³⁺) on the sample surface. This is confirmed with the oxygen spectrum (Figure 3.10c) and S 2p (Figure 3.10d), where the CeO₂ bond is shown at a binding energy of 530.6 eV (Figure 3.10c) [237]. On the other hand, the binding energy at 532.76 and 530.6

eV can be attributed to the union of cerium with iron through oxygen as Ce-O-Fe and CeFeO₃, respectively, which confirms the formation of bimetallic oxides (NIST XPS Database). Studies indicate that the higher ratio of Ce³⁺/Ce⁴⁺ can generate a charge imbalance, oxygen vacancies and unsaturated chemical bonds on the surface of cerium oxide promoting a bond with other cations (i.e. Ce-O-Fe).

3.3.3. Synthesis mechanism of Ce:Fe-P's

As known, metal ions (M⁺) in aqueous medium are covered by a solvation sphere, forming hexacoordinated aquo-complexes such as [Fe(OH₂)₆]³⁺ [238]. The formation of metal oxyhydroxides is carried out by the neutralization of this aquo-complex by a mechanism of condensation reactions given by two steps called initiation and propagation. Initiation is considered as the first step in which the hydroxy complex [M(OH)(OH₂)₅]²⁺ is formed, either by an acid-base reaction or by an increase in temperature (Figure 3.11a) [4].

In the second step, propagation occurs as soon as a hydroxylated (OH) species appear, and then condensation is conducted leading to oxygenated bridges between complex cations (Figure 3.11b). This means that the hydroxy-ligand (OH) formed can act as a nucleophile and reacts with another aquo-complex by removing an aquo-ligand (H₂O). Subsequently, an oxo-bond (M-O-M) characteristic of the metal oxides is generated, because the hydroxyl-ligand undergoes a deprotonation [4]. The process ends until the minimum energy state is reached thermodynamically. Therefore, the hydroxyl-ligand loses its nucleophilic character and iron, for example, loses its electrophilic character [4].

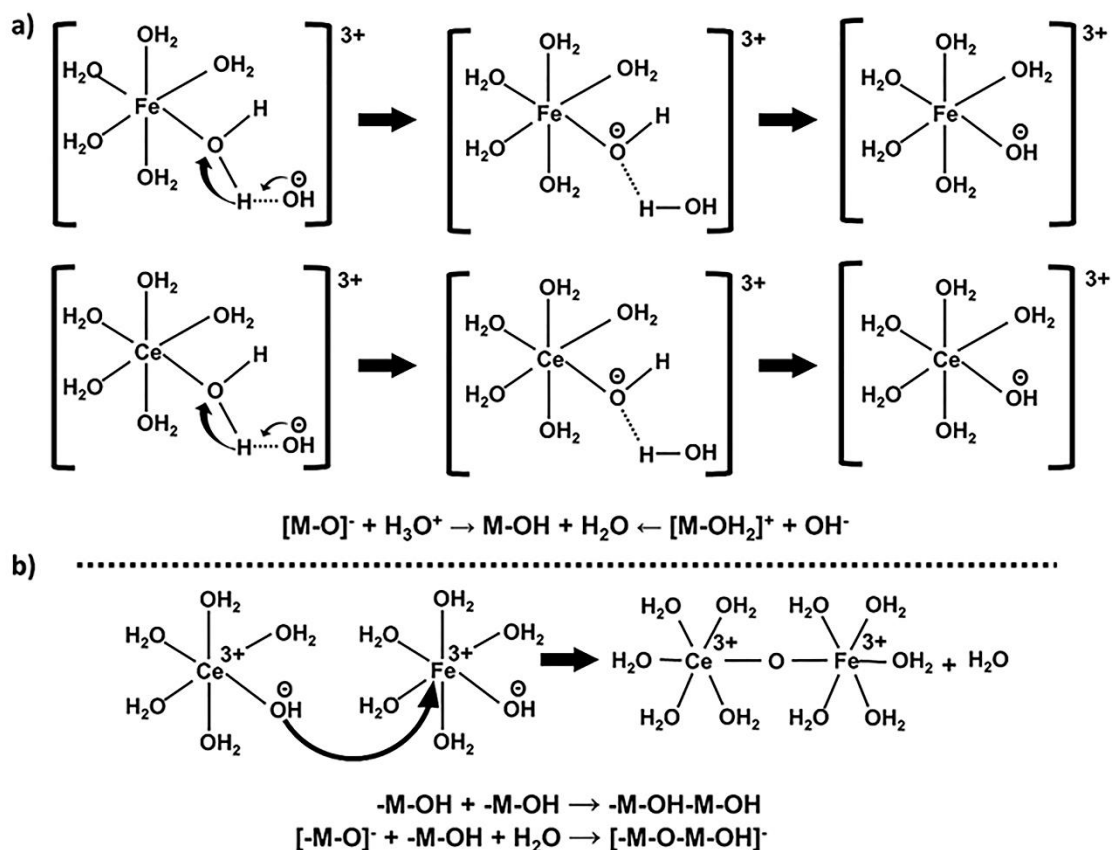


Figure 3.11. Mechanism of condensation reactions given by two steps called **(a)** initiation and **(b)** propagation and condensation [4].

Ce can exhibit different electronic states $[Xe] Ce 4f^0$ (Ce^{4+}), $[Xe] Ce 4f^1$ (Ce^{3+}) with mixed or intermediate valence. Therefore, $Ce 4f^0$ electron has the ability to adopt a different state in bimetallic compounds providing different properties and crystalline structures [239]. The physical and chemical properties of bimetallic compounds between Ce and a transition metal are highly related to the behavior of the 4f and 3d electrons of Ce and transition metals, respectively [240]. Xiaorui Sun, 2017, simulated the Ce-Fe crystal structure and indicated that the binary compound can adopt two crystalline forms: Ce_1Fe_{2-e} and Ce_1Fe_{5-e} . In Ce_1Fe_{2-e} , each Ce atom is coordinated to four Ce atoms and twelve Fe atoms, while each Fe atom

is coordinated to six Ce atoms and six Fe atoms, forming a distorted icosahedron. In $Ce_1Fe_{5.6}$, Ce is coordinated to eighteen Fe atoms, and Fe is coordinated to three Ce atoms and nine Fe atoms (the Fe atoms form a tetrahedral) [240]. The Fe in the tetrahedral are connected to each other sharing the vertex, forming the structural frames. However, this occurred under ideal conditions, without the presence of other intermediate compounds. In our case, the synthesis solution contained SO_4^{2-} and NO_3^- due to the precursor solutions, and according to FT-IR, XRD and XPS studies, SO_4^{2-} plays an important role in the bimetallic structure.

The SO_4^{2-} ions form direct bonds with rare earth atoms (Ce, La, Th, Gd, etc.) that involve their four oxygen atoms. The number of SO_4^{2-} present in the lanthanide coordination sphere is relatively small despite its high degree of hydration. Water molecules fill the cavities formed within the three-dimensional framework of lanthanides polyhedral and SO_4^{2-} tetrahedral [241]. The main function of SO_4^{2-} groups in the structure of rare earth sulfates is to create bridges, however, the individual oxygen atoms of these structures also comply this function [241]. Regarding cerium, structural studies of a variety of hydrated Ce(III) and Ce(IV) sulfates have shown that the coordination sphere around the cerium ion reflects its oxidation state [242]. Ce(IV) and Ce(III) sulfates contain cerium at 8 and 9 coordinate sites, respectively. Therefore, the cerium sulfate structures consists of cerium(III) ions in irregular coordination to eight oxygens from sulfate ions and one from a water molecule. The sulfate ions bind the cerium ions thus forming a three-dimensional matrix within which are the sites for the hydrated hydrogen ions [242]. In addition, there may be changes in the coordination number (CN = 9 to CN = 8) because SO_4^{2-} can generate vacancies, some of which are filled with additional water molecules and others are lost [241]. Within these vacancies of the lanthanides, transition metals can be introduced, this because cerium in addition to being an oxidant, the ion Ce(IV) for example can facilitate the O–O bonds formation process through an internal sphere pathway [243]. On the other hand, the bimetallic oxyhydroxide of

Ce-O-Fe can be formed by joining water at Ce(III), which would position itself well to Ce(III) for electrophilic attack to give rise to the formation of OH groups in the bimetallic compound, this was visualized by Codolá et al., 2015 [244]. In addition, cerium does not simply behave as an oxidant of the external sphere, but can form an intermediate of Fe-O-Ce of internal sphere [244].

3.3.4. Arsenic adsorption test

The experimental data of the As(V) adsorption isotherms for Fe-P's, Ce-P's and Ce:Fe-P's were adjusted by the Langmuir and Freundlich models (Figure 3.12a). Although it is important to mention that the Freundlich and Langmuir models are used only to quantitatively describe the data and to compare the performance of adsorbents, but they do not provide information to elucidate the arsenic adsorption mechanism [21].

The results showed that the experimental data adjusted better by the Langmuir model; the corresponding parameters and the correlation coefficients are reported in Table 3.3. It is important to highlight the massive difference in Q_{\max} among the one for Ce:Fe-P's, 179.78 mg g⁻¹, and that of the blanks Fe-P's and Ce-P's, 13.1 mg g⁻¹ and 3.15 mg g⁻¹, respectively. This indicates that the bimetallic oxyhydroxide Ce:Fe-P's has about 14 and 57 times more As adsorption capacity than Fe-P's and Ce-P's, accordingly, which is a large difference. This can be attributed to the noticeable increase in the hydroxyl groups concentration as already discussed. According to the literature, the adsorption capacity of the hybrid adsorbent reported in this work is superior to that reported by Yu Zhang, et al., 2003 ($Q_{\max} = 70.4$ mg g⁻¹), Tina Basu et al., 2013 ($Q_{\max} = 55.5$ mg g⁻¹), Bo Chen, et al., 2013 ($Q_{\max} = 91.74$ mg g⁻¹), Uttam Kumar Sahu, et al., 2016 (32.12 mg g⁻¹) and Zhipan Wen, et al., 2018 ($Q_{\max} =$

164.94 mg g⁻¹) who reported the synthesis of a bimetallic oxide of Ce-Fe synthesized by precipitation with NaOH or by the solvothermal method using ethanol and NaOH (see Table 3.4 for details) [192–196]. This indicates that the synthesis method greatly influences the physicochemical characteristics of the hybrid material, and hence its arsenic adsorption capacity. It is important to mention that recently, Zhipan Wen et al., 2020, obtained Ce-Fe bimetallic oxides, by the modified inverse micelles method, with an adsorption capacity of 281 and 175 mg g⁻¹ but at an arsenic equilibrium concentration of 100 and 15 mg L⁻¹, respectively [71], while in the present work an adsorption capacity of 179.78 mg g⁻¹ was obtained at an As equilibrium concentration of just 3 mg L⁻¹ that shows the great affinity of the adsorbent material.

Table 3.3. Langmuir and Freundlich isotherm parameters for arsenic adsorption onto Fe-P's, Ce-P's and Ce:Fe-P's.

Sample	Langmuir			Freundlich		
	Q _{máx} (mg g ⁻¹)	b (L mg ⁻¹)	R ²	k	N	R ²
Fe-P's	13.1	36.56	0.83	11.683	0.200	0.83
Ce-P's	3.5	2.77	0.94	2.057	0.368	0.88
Ce:Fe-P's	179.8	55.84	0.93	171.850	0.160	0.89

Figure 3.12b reports the As adsorption isotherm for Ce:Fe-P's at low equilibrium concentrations (from 5 to 40 µg L⁻¹) that are within those established for drinking water. A very considerable adsorption capacity of 120 mg g⁻¹ at 40 µg L⁻¹ indicates the high affinity of the hybrid adsorbent for As.

Table 3.4. Comparison of As(V) adsorption capacities between Ce-Fe-P's and other reported adsorbents.

Ref.	Bimetallic adsorbents	Adsorption Capacity, mg/g	Ce, mg/L	pH/temperature	Synthesis Method
Zhang, et al., 2003	Ce-Fe	70.4		5.0 a 20 °C	Precipitation
TBasu et al., 2013	Ce-Fe	55.5	4.5	7.0 a 30 °C	Precipitation and drying at 100 °C
Chen, et al., 2013	Ce-Fe-CTAB*	91.74	22	^a 5.5 a 25 °C	Thermostatic oven assisted precipitation and calcination at 353, 373 and 673 K (80, 100 and 400 °C) for 12, 12 and 4 h, respectively.
Sahu, et al., 2016	Ce-Fe	32	30	^a 3.0 a 25°C	Autoclave-assisted precipitation at 180 °C for 5h
Wen, et al., 2018	Ce-Fe	164.94	50	^a 6.0 a 25 °C	Solvothermal with glycerol assisted by autoclave
This work	Ce-Fe	179.78/120	3/0.035	^a 7.0 a 25 °C	Hydrothermal synthesis assisted by microwave oven at 110 °C

*CTAB = Cetyltrimethylammonium bromide surfactant

^a initial pH

Adsorption kinetics were performed in order to evaluate the arsenic adsorption rate in Fe-P's, Ce-P's and Ce:Fe-P's (Figure 3.12c). In the first stage of just 3 minutes, Ce:Fe-P's removed 80% of the initial arsenic concentration, 5 mg L⁻¹, which is considered very fast (0.123 mg min⁻¹). On the other hand, Fe-P's and Ce-P's removed only 30 and 2% of the initial arsenic concentration at the same time, respectively. These results indicate that the

high and exposed concentration of hydroxyl groups on Ce:Fe-P's no only results in a very high As adsorption capacity but also in substantial fast rate, which is ideal in water treatment systems. In the next stage, the intraparticle diffusion takes place and the process becomes slower. Fe-P's require 20 min to reach equilibrium while Ce:Fe-P's require only 3 minutes, which indicates that the As adsorption process onto Ce:Fe-P's is specific [245]. It is important to consider that the rapid As adsorption by Ce:Fe-P's is also attributed to their particles size (between 578 and 818 nm).

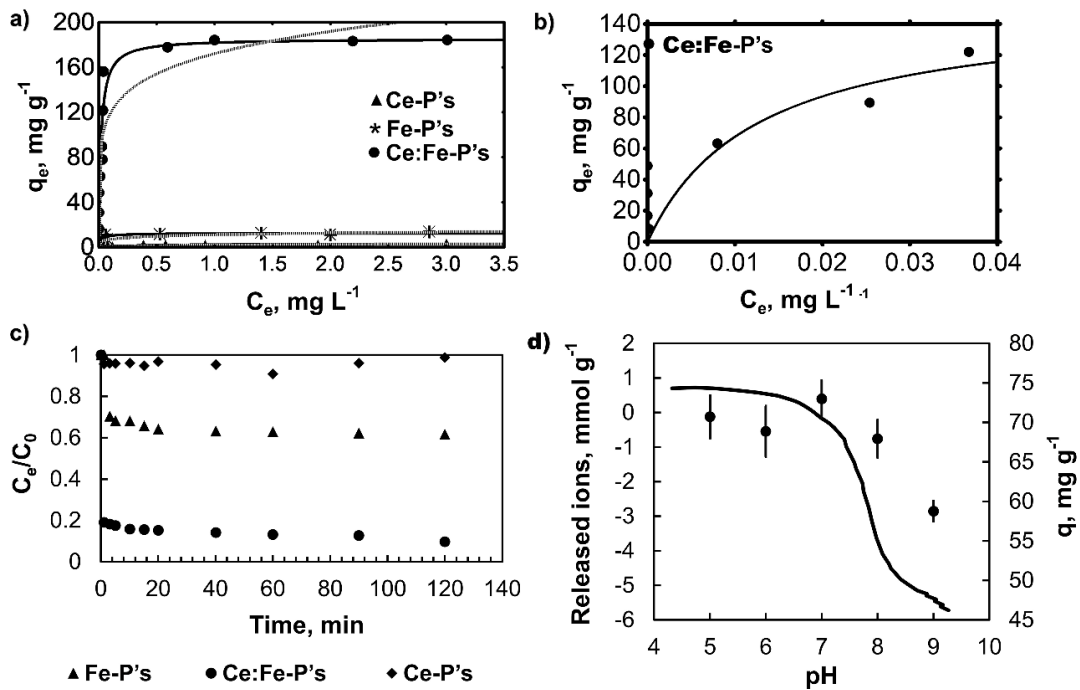


Figure 3.12. (a) Arsenic adsorption isotherm for metal oxyhydroxides Fe-P's, Ce-P's and bimetallic Ce:Fe-P's at pH 7 and 25 °C. (b) Arsenic adsorption isotherm for Ce:Fe-P's at low concentrations at pH 7 and 25 °C. The solid lines represent the Langmuir model and the dotted line the Freundlich model. (c) Adsorption kinetics of Fe-P's, Ce-P's and Ce:Fe-P's at pH 7, 25 °C and initial As concentration of 5 mg L⁻¹. (d) Relationship between the surface charge distribution and arsenic adsorption capacity of Ce:Fe-P's at different pH values.

In addition, two kinetic models were used to describe the adsorption rate of As (V) onto Fe-P's, Ce-P's and Ce: Fe_P's. According to the correlation coefficients (R^2), both pseudo first and second order models describe the experimental data of the studied materials (see Table 3.5). The adsorption rate constants (k_1) were 0.309, 28.22 and 2.77 (min^{-1}) for Fe-P's, Ce-P's and Ce: Fe_P's, respectively. The adsorption rate constants (k_2) were 0.012, 3.5×10^3 and 0.144 ($\text{g mg}^{-1} \text{min}^{-1}$), for Fe-P's, Ce-P's and Ce: Fe_P's, respectively. The high arsenic adsorption rate onto Ce-P's is attributed to the easy access to its active sites, due to low surface area ($1 \text{ m}^2 \text{ g}^{-1}$). On the other hand, it is observed that Ce:Fe-P's has a higher adsorption rate with respect to Fe-P's, which is due to its mesoporous and macroporous structure with a surface area of $6 \text{ m}^2 \text{ g}^{-1}$ (see Table 3.2). Low values of k_1 and k_2 from Fe-P's is attributed to its mesoporous structure and a surface area of $21 \text{ m}^2 \text{ g}^{-1}$, which indicates that arsenic does not have de same accessibility to its active sites, as in the case of Ce-P's and Ce:Fe-P's. In our study, the experimental data fit both pseudo first and second order models, indicating that the adsorption rate is not limited by concentration or intraparticle diffusion [246]. Also, the theoretical values of q_e obtained by both the pseudo first and second order models agree with the experimental value of q_e .

Table 3.5. Kinetic constants for As(V) adsorption onto Fe-P's, Fe-P's and Ce:Fe-P's.

Equation parameters	Fe-P's	Ce-P's	Ce:Fe-P's
Pseudo first-order			
k_1 (min^{-1})	0.309	28.22	2.77
q_e (mg/g)	31.46	3.27	65.55
R^2	0.95	0.97	0.99
Pseudo second-order			
k_2 ($\text{g}/(\text{mg} \cdot \text{min})$)	0.012	3.5×10^3	0.144
q_e (mg/g)	33.66	3.27	66.2
R^2	0.95	0.97	0.99

3.3.4.1. Effect of pH and co-existing anions on the arsenic adsorption capacity

Adsorption experiments were performed at different pH values (5, 6, 7, 8, 9) with Ce:Fe-P's, considering the pH of naturally occurring waters (pH 6 to 8) at an initial arsenic concentration of 5 mg L⁻¹. Figure 3.12d shows that the highest adsorption capacity was obtained at pH 5, 6 and 7 (70.72, 68.86 and 72.98 mg g⁻¹, respectively), and this decreases to 58 mg g⁻¹ as the pH increases to 9. The above is strongly related to the pHPZC of this material, which was 6.8, therefore, at pH 5 and 6 the material is positively charged and consequently attracts As(V) species that are anions. At pH 7 the material is more less neutral, but the high density of OH groups in the material contributes to the arsenic adsorption capacity on Ce:Fe-P's. However, as the pH increases (> 7) the surface of the material becomes more negative, increasing the electrostatic repulsions between arsenate and Ce:Fe-P's. This explains the lower adsorption capacity of the material at pH 9. However, it is important to notice that the effect of pH on the arsenic adsorption capacity on Ce:Fe-P's was not very noticeable, since this only decreases to 58 mg g⁻¹ (20%) at pH 9, being this adsorption capacity still considerable high.

Moreover, the effect of co-existing anions such as, chloride (Cl⁻), sulfate (SO₄²⁻), nitrate (NO₃⁻), phosphate (PO₄²⁻) and carbonate (CO₃²⁻), which are normally found in groundwater, on the arsenic adsorption capacity of Ce:Fe-P's is shown in Figure 3.13. The results showed that the arsenic adsorption capacity was affected 21% by the presence of 10 mg L⁻¹ of each competing anion (Cl⁻, SO₄²⁻, NO₃⁻, PO₄²⁻ y CO₃²⁻). Moreover, the arsenic adsorption capacity of Ce:Fe-P's decreases 78 (16.88 mg g⁻¹) and 82% (13.68 mg g⁻¹) when increasing the concentration of each competing anion to 30 and 50 mg L⁻¹, respectively,

which is similar to that reported by others adsorbent materials but without the presence of anions [247]. Among these co-existing anions, phosphate the greatest decrease in arsenic adsorption capacity: both phosphate and arsenic are in the same major group, and the molecular structure of the phosphate ion is very similar to that of the arsenic ion, therefore, the phosphate strongly competes with arsenic for the active sites of Ce:Fe-P's [245].

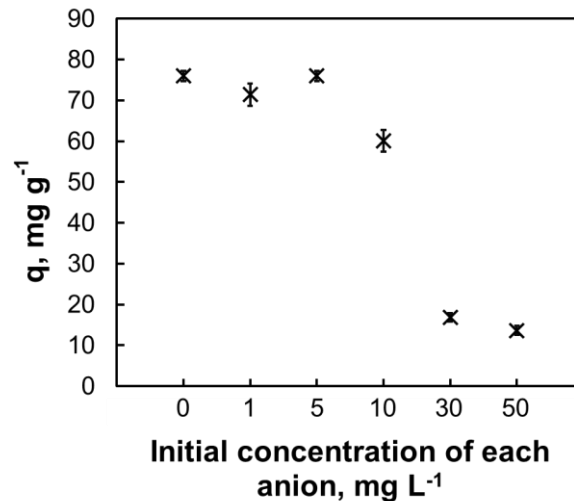


Figure 3.13. Effect of co-existing anions chloride (Cl^-), sulfate (SO_4^{2-}), nitrate (NO_3^-), phosphate (PO_4^{2-}) and carbonate (CO_3^{2-}) in the arsenic adsorption capacity of Ce:Fe-P's when using 5 mg L⁻¹ of arsenic at pH 7 and 25 °C.

3.3.5. Arsenic adsorption mechanism onto Ce:Fe-P's

To determine the arsenic adsorption mechanism onto Ce:Fe-P's, pK_a's distribution by titration and FT-IR analysis were conducted after the adsorbent material was contacted with an arsenic solution with an initial concentration of 5 mg L⁻¹. The pH_{PZC} of Ce:Fe-P's changed from 6.8 to 3.8 due to the presence of arsenic on the materials surface (Figure 3.14a). It has been reported that metal oxides reduce their pH_{PZC} after the anions adsorption process due

to a specific interaction by ligand exchange [248]. In addition, the pK_a attributed to OH groups of Ce:Fe-P's disappeared, due to a ligand exchange mechanism, and three new pK_a 's were observed between 2.5 and 11.5 (Figure 3.14b). This is closely related to the three pK_a values of arsenic(V) ($pK_{a1} = 2.24$, $pK_{a2} = 6.96$ and $pK_{a3} = 11.5$) [249,250].

Finally, the FT-IR analysis of saturated Ce:Fe-P's (Figure 3.14c) shows a wide band at 815 cm^{-1} due to the As-O vibration [247]. In addition, the bands at 1180 and 1430 cm^{-1} disappeared, and there is a decrease in the intensity of the 1100 cm^{-1} band assigned to the vibrations of hydroxyl groups in metal oxides (Ce-OH, Fe-OH). In addition, a doublet between 1450 and 1400 cm^{-1} corresponding to vibrations of OH groups are observed. The above suggests an interaction of arsenate with Ce:Fe-P's. Therefore, it is suggested that arsenic could form monodentate, mononuclear bidentate and binuclear bidentate inner sphere complexes by exchange of ligands with the OH groups of Ce:Fe-P's, as illustrated in Figure 3.15.

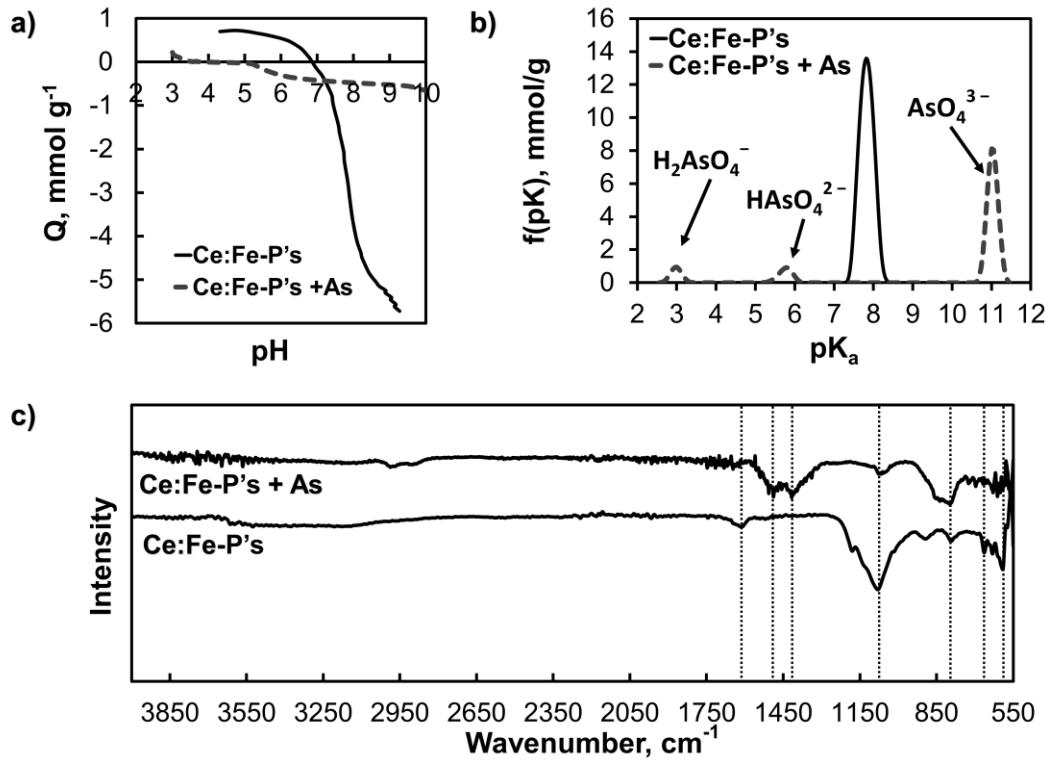


Figure 3.14. (a) Surface charge distribution, (b) pK_a 's distribution and (c) FT-IR of Ce:Fe-P's before and after arsenic adsorption.

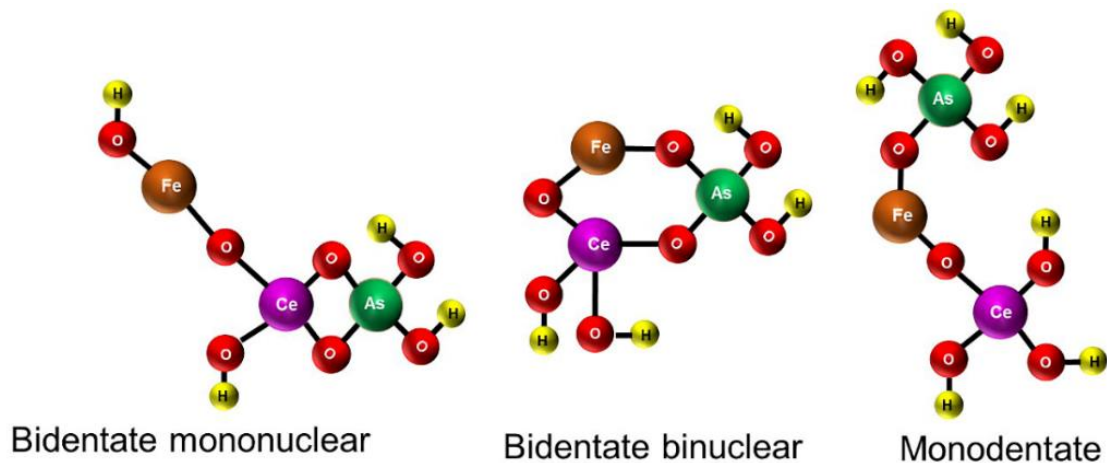


Figure 3.15. Proposed arsenic adsorption mechanism on Ce:Fe-P's.

3.4. Conclusions

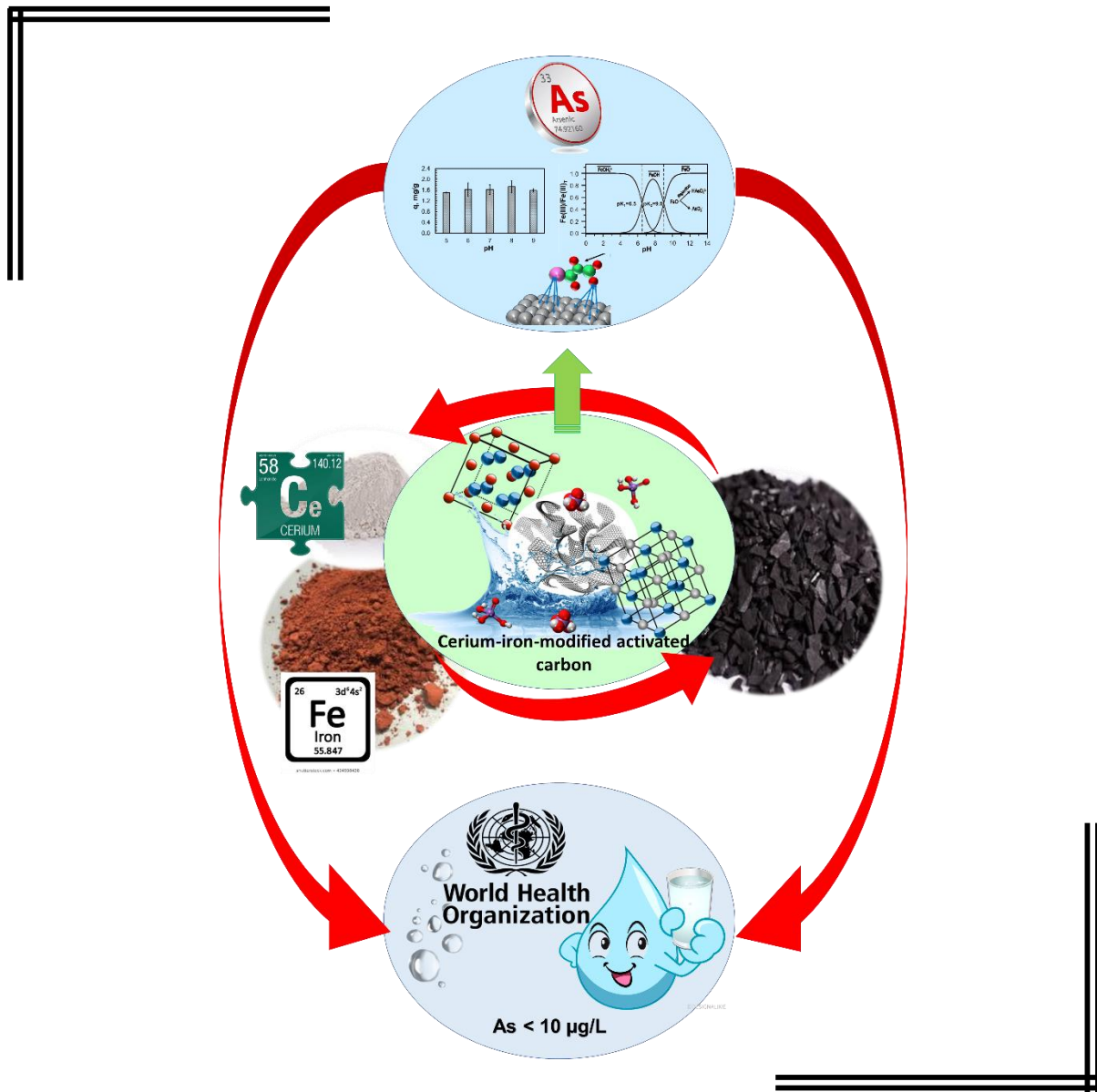
The Ce-Fe-P's presented a remarkable arsenic adsorption capacity of 179.78 mg g^{-1} (at 3 mg/L , $\text{pH } 7$ and $25 \text{ }^\circ\text{C}$) which required only 3 minutes to achieve equilibrium reaching a removal of 80% of the initial arsenic concentration of 5 mg L^{-1} . Even at low As(V) concentrations, for instance at $37 \text{ } \mu\text{g L}^{-1}$, Ce:Fe-P's presented a very considerable adsorption capacity of 120 mg g^{-1} . On the other hand, the adsorption capacity was slightly affected by the solution pH. The presence of co-existing anions such as chloride, sulfate, nitrate, phosphate and carbonate decreased the adsorption capacity in 20% at pH 9 and 21% in solution containing 10 mg L^{-1} of these competing anions.

XPS results demonstrate that the binary oxides of Fe and Ce formed a union between the two metallic elements by means of an oxygen (Ce-O-Fe). SO_4^{2-} could generate vacancies in Ce facilitating the formation of Fe-O-Ce. Also, As(V) can occupy one of the vacancies generated by SO_4^{2-} in the crystal lattice of Ce-O-Fe. Moreover, the high coordination number of Fe and Ce (Ce NC=9 and Fe NC=9), allows the formation of a high density of OH groups where arsenate is adsorbed through ligand exchange. All these factors are reflected in the high arsenic adsorption capacity of Ce:Fe-P's. On the other hand, XPS and XRD studies show the presence of $\text{FeSO}_4 \cdot 7\text{H}_2\text{O}$, FeOOH , $\text{Ce}_2(\text{SO}_4)_3(\text{H}_2)_5$, $\text{Fe}(\text{SO}_4)_2\text{H}$ and CeO_2 .

Finally, the bimetallic oxyhydroxide of Ce-Fe, which is in the process of being patented (MX/a/2019/010551), has the potential to be used as it is or in combination with other materials to efficiently remove As(V) from aqueous solutions.

CHAPTER IV

Immobilization of metallic oxyhydroxides Ce^{3+} and Fe^{2+} on graphitic matrices to remove arsenate and fluorides from water



CHAPTER IV

Immobilization of metallic oxyhydroxides Ce^{3+} and Fe^{2+} on graphitic matrices to remove arsenate from water

Abstract

For an adsorbent material to be highly efficient in removing arsenic, it is important that its surface has a high OH groups density. Due to this, metallic oxyhydroxides were anchored on the surface of an activated carbon (AC). The anchorage was carried out by a microwave-assisted hydrothermal method using F400 carbon and Fe^{2+} and Ce^{3+} ions in the hydrolysis solution. The characterization indicated that a very low Ce content (0.63% w) is anchored on the surface AC and that it also acts as a morphological modulator of the Fe particles anchored on the AC surface. The presence of cerium in the synthesis of AC-Ce:Fe increased the iron content 1.6 times with respect to AC-Fe. The iron presented an acicular particles morphology. AC-Ce:Fe showed an adsorption capacity of 5.6 mg g^{-1} and pH does not have a significant effect on the arsenic adsorption capacity, due to the increase of OH groups on the AC surface. However, the presence of anions such as (F^{-} , Cl^{-} , SO_4^{2-} , NO_3^{-} , PO_4^{2-} y CO_3^{2-}) have a significant effect on the adsorption capacity of the material with a decrease of 46% in the presence of 5 mg L^{-1} of each anion.

Key words: *Bimetal oxides, cerium, iron, activated carbon, adsorption, arsenic*

4.1. Introduction

In the last years, water pollution has increased due to the discharge of various pollutants from the industrial sector and geogenic factors. Among the most interesting pollutants to remove from water is arsenic [251]. Water contaminated by arsenic in a natural way is mainly due to the minerals presence such as Realgar (AsS), Oropimenta (As₂S₃), Arsenolite (As₂O₃), Claudetile (As₂O₃), Domeykite (Cu₃As), Leollingite (FeAs₂), Scorodote (FeAsO₄·2H₂O), etc [252]. Arsenic has two main oxidation states As (III) and As (V). Where As (V) is less toxic than As (III) and appears according to the solution pH as H_3AsO_4 , $H_2AsO_4^-$ y $HAsO_3^{2-}$ [253]. According to the World Health Organization (WHO), 14 countries in Latin America have been affected by arsenic contamination from water [254]. The water consumption contaminated by arsenic with a concentration higher than the limit established (10 µg L⁻¹) by the WHO and USEPA (United States Environmental Protection Agency) can affect the health of at least 4 million people [254].

Therefore, the search for highly efficient technologies for the arsenic removal from water continues. Currently, it is known that metallic and bimetallic oxides have physical and chemical properties that allow them to be applied in various areas. Metal oxides such as Fe [255], Zr [256], Ce [257], Mn [258], have been used to remove arsenic from water, due to the high capacity of these oxides. On the other hand, efforts to find much more efficient adsorbent materials for removing arsenic from water have studied bimetallic oxides. Bimetallic compounds have the advantage of inheriting the properties of the individual oxides that make them up. Among these properties the one with the highest hierarchy is the high OH groups density [259]. Cerium has been used as a highly efficient adsorbent in the removal of arsenic from water, due to its large surface/volume ratio and remarkable selectivity to arsenic [260,261]. On the other hand, ferric oxides also have a high affinity for arsenic and are preferably used for the removal of arsenic from water due to their low cost,

ease of synthesis, and respect for the environment [262–264]. Therefore, Ce-Fe bimetal has been shown to have excellent arsenic removal capacity since the combined property of cerium and iron oxides shows a higher affinity for arsenic [265–268].

Although bimetallic oxides have shown excellent adsorbents, their application in continuous systems is difficult. For this reason, an attempt has been made to anchor bimetallic oxides on the surface of a support to help their application in continuous systems [269]. Activated carbon has shown to be a promising material for anchoring various cations on its surface, due to the oxygenated groups diversity that it has on its periphery and its defects. Hybrid materials possess both the carbon properties (high surface area) and bimetallic oxide, which has a high affinity for arsenic [265]. However, reports have indicated that, when trying to anchor a bimetallic oxide on the surface of activated carbon, one of these has more of a complexing agent effect [269]. Therefore, one of the oxides will only have an effect on the morphology and particle size of the oxide that is able to anchor on the activated carbon surface [269]. In the present work, activated carbon was contacted with a solution of Ce, Fe and Ce:Fe. The metal oxides were hydrothermally synthesized using a microwave oven to generate a highly efficient material for the arsenic removal. The hydrothermal synthesis process has the ability to anchor oxyhydroxide nanoparticles within the pores of activated carbon [270,271]. The hydrothermal method allows for higher yields and better reproducibility due to the fact that microwave heating is fast and homogeneous [270,272,273]. In this work, cerium had a synergistic effect on the formation of oxyhydroxide as a morphological regulator similar to that presented by Delgado et al., 2019.

4.2. Experimental

4.2.1. Materials and chemicals

The materials used to develop this research were reactive grade with a purity higher than 99%. Cerium nitrate hexahydrate ($\text{Ce}(\text{NO}_3)_3 \cdot 6\text{H}_2\text{O}$), ferrous sulfate heptahydrate ($\text{FeSO}_4 \cdot 7\text{H}_2\text{O}$), hydrochloric acid 0.1N (HCl), sodium hydroxide 0.1N (NaOH), arsenic salt ($\text{Na}_2\text{HAsO}_4 \cdot 7\text{H}_2\text{O}$) were used. The solutions were prepared in double desionized water with a resistance of 18 M Ω /cm.

4.2.2. Synthesis and characterization of adsorbent material

The modification of activated carbon (AC) was performed using the following method: 0.1 g of activated carbon (AC) was contacted with a solution of Ce-Fe for 2 hours at 25 °C and 130 rpm. Subsequently, the mixture, AC and the Ce-Fe solution was introduced in a microwave oven for 30 minutes at 110 °C.

For the synthesis, the microwave oven was programmed in the following way: the microwave oven was brought from room temperature to 110 °C by means of a heating ramp of 5 min and maintained at 110 °C for 30 min. After the synthesis, the supernatant was decanted, and the modified activated carbon was washed with deionized water to eliminate the remaining. Finally, the modified activated carbon was dried for 12 h at 80 °C in the oven.

The surface charge distribution (pK_a 's) and the point of zero charge (pH_{PZC}) of each adsorbent were obtained by means of an automatic titrator (Mettler-Toledo T70). A 0.1 g sample was dispersed in 50 ml of 0.1 M NaCl as a bottom electrolyte and stirred for 12 h to ensure equilibrium was reached. Then, a titration was carried out with 0.1 N NaOH under a nitrogen atmosphere to avoid CO_2 interferences. The distribution of pK_a was obtained with the program SAEIUS-pK-Dist © (1994).

Infrared analyzes (Thermo-Nicolet, Nexus 470 FT-IR E.S.P) were performed to identify the possible interactions that occur between the AC and Ce and Fe oxyhydroxides. The samples for the analysis were dried for 12 h and analyzed by the ATR technique. The powder materials dried in the stove at 80 °C were analyzed by X-ray diffractometry (XRD) using a Bruker D8 Advance diffractometer (CuK α radiation $\lambda = 1.5406 \text{ \AA}$, 35 kV and 25 mA, with step time of 2 s and step size of 0.01°) and a zero-background holder to identify the compounds and phases of the oxyhydroxides of Ce-AC, Fe-AC and Ce:Fe-AC. The analysis of diffractograms was carried out by using the Hannawalt method.

4.2.3. Adsorption experiments

The adsorption isotherms were made in the following way: 30 mL of As(V) solution at different concentrations (0.05 to 10 mg L⁻¹ of As) was added in conical polypropylene tubes containing 30 mg of adsorbent material at pH 7 and 25 °C (pH will be adjusted with NaOH and/or 0.1 N HCl). The arsenic concentration in the solution was determined by ICP-OES (varian 730-ES) at a wavelength of 188.98 nm.

Adsorption kinetic was developed using a stock solution of 2 mg L⁻¹ of As (V) at pH 7. Subsequently, 30 mL of the stock solution was added to 13 polypropylene falcon tubes 50 mL containing 30 mg of the adsorbent material and placed at 25 °C and 120-130 rev/min in an incubator. Samples were taken at different times (30 seconds, 1, 5, 10, 20, 40, 60, 90, 120, 180 and 240 minutes).

The effect of co-existing anions such as: chloride (Cl^-), sulfate (SO_4^{2-}), nitrate (NO_3^-), phosphate (PO_4^{2-}) and carbonate (CO_3^{2-}), which are normally found in groundwater, on the arsenic adsorption capacity on adsorbent material. Synthetic water will be prepared that will

contain a concentration of 5, 10, 30 and 50 mg L⁻¹ of each anion (Cl^- , SO_4^{2-} , NO_3^- , PO_4^{2-} and CO_3^{2-}), in the presence of 2 mg L⁻¹ of As. The coexisting anion effect experiments were performed in batch systems. The arsenic concentration in the solution was determined by ICP-OES (varian 730-ES) at a wavelength of 188.98 nm.

4.3. Results and discussion.

4.3.1. Effect of the cerium and iron concentration on the activated carbon surface in the arsenic removal.

The following results provide the optimum iron and cerium concentration needed to obtain the highest arsenic adsorption capacity by modified activated carbons. Figure 4.1 shows the arsenic adsorption capacity (q , mg g⁻¹), for each modified activated carbon with different molar ratios (MR) of Ce:Fe. The AC-Ce:Fe with an MR of 5:1 showed a greater adsorption capacity in comparison with the AC-Ce:Fe with an MR 8:1 (4.7 and 3.6 mg g⁻¹, respectively). The low arsenic adsorption capacity of AC-Ce:Fe (8:1) can be attributed to a decrease in exposed active sites due to pore clogging. In this design, it was observed that cerium plays an important role in the capacity of arsenic adsorption, since as the concentration of cerium increased (from 0.25 to 1.25 M) the capacity was higher, however, at cerium concentrations higher than 1.25 M, the capacity of arsenic adsorption decreases. Therefore, it was determined that an increase in the concentration of cerium and/or iron in the synthesis process does not guarantee an increase in the adsorption capacity of the AC. In the next experiments, the AC-Ce:Fe was evaluated with a RM of 5:1, since this was the optimal ratio to obtain a high capacity of arsenic adsorption.

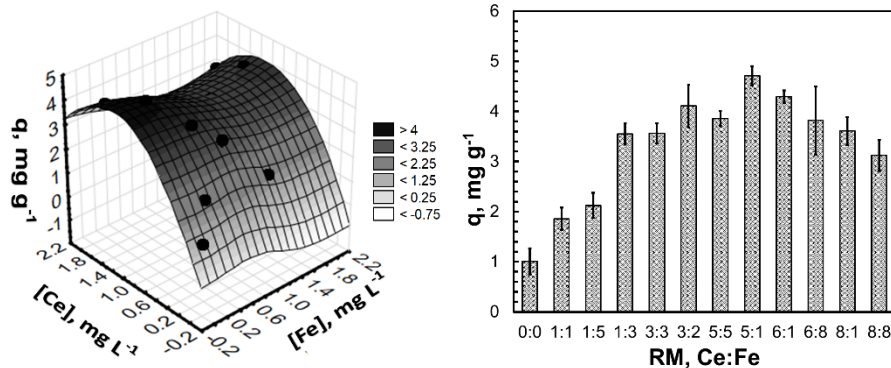


Figure 4.1. Effect of the cerium and iron concentration during the AC modification and consequently its arsenic adsorption capacity (q , $mg\ g^{-1}$).

4.3.2. Adsorbent material characterization

4.3.2.1. Physical properties

Scanning electron microscopy (SEM) studies were conducted to obtain information about the activated carbon morphology modified by a hydrothermal synthesis process assisted by a microwave oven. Figure 4.2 shows the micrographs of AC-Fe, AC-Ce and AC-Ce: Fe at 2500 and 200000x as well as their EDS analysis. In Figure 4.2a shown that the AC-Ce:Fe has a morphology of acicular particles, characteristic of goethite with a particle size of 20 nm. The point analysis by EDS detector reveals that the weight percentage of C, O, Al, Si, S, Ce and Fe was 31.64, 40.47, 0.5, 0.59, 2.09, 0.34 and 24.37 %W, respectively. The low percentage obtained from Ce, is due to a low content in the sample (0.63%W). The presence of Al and Si is due to the bituminous origin of activated carbon. The micrographs corresponding to AC-Ce (Figure 4.2b) reveal a uniform distribution of cerium nanoparticles on activated carbon with a size of approximately 10 nm. In addition, a very amorphous cerium morphology on activated carbon was observed. In the micrographs of AC-Fe (Figure 2c), iron nanoparticles were observed on activated carbon with acicular and rhombohedral morphology characteristic of goethite and hematite, respectively, being the phases identified

in XRD. The size of the iron particles ranges between 70 and 80 nm. The EDS point analysis shows a weight percent of C, O, Al, Si, S and Fe of 62.92, 20.98, 0.65, 0.96, 0.9 and 13.59 %W, respectively.

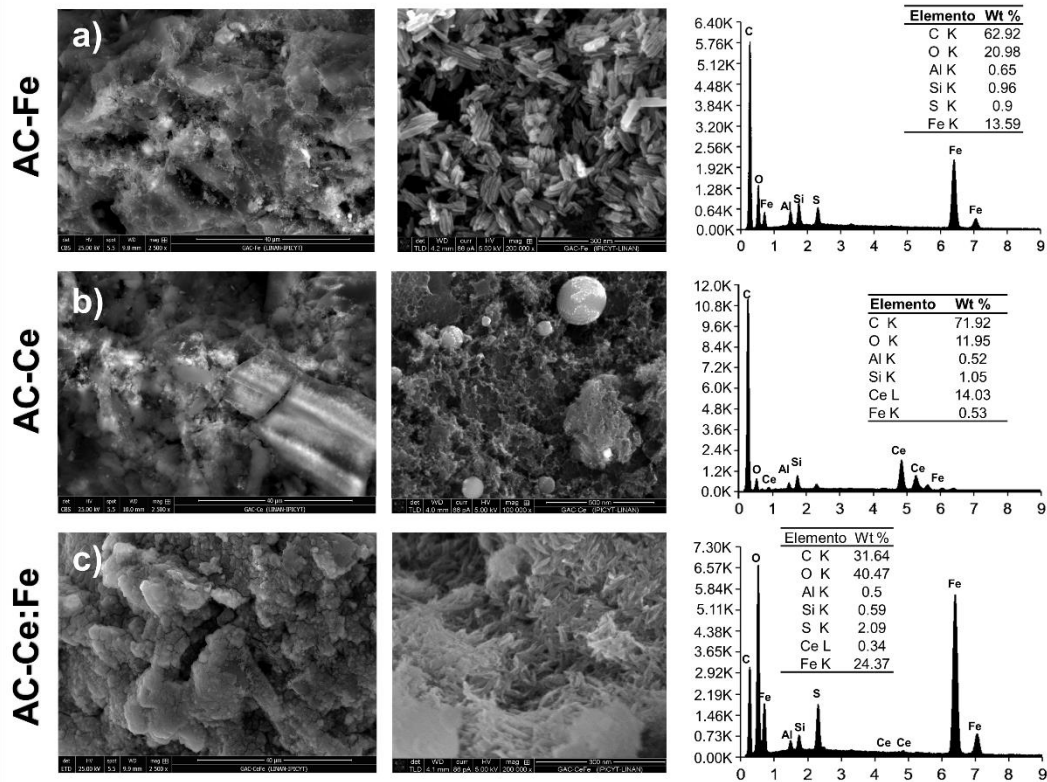


Figure 4.2.- SEM images of the surface of **(a)** AC-Fe, **(b)** AC-Ce y **(c)** AC-Ce:Fe and their respective EDS.

It was also observed that the iron particles in AC-Ce:Fe are smaller with respect to the AC-Fe particles, which can be attributed to the fact that the sulfate ion could act as a complexing agent, that is, after forming the nucleation center on the activated carbon surface, crystal growth could be controlled by the presence of this anion [274].

N_2 adsorption isotherms at 75 K for modified carbons are shown in Figure 4.3a. These isotherms are type I, which are typical of microporous adsorbents according to the IUPAC [275]. H4 type hysteresis loops were observed in all isotherms, which indicates that the material has porous structures in the form of sheets but very narrow, indicating the additional presence of micropores. This fact is common in real porous materials since they present the combination of pores, micro, meso and macropores [276,277].

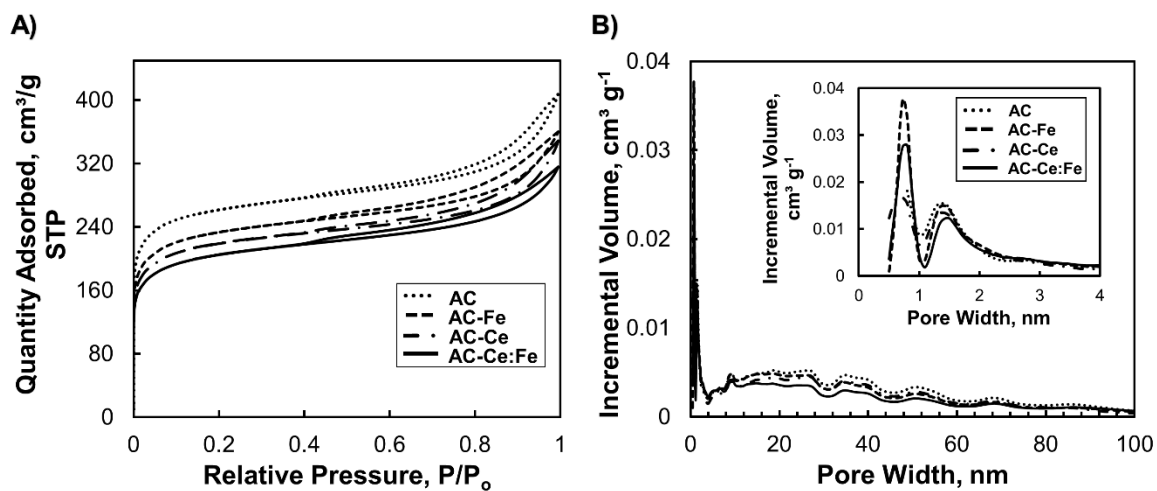


Figure 4.3. (a) N_2 adsorption isotherms at 75 K and (b) pore distribution of modified carbons.

Table 4.1 shows that the surface area of AC was $978 \text{ m}^2 \text{ g}^{-1}$ and decreased 11 and 17.5% when contains Fe and Ce, but when the AC is modified with Ce:Fe the surface area falls about 23.3%. The increase of mesopore volume in AC-Fe and AC-Ce was 4.5 y 4 time more, respectively, than pristine AC. This can be attributed to partially blocked micropores that create more mesopores between aggregates. In de case of AC-Ce:Fe can see that the micropores and macropores decrease around of 23% with respect to AC. However, Figure 4.3b can see that AC-Fe and AC-Ce:Fe have an increase mainly in the ultra-micropores with

effective pore radius less than 0.6–0.7 nm and super-micropores showing radius of approximately 0.7–2 nm.

Table 4.1. Physicochemical Characterization of nonmodified and modified activated carbon.

Sample	m ² /g		cm ³ /g		nm
	S _{BET}	V _{mic}	V _{mes}	V _{mac}	P. D.*
GAC	978	0.308	0.034	0.142	2.52
GAC-Fe	870	0.267	0.154	0.013	2.53
GAC-Ce	814	0.253	0.136	0.014	2.57
GAC-Ce:Fe	750	0.233	0.039	0.109	2.52

*Poro Dimeter

4.3.3. Chemical properties.

The iron and cerium content in the modified and unmodified activated carbon is shown in Figure 4.4a. The Fe content for AC was 0.42% w, which is attributed to the bituminous origin of the AC (F400). The iron-modified carbon (AC-Fe) presented 2.17% w of Fe, this low iron content is due to the relatively low concentration of iron solution (0.25M). On the other hand, the carbon modified with cerium (AC-Ce) showed an iron content of 0.42% w, associated to the AC and 1.8% w of Ce. The content of cerium in the AC-Ce is quite low considering that the concentration of the cerium solution was 1.25M, however, the low content of Ce can be attributed to the fact that the condensation temperature of the cerium oxyhydroxides is higher than 160 °C and the synthesis was carried out at 110 °C. Finally, the content of cerium in AC modified with the Ce:Fe (5:1), was quite low (0.63% w), while

that of Fe was 3.62% w, being 1.6 times greater than that anchored in the AC-Fe. The above can be attributed to the fact that the Fe condensation is directed by the addition of ions such as Ce in the material during the synthesis process, being the reason why the concentration of Ce:Fe is the factor that controls the Fe percentage in the modified carbon [278]. Furthermore, if we consider the presence of HNO₃ by the reaction: $Ce(NO_3)_3 + 3H_2O = Ce(OH)_3 + 3HNO_3$, carried out in the cerium solution, the AC could undergo an oxidation and therefore an increase in the groups oxygenated favoring the Fe anchorage on the AC surface, which is reflected in the increase of iron content in Ce:Fe-AC.

Figure 4.4b shows the charge distribution of AC, AC-Ce and AC-Fe. Point of zero charge (pH_{PZC}) of AC (F400) was 9.0, indicating the predominance of basic groups. When the AC was modified with iron (AC-Fe) the pH_{PZC} shifted to 7.8. This displacement in the pH_{PZC} is attributed to the fact that as the iron anchors on the AC surface an increase in the acidity is obtained, decreasing the AC pH_{PZC} after being modified [279]. The AC modified with cerium (AC-Ce) showed a pH_{PZC} of 8.0, which is due to the pH_{PZC} of CeO₂ is between 7 and 8. On the other hand, the material modified with bimetallic oxyhydroxide (Ce:Fe) showed a pH_{PZC} of 7.9, this being very similar to the pH_{PZC} of AC-Ce and AC-Fe. The pH_{PZC} reduction in the modified materials can be due to the acidic conditions that were found during the synthesis process (pH = 2 to 5), which, accompanied by the large amount of chemisorbed oxygen, favored the formation of acidic groups when oxidizing the carbon graphitic sheets [280].

The metal oxides surface consists mainly of hydroxyl groups that determine the chemistry and reactivity of the surface [281]. Figure 4.4c shows the pK_a distribution obtained by SAEIUS software. AC-Fe showed an increase in the phenolic groups (8 <pK_a <11) from 0.067 to 0.1 mmol g⁻¹, attributed to the OH⁻ groups of iron oxyhydroxides anchored on the activated carbon surface. A slight increase in carboxyl groups is also observed (3 <pK_a <6), which is attributed to the acidic conditions present during the synthesis process. In AC-Ce,

the concentration of carboxyl groups decreased, because Ce is considered a strong acid, therefore, it prefers binding to the carboxylic and phenolic groups of AC. In addition, the OH groups concentration was 3 times higher than that of AC-Fe. On the other hand, the carbon modified with Ce:Fe showed an increase in the OH groups density characteristic of metal oxyhydroxides.

The changes in the vibrational frequencies of the cerium bonds with the functional groups of the AC surface were studied by FTIR to elucidate the interaction of the metallic ion with the AC surface. The FT-IR of the AC, AC-Fe, AC-Ce, AC:Ce-Fe are shown in Figure 4.4d. The AC spectra showed low intensity bands at 1550 cm^{-1} corresponding to the vibration of C=O (carboxylic groups), in 1500 and 1130 cm^{-1} that indicate the vibration of -C=C and C-O of the aromatic and lactonic groups, respectively. The bands in the region of 3720 to 3580 cm^{-1} are attributed to the O-H vibrations. When the AG was modified with Fe, showed low intensity band at 620 cm^{-1} bands, which are attributed to the Fe-O vibrations. When AC was modified with Ce (III), the FT-IR spectrum showed vibration bands in 1200 and 928 cm^{-1} , which are attributed to the union of the Ce with the OH of the metal oxyhydroxide. It also shows a high intensity peak in the 620 cm^{-1} regions, which is attributed to the Ce-O. In addition to the characteristic bands of pristine activated carbon. On the other hand, when modifying the AC with the Ce:Fe oxyhydroxides, the bands in the region 1200 and 620 cm^{-1} characteristic of the union Fe-OH and Fe-O, respectively, were observed. The results indicated that the iron oxyhydroxides have a greater interaction with the OH of the carboxylic and phenolic groups to form a complex.

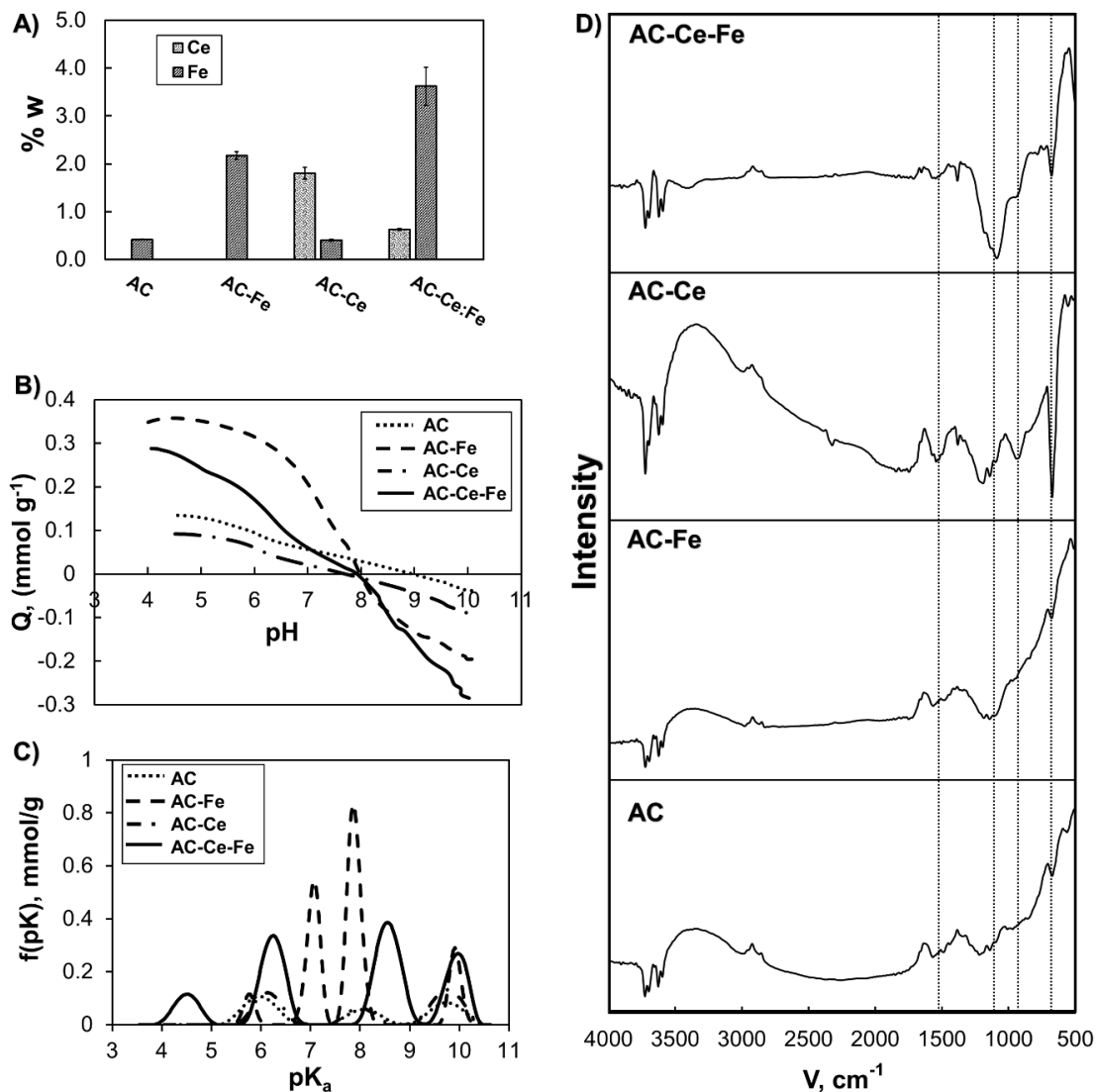


Figure 4.4. (a) Content of cerium and iron in modified activated carbon and unmodified. (b) Surface charge distribution and Q_s (c) pK_a 's distribution of pristine activated carbon and modified activated carbon, using 0.1M NaCl as electrolytic support. (d) FT-IR of AC, AC-Fe, AC-Ce and AC-Ce:Fe.

Figure 4.5 shows the XRD pattern of the activated carbon before and after the synthesis process. The AC diffractogram shows a characteristic amorphous behavior of the carbon materials with peaks at 26° and 44° (PDF Card-00-056-0160), which correspond to

the planes (002) and (100), respectively [280]. The activated carbon is of bituminous origin; therefore, it presents isomorphous impurities such as goethite, hematite, alumina and silica [282]. However, the characteristic peaks of goethite were more evident (PDF Card-00-029-0713), due to the iron content of the pristine activated carbon. The diffraction pattern of AC-Ce showed low intensity peaks characteristic of CeO_2 at 28° , 33° , 46° and 58° . The low intensity of the peaks is due to the low percentage of cerium that was anchored on the surface of the AC (1.8 %W). The AC-Fe diffractogram shows the peaks corresponding to the hexagonal Hematite structure (PDF Card-01-071-0469) [283]. The intensity of the peaks in 21° , 34° , 36° and 41° of goethite detected in the AC diffractogram increased after the synthesis process, and two peaks at 53° and 58° are appreciated attributed to the same orthorhombic goethite structure (PDF Card-00-029-0713). On the other hand, the AC-Ce:Fe diffractogram shows the characteristic peaks of goethite and three peaks of very low intensity attributed to the presence of CeO_2 .

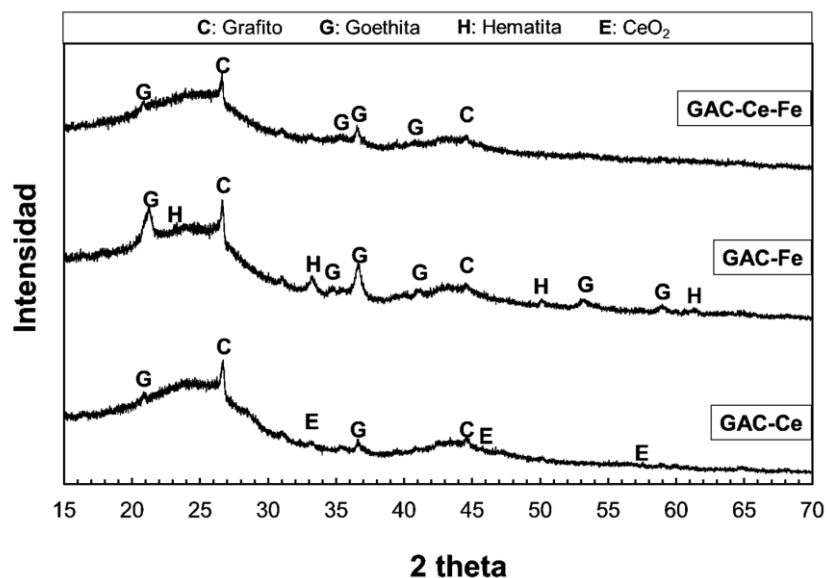


Figure 4.5. XRD patterns of GAC, GAC-Ce, GAC-Fe and GAC-Ce-Fe with a step of 0.02° 2θ at 10 s per step. The letters show the crystalline phase of each material.

XPS analyzes were performed to discover the possible structure of Ce:Fe, formed during the hydrothermal process on the activated carbon surface. Figure 4.6 shows the complete XPS spectra referenced at the C 1s level at 284.6 eV. The binding energy of the Fe 2p region, corresponding to AC-Ce:Fe was 711 eV in good agreement with 711 and 711.15 eV for Fe²⁺ and Fe³⁺ in FeSO₄ · 7H₂O [284] and FeOOH, respectively, (Fe 2p_{3/2}) [285]. Which agrees with XRD studies.

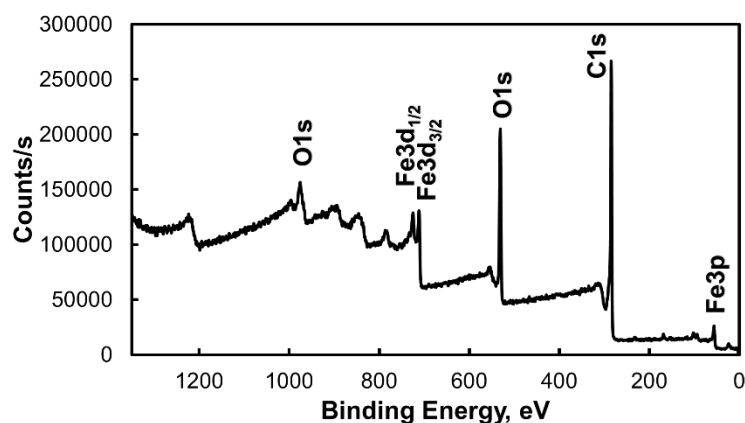


Figure 4.6. XPS full spectra referenced to C 1s level at 284.6 eV for AC-Ce:Fe

The XPS spectra in the C 1s region referenced at 284.6 eV (Figure 4.7a) showed the characteristic peak of C = C (284.6 eV) that corresponded to the sp² carbon bond, also showed the CO bonds at 285.6 eV and carbonyl groups (C = O) at energies of binding of 286.6-287.7 eV. The XPS peaks of Fe 2p_{3/2} and Fe 2p_{1/2} for the standard AC-CeFe sample are shown in Figure 4.7b. Of the two peaks, the Fe 2p_{3/2} peak is narrower and with high intensity, therefore, its area is greater than Fe 2p_{1/2}, this may be associated with Fe 2p_{3/2} degeneration of four states, while Fe 2p_{1/2} has only two. Several researchers have studied the maximum position of Fe 2p_{3/2}, which is between values of 710.6 and 711.2 eV [284]. The Fe 2p_{3/2} peak has associated satellite peaks. In the sample, a satellite peak of Fe 2p_{3/2} was

observed, which is generally approximately 8 eV higher than the main peak of Fe 2p_{3/2} [284]. The binding energies of Fe 2p_{3/2} and Fe 2p_{1/2} of the Fe particles anchored in the AC are obtained 710.68 eV. A satellite peak is clearly observed at 719.3 eV, which does not overlap the Fe 2p_{3/2} and/or Fe2p_{1/2} peaks. Also, there appears to be another satellite peak at 732.98 eV, which may be a satellite peak for Fe 2p_{1/2}. Fe 2p_{3/2} peaks at a binding energy of 710.7 and 712.6 eV are associated with FeOOH and Fe₂(SO₄)₃, respectively [284,286]. This is stated with the oxygen spectrum (Figure 4.7c) and S (Figure 4.7d), where the Fe-O bond (530 eV) and the presence of FeSO₄ (168.3 eV) and SO₄²⁻ (169.6 eV) are observed, respectively [284,287,288].

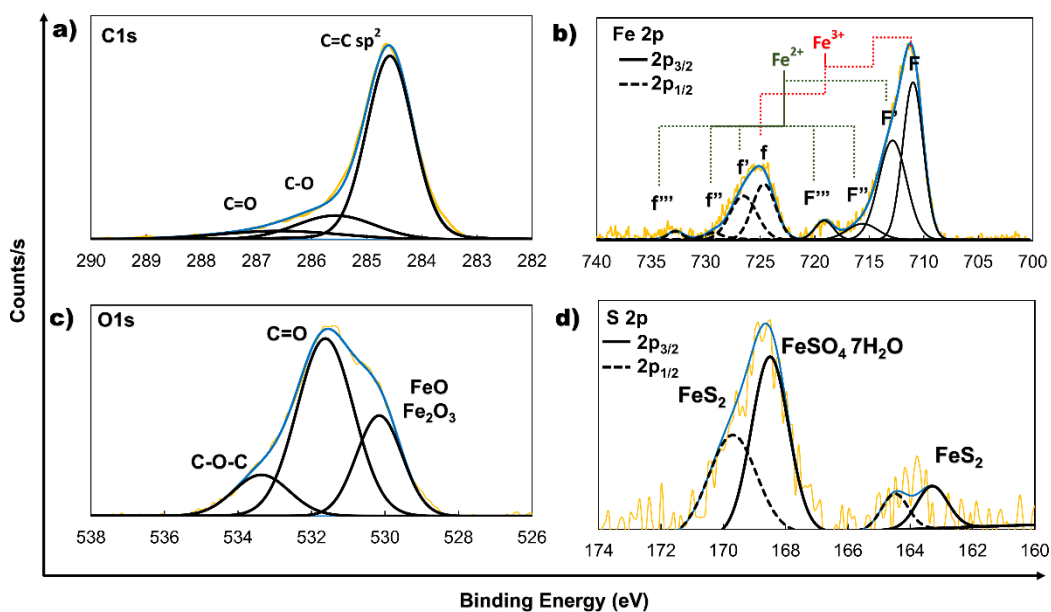


Figure 4.7. XPS spectra (a) in the C 1s region referenced at 284.6 eV, (b) O 1s, (c) S 2p and (d) Fe 2p for AC-CeFe

4.4. Anchorage mechanism of Ce-Fe in activated carbon

In the first instance, the species distribution in the precursor solutions of metal oxyhydroxides should be considered. Prior to the hydrothermal synthesis process, the AC and the reactive solution were kept in agitation for 2 h, with the aim of favoring the diffusion of the species in the porous matrix of the activated carbon. The species diagrams (Figures, Annexe A-1) show the formation of ion pairs, which are susceptible to formation in concentrated solutions [289]. This saturation of the aqueous medium prevents the metal cations (M^+) from presenting their complete solvation sphere, associating with opposite charge ions (SO_4^{2-}) to form different chemical complexes called *ion pairs*. The ion pairs $FeSO_4$ and $FeHSO_4^+$ could be present on the activated carbon surface before the synthesis process. It is also important to mention that the solutions were not found in anoxic conditions, so during the synthesis process Fe^{2+} could be oxidized to Fe^{3+} .

Figure 4.8 shows how surface oxygenated groups can be part of the condensation reaction of cerium and iron. The delocalized electrons in the graphitic structure and mainly the electrons found in the oxygenated activated carbon surface groups can act as nucleation centers for the aquo-complex $[M^+(OH_2)_6]^{+3}$ [290]. This can generate a covalent bond between the activated carbon surface and the metallic particles, allowing the anchoring of the oxyhydroxides of Ce:Fe [291]. Once the nucleation centers are formed, the aquocomplexes continue their deprotonation forming hydroxy complexes $[M^+(OH)(OH_2)_5]^{+2}$ that favor crystal growth. When the activated carbon (F400) was contacted with the acid solution (pH 2-3) of the metal ions, the surface oxygenated groups were protonated (Figure 4.8a), giving it a positive surface charge ($pH < pH_{PZC}$), therefore, Anions such as SO_4^{2-} and HSO_4^- will be attracted by electrostatic interactions. Likewise, the $[M(H_2O)_6]^{3+}$ acuocomplexes present are deprotonated and attracted in the form of hydroxy complexes $[M(OH)(H_2O)_5]^{2+}$ by the oxygenated groups of the AC, becoming specific ions (Figure 8b).

The delocalized electrons in the graphitic structure and mainly the pairs of free electrons present in the oxygenated surface groups of the activated carbon carry out a nucleophilic attack on the specific ions [280], eliminating H_2O and SO_4^{2-} . This allowed the anchoring of the metal particles by forming a covalent bond with the activated carbon surface of the O-M^+ type. It is important to consider that the cerium percentage anchored in the AC is quite low (0.63% w) compared to the iron percentage present in AC (3.62% w), therefore, there will be a greater anchoring of $[\text{Fe}(\text{OH})(\text{H}_2\text{O})_5]^{2+}$ on the activated carbon surface.

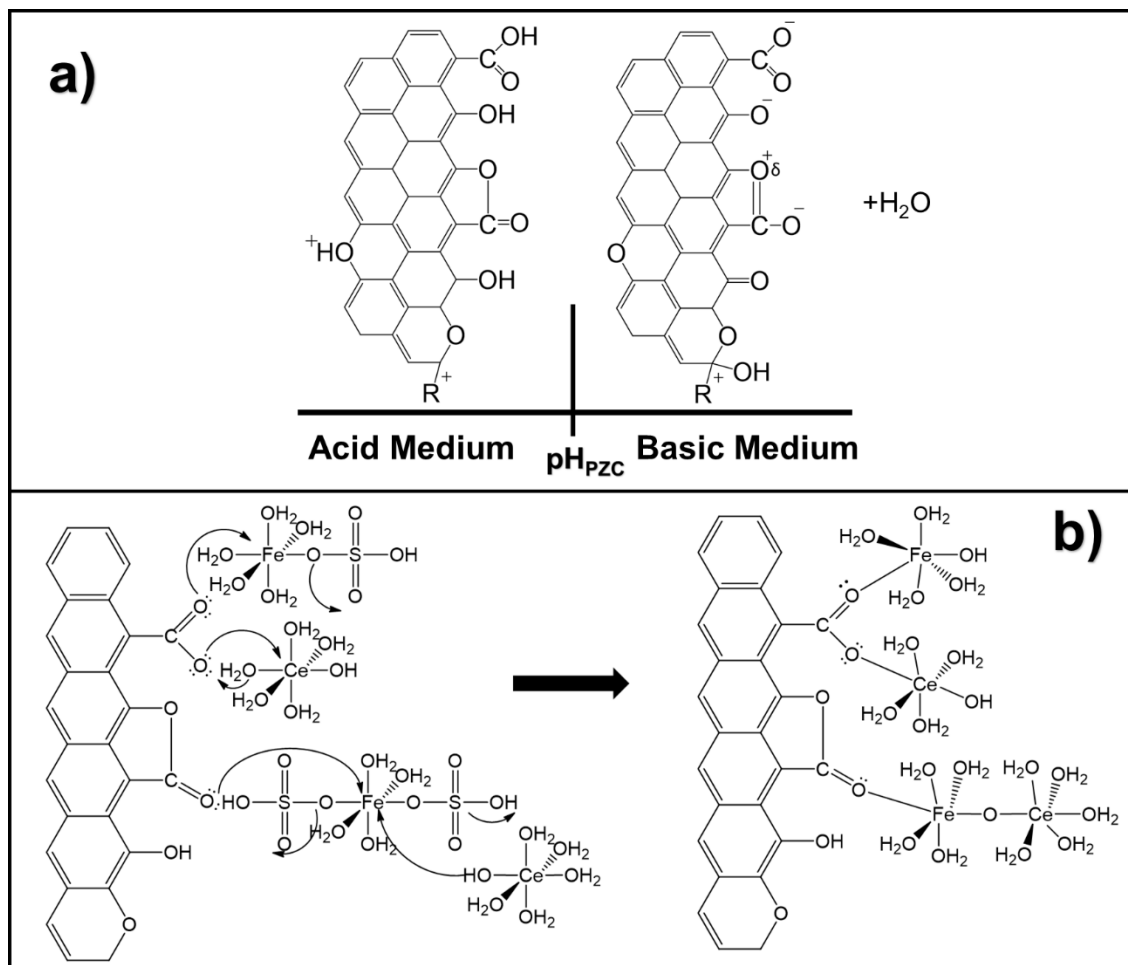


Figure 4.8. (a) Dissociation of Activated Carbon and (b) Nucleophilic attack of the surface oxygenated groups of activated carbon on the metal aquo-complex (Fe and Ce).

4.5. Adsorption experiments

Figure 4.9a the arsenic adsorption isotherms of AC, AC-Ce, AC-Fe and AC-Ce:Fe are shown. The Langmuir and Freundlich models were adjusted to the adsorption equilibrium data (Table 4.2). The Langmuir model presented the best mathematical fit by better describing the experimental data of all the materials. Although these models only indicate adjustment parameters, their interpretation is congruent, indicating the formation of a monolayer of arsenate molecules on the surface of the AC, AC-Fe, AC-Ce and AC-Ce:Fe. The presence of this monolayer is due to the formation of a chemical bond between the adsorbate and adsorbent, which forms an internal sphere complex through the exchange of ligands. In addition, the q_{\max} Langmuir parameter can be interpreted as the maximum coverage for the formation of this monolayer. Adsorption capacity of AC is due to its bituminous origin, which involves the presence of metal oxides such as Al, Si, Mn and Fe, being related to arsenic.

Table 4.2. Langmuir and Freundlich parameters for the As(V) adsorption onto AC, AC-Fe, AC-Ce and AC-Ce:Fe.

Simple	Langmuir			Freundlich		
	q_{\max} , mg g ⁻¹	b	R ²	K	n	R ²
GAC	2.84	0.20	0.99	0.54	0.58	0.97
GAC-Fe	1.18	1.02	0.99	0.53	0.37	0.95
GAC-Ce	8.52	2.99	0.78	5.24	0.32	0.81
GAC-Ce-Fe	5.60	3.21	0.95	3.40	0.35	0.92

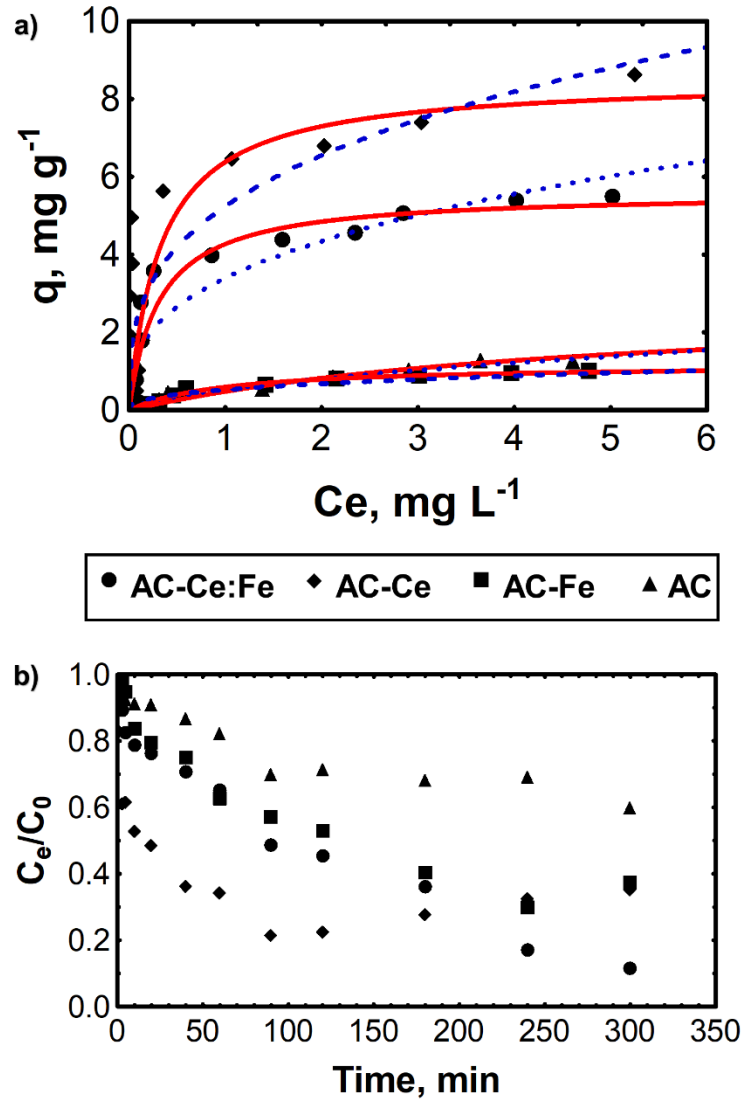


Figure 4.9. (a) Arsenic adsorption Isotherms at pH 7 and 25 °C. The solid line corresponds to the Langmuir model and the dotted line to the Freundlich model. **(b)** Adsorption kinetics of GAC, GAC-Fe, GAC-Ce and GAC-Ce-Fe at pH 7, 25 °C and As(V) initial concentration of 2 mg L⁻¹.

The AC-Ce:Fe showed an adsorption capacity (q_{max}) of 5.6 mg g⁻¹, this can be associated with a higher content of hydroxide groups provided by the oxyhydroxides anchored on the AC surface. From the adsorption isotherms, it was determined that the AC-

Ce-Fe material had the maximum adsorption capacity, at pH 7, 25 °C and $C_e = 2 \text{ mg L}^{-1}$, with a q_{max} value of 4.6 mg g^{-1} while AC and AC-Fe only reached 0.84 and 0.80 mg g^{-1} , respectively. Therefore, the increase in the adsorption capacity of AC-Ce:Fe was 5.5 times greater than AC. However, the carbon modified with cerium (AC-Ce) obtained an adsorption capacity of 6.78 mg g^{-1} , this being 1.5 higher than that of AC-Ce:Fe. This is due to the increase of OH groups on the surface of the GAC and to the fact that cerium has a high affinity for arsenic. On the other hand, the characterization indicated that the pH_{PZC} (Figure 3A) of the AC-Ce:Fe is lower ($\text{pH}_{\text{PZC}} = 7.2$) than the pH_{PZC} of AC ($\text{pH}_{\text{PZC}} = 9$), However, an increase in the positive groups of the modified material. The experimental pH was lower than the pH_{PZC} of the modified material, indicating a positive surface favoring the adsorption capacity. However, the high adsorption capacity of AC-Ce:Fe suggests that the exchange of ligands between the iron-cerium species and the arsenic is not prevented by electrostatic attractions between activated carbon and adsorbate. Thus, the high content of OH groups on the modified material (Figure 4.3C), plays an important role in the As(V) adsorption. The low adsorption capacity of AC and AC-Fe was due to the exchange of ligands it is favored mainly by the presence of OH groups found on the surface of metal oxides (M-OH) for the formation of the internal sphere complex, and not by the phenolic groups of activated carbon (C-OH).

The adsorption kinetics was carried out in order to evaluate the speed of arsenic adsorption, as well as the time necessary to reach equilibrium. Figure 4.9b shows the kinetics of arsenic adsorption on GAC, GAC-Fe, GAC-Ce and GAC-Ce-Fe. The GAC-Ce-Fe material removed 50% of the initial concentration of arsenic in the first 90 minutes, while the GAC-Fe and the GAC removed only 40 and 30% of the initial arsenic concentration. On the other hand, the GAC-Ce presented the fastest adsorption kinetics in the first 90 min by removing 80% of the initial concentration of arsenic. After 90 minutes a slight desorption of

arsenic from GAC-Ce was observed. The adsorption kinetics of GAC-Ce-Fe removed 90% of the initial concentration of As at a time of 5 h. In addition, from this time the adsorption kinetics of GAC-Fe was greater than that of the GAC, removing 10% more arsenic in 5 h. However, the kinetics were considered slow because it took more than 1 h for materials to reach equilibrium.

4.5.1. Effect of solution pH and co-anion presents in the solution on the arsenic adsorption capacity.

Figure 4.10a shows the effect of pH on the arsenic adsorption capacity for AC-Ce:Fe. The results showed that the pH does not have a significant effect on the arsenic adsorption capacity of AC-Ce: Fe. The pH_{PZC} of the AC-Ce: Fe is 7.9 the material is positively charged therefore it will attract anions such as arsenate. Likewise, if we consider that at pH 5 the $FeOH_2^+$ species was present in 95% (see Figure 4.10b), electrostatically attracting the $H_2AsO_4^-$ species, at pH 9 the active sites will be 90% $FeOH_3^+$, 50% $FeOH$ and 50% FeO^- , which form internal sphere complexes with $HAsO_4^{2-}$.

The effect of co-existing anions such as, chloride (Cl^-), sulfate (SO_4^{2-}), nitrate (NO_3^-), phosphate (PO_4^{2-}) and carbonate (CO_3^{2-}), which are normally found in groundwater, on the arsenic adsorption capacity in AC-Ce:Fe is shown in Figure 4.10c. The results showed that the arsenic adsorption capacity is affected by the presence of competing anions when a concentration was obtained from 5 mg L⁻¹ of each anion (Cl^- , SO_4^{2-} , NO_3^- , PO_4^{2-} y CO_3^{2-}). The arsenic adsorption capacity on the AC-Ce-Fe, decreases 46% in the presence of 5 mg L⁻¹ of each anion and this decreases to one more when increasing the concentration of anions at 10, 30 and 50 mg L⁻¹ (64, 66 and 74%, respectively). Among the anions, phosphate causes the greatest decrease in the capacity of arsenic adsorption, which may be due to the

strong competition for the active sites of the adsorbent (AC-Ce-Fe) between phosphate and arsenic. Both phosphate and arsenic are in the same major group, and the molecular structure of the phosphate ion is very similar to that of the arsenic ion. Therefore, the phosphate ions present compete strongly for the active sites of AC-Ce:Fe, with the arsenic ion (Figure 8D) [292,293]. In Figure 4.10d it is observed how phosphate adsorption capacity increases with form decreasing arsenic capacity.

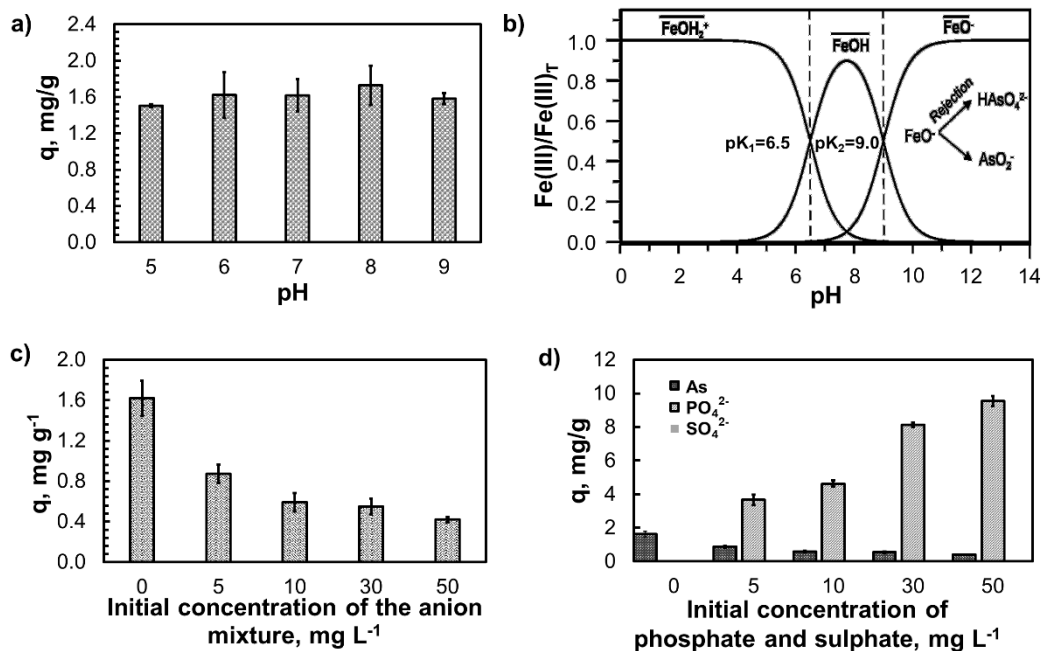


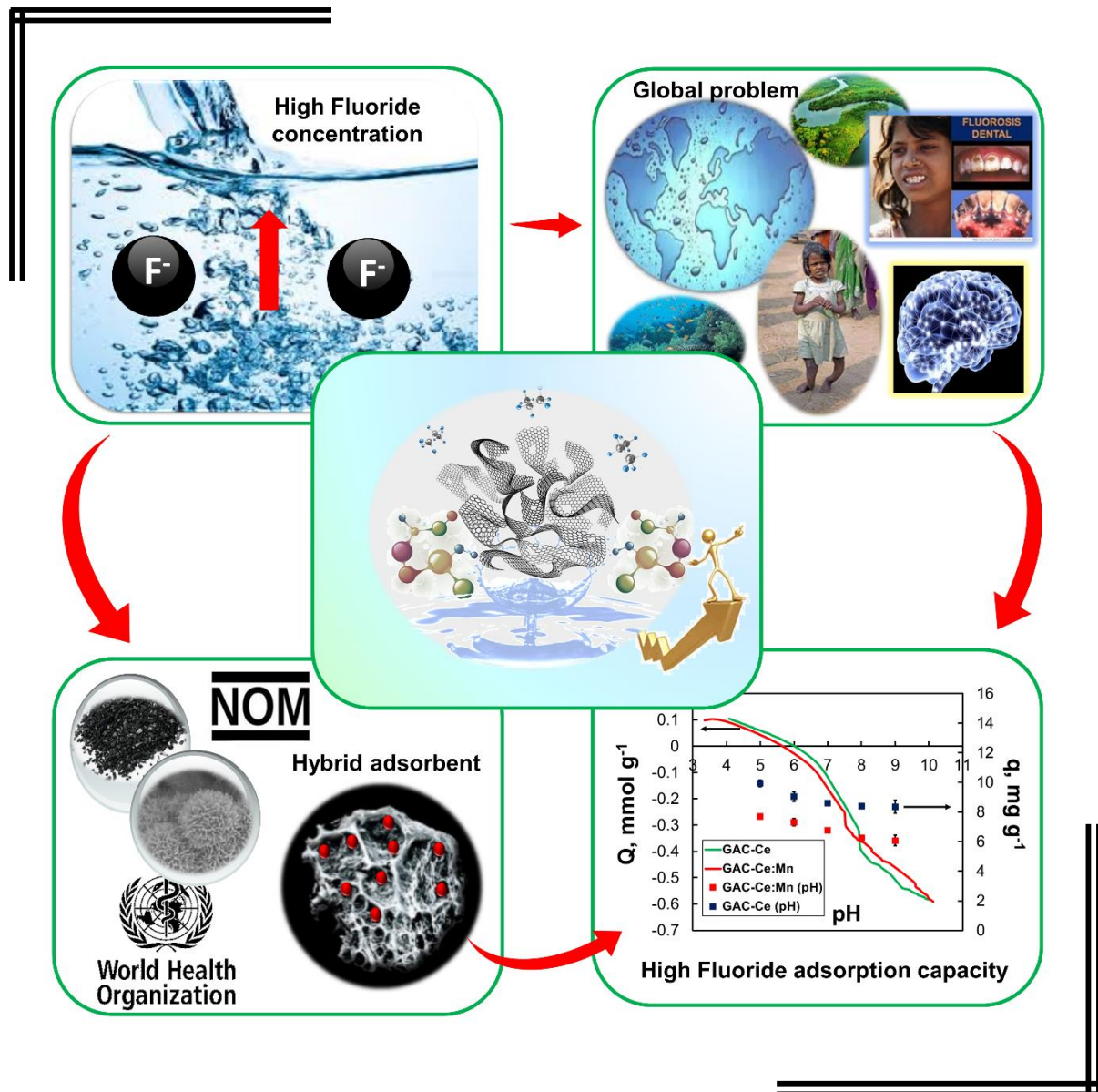
Figure 4.10. (a) Effect of pH on the As(V) adsorption capacity of GAC-Ce:Fe at arsenic initial concentration. (b) Iron species diagram. (c) The effect of co-existing anions such as, chloride (Cl^-), sulfate (SO_4^{2-}), nitrate (NO_3^-), phosphate (PO_4^{2-}) and carbonate (CO_3^{2-}), in the arsenic adsorption capacity on the Ce-Fe ($C_0 = 0, 1, 5, 10, 30$ and 50 mg L⁻¹ of each anion in the presence of 2 mg L⁻¹ of arsenic at pH 7 and 25 ° C). (d) Phosphates adsorption capacity on the GAC-Ce:Ce.

4.6. Conclusions

The hydrothermal synthesis process allows to anchor satisfactorily iron oxyhydroxides on the surface of the activated carbon at the time of synthesis for 30 min, obtaining a material with an iron content of 3.62% w. The presence of Ce during the synthesis allows to increase the iron content in the activated carbon from 2.17 (AC-Fe) to 3.62% and consequently increase the OH groups density. In addition, the presence of the Ce^{3+} ion during the synthesis of iron oxyhydroxides reduces the Iron particles size anchored on the activated carbon surface up to 30 nm, also controls the iron oxyhydroxide morphology by forming crystalline habits in the form of interconnected fibrils, which allow to obtain material with a high adsorption capacity. X-ray diffraction reveals the presence of goethite and hematite, with thermodynamically more stable phases of iron. On the other hand, XPS shown two oxidation states by Fe and the species of $FeSO_4$, due to precursor solution for the oxihydroxides formation. The arsenic adsorption capacity on AC-Ce:Fe was 5.6 mg g^{-1} , being higher than other activated carbons modified with iron oxyhydroxides reported in the literature. The presence of anions affects the arsenic adsorption capacity on the AC-Ce-Fe 46% at a concentration of 5 mg L^{-1} of each anion. The above is attributed mainly to the presence of phosphates. Also, the pH does not have a significant effect on the arsenic adsorption capacity of the hybrid adsorbent material. It is important to mention that the AC modified with cerium, shows a high arsenic adsorption capacity than the AC-Ce:Fe, due to less obstruction of active sites. This is because AC-Ce has a particle size of 10 nm, smaller than AC-Ce:Fe (20 nm particle size), which indicates that it has a greater surface area and a greater availability of sites active, therefore a higher arsenic adsorption capacity.

CHAPTER V

Modification of activated carbon with Ce^{3+} and Mn^{2+} ions in hydrolysis solution by hydrothermal synthesis to remove fluoride from aqueous solutions



CHAPTER V

Modification of activated carbon with Ce^{3+} and Mn^{2+} ions in hydrolysis solution by hydrothermal synthesis to remove fluoride from aqueous solutions

Abstract

Metal oxides have high fluoride adsorption capacities, which is why they have been anchored on the various supports surface for continuous application. Activated carbon (gAC) has shown to be a highly efficient support for the anchorage of Ce and Mn oxides, considering that the efficiency of the material depends largely on the surface-active sites of the anchored oxyhydroxides. To generate a greater quantity of active sites in the adsorbent material, an attempt has been made to anchor two metals on its surface, since this will provide a higher density of OH groups. Therefore, in the present work cerium and manganese were anchored on the gAC surface and the Mn^{2+} influence on the fluoride adsorption capacity was evaluated. EDS analyzes show that the percentage of Ce^{3+} anchored on the gAC increases up to 17% by mass in the presence of Mn^{2+} . Furthermore, the Ce particle size decreases by 80%, which suggests that Mn acts as a capping agent. However, adsorption experiments show that Mn^{2+} does not have a positive effect on fluoride adsorption capacity. The gAC modified with Ce and Ce:Mn showed an adsorption capacity of 11 and 8.3 mg g⁻¹. The solution pH affects the fluoride adsorption capacity in both materials by 10%. Additionally, through various characterization techniques (FTIR, XRD, XPS) the anchoring mechanism of Ce and Mn oxyhydroxides on the gAC surface was elucidated.

Key word: Fluoride, cerium, manganese, activated carbon, anchored mechanism.

5.1. Introduction

Fluorine is considered an essential element for dental health, as it prevents tooth appearance decay in children is development teeth. Thus, the dentists recommend using fluorine (0.8 to 1.0 mg L^{-1}) in order to strengthen the tooth enamel. However, the World Health Organization (WHO), considers fluoride intake at concentrations higher than 1.5 mg L^{-1} to be dangerous, which is the maximum permissible limit [294]. Groundwater pollution by fluorides is a problem that affects to people around the world. When the water passes through soils by percolation, it dissolves various compounds, including fluorine, results in fluoride concentrations in aquifers, which increase in cesium, lithium, chlorine, bromide presence and in thermal and underground waters [295,296]. Exposure to high fluoride concentrations often occurs when drinking groundwater, one of the main drinking water sources, and it can cause dental and skeletal fluorosis or neurological damage in severe cases, increased susceptibility to kidney disease and cancer, as well as affectation in brain development and the reduction of the intellectual coefficient of school-age children [294,297]. Fluoride is present at least 25 countries, within which fluoride concentrations up to 30 mg L^{-1} can be found in groundwater [294,298,299]. In Mexico fluoride concentration in water is above the permissible limit (1.5 mg L^{-1}) by the Official Mexican Standard, NOM-127_SSAI-1994, mainly in the states of Aguascalientes, Chihuahua, Durango, Guanajuato, Mexico, Jalisco; San Luis Potosí, Sonora and Zacatecas [300].

The chemical precipitation and coagulation, membranes, ion exchange and adsorption have been used as methods for the removed fluorides from water. Moreover, adsorption is the method most widely used by researchers to remove various pollutants from water. The use of adsorption in removal contaminants such as fluoride from water is due to the great advantages that this method has (design flexibility and simplicity and easy operation and maintenance). Currently, various adsorbent material has been studied, which include

activated and impregnated alum [301,302], clays, minerals and plants [303,304], activated carbon, nanotubes [305,306], rare earth oxides [307], polymeric and resins materials [308,309]. It is also known that the incorporation of some metal oxides such as iron (III), manganese (II, IV), lanthanum (III), alum (III), zirconium (IV) or tin (IV) on the adsorbent surface can significantly increase the fluoride adsorption capacity [310–312]. However, these metallic oxides have been studied in colloidal or nanoparticles form, which make their application in continuous systems completely difficult. Therefore, it is important anchored these nanoparticles with high fluoride adsorption capacity onto a support, that allows the application of these adsorbent materials. Granular activated carbon (gAC) is a poor adsorbent to remove fluorides from water, but it can provide a stable support to achieve high dispersion of metallic phases that are powerful fluoride adsorbents and can also inhibit sintering or massive precipitation of the active metal particles. When this carbonaceous material is impregnated with metallic oxides, it has been reported that the adsorption capacity improves by a factor of 3-5 [312]. The control over the carbon surface area and the size distribution of the charges metallic phases are key factors to increase the fluoride adsorption capacity. In addition, some works have studied in the cations influence as Mn^{2+} on the modification of activated carbon with other cations as Fe^{2+} . The presence of Mn^{2+} in the hydrolysis solution has a synergistic effect in the oxide particles anchorage onto surface activated carbon, as it regulates the morphology of the anchored metallic particles [313]. Therefore, the objective of this research is to improve the fluoride adsorption capacity of granular activated carbon, modifying with Ce^{3+} and Mn^{2+} ions in hydrolysis solution by microwave-assisted hydrothermal synthesis method. On the other hand, evaluate the Mn^{2+} ion presence in the synthesis process to modify activated carbon with Ce^{3+} ions.

5.2. Experimental

5.2.1. Synthesis of adsorbent materials

Granular activated carbon was contacted with a Ce:Mn solution, during 24 h at 25 °C y 130 rpm. Continuously, gAC impregnated was introduced in microwave at 150 °C for 30 minutes. The modified material was wash with enough desionized water and dry in heating stove at 80 °C for 12 h. The gAC was modified with different molar relation (MR) of cerium-magnesium.

5.2.2. Characterization of adsorbent material.

Determination of the cerium and manganese content onto activated carbon was performed by acidic digestion in the microwave. 40 mg of sample was contacted with 20 mL of acid aqueous solution ($\text{HNO}_3:\text{H}_2\text{SO}_4$, 5:1). They were placed in teflon container, after the containers were closed hermetically tightly sealed heated at 10 °C/min from room temperature to 150 °C where they kept for 40 min. Later, the samples were diluted at 50 mL and analyzed by Plasma coupled atomic emission spectroscopy, ICP-AES (Varian 730-ES).

Charge Distribution and Point of Zero Charge (PZC) of modified material and pristine were determined through potentiometric titrations. For it, 30 mg of sample was mixed with 25 mL of 0.1M NaCl aqueous solution through magnetic stirring by 12 h. To the sample was add 0.1M HCl drop by drop up that the aqueous solution has a pH of 3. Subsequently, for 3 minutes the solution was gasified with and titrated with 0.1N NaOH aqueous solution.

5.2.3. Adsorption Experiments

Adsorption isotherms were performed as follows for both the gAG and modified gAC: 30 mL of fluoride solutions at different concentrations (1 ppm at 80 ppm) were added in 0.03g of adsorbent at 25 ° C and pH 7 (the pH was adjusted by adding NaOH or 0.1N HCl). Once the samples reached equilibrium, the final fluoride concentration was measured with a selective ion electrode (Thermo Electron Corp), using a TISAB II regulatory buffer. The adsorption isotherms were adjusted to the Langmuir and Freundlich models through the STATISTICA program.

To perform the adsorption kinetics, a stock solution of fluorides was prepared at a concentration of 20 mg / L at pH 7. Subsequently, 30 mL of the stock solution was mixed with 0.03 g of the adsorbent material and placed in an incubator at 25 °C and 130 rev/min. Samples were taken at different times (0.5 to 270 minutes).

5.3. Results and discussion

5.3.1. Effect of manganese and cerium concentration in activated carbon to remove fluoride.

The following results gave us the concentration of cerium and manganese anchored on the surface of granular activated carbon (gAC), optimal for obtaining the highest fluoride adsorption capacity at fluoride initial concentration of 20 mg L⁻¹, pH 7 and 25 °C. The design was based on a previously conducted studies [314,315].

In Figure 5.1a, the results obtained from the nanoparticles synthesized in the presence of gAC are shown, where we can see that the particles with a 1:1 molar ratio (MR) of Ce:Mn,

had a fluoride adsorption capacity of 24 mg g^{-1} , when increasing the content of Mn (Ce:Mn 1:2) the fluoride adsorption capacity increased 1.5 times (36.5 mg g^{-1}), with respect to the Ce:Mn 1:1 material. The nanoparticles with an MR of Ce:Mn 1:4 and 2:1 showed a low fluoride adsorption capacity between 17 and 18 mg g^{-1} , respectively. On the other hand, the fluoride adsorption capacity was evaluated of the activated carbon modified by Ce and Mn. In Figure 5.1b we can see that the gAC modified with Ce:Mn (1:1, MR) showed an adsorption capacity of 9.42 mg g^{-1} , when the content of Mn is increased the adsorption capacity was 10.7 mg g^{-1} (gAC-Ce:Mn (1:2)), however, this decreased to 7.9 , 2.9 and 4.3 mg g^{-1} for adsorbent materials gAC-Ce:Mn (1:4), gAC-Ce:Mn (1:8) and gAC-Ce:Mn (1:14), respectively. On the other hand, by modifying activated carbon with a MR of Ce:Mn 2:1, a fluoride adsorption capacity of 9.12 mg g^{-1} was obtained, this being similar to that obtained by gAC modified with Ce:Mn 1:1 and 1:2.

Figure 5.1c shown that the Mn^{2+} has an effect in the fluoride adsorption capacity, due depending to the manganese concentration the fluoride adsorption capacity of hybrid material increases or decrease. The activated carbon modified with a MR of Ce:Mn, 1:8 and 1:14, both were not efficient to fluoride removal. While the gAC modified with low manganese concentration were greater efficient in the fluoride removal from aqueous solutions. The hybrid material gAC-Ce:Mn(2:1) was compared whit gAC modified uniquely with cerium (gAC-Ce) and manganese (gAC-Mn), using the same concentrations used to modified the gAC-Ce:Mn (2:1). Figure 5.1c shown that the gAC-Mn has a less adsorption capacity (1 mg g^{-1}) similar than the pristine gAC (0.7 mg g^{-1}) [316]. However, we can see that the gAC-Ce has a high adsorption capacity compared with gAC-Ce:Mn, thus the manganese presence has a negative effect in the fluoride removal. This can be associated with the pores clogging due to the possible clusters formation due to an increase in Ce on the gAC-Ce:Mn surface of 51.55% w (gAC-Ce, 34.7% w) according to the EDS analysis. Therefore, the active sites

of the hybrid material will be less exposed for adsorption to take place efficiently. Therefore, for the following experiments, the modified gAC with an RM of Ce:Mn 1:2 was used since it was the material that obtained a greater adsorption capacity with respect to the other materials. Said material shall be represented as follows: gAC-Ce:Mn.

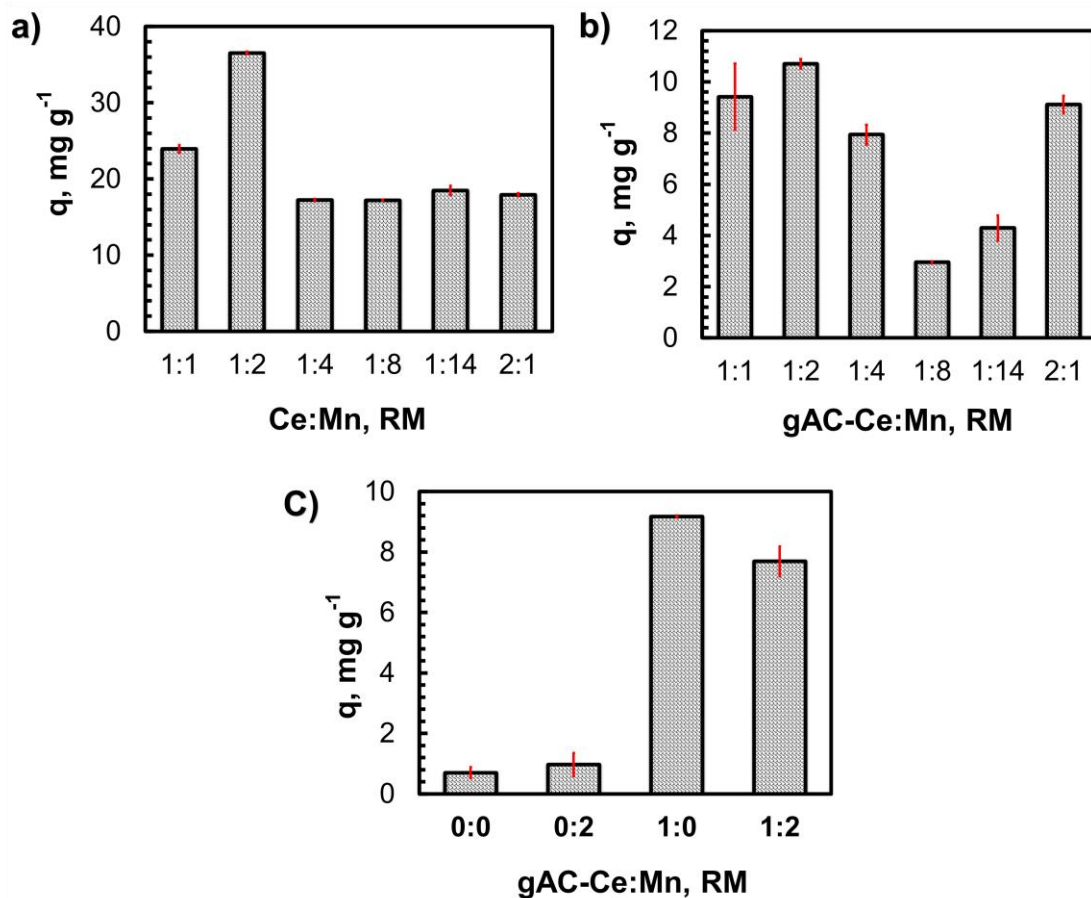


Figure 5.1. Effect of Ce³⁺ and Mn²⁺ concentration on the adsorption capacity (q), **(a)** of nanoparticles in the presence of gAC, **(b)** of modified gAC with Ce:Mn and **(c)** Fluoride adsorption capacity of gAC-Ce:Mn (2:1), gAC-Ce, gAC-Mn and GAC. Adsorption experiments were carried out in batch with an initial fluoride concentration of 20 mg L⁻¹ at pH 7 and 25 °C. Adsorbent dose was 30 mg and solution volume 30 mL

According to the literature, the anchoring of metal oxides is a process controlled by mass transfer. During hydrothermal precipitation, metal cations within the pores begin to condense through inorganic polymerization [317], decreasing the metal concentration within the pores. At this point, the concentration gradient between the solution inside and outside the pores becomes the driving force that promotes the migration of metal cations and their subsequent anchorage on the activated carbon surface [313,318,319]. This correlation between the concentration of the solution and the amount of the cation anchored on the carbon surface will take place as long as the anchored particles do not obstruct the diffusion of the cations in the pores.

Figure 5.2 shows the cerium and manganese content for each of the modified carbons, in it we can see that the gAC-Ce: Mn 1:1 showed a high content of cerium (9.5% w). On the other hand, increasing the manganese concentration decreases the mass percentage of cerium 41 and 64% (gAC-Ce: Mn 1:2 and 1:4, respectively) with respect to gAC-Ce:Mn 1:1. In addition, the null content of Mn^{2+} in the modified materials indicated that it did not participate in the fluoride adsorption process, however, it could probably affect the size and morphology of the cerium particles anchored on the activated carbon surface [313]. This, because the presence of Mn^{2+} generates a crystallization microenvironment that modulates the growth of cerium oxyhydroxide crystals [313].

In Table 5.1 we can observe that the gAC with 5.6% w of Ce obtained the highest fluoride adsorption capacity with respect to the gAC with 9.4 and 3.4% w of Ce. This indicates that not necessarily a higher concentration of cerium generates a greater capacity of fluoride adsorption, because the concentration of active sites plays an important role.

Table 5.1. Percentage of Ce and Mn anchored in the gAC and its adsorption capacity.

gAC modified	% W de Ce	% W de Mn	q mg g ⁻¹
Ce:Mn 1:1	9.5	0.0	9.4
Ce:Mn 1:2	5.6	0.1	10.7
Ce:Mn 1:4	3.4	0.0	7.9

5.3.2. Physicochemical Characterization

5.3.2.1. Textural proprieties of activate carbon unmodified and modified.

N₂ adsorption-desorption isotherms from the adsorbent materials correspond to the IUPAC type I isotherm (Figure 5.2a). This isotherm is characteristic of microporous materials, having mainly narrow micropores with a diameter less than 1nm. The type I isotherm is known not to form hysteresis; However, it can be observed that the isotherm of the samples presents a slight hysteresis type H4, typical of microporous activated carbons.

The results of the specific area determined by the Brunauer–Emmett –Teller equation, and the pore size distribution, calculated by the density functional theory, are condensed in Table 5.2. When gAC is modified with cerium, manganese and cerium-manganese, its area (978 m² g⁻¹) decreases by 40, 358 and 208 m² g⁻¹, respectively, which may be due to the anchoring of the oxyhydroxide nanoparticles. On the other hand, the mesopore volume decreased 4.2, 36.7 and 20.8% for gAC-Mn, gAC-Ce and gAC-Ce: Mn, respectively. This indicates that the oxyhydroxide nanoparticles are small enough to clog the micropores and create mesopores, thus decreasing the surface area. The mesopores in gAC-Mn, gAC-Ce and gAC-Ce: Mn increased, 3.9, 2.6 and 3.1 times with respect to the mesopores of the pristine gAC. Also, the macropores decreased approximately 94% when the gAC was modified with the oxyhydroxides (Ce, Mn, and Ce:Mn).

Table 5.2. Specific area and pore size distribution of granular activated carbon unmodified (gAC) and modified (gAC-Mn, gAC-Ce and gAC-Ce:Mn).

Sample	m ³ /g		cm ³ /g		nm
	S _{BET}	V _{mic}	V _{mes}	V _{mac}	PD*
gAC	978	0.308	0.034	0.142	2.52
gAC-Mn	938	0.295	0.131	0.009	2.36
gAC-Ce	620	0.195	0.087	0.008	2.31
gAC-Ce:Mn	770	0.244	0.105	0.010	2.34

*PD = Pore Diameter

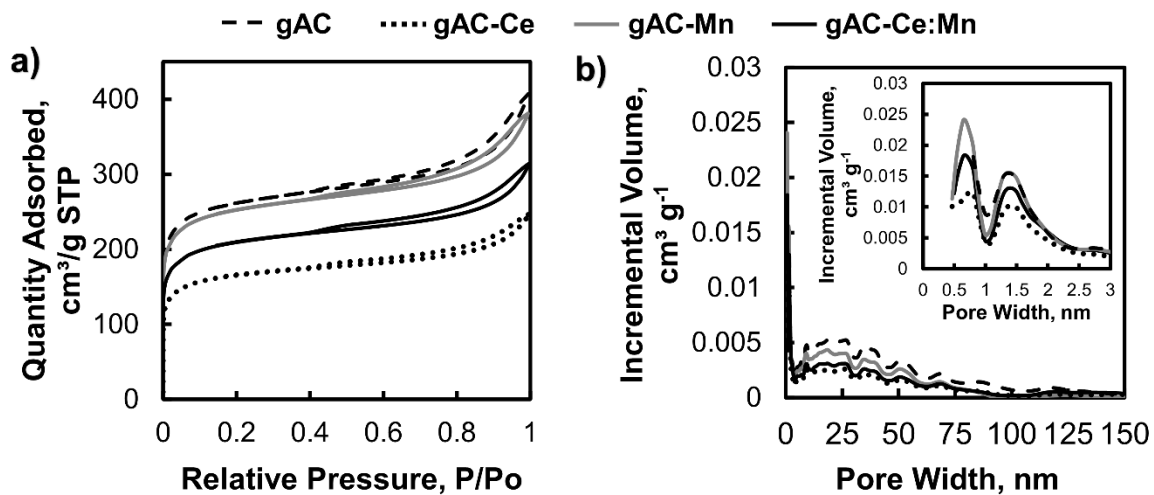


Figure 5.2. (a) N₂ adsorption-desorption isotherms and (b) size pore distribution from the granular activated carbon (gAC) unmodified and modifies with manganese (gAC-Mn), cerium (gAC-Ce) and Ce:Mn (gAC-Ce:Mn).

Figure 5.2b shown that the modified gAC exhibited an increase in the cumulative pore volume from micropores with size between 0.5 to 2 nm, which suggests that the Mn ion plays an important role in controlling the size and distribution of cerium oxyhydroxide particles anchored in the gAC porous structure. According to the results obtained, it can be said that the gAC porous structure facilitated the diffusion of cerium nanoparticles, avoiding a high pore blocking and a reduction in the specific area of the gAC due to the formation of ultramicroporous (<0.7 nm).

3.3.2.2. Activated carbon modified morphology by Scanning Electron Microscopy (SEM).

Scanning electron microscopy studies were performed to obtain information about the morphology of activated carbon modified with Mn, Ce and Ce:Mn by the microwave-assisted hydrothermal process, in addition to examining particle size and distribution of the Ce and Mn oxyhydroxide anchored on the activated carbon surface. The activated carbons micrographs and their elemental chemical analyzes of dispersed energy spectroscopy (EDS) are shown in Figures 5.3. In the case of gAC-Mn (Figure 5.3a), the presence of manganese particles, which is confirmed in the EDS. The punctual analysis by the EDS detector reveals that the weight percentage of C, O, Al, Si, S, K and Fe was 39, 27, 8, 9, 1, 1 and 15, respectively. The element Mn was not detected, due to a low content in the sample (0.1%), according to the XRD analysis where no crystalline phases of Mn were detected. The presence of Fe, Al and Si is due to the bituminous origin of activated carbon.

The micrographs corresponding to gAC-Ce (Figure 5.3b) reveal a uniform distribution of cerium nanoparticles on activated carbon with particle size between 50 and 100 nm, as well as characteristic cubic morphology of CeO₂, this being the phases identified in XRD.

These particles are mainly found in the relocations of activated carbon, where unsaturated carbon atoms are expected to be more reactive [320]. In the EDS point analysis (Figure 3B) it shows a weight percentage of C, O, Al, Si and S of 49, 11, 2, 2 and 1, respectively. The weight percentage of the Ce of 35 is due to anchored cerium oxyhydroxides.

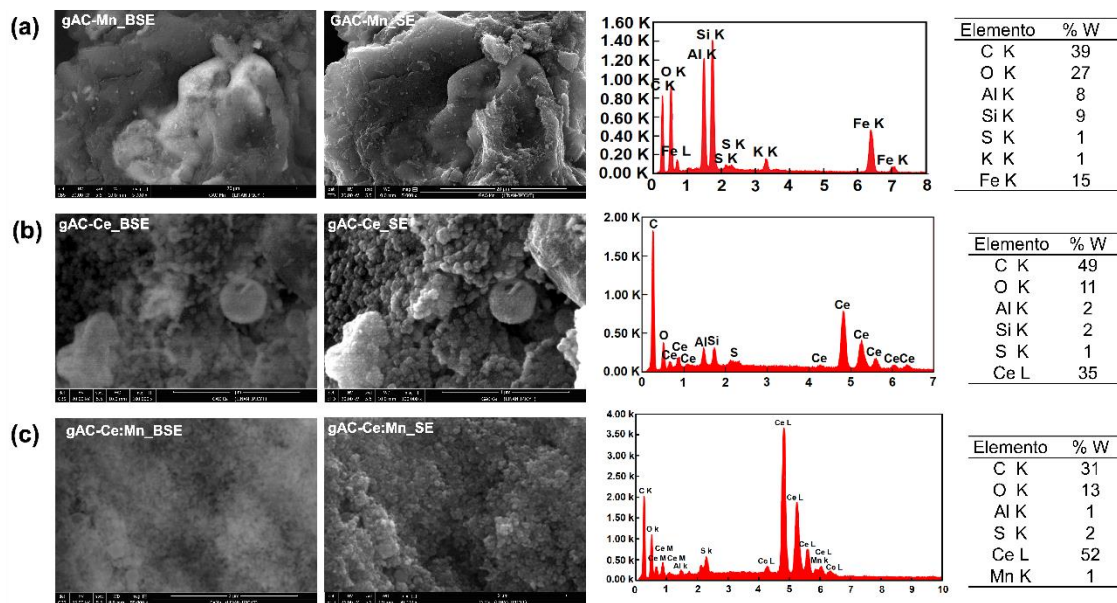


Figure 5.3. (a) SEM and EDS images of the gAG-Mn, (b) SEM and EDS images of the gAG-Ce and, (c) SEM and EDS images of the gAG-Ce:Mn.

Figure 5.3c shows the chemical composition contrast of gAG-Ce:Mn by the backscattered electron technique. This micrograph suggests a homogeneous coating of cerium oxyhydroxides and was corroborated by the EDS analysis, which revealed 52 and 13% by weight of Ce and O, respectively. Sulfur came from the manganese source used for the synthesis of the material, which was not completely removed after washing. In addition, we can observe a much smaller particle size due to the presence of Mn^{2+} who acted as a complexing agent. Therefore, the Mn participated in the size (10 to 20 nm) and morphology

of the cerium nanoparticles anchored on the surface of activated carbon. The results obtained by SEM in this study agree with the cerium oxide dispersed characterization on activated carbon for desulfurization performed by Zheng Yan et al., 2012 [321].

5.3.2.3. Surface charge and pK_a distribution

The surface charge distribution of gAC, gAC-Mn, gAC-Ce and gAC-Ce:Mn is shown in Figure 5.4a. The pH_{PZC} of the gAC is 10 which indicates the predominance of the basic groups. By modifying the gAC with manganese (gAC-Mn) the pH_{PZC} changed to 8.5, which may be associated with the acidic conditions in the material synthesis process. In the case of materials modified with Ce and Ce:Mn they showed a similar pH_{PZC} with a value of 6.0 and 5.6, respectively. This shift in the pH_{PZC} is reported by Lodeiro et al. [25], who indicate that the pH_{PZC} of activated carbon decreases as the anchoring of metal oxides on activated carbon increases due to an increase in acidity. Further, they reported that the adsorption capacity depending on the content of metal oxide on activated carbon surface, is independent of the material charge. In addition, the reduction of the pH_{PZC} could be due to the acidic conditions that were found during the hydrothermal synthesis process, accompanied by a large amount of chemisorbed oxygen, which favored the formation of acid groups by oxidizing the graphite sheets of carbon [322].

On the other hand, the pK_a 's intensity and distribution are presented in Figure 5.4b, where chemical changes in the surface of commercial and modified activated carbon are illustrated. The gAC-Mn and gAC-Ce: Mn, presented an increase in the phenolic groups ($8 < pK_a < 11$) of 0.18 and 0.12 mmol g^{-1} , respectively. In the case of gAC-Ce:Mn the increase in phenolic groups can be attributed to the OH groups of the Ce oxyhydroxides anchored on the activated carbon surface. In addition, the acidic conditions present during the synthesis

process generated carboxy groups ($3 < pK_a < 6$). The high intensity peaks at $7 < pK_a < 8$, of the activated carbons gAC-Ce and gAC-Ce:Mn are attributed to the presence of cerium oxyhydroxide, the pK_a between $7 < pK_a < 9$ can be associated to $Ce(OH)^{2+}$ y $Ce(OH)_2^+$, while the peak to $10.5 < pK_a < 11.5$ is attributed to the presence of $Ce(OH)_3$ [323].

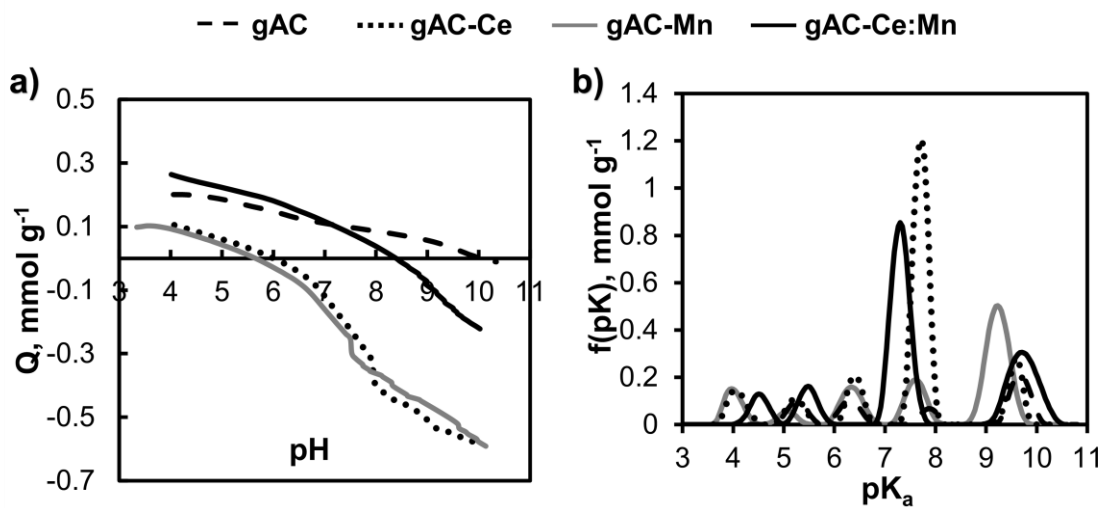


Figure 5.4. a) Charge distribution (PZC) and **(b)** distribution of pK_a for the gAC, gAC-Mn, gAC-Ce and gAC-Ce: Mn.

5.3.2.4. Fourier-transform infrared spectroscopy, X-Ray Diffraction (XRD) and X-ray photoelectron spectroscopy (XPS)

The changes in the vibrational frequencies of the cerium bonds with the functional groups on the gAC surface were studied to elucidate the interaction of the metal ion with the gAC surface. Fourier-transform infrared spectroscopy (FT-IR) of the gAC, gAC-Mn, gAC-Ce, gAC-Ce:Mn are shown in Figure 5.5a. The spectra of the gAC showed bands of low intensity in 1550 cm^{-1} that corresponds to the vibration of C=O of the carboxylic groups, at 1548 and 1130 cm^{-1} that indicate the vibration of -C=C and CO of the aromatic and lactonic

groups, respectively. Bands in the 3720 to 3580 cm^{-1} regions are attributed to O-H vibrations [324–326]. Mn(II)-modified gAC (gAC-Mn), bands were observed at 3335 to 2280 cm^{-1} which are attributed to the O-H vibrations of the carboxylic groups. The bands in the region 1380 to 1060 cm^{-1} corresponding to the vibrations of the -C-O of the lactonic groups and the bands in 1650 and 875 cm^{-1} corresponding to -C=C and -C-H, respectively. Bands were also observed in the region 627 to 576 cm^{-1} corresponding to the vibrations of the sulfate ions, which is attributed to the adsorption of these ions in the synthesis process, since the precursor of Mn(II) was MnSO_4 [327]. The presence of high intensity bands of oxygenated groups is mainly due to gAC oxidation due to acidic conditions during the microwave oven assisted hydrothermal synthesis process. When gAC was modified with Ce(III) (gAC-Ce) and Ce:Mn (gAC-Ce:Mn), the FT-IR spectrum showed a vibration band at 520 cm^{-1} which is attributed to the union of cerium with the carboxyl groups (Ce-O). This was compared with the FT-IR of CeO_2 nanoparticles which shows a high intensity peak in the 550 cm^{-1} regions attributed to Ce-O binding [328]. The results indicated that the Ce (III) ions have a greater interaction with the OH of the carboxylic and phenolic groups to form a complex.

In order to identify the polymorphic phases of Mn, Ce and Ce:Mn anchored in activated carbon, the X-ray diffraction technique (XRD) was used. Figure 5.5b shows the XRD patterns for activated carbon (gAC), gAC-Mn, gAC-Ce and gAC-Ce:Mn. The International Center for Diffraction Data software and the PDF-2010 database were used to identify the crystalline phases. The diffraction pattern of the gAC shows a characteristic amorphous behavior of carbon materials with 26° and 44° peaks (PDF Card-00-056-0160) [322]. Characteristic peaks of goethite were also identified (PDF Card-00-029-0713), due to the iron content of pristine activated carbon (0.41%), which because it is of bituminous origin presents these isomorphous impurities, in addition to hematite, alumina and silica [329].

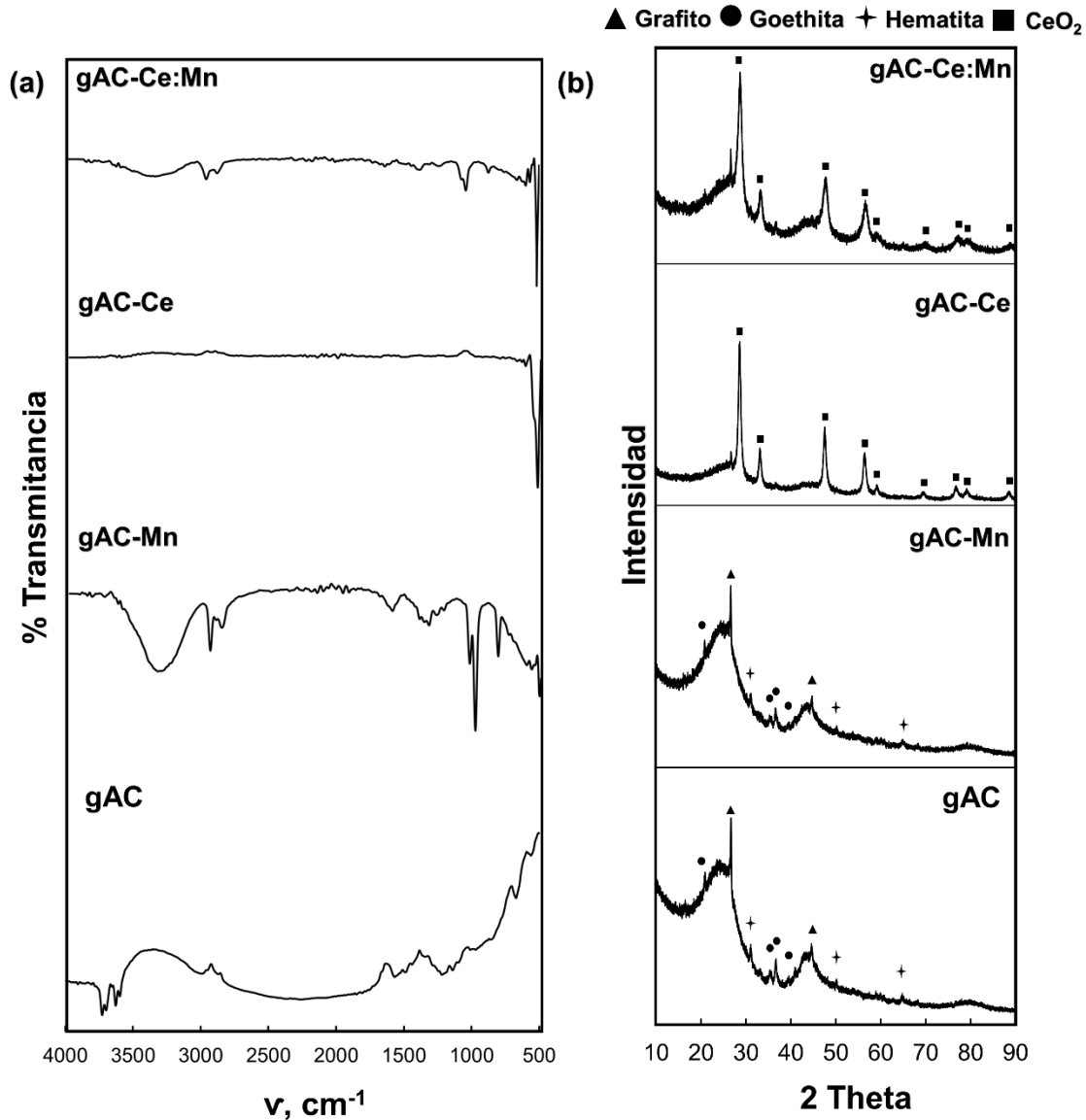


Figure 5.5. (a) Fourier Transform Infrared (FTIR) and (b) X-ray diffraction (XRD) of gAC unmodified and modified. The symbols show the crystalline phase of graphite, goethite, hematite and cerium oxide, in a step size of $0.02^\circ 2\theta$ in 10s per step.

The diffraction pattern of gAC-Mn did not show a change compared to GAC, which indicates that the conditions of hydrothermal synthesis by microwave did not favor the anchoring of any manganese phase on the gAC surface. The diffraction patterns of gAC-Ce

and gAC-Ce:Mn show peaks corresponding to the cubic structure of cerium (PDF Card-01-080-5548). The diffraction pattern of gAC-Ce showed characteristic peaks of CeO_2 at 28° , 33° , 47° , 56° , 59° , 69° , 76° , 79° and 89° . (PDF Card-01-080-5548). Estos resultados indican que después de modificar el carbón activado con cerio mediante un proceso hidrotérmico, el óxido de cerio es la fase principalmente formada [315,321]. In addition, diffractograms indicate that the effect of the Mn(II) ion is not related to the formation of new crystalline cerium phases, or the presence and quantity of these phases is so small that they cannot be detected by XRD.

The C 1s XPS spectra in the region referenced at 284.6 eV to gAC-CeMn (Figure 5.6a) showed the bond C=C peak at 284.6 eV corresponding to the sp^2 carbon bond. The gAC-Ce:Mn showed C-O bonds at 285.6 and carbonyl groups (C=O) at binding energy of 287.7 [330,331]. Figure 5.6b shows the Ce XPS spectra for the GAC-CeMn. The peaks at 917 and 898.4 eV (u'' and v'', respectively) are the main lines for the Ce $3d_{3/2}$ and Ce $3d_{5/2}$ states, respectively, and correspond to the Ce^{4+} ion ($3d^{10} 4f^0$ configuration). Each of the main lines has two satellites at 907.7 eV (u'''), 901 eV (u) and 889.5 eV (v'''), 882.4 eV (v) located near the lower junction power side due to the states of union that arise from the transfer of one or two electrons from a full or 2p orbital to an empty Ce 4f orbital. The peaks at 904.1 eV (u') and 885.7 eV (v') are the initial electronic state $3d^{10} 4f^1$ of the Ce^{3+} ions [332–334]. Therefore, the presence of all these peaks for gAC-CeMn indicates the coexistence of Ce^{4+} and Ce^{3+} on the surface of activated carbon. Figure 5.6c shows the O-Ce-(OH)₂ and CeO_2 bonds at a binding energy of 530.3 eV [332]. In addition, it is important to highlight the presence of sulfates on the surface of the material (Figure 5.6d). The peaks at binding energy of 168.3 and 169.5 eV correspond to M-SO₄ (M = metal) and SO_4^{2-} , respectively [335–339].

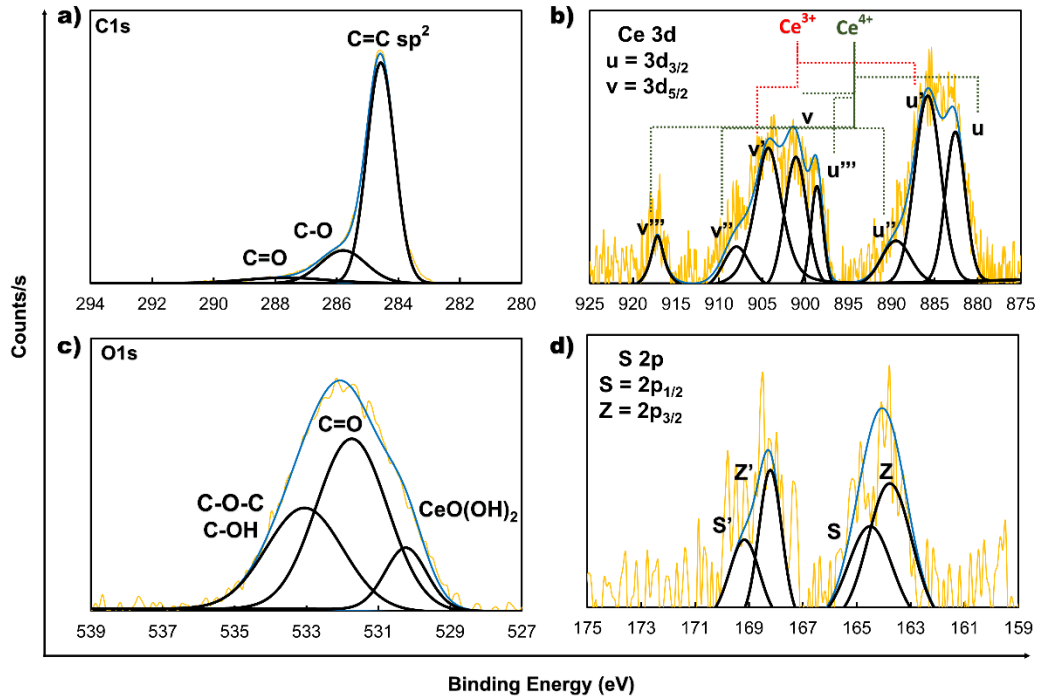


Figure 5.6. XPS spectra in the (a) C 1s region referenced at 284.5 eV for: (b) Ce 3d, (c) O 1s, (d) S 2p, of gAC-Ce:Mn.

5.3.3. Mechanisms for anchoring metal oxides.

The speciation diagrams of Ce³⁺ and Mn²⁺ show the formation of ionic pairs (Figures, Annexe A-2), which are susceptible to forming in concentrated solutions [340]. This saturation of the aqueous medium prevents the metal cations (M⁺) from presenting their full solvation sphere, associating with ions of opposite charge (SO₄²⁻) to form different chemical complexes called ionic pairs. The ionic pairs MnSO₄ and CeSO₄⁺ could be present on the surface of the activated carbon before the synthesis process.

Figure 5.7 shows how the surface oxygenated groups can be part of the cerium and manganese condensation reaction. When the activated carbon (F400) was contacted with the metal ions acidic solution (pH 2-3), the surface oxygenated groups were protonated

(Figure 5.7a), giving it a positive surface charge ($\text{pH} < \text{pH}_{\text{PZC}}$), therefore, anions such as SO_4^{2-} and HSO_4^- will be attracted by electrostatic interactions (Figure 5.7b). These anions stabilize the positive charge on the gAC surface and then the cerium and manganese aqueous complexes can bind with the gAC oxygens. The delocalized electrons in the graphitic structure and mainly the electrons found in the activated carbon oxygenated surface groups can act as nucleation centers for the aqueous complex $[\text{M}^+(\text{OH}_2)_6]^{3+}$ [317]. Once the nucleation centers have been formed, the aqueous complexes continue their deprotonation, forming hydroxy complexes $[\text{M}^+(\text{OH})(\text{OH}_2)_5]^{2+}$ that favor crystal growth (Figure 5.7c). This allowed the anchorage of the metallic particles by forming a covalent bond with the activated carbon surface of type O-M⁺ [311].

Crystal growth begins with the neutralization of the aqueous complexes, followed by the formation of hydroxides $\text{M}(\text{OH})_z^0$ via condensation of hydroxo complexes. Hydroxides can be unstable and generate oxyhydroxides ($\text{MO}_x(\text{OH})_{z-2x}$) by spontaneous dehydration. The reaction takes place through oxolation in the solid phase with the removal of water from the hydroxo ligands. The $\text{M}(\text{OH})_z^0$ stability is related to the charge generated by the water molecules ($\delta(\text{H}_2\text{O})$). Therefore, the more negative the $\delta(\text{H}_2\text{O})$, the more feasible it is to obtain the $\text{M}(\text{OH})_z^0$. However, if $\delta(\text{H}_2\text{O})$ is greater than zero, $\text{M}(\text{OH})_z^0$ will be unstable and will form a $\text{MO}_x(\text{OH})_{z-2x}$ in aqueous solution. Usually, elements with +2 valence, such as Mn, precipitate as hydroxides, and those with +3 valence, in the case of Ce, form oxyhydroxides (the final stage of their evolution is the oxide). Based on the above, if $\delta(\text{H}_2\text{O}) < 0$ in the hydroxy complex, the ligands (H_2O and OH^-) will be quite negative and therefore weakly polarized by the cation, forming a stable $\text{Mn}(\text{OH})_z^0$. This means that the metal-oxygen bond will be strongly ionic (Figure 5.7d) On the other hand, if $\delta(\text{H}_2\text{O}) > 0$ the Mn $(\text{OH})_z^0$ complex will be unstable, allowing the oxygen of the hydroxyls to bind covalently with the cation, forming a highly polarized complex (Figure 5.7e).

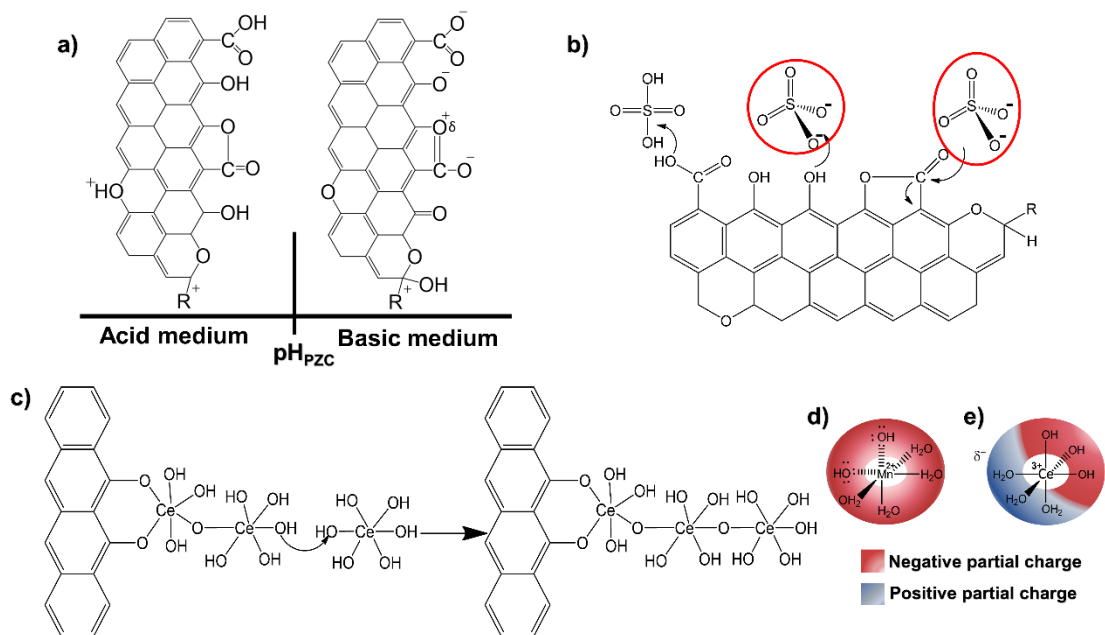


Figure 5.7. (a) gAC surface oxygenated groups in acidic and basic medium. (b) Adsorption and stabilization of the surface charge by anions. (c) Crystal growth and $M(OH)_z^0$ adsorption. (d and e) Metal ion partial charge.

Finally, the dipole generated in the cerium complexes (Figure 5.8a) favored crystal growth on activated carbon, conserving the dipole between the cationic part of the crystal and its ligands. Once this new dipole is present, the electrostatic interaction between the positive partial charge of the cerium crystal and the manganese hydroxides is favored, which prevents the growth of the crystal in this plane of cerium-manganese interaction (Figure 5.8b). The absence of manganese particles in the characterization analyzes of the new adsorbent material suggests that Mn species are only adsorbed on the crystal during the M-H process but are removed during the washing of the material with deionized water (Figure 5.8c).

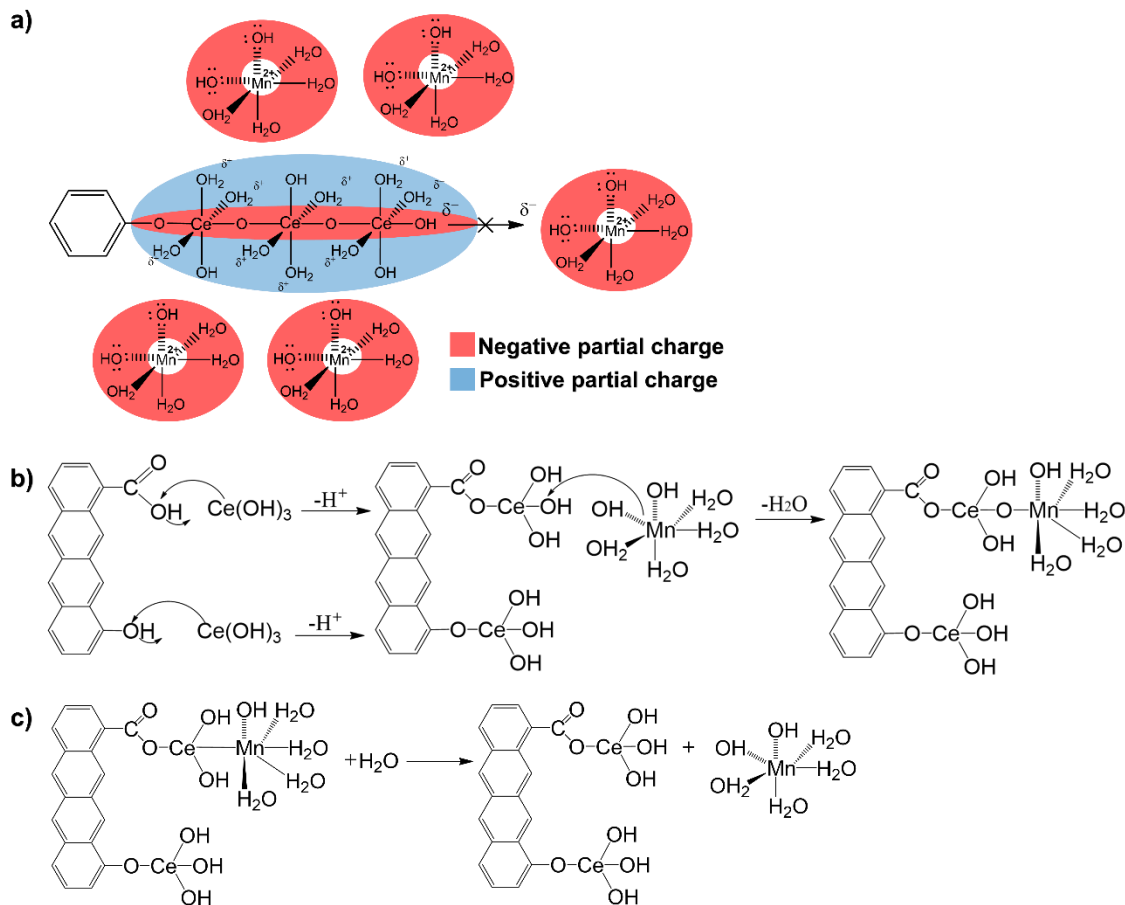


Figure 5.8. (a) Electrostatic attraction and repulsion between manganese hydroxy complexes and cerium oxide in the propagation process (modified from Gutiérrez Martínez et al, 2016). Anchoring mechanism of: **(b)** Ce:Mn and **(c)** removal of manganese from the particles surface.

In addition, through characterization analyzes, it was possible to identify that the main functional groups involved in the Ce(III) ions anchorage in commercial activated carbon (F400) are carboxylic and phenolic groups. $\text{Ce}(\text{OH})_3$ is anchored in the carboxyl and phenolic groups through the displacement of H^+ ions, forming a tetrahedral structure (Figure

5.9). In addition to this, reports have been found that indicate the affinity of rare earths such as lanthanum for carboxyl and phenolic groups [341–343]. Ce can exhibit different electronic states $[Xe] Ce 4f_0 (Ce^{4+})$, $[Xe] Ce 4f_1 (Ce^{3+})$ with mixed or intermediate valence. Therefore, Ce $4f_0$ electron has the ability to adopt a different oxidation state in bimetallic compounds or when it form complex with different functional group as carboxylic and phenolic groups that are presente in activated carbon structure (Piro et al., 2014).

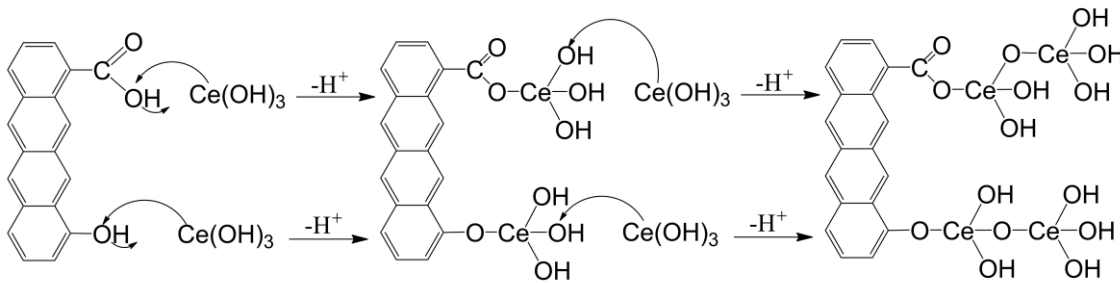


Figure 5.9. Anchoring mechanism of Ce(III) onto surface oxygenated groups of gAC.

5.3.4. Adsorption experiments.

5.3.4.1. Adsorption isotherms and kinetic of gAC-Ce and gAC-Ce:Mn.

The model parameters and correlation coefficients are shown in Table 5.3. The experimental data fit the Langmuir model better for all samples. Figure 9a shows the adsorption isotherms of gAC, gAC-Mn, gAC-Ce and gAC-Ce:Mn. The gAC can remove fluorides which is possible due to its bituminous origin, which involves the presence of other metal oxides, such like Al, Fe and Si that are related to the F⁻ ion. In addition, the adsorption experiments were carried out at a pH lower than its pHPZC therefore, the carbon is positively charged favoring the fluoride electrostatic attraction and therefore its adsorption. The activated carbon modified with Mn showed a lower adsorption capacity with respect to gAC, probably as a result of the dissolution of iron, aluminum and silicon oxyhydroxides during

hydrothermal treatment [313]. When modifying activated carbons, it is observed that their adsorption capacity increases; This is attributed to the presence of Ce(III) which has a high affinity for fluoride and makes the adsorption process more efficient. The cerium content, specific area and point zero charge (PZC) influence the materials adsorption capacity.

Table 5.3. Langmuir and Freundlich parameters for the fluoride adsorption on activated carbon unmodified (gAC) and modified (gAC-Ce:Mn).

Material	Langmuir			Freundlich		
	q mg g ⁻¹	b (L mg ⁻¹)	R ²	K _R	n	R ²
gAC	2.30	0.02	0.97	0.15	0.66	0.96
gAC-Mn	1.29	0.08	0.96	0.19	0.41	0.91
gAC-Ce	11.02	0.62	0.97	4.08	0.26	0.91
gAC-Ce:Mn	8.31	0.49	0.98	2.90	0.27	0.93

The Q_{\max} parameter of Langmuir can be interpreted as the monolayer coverage and in addition the value of the maximum adsorption capacity of the adsorbent is obtained. From the adsorption isotherms (Figure 5.10a), it was determined that Q_{\max} was 11.02 and 8.31 mg g⁻¹ to gAC-Ce and gAC-Ce:Mn, respectively. The adsorption capacity of gAC-Ce:Mn is 25% lower with respect to gAC-Ce. The above indicates that Mn really does not play any role in the fluoride adsorption capacity. However, the carbons modified with Ce and Ce:Mn increased 4.8 and 3.6 times, respectively, their adsorption capacity with respect to the pristine gAC. Although the pH_{PZC} of the gAC-Ce:Mn is similar to the pH_{PZC} of the gAC-Ce (5.7 and 6.0 respectively), the adsorption capacity of the gAC-Ce is greater, which can be attributed to a greater exposure of OH groups [316].

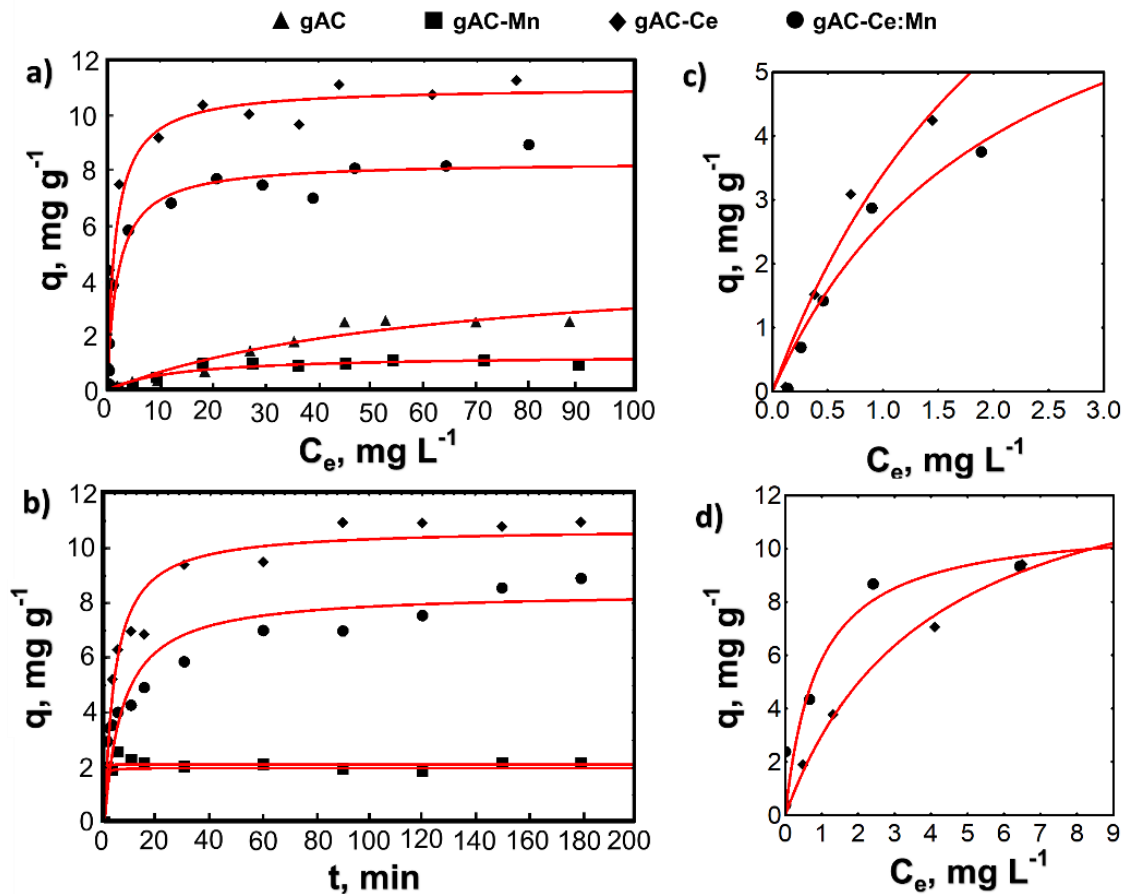


Figure 5.10. (a) Fluoride adsorption isotherms on gAC, gAC-Mn, gAC-Ce and gAC-Ce:Mn, at pH 7 (± 0.2) and 25 ° C. The solid line indicates the Langmuir model. (b) Fluoride adsorption kinetics at fluoride initial concentration (C_0) of 20mg L⁻¹, pH 7 and 25 °C. Adsorption isotherms of (c) fluoride and (d) arsenic on CAG-Ce:Mn and GAC-Ce in the presence of both contaminants at pH 7 (± 0.2) and 25 ° C. The solid line indicates the Langmuir model.

The adsorption capacity of materials depends to a great extent on their physicochemical properties. The adsorption capacity is highly dependent on the OH groups density available on the adsorbent material surface. The gAC-Ce:Mn has a greater quantity of particles anchored on the activated carbon surface, thus making the diffusion of the

pollutant more difficult. Furthermore, considering that the presence of hydroxyl groups decreases the positive charge of cerium [323], there may be a greater electrostatic repulsion between the adsorbent material and the adsorbate due to the presence of adjacent groups. On the other hand, if it is considered that the solvated Ce^{3+} forms an aqueous complex with an internal sphere $\text{Ce}(\text{H}_2\text{O})_9^{3+}$ [323]. The addition of another water molecule in $\text{Ce}(\text{H}_2\text{O})_9^{3+}$ can alter the coordination of its water molecules $\text{Ce}(\text{H}_2\text{O})_{10}^{3+}$, therefore, the solvation of the species $\text{Ce}(\text{OH})_2^+$, $\text{Ce}(\text{OH})_2^+$ and $\text{Ce}(\text{OH})_3$ will form the following complexes $[\text{Ce}(\text{OH})(\text{H}_2\text{O})_8]^{2+}$, $[\text{Ce}(\text{OH})_2(\text{H}_2\text{O})_7]^+$ and $[\text{Ce}(\text{OH})_3(\text{H}_2\text{O})_6]$, respectively with a coordination number of up to 10 [323]. Thus, gAC-Ce has a high adsorption capacity since fluoride is adsorbed on the adsorbent material by exchanging ligands with the hydroxyl groups. However, there are reports where the quaternary cerium coordinated with 16 or up to 30 fluorides (Ce_3F_{16} and Ce_6F_{30}) can be obtained [344]. The presence of Mn^{2+} generates a crystallization microenvironment that modulates the oxyhydroxide crystals growth, which suggests an inhibition of cerium species, that is, a low OH groups density on the material surface that can coordinate in Ce^{3+} and therefore a lower density of OH groups available for the fluoride adsorption. The presence of Mn has an influence on the particle size, but not on the adsorption capacity.

The adsorption kinetics was performed to assess the fluoride adsorption rate, as well as the time needed to reach equilibrium, the results are shown in Figure 5.10b. The activated carbon modified with Ce:Mn and Ce removed on 30 and 40% of the initial fluoride concentration in the first 30 minutes, respectively. The gAC and gAC-Mn removed only 10% of the fluoride initial concentration at the same time. The carbonaceous materials require approximately 60 minutes to reach equilibrium. This is attributed to the high porosity present in the materials. The gAC-Ce and GAC-Ce:Mn removed 50 and 40%, respectively, of

fluoride initial concentration in 2h. The adsorption rate of gAC-Ce and gAC-Ce:Mn was 0.11 and 0.1 mg min⁻¹, respectively. Nagendra Rao and Karthikeyan, 2012 reported that with a dose of 2 g/L of lanthanum oxide 35% of fluoride is removed in 1h and increasing the dose to 5 and 6 g/L removes 92 and 96% [37]. In the case of the present work, only one dose of adsorbent of 1 g/L was used. On the other hand, Velázquez et al., 2013 reported a 90% removal of fluorides in 1h using activated carbon modified with zirconium and oxalic acid [36]. Alagumuthu & Rajan, 2010, used zirconium impregnated in walnut shell reaching a removal of 80.33% in a time of 3h [345]. Given the above, we can say that the highest removal rate occurs in the first 2 hours for the materials under study (gAG-Ce and gAC-Ce:Mn).

In addition, the isotherms were performed in the presence of arsenic (0.5 to 15 mg L⁻¹ initial concentration) and fluoride (0.1 to 5 mg L⁻¹ initial concentration) at pH 7 and 25 ° C for 24 hours. From the adsorption isotherms, the maximum fluoride adsorption capacity (Q_{max}) on the gAC-Ce:Mn and gAC-Ce (Figure 5.10c) was determined and the results showed a Q_{max} of 8.2 and 15.2 mg g⁻¹, respectively (Table 4), indicating that gAC-Ce is a material with highest affinity for fluoride ions. On the other hand, the maximum arsenic adsorption capacity (Q_{max}) on gAC-Ce:Mn and gAC-Ce (Figure 9d) was 11.05, 8.47 and 14.65 mg g⁻¹, respectively (Table 4), being again the GAC-Ce who had the highest arsenic adsorption capacity. The above indicates that the activated carbon modified with Ce:Mn does not show a synergy in the adsorption capacity of both pollutants, therefore, the gAC-Ce adsorbent material has proven to be a highly adsorption efficient material of fluorides and arsenic.

Table 5.4. Langmuir parameters for the arsenic and fluoride adsorption in the gAC-Ce:Mn and gAC-Ce.

Material	Arsenic			Fluoride		
	q mg g ⁻¹	b (L mg ⁻¹)	R ²	q mg g ⁻¹	b (L mg ⁻¹)	R ²
gAC-Ce:Mn	11.05	1.12	0.94	8.20	0.48	0.98
gAC-Ce	14.65	0.26	1.00	15.80	0.09	1.00

5.3.4.2. Effect of solution pH about the fluoride adsorption capacity.

Adsorption experiments were performed at different pH (5, 6, 7, 8, 9) using gAC-Ce:Mn and gAC-Ce to study the impact of pH on the fluoride adsorption capacity. Figure 5.11 shows that the highest adsorption capacity is obtained at pH 5 and 6 in both materials (7.7 and 10 mg g⁻¹ for gAC-Ce:Mn and gAC-Ce, respectively) which decreases with pH increasing. The above is strongly related to the pHPZC, in Figure 5.11 can observed that at pH less than 5.6 and 6.0 (pHPZC of gAC-Ce:Mn and gAC-Ce, respectively) the material is positively charged and consequently attracts fluoride ion. However, as the pH increases (> 8.9) the hybrid material surface becomes more negative, indicating an increase in electrostatic repulsions between the F⁻ and the modified activated carbons. Moreover, the results indicate that the pH from aqueous solution does not have significant effect on the fluoride adsorption capacity. The above indicates that the adsorption capacity is a function of the metal oxide content in the activated carbon, regardless of the load of the material [346].

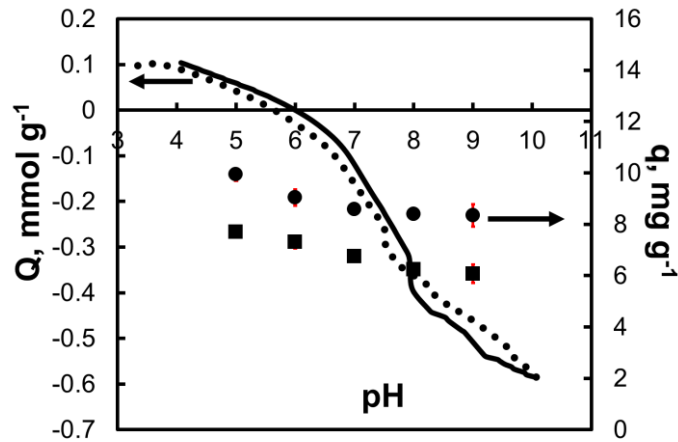


Figure 5. 11. Surface charge distributions of the materials studied at 25 ° C (dotted (gAC-Ce:Mn) and solid (gAC-Ce) line) and effect of pH on the fluoride adsorption capacity (square (gAC-Ce:Mn) and circle (gAC-Ce) symbols).

5.3.5. Fluoride adsorption mechanisms onto gAC-Ce:Mn.

5.3.5.1. Determination of the point of zero charge (PZC) and pK_a 's distribution of the gAC-Ce and gAC-Ce:Mn loaded with fluorides.

Figure 5.12a shows the charge distribution for gAC-Ce and gAC-Ce: Mn in the presence and absence of fluorides. The pH_{PZC} for gAC-Ce and gAC-Mn was 6.0 and 5.6, respectively, however, after the fluoride adsorption process at 25 °C, the pH_{PZC} became more positive, increasing its value to 6.6 and 7.7 for gAC-Ce + F^- and gAC-Ce:Mn + F^- , respectively. According to the research carried out regarding the study of Metal oxide surface chemistry, they have reported that once the anion adsorption process is carried out due to a specific interaction by ligand exchange, a reduction in pH_{PZC} is observed [347], however, in heterogeneous materials with different surface functional groups, such as activated carbon, this behavior is very different, so the pH_{PZC} increases after the adsorption

process due to a reduction in the density of oxygenated groups acids, mainly carboxylic and OH groups.

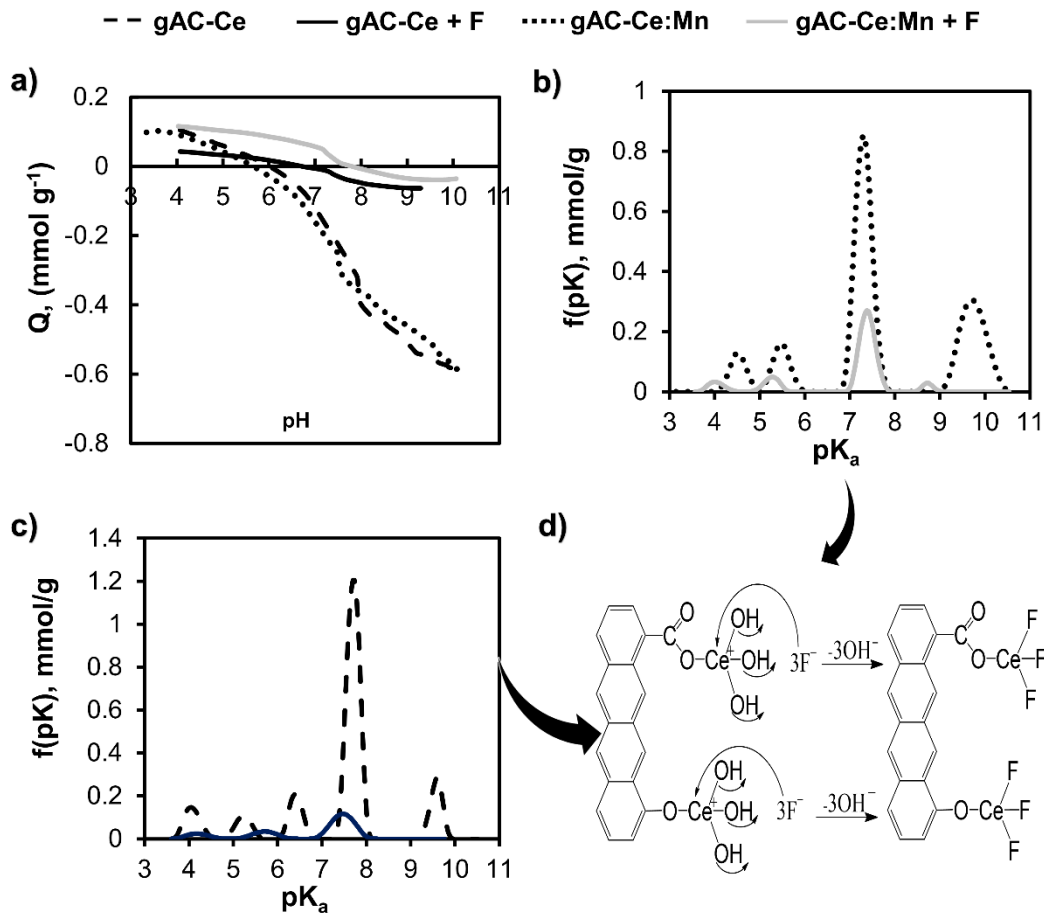


Figure 5.12. (a) Load distribution (PZC) and distribution of pK_a for GAC-Ce: Mn (b) and GAC-Ce (c) before and after the fluoride ion adsorption process. (d) Fluoride adsorption mechanism on the material modified with Ce (III).

Figure 5.12b and 5.12c shows the changes in surface chemistry of gAC-Ce and gAC-Ce:Mn after the fluoride adsorption process. The results showed a reduction in the peaks corresponding to the pK_a of carboxyl, lactonic and phenolic groups, which is associated with

the increase in the pH_{PZC} of the fluoride-loaded adsorbent materials. This result suggests that the acid oxygenated groups of activated carbon also play an important role in fluoride adsorption. In addition, the reduction in the density of phenolic groups ($8 < pK_a < 11$), $Ce(OH)_3$ ($10.5 < pK_a < 11.5$) and peaks attributed to $Ce(OH)^{2+}$ y $Ce(OH)_2^+$ ($7 < pK_a < 8$), was mainly attributed to the exchange of ligand between fluoride ions and OH surface groups of cerium oxyhydroxide during adsorption. Based on our results, a simple fluoride adsorption mechanism can be proposed on gAC-Ce and gAC-Ce:Mn, where fluoride ion displace an OH group from cerium oxyhydroxide as indicated in Figure 5.11d [326].

5.4. Conclusions

The hydrothermal synthesis process allows to successfully anchor iron oxyhydroxides on the surface of activated carbon at a synthesis time of 30 min, obtaining a material with a cerium content of 9.5% w. The significant presence of Mn in the modified material, gAC.Ce:Mn, was not observed. In addition, the presence of the Mn^{2+} ion during the cerium oxyhydroxides synthesis reduces the cerium particles size anchored on the activated carbon surface, obtaining sizes between 10 and 20 nm, which allows to obtain material with a high adsorption capacity. X-ray diffraction reveals the presence of CeO_2 , but no crystalline phase of manganese, which is confirmed by XPS. The fluoride adsorption capacity on the gAC-Ce:Mn was 8.31 mg g^{-1} , however, the adsorption capacity of the gAC-Ce was 11.03 mg g^{-1} , this being greater than that obtained by the gAC-Ce:Mn. This suggests that the presence of a complexing agent to control particle size does not guarantee an increase in adsorption capacity in the case of Ce^{3+} anchored on the gAC surface. On the other hand, functional groups such as; carboxylic and phenolic play an important role in anchoring Ce^{3+} on activated carbon surface and the adsorption of fluoride ion does not depend to a large extent

on the adsorbent material surface charge, because the adsorption is carried out by displacing of OH groups from cerium oxyhydroxides.

CHAPTER VI

Bimetallic oxyhydroxides anchored on graphitic matrices for their application in the removal of arsenic and fluorides from water.

Abstract

The search for a suitable support for the anchoring of bimetallic oxides has aroused interest in recent years. Activated carbon modified with bimetallic solutions has shown to be a promising material for the contaminants remove from water such as arsenic and fluorides. In this work, granular activated carbon was used as a support to anchor metal oxyhydroxides on its surface from a bimetallic solution of Ce-Fe, Ce-Mn, Ce-Zr and La-Zr. The arsenic and fluoride adsorption capacity of the hybrid adsorbent materials was evaluated. The material with the highest adsorption capacity for both pollutants was used in packed bed columns. In addition, it was characterized by FTIR, XRD, point of zero charge and pK_a 's distribution, to evaluate the chemical composition of the hybrid adsorbent material. The results showed that Ac-CeZr and Ac-LaZr showed a similar adsorption capacity for both pollutants. However, Ac-LaZr was used to evaluate its efficiency in packed bed columns. The characterization showed that the Ac modified with the LaZr bimetallic solution has a high OH groups density. Therefore, Ac-LaZr was shown to be more efficient in removing arsenic from water at low concentrations. The results of the packed bed column showed an adsorption capacity of As and F⁻ of 38 and 270 $\mu\text{g g}^{-1}$, respectively, after having processed 0.5 L.

Keywords: *activated carbon, lanthanum-zirconium, arsenic, fluorides, packed bed columns*

6.1. Introduction

Human activities have caused water bodies to be contaminated with many elements, an example of these is metals. Of these, arsenic and fluorides have the highest priority due to their effects on human health at low concentrations. According to the world health organization (WHO) the maximum permissible limit for As and F⁻ is 0.01 and 1.5 mg L⁻¹ in water for human consumption, respectively, which in the near future will become undetectable and 1.0 mg L⁻¹, respectively [348]. Due to the risk presented by this type of inorganic pollutant, much more efficient materials and technologies must be developed for the removal of arsenic and fluorides at concentrations lower than the maximum limit established by the WHO. Among the various technologies used for the removal of these pollutants is the adsorption process. Adsorption is considered one of the most promising for the elimination of various inorganic pollutants from water, due to its simplicity of design, easy handling and maintenance, as well as its high removal capacity. Various adsorbent materials have been used for the removal of arsenic and fluoride, where the metal and bimetallic oxide particles have been of great interest in recent years, due to their excellent adsorption capacity [349–354]. However, their disadvantage is their size, since their recovery is difficult after being used, which is why it is necessary to look for a support that allows us to retain the nanoparticles without losing their appreciable adsorption capacity. Among the various supports, activated carbon is considered an excellent candidate due to its mechanical properties and low cost. Therefore, in this work granular activated carbon was used as a support to anchor metal oxyhydroxides on its surface from a bimetallic lanthanum-zirconium solution. The arsenic and fluoride adsorption capacity of the hybrid material (Ac-LaZr) was evaluated continuously, using packed bed columns.

6.2. Experimental

Reagents with purity greater than 99% were used in experiments. Zirconium oxynitrate hydrate ($\text{ZrO}(\text{NO}_3)_2 \cdot x\text{H}_2\text{O}$), ferrous sulfate heptahydrate ($\text{FeSO}_4 \cdot 7\text{H}_2\text{O}$), cerium nitrate hexahydrate ($\text{Ce}(\text{NO}_3)_3 \cdot 6\text{H}_2\text{O}$), Lanthanum nitrate hydrate ($\text{Ce}(\text{NO}_3)_3 \cdot x\text{H}_2\text{O}$), manganese sulphate hydrate ($\text{MnSO}_4 \cdot x\text{H}_2\text{O}$), arsenic salt ($\text{Na}_2\text{HAsO}_4 \cdot 7\text{H}_2\text{O}$), fluoride salt (NaF), sodium hydroxide (NaOH) and hydrochloric acid (HCl) were used.

6.2.1. Synthesis of bimetallic oxyhydroxides

The activated carbon was contacted with the bimetallic solutions of Ce-Fe, Ce-Mn, Ce-Zr and LaZr at a molar ratio of 5: 1, 2: 1, 1: 1 and 1: 1, respectively, for 12 h at 25 ° C and 120 rpm. Subsequently, the material was synthesized by hydrothermal method assisted by microwave. The synthesis was carried out in an Anton Paar Monowave 400 microwave oven at 110 °C for Ac-CeFe, Ac-CeZr and Ac-LaZr and 150 °C for Ac-Ce:Mn during 30 min.

6.2.2. Physicochemical characterization of hybrid adsorbents materials

Potentiometric titrations were performed in an automatic titrator (Mettler-Toledo T70), to determine the pH_{PZC} and distribution of pK_a 's of the adsorbent materials. The pK_a distribution was obtained by using the program SAEIUS-pK-Dist © (1994) [151].

The pore size and surface area of adsorbent material was calculated from N_2 adsorption-desorption isotherms at 77 K (Micrometrics ASAP 2020). Surface area was estimated from the BET isotherms, and the pore size distribution was obtained by using the density functional theory (DFT).

To perform the infrared analyzes (FTIR), the ZrOx-FeOx oxyhydroxides were dried for 12 h. Subsequently, 0.03 g of adsorbent material were analyzed using KBr pellets and

subtracting the presence of water and CO₂. For this analysis, an infrared Thermo-Nicolet, Nexus 470 FT-IR E.S.P was used.

The particle size and morphology of the anchored oxyhydroxides particles were determined by scanning electron microscopy (SEM, FEI XL 30SFEG). Diffraction analyzes were carried out using a Bruker D8 Advance diffractometer, with a time and step size of 2 s and 0.01°, respectively, and a blank support to identify the crystalline phases of the oxyhydroxides anchored onto activated carbon surface. X-ray diffractograms were analyzed using the Hannawalt method.

6.2.3. Adsorption Experiments

The adsorption isotherms were performed using 30 mL of As(V) and fluoride solution at different concentrations (1 to 20 and 0.05 to 5 mg L⁻¹ of F⁻ and As, respectively), the solution was added in conical polypropylene tubes containing 30 mg of adsorbent material at pH 7 and 25 °C for 24 h (pH will be adjusted with NaOH and/or 0.1 N HCl). The arsenic concentration in the solution was determined by ICP-OES (varian 730-ES) at a wavelength of 188.98 nm. The fluoride concentration was measured by an Orion potentiometer coupled with a fluoride ion selective electrode. The adsorption capacity was determined by the mass balance (section 2.2.4.1).

A standard As(V) and F⁻ solution of 2 and 10 mg L⁻¹, respectively, at pH 7 was prepared. Then, 30 mL of the stock solution was added to 13 polypropylene tubes of 50 mL that contained 30 mg of the adsorbent material and placed at 25 °C and 120-130 rev/min in an incubator. About 15 mL aliquot was withdrawn of each sample at different times, namely, 0.5, 1, 5, 10, 20, 40, 60, 90 and 120 minutes and the pH variation was recorded all time.

Adsorption columns: The arsenic and fluoride adsorption was carried out in a column 7 cm high and 0.9 cm internal diameter. The activated carbon packing volume was 4×10^{-3} cm³. A solution was prepared with a fluorides and arsenic concentration of 10 and 0.5 mg L⁻¹, respectively, which was passed through the adsorption column with a flow of 0.13 mL min⁻¹.

6.3. Results and discussion

6.3.1. Evaluation of the adsorption capacity of different carbon-based adsorbent materials.

Different activated carbons (Ac) modified with bimetallic solutions were evaluated by hydrothermal synthesis assisted by microwave oven. The Ac were modified with bimetallic solutions of cerium-iron, cerium-manganese, cerium-zirconium, and lanthanum-zirconium, which were identified as follows: Ac-CeFe, Ac-CeMn, Ac-CeZr and Ac-LaZr, respectively. The value of the maximum adsorption capacity of the adsorbent (Q_{max}) was obtained by fitting the Langmuir model, which can be interpreted as monolayer coverage. Table 6.1 and Table 6.2 show the experimental data obtained in the fluoride and arsenic adsorption experiments, respectively, adjusted to the Langmuir and Freundlich models, based on the correlation coefficient (R^2).

Figure 6.1 shows the fluoride (Figure 6.1a) and arsenic (Figure 6.1b) adsorption isotherms of the different adsorbent materials (Ac-CeZr, Ac-LaZr, Ac-CeFe and Ac-CeMn). The Ac modified with CeFe showed a lower adsorption capacity for arsenic and fluoride, with respect to the rest of the materials. This may be associated with the fact that Fe does not have a high affinity for the fluoride ion.

Table 6.1. Langmuir and Freundlich parameters of modified carbons in the fluoride adsorption.

Samples	Fluoride					
	Langmuir			Freundlich		
	q, mg/g	b	R ²	K	n	R ²
Ac-CeZr	11.2	1.07	0.99	5.24	0.32	0.96
Ac-LaZr	10.7	1.66	0.98	5.69	0.29	0.95
Ac-CeFe	4.9	0.33	0.92	1.49	0.39	0.88
Ac-CeMn	7.7	0.31	0.95	2.20	0.41	0.91

Table 6.2. Langmuir and Freundlich parameters of modified carbons in the arsenic adsorption.

Muestra	Arsénico					
	Langmuir			Freundlich		
	q, mg/g	b	R ²	K	n	R ²
Ac-CeZr	3.30	5.25	0.89	2.71	0.25	0.89
Ac-LaZr	3.35	4.67	0.89	2.67	0.25	0.89
Ac-CeFe	1.18	7.07	0.92	0.96	0.18	0.92
Ac-CeMn	2.66	4.89	0.98	2.08	0.29	0.98

Activated carbons modified with CeZr and LaZr showed the highest adsorption capacity for both fluorides (11.19 and 10.67 mg g⁻¹, respectively) and arsenic (3.30 and 3.35 mg g⁻¹, respectively), being this 2.2 and 2.8 times higher, respectively, than that obtained by Ac-CeFe. This can be attributed to the Ac-CeFe losing its efficiency in the presence of other anions [355]. Regarding the carbon modified with CeMn, it was observed that its fluoride and arsenic adsorption capacity was 1.6 and 2.3 times greater, respectively, than that obtained by Ac-CeFe. The high removal of arsenic and fluorides by Ac-CeZr and Ac-LaZr is

attributed to the fact that the union of both metallic oxyhydroxides increased the OH groups density favoring the arsenic and fluoride capacity. Furthermore, according to research conducted, rare earth oxides impregnated in porous materials were found to be significantly effective in improving the fluoride selectivity and adsorption capacity [353,356,357].

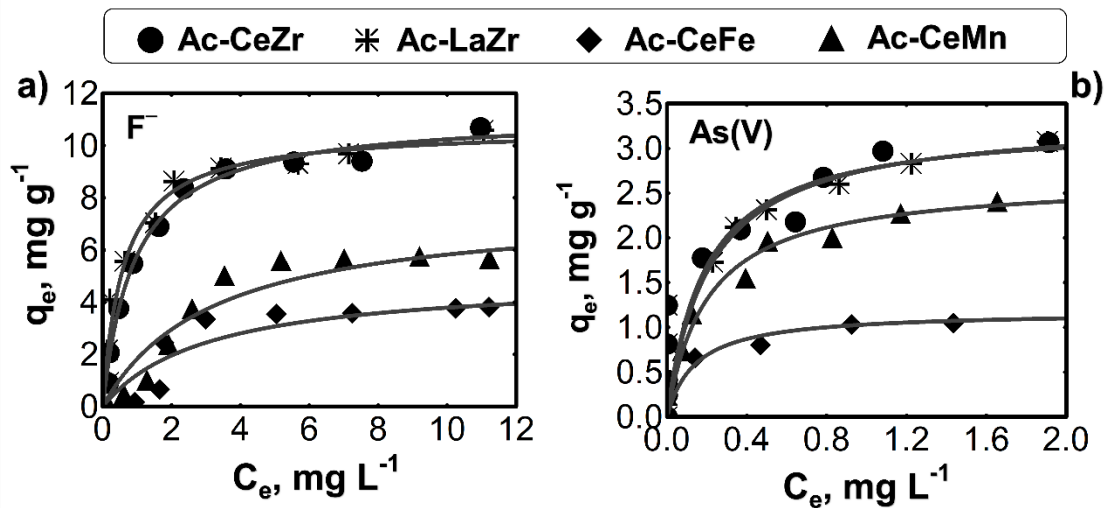


Figure 6.1. (a) Fluoride and (b) arsenic adsorption isotherms on Ac-CeZr, Ac-LaZr, Ac-CeFe and Ac-CeMn, at pH_i 7 (± 0.2) and 25 °C. The solid line indicates the Langmuir model.

The adsorption kinetics were performed to evaluate the fluoride (Figure 6.2a) and arsenic (Figure 6.2b) adsorption rate, as well as the time required to reach equilibrium. The activated carbon modified with CeMn and CeZr removed 40 and 30% of the fluoride and arsenic initial concentration, respectively, in the first 20 minutes. The LaZr-modified Ac removed 30 and 15% of the initial concentration of fluorides and arsenic, respectively, at the same time. On the other hand, Ac CeFe only removed 20% of arsenic and fluoride initial concentration. Carbonaceous materials require approximately 60 minutes to reach

equilibrium. However, it is considered that the kinetics is fast because the F- and As (V) initial concentration decreases up to 60 and 57%, respectively, in 2h for the Ac-CeZr, 60 and 50% for the Ac- LaZr, 48 and 50% for Ac-CeMn, and 36 and 36% for Ac-CeFe, respectively. Arsenic species adsorption by amorphous zirconium oxide nanoparticles require approximately 24 hours to reach equilibrium according to the study carried out by Cui et al., 2012 [358].

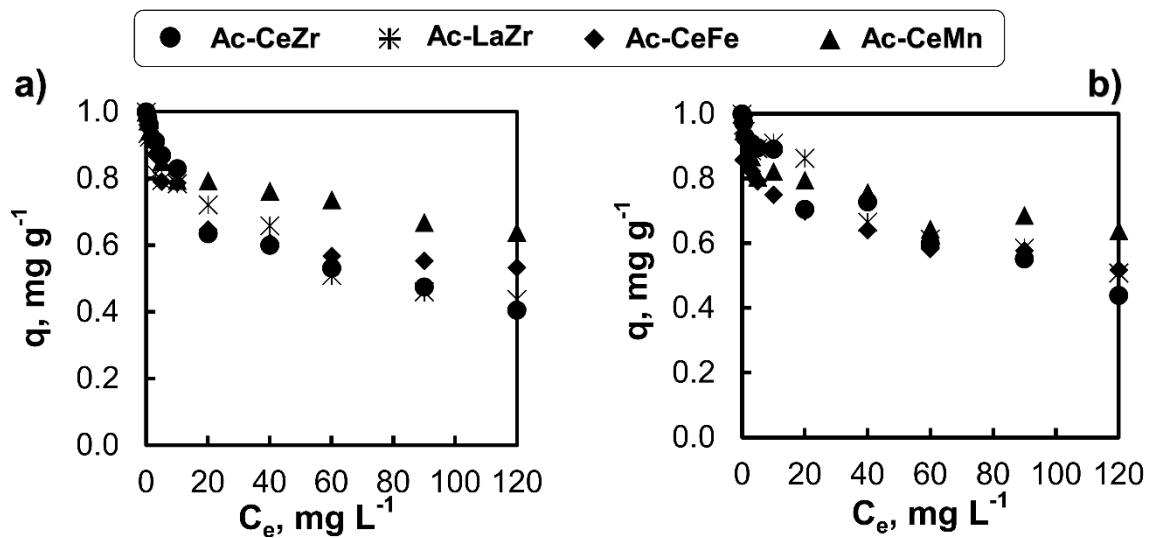


Figure 6.2. (a) Fluorides and (b) arsenic adsorption kinetics of the adsorbent materials at pH 7, 25 °C and fluorides and arsenic initial concentration of 10 and 25 mg L^{-1} , respectively.

6.3.1.1. Surface charge and pK_a 's distribution of adsorbents materials

In Figure 6.3a shows the charge distribution of Ac, Ac-CeFe, Ac-CeZr, Ac-CeLa and Ac-CeMn. The point of zero charge (pH_{PZC}) of the Ac (F400) was 9.0, indicating the predominance of basic groups. When Ac was modified with cerium-iron (Ac-Fe) the pH_{PZC}

shifted to 7.9, while the CeMn modified carbon had a much more acidic pH_{PZC} of 5.7. This shift in the pH_{PZC} is attributed to the fact that as the CeFe and CeMn are anchored on the surface of the Ac, an increase in acidity is obtained, decreasing the pH_{PZC} of the activated carbon after being modified. Therefore, the reduction of the pH_{PZC} in the modified materials may be due to the acidic conditions that were found during the synthesis process ($\text{pH} = 2$ to 5), which accompanied by the large amount of chemically absorbed oxygen, favored the formation of acid groups when oxidizing the graphitic sheets of carbon.

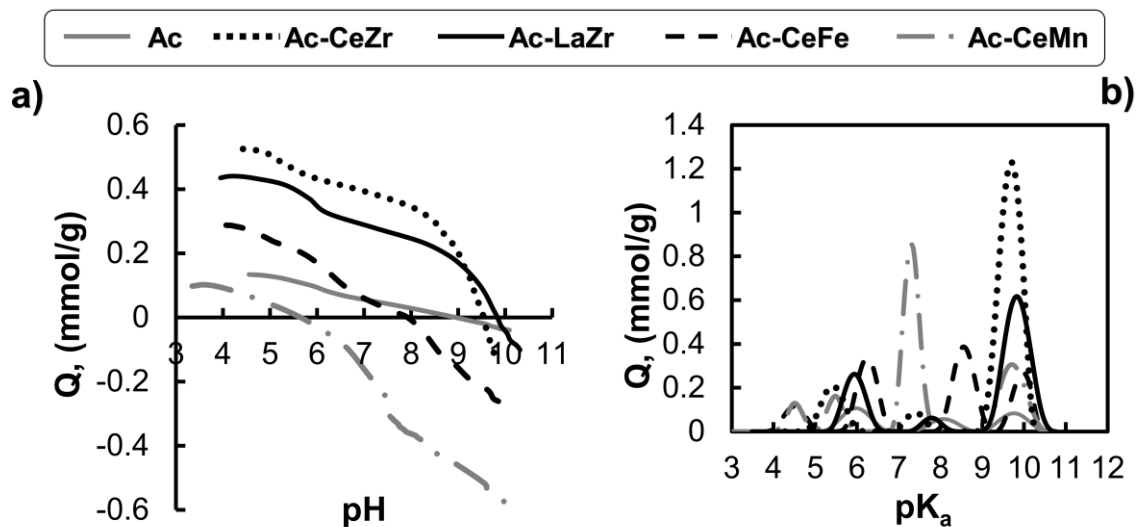


Figure 6.3. (a) Point of zero charge (pH_{PZC}) and (b) surface distribution (pK_a 's) of unmodified and modified carbons.

The Ac modified with cerium-zirconium and lanthanum-zirconium (Ac-CeZr and Ac-LaZr) showed a pH_{PZC} of 9.5 and 9.8, respectively, which contributes to the fact that the pH_{PZC} reported in the literature of CeO_2 , lanthanum hydroxide and (hydr)oxide of zirconium is 8, 8.8 and 8.6 respectively [359–365]. Therefore, when these oxides are anchored to the oxygenated functional groups of Ac, the material remains basic at a pH_{PZC} greater than 8.

Ac-CeZr and Ac-LaZr have a greater positive charge on the pH of adsorption experiments of arsenic and fluorides (pH = 7). These conditions are favorable for the adsorption of fluorides, due to the electrostatic attraction between the positively charged adsorbent, the anions F⁻ and As (V).

The metallic oxides surface is mainly constituted by surface hydroxyl groups that determine the chemistry and reactivity of the surface [366]. Figure 6.3b shows the pK_a distribution obtained by the SAEIUS software. Ac-CeFe and Ac-CeMn showed an increase in the phenolic groups (8 < pK_a < 11) with respect to Ac from 0.08 mmol g⁻¹ to 0.25 and 0.3 mmol g⁻¹, respectively, attributed to the OH groups of the iron and cerium oxyhydroxides anchored on the activated carbon surface. A slight increase in carboxyl groups (3 < pK_a < 6) is also observed, which is attributed to the acidic conditions present during the synthesis process. In Ac-CeZr and Ac-LaZr, a displacement of the peaks associated with carboxylic groups is observed, because Ce, Zr and La are considered strong acids, therefore, it has preference to form a bond with carboxylic and phenolic groups of activated carbon. Furthermore, the OH groups concentration in Ac-LaZr and Ac-CeZr was 2 and 4 times higher, respectively, with respect to Ac-CeFe and Ac-CeMn. These results justify the high adsorption capacity of the CeZr and LaZr modified carbons. An important factor to consider for obtain a highly efficient adsorbent material is that the metallic oxides have a very good distribution on the support material surface. These studies show that a high OH groups density results in a high adsorption capacity due to an increase in positive sites. Ac-LaZr and Ac CeZr showed a OH groups concentration of 0.57 and 1.23 mmol g⁻¹, respectively, and a fluoride and arsenic adsorption capacity of 11.2 and 3.30 mg g⁻¹ and 10.7 and 3.35 mg g⁻¹, respectively. Therefore, the OH groups concentration of Ac-CeZr was double compared to Ac-LaZr, however the fluorides and arsenic adsorption capacity was similar. The high OH groups density plays an important role in the arsenic and fluoride adsorption

capacity. However, it should not be forgotten that an excess of these groups can ultimately be detrimental to the fluoride adsorption capacity due to electrostatic repulsion between adjacent ions (Figure 6.4) as in the case of Ac-CeZr. Due to this, to continue with the present study, it was chosen to work with the carbon-based material, Ac-LaZr, in addition to the low cost of lanthanum compared to cerium.

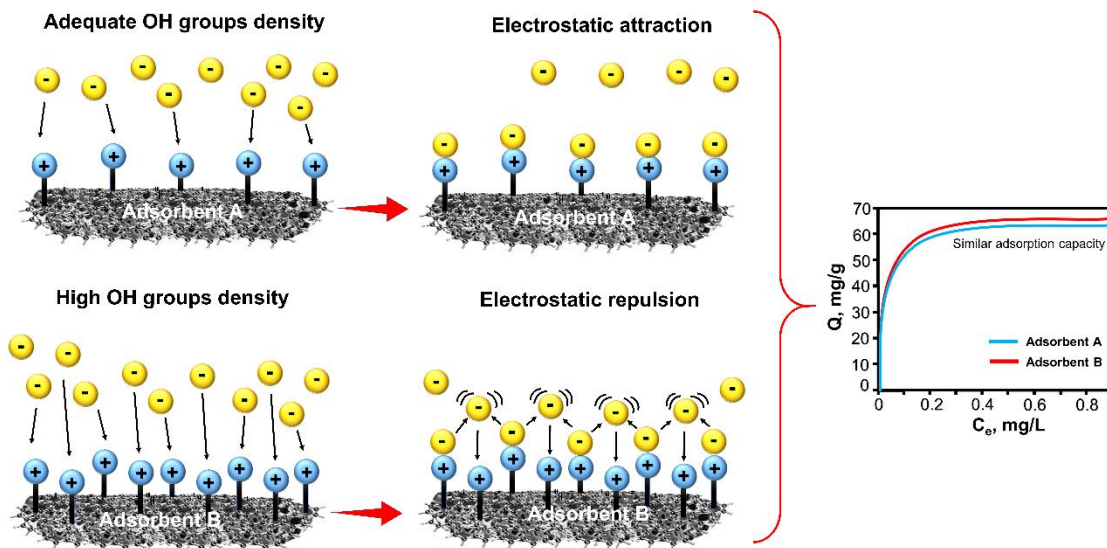


Figure 6.4. Schematics represent of electrostatic attraction and repulsion onto adsorbent material with high OH group density.

6.3.2. Characterization physicochemical of Ac-LaZr

SEM was performed to know the morphology and distribution of the oxyhydroxides anchored on the adsorbent material surface. Furthermore, the changes in the vibrational frequencies of the La (III) and Zr (IV) bonds with functional groups on the Ac surface were studied to elucidate the interaction of metal ions with the carbonaceous surface. XRD was

carried out to know the crystalline phase of the oxyhydroxide present on the activated carbon surface.

The surface morphology of Ac-LaZr is shown in Figure 6.5. The bright regions correspond to the Zr-containing particles, confirmed by EDS analysis (45.31%). The physicochemical characterization indicated that the carbon modified with zirconium-lanthanum shows an agglomerated morphology of the metal in certain areas of the activated carbon (Figure 6.5a) and the EDS analyzes indicate the null presence of lanthanum on its surface (Figure 6.5b). The presence of Al (0.83%) was noted in the modified activated carbon due to the main components of activated carbon, in addition to elements C (12.49%) and O (41.46%).

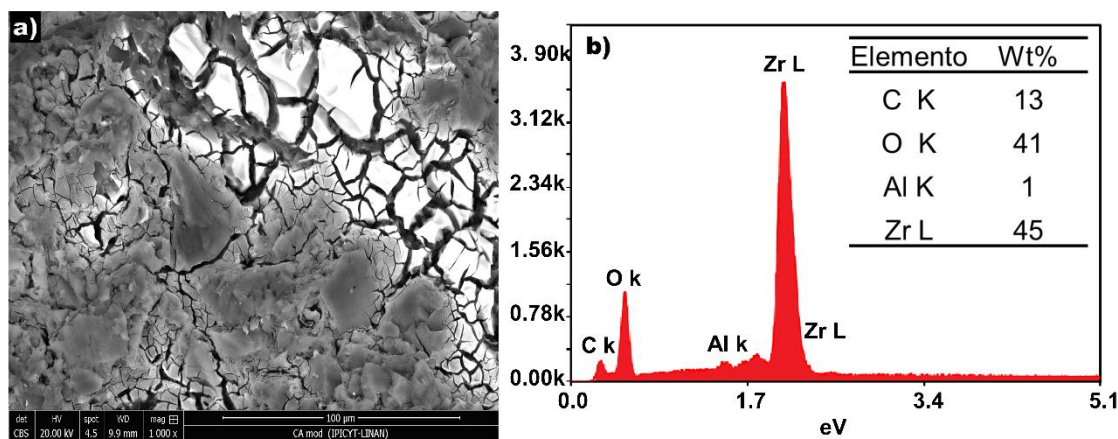


Figure 6.5. (a) SEM and (b) EDS micrograph of LaZr-modified Ac.

N₂ adsorption isotherms at 75 K for modified carbons are shown in Figure 6.6a. These isotherms are type I, which are typical of microporous adsorbents according to the IUPAC [275,367]. H4 type hysteresis loops were observed in both isotherms (Ac and Ac-LaZr), which indicates that the material has porous structures in the form of sheets but very narrow,

indicating the additional presence of micropores. This fact is common in real porous materials since they present the combination of pores, micro and mesopores [276,277].

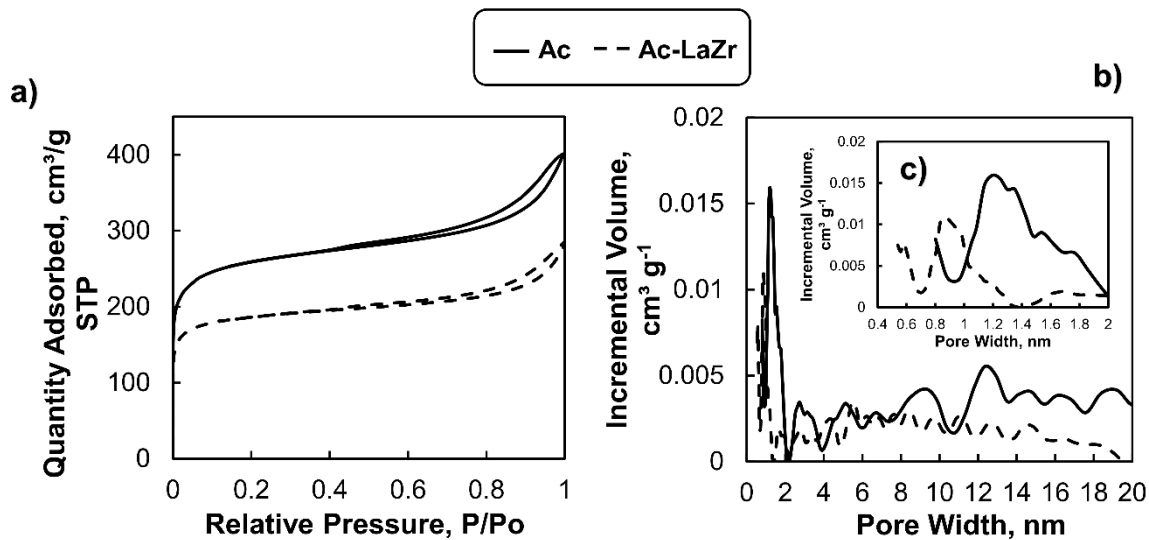


Figure 6.6. (a) N₂ adsorption isotherms at 75 °K and pore distribution of (b) micropores, mesopores, (c) super-micropores and ultra-micropores of modified carbons.

Table 6.3 shows that the surface area of Ac was 978 m² g⁻¹ and decreased 26% when is modified with LaZr. The Ac-LaZr adsorbent material can see that the micropores and macropores decrease 26 and 38%, respectively, with respect to AC (Figure 6.6b). This can be attributed to the presence of the zirconium particles, which are small enough to penetrate down to the micropores. However, Figure 4.3c can see that AC-LaZr has an increase mainly in the ultra-micropores with a pore width between 0.6 to 0.7 nm and super-micropores with a pore width of 0.7 to 1 nm.

Table 6.3. Physicochemical Characterization of nonmodified and modified activated carbon.

Muestra	$\text{m}^3 \text{g}^{-1}$		$\text{cm}^3 \text{g}^{-1}$		Nm
	S_{BET}	V_{mic}	V_{mes}	V_{mac}	Pore diameter
Ac	975	0.3509	0.2041	0.0145	2.38
Ac-LaZr	719	0.2589	0.1264	0.0111	2.25

The FTIR spectra of Ac and Ac-LaZr are shown in Figure 6.7a. Ac spectra showed low intensity peaks around 1211 and $1126\text{-}846 \text{ cm}^{-1}$ that indicate the vibration of carbonyl $\text{C}=\text{O}$, CO and -OH , lactones and phenolic groups, respectively. A band at $3600\text{-}3720 \text{ cm}^{-1}$ can be associated with the groups of silanol (Si-OH) and adsorbed water. Due to its bituminous origin, activated carbon F400 may contain Si, Al, and Fe in its structure.

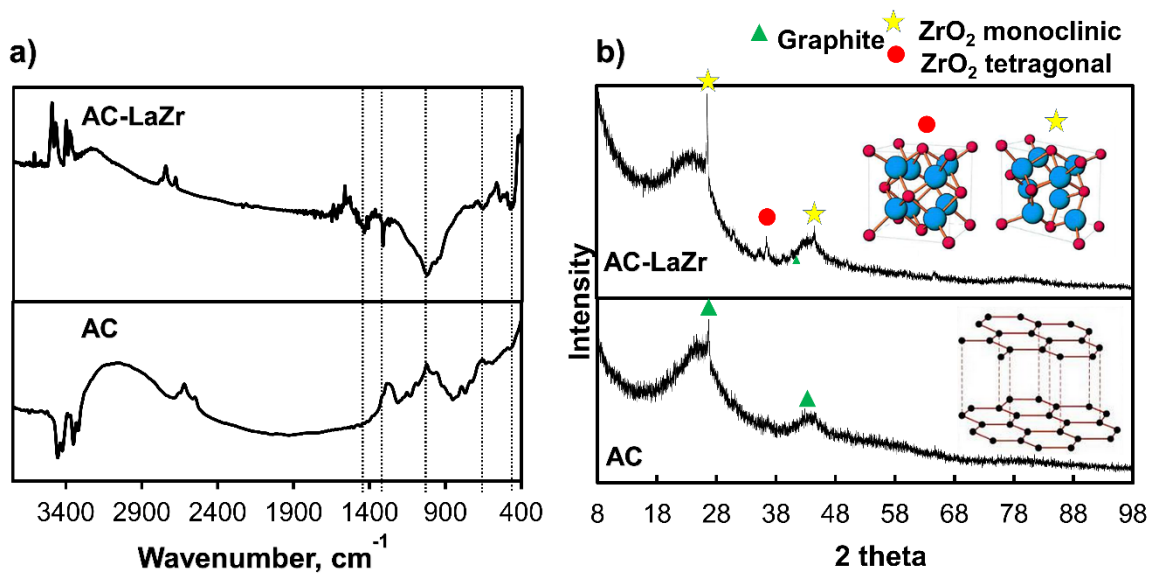


Figure 6.7. (a) FTIR and (b) XRD of the Ac and LaZr-modified Ac.

When Ac was modified with lanthanum and zirconium, the FTIR spectra showed absorption bands in the 460–672 cm^{-1} region that were attributed to Zr-O and ZrOOH bonds in coordinate complexes [357,368]. The weak band at 460 cm^{-1} indicates that Zr (IV) can be found in a monoclinic and tetragonal phase of ZrO_2 [369]. A weak vibration band at 1060 cm^{-1} was related to Z-O of the zirconyl groups [352]. Furthermore, a broad band centered at 1382 and 1510 cm^{-1} was attributed to Zr-OH bonds [366,370,371].

X-ray powder diffraction was performed to identify the polymorphic phases of ZrO_2 found in the FTIR and EDS analysis when the Ac was modified with lanthanum-zirconium. Figure 6.7b shows the XRD patterns for GAC-LaZr, where two peaks at 2θ angles of 26.58 and 43° correspond to monoclinic structures. The monoclinic phase is described as a distorted fluorite structure, each Zr^{4+} ion is coordinated triangularly by seven oxygen ions in the foreground and tetrahedrally in the background. On the other hand, the peak corresponding to angle 2θ between 35-36.5° is attributed to tetragonal zirconia structures [356]. In the tetragonal phase, the Zr^{4+} ion is surrounded by eight oxygen ions, four of them at a distance of 2.455 Å and the other four at a distance of 2.064 Å [372].

6.3.3. Adsorption experiments

The adsorption experiments showed that the Ac modified with LaZr, has an adsorption capacity of 10.67 and 3.35 mg g^{-1} of fluorides and arsenic, respectively. The adsorption kinetics showed that in the first 40 minutes, 75% of the initial concentration of arsenic and 45% of the initial concentration of fluorides were removed (Figure 6.8a). Furthermore, a 100% arsenic removal efficiency was observed in the first 60 minutes, thereby reaching equilibrium (Figure 6.8b).

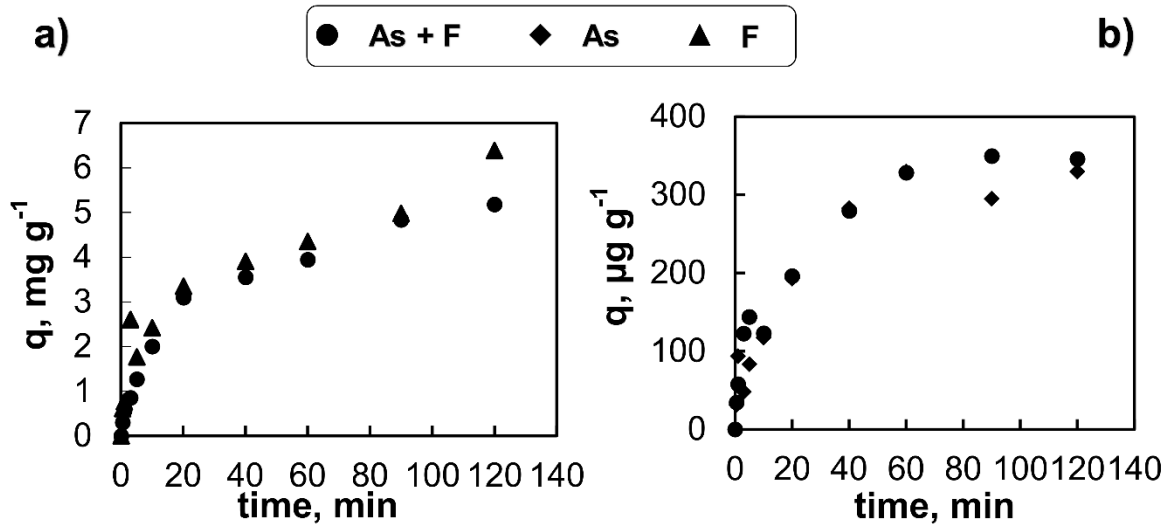


Figure 6.8. Effect of arsenic and fluoride on the adsorption capacity of GAC-LaZr.

Adsorption kinetics at pH 7 and 25°C . Initial concentration of **(a)** fluorides and **(b)** arsenic of 5 and 0.5 mg g^{-1} , respectively, of GAC-LaZr.

On the other hand, the breaking curves show the adsorption profiles for F^- and As (V) present in the studied solution (Figure 6.9a). It was observed that the concentration of fluorides in the effluent remained at a constant value in the first 0.14 L. This corresponds to a fluoride adsorption efficiency of approximately 85%. After treating 0.14 L, the fluoride concentration in the effluent began to gradually increase at a rate of 0.47 mg L^{-1} every hour, reaching the saturation point of the column after 0.31 L. In addition, it was observed that arsenic did not broke into the treated volume in which the F-saturated completely. The results of the packed bed column showed an adsorption capacity of As and F^- of 38 and $270 \mu\text{g g}^{-1}$, respectively, after having processed 0.5 L. The results indicate that the adsorbent material has a higher affinity for arsenic than fluorides. A high arsenic and fluoride removal

efficiencies from the water can be associated with the fact that it was worked at a pH of 7, being lower than the pH_{PZC} of activated carbon modified with Zr-La (9.8), where its surface is positively charged. Fluoride is adsorbed through electrostatic interactions, this being a much faster process than the one that occurs when adsorption is carried out through specific sites such as arsenic.

In Figure 6.9b it was observed that the arsenic concentration in the effluent was kept at a constant value in the first 3 L. This corresponds to an arsenic adsorption efficiency of approximately 100%. After treating 3 L, the arsenic concentration in the effluent began to increase gradually at a rate of $4.95 \mu\text{g L}^{-1}$ every hour, reaching the saturation point of the column after 10.6 L. The results obtained in this study indicate that the adsorbent material has excellent adsorption capacity for both pollutants, especially arsenic. The high arsenic removal capacity is due to the fact that the concentration of this pollutant is 20 times lower than that of F^- , however, even with the low As (V) concentration present in the solution, Ac-LaZr is capable of removing $464 \mu\text{g g}^{-1}$.

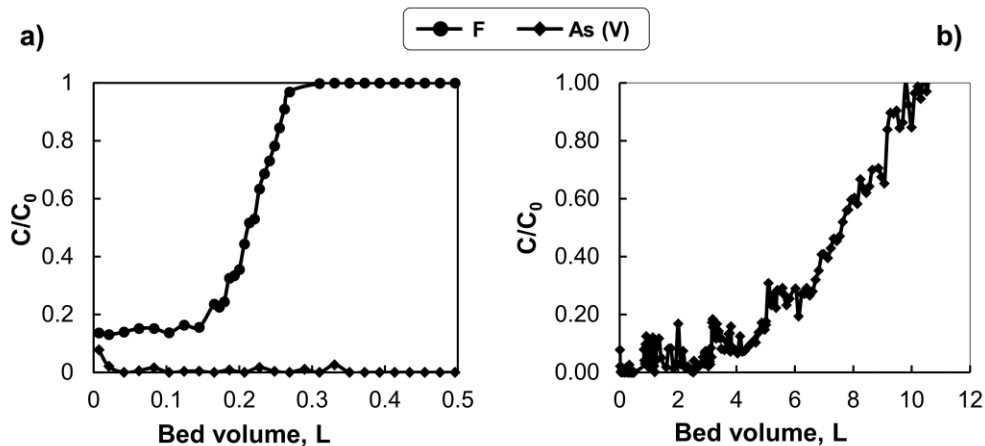


Figure 6.9. (a) Breakdown curves for arsenic and fluorides in a packed bed column at pH 7 and EBCT for 10 min. (b) Breakdown curves for arsenic.

According to the literature, when zirconium is adsorbed on carbon surfaces, Lewis acid sites are generated [8, 9], so that the zero charge point of carbons modified with Zr oscillates at 3.28 [373], Sin However, the presence of lanthanum favors an increase in pH_{PZC} on the surface of the material, in addition, an increase in the density of active sites of Ac-LaZr ($0.4346 \text{ mmol g}^{-1}$) can be observed in Figure 1B with respect to pristine Ac . Therefore, ZrLa-modified Ac has a positive charge at the pH of the adsorption experiments (pH 7). These conditions are favorable for fluoride adsorption due to the electrostatic attraction between the positively charged adsorbent and the anionic F^- . In addition, the high density of OH groups that the material presents plays an important role in the arsenic adsorption. It is well documented that arsenic is adsorbed onto the material by exchanging ligands with OH groups.

6.4. Conclusions

The adsorption isotherms showed that the materials Ac-CeZr and Ac-LaZr have a high adsorption capacity of 11.19 and 10.67 mg g^{-1} , being these more than 2 times high compared to Ac-CeFe and Ac-CeMn. On the other hand, it was concluded that the presence of fluorides significantly affects the arsenic adsorption capacity of Ac-CeFe. In the case of Ac-CeMn, the presence of arsenic has a very low effect on its fluoride adsorption capacity. The adsorption kinetics indicated that the kinetics are fast because the initial concentration of F^- and As (IV) decreases to 60 and 57%, respectively, in 2h for Ac-CeZr, 60 and 50%, respectively, for Ac-LaZr. The arsenic and fluoride adsorption capacity of activated carbon can be substantially increased, with the anchoring of nanoparticles highly efficient in the removal of these contaminants. The high adsorption capacities of Ac-CeZr are mainly due to the presence of

OH groups as indicated by the charge distribution and the XPS studies. Not all materials have high crystallinity and the presence of sulfates in Ac-CeFe and Ac-CeMn was observed, indicating that the particles are made up of more than one crystalline phase. However, the low crystallinity of the materials contributes to increasing the adsorption capacity of activated carbon.

Activated carbon modified with La:Zr has been shown to have an excellent arsenic and fluoride adsorption capacity of 4.4 and 9.3 mg g⁻¹, respectively at an initial concentration of 5 and 15 mg g⁻¹, respectively. Furthermore, it was observed that the presence of both contaminants does not significantly inhibit the adsorption capacity of both contaminants. The results of the packed bed column showed an adsorption capacity of As and F⁻ of 38 and 270 µg g⁻¹, respectively, after having processed 0.5 L. The results indicate that the adsorbent material has a higher affinity for arsenic than fluorides. The good efficiencies in removing arsenic and fluorides from the water can be associated with the fact that it was worked at a pH 7, being lower than the pHPZC of activated carbon modified with Zr-La (9.8), where its surface is positively charged and the high content of OH groups on the surface of the material.

CHAPTER VII

General Conclusion

Zirconium oxide
Iron oxide

● Zr^{4+}
● Fe^{2+}
● O^{2-}
● OXYGEN VACANCY

World Health Organization

agua contaminada
gránulos de carbón activado

©DESIGNALIKR

4.00 μm

CHAPTER VII

General Discussion

7.1. Final Remarks

The adsorption process has been widely used for the remove arsenic and fluoride from water. Among the adsorbent materials used to remove arsenic and fluorides from water we find activated carbon, biosorbents, metallic oxyhydroxides and bimetallic oxides. Iron in its various forms (oxyhydroxide, hydroxide, goethite, hematite, and iron oxide) has been further explored to develop efficient arsenic removal technologies.

Materials based on rare earth elements have been proposed for the removal of arsenic and fluoride given their capacity and high specific affinity for these pollutants, of which lanthanum (La) and cerium are typical representatives. Cerium and lanthanum are inexpensive and relatively harmless rare earths [374]. CeO_2 has the ability to have a redox cycle between its two oxidation states (Ce^{3+} and Ce^{4+}), because cerium has a high oxygen storage capacity and oxygen ion conductivity [375]. Generally, this property improves the performance of transition metal catalysts used in wastewater treatment. On the other hand, the high arsenic and fluoride capacity that has cerium is due to the presence of high affinity of surface hydroxyl groups.

Zirconium oxide (ZrO_2) is another adsorbent material that has attracted the attention of researchers because it is non-toxic, moisturizing, and has high porosity. ZrO_2 is more stable compared to other oxides such as titanium oxide [376] and aluminum oxide [377] and it should be noted that it has a high affinity for the arsenic and fluorine species.

Bimetallic oxyhydroxides have been designed with the oxides, in order to increase the hydroxylated surface. The distinguishing advantage of bimetallic oxides is that they inherit the properties of the pristine oxides that make them up. Bimetallic oxides such as Fe(III)-Sn (IV) [378], ZrOx-FeOx, Ce (IV) doped iron oxide [379] and Fe-Mn have shown notably greater arsenic adsorption capacity than any of pure oxides. On the other hand, the metal oxides of Ce-Mn, Ce-Zr and La-Zr have shown a high affinity for fluorine and arsenic. Therefore, current research on adsorbent materials for the removal of arsenic and fluorides has focused on designing bimetallic combinations. However, to achieve their application in continuous systems, these bimetallic oxides have been anchored on the activated carbon surface. Various studies have shown that activated carbon is an excellent candidate for the bimetallic oxides anchoring on its surface. The advantages of using activated carbon as a support are its high surface area, versatility and low cost. In addition, the oxygenated groups of activated carbon act as active centers for crystal nucleation and growth.

A much more efficient and simple method was used to synthesize the adsorbent materials. The microwave-assisted hydrothermal method has the advantage of performing a more homogeneous synthesis of the particles, in comparison with other methods. The hydrothermal-microwave method resulted in a fast nucleation rate due to more homogeneous heating. Furthermore, particles with a homogeneous size and morphology were obtained without forgetting that the synthesis time was much shorter compared to other methods.

In the first instance, bimetallic oxides of ZrOx-FeOx and Ce: Fe-P's were synthesized to remove arsenic from water. According to the characterization of the materials, Ce: Fe-P's has an area 8 times smaller than that of FeOx-ZrOx (6 and 49 m² g⁻¹, respectively). The N₂ adsorption-desorption isotherms of the materials showed type IV isotherms with a hysteresis

of H3, which indicates that they are mesoporous materials. The morphology of the materials shows that the Ce: Fe-P's bimetallic oxyhydroxides show a hedgehog and fibril shape, while the ZrOx-FeOx showed a morphology of agglomerated particles and flat cube shapes. The XRD standards for bimetallic oxide ZrOx-FeOx show the crystalline phase of ZrO₂ and compounds of FeO(OH) and Fe(SO₄)(H₂O). In the case of Ce:Fe-P's, it presented a monoclinic structure of Ce₂(SO₄)₃(H₂O)₅ and the structure of the orthorhombic compound of Fe(SO₄)₂H, which was confirmed by XPS studies.

The charge distribution showed that ZrOx-FeOx and Ce: Fe-P's have a pHPZC of 7.2 and 6.8, this being similar for both materials. Furthermore, the OH groups density for both materials were higher than that of the pristine oxides (2.4 and 14 mmol g⁻¹ for ZrOx-FeOx and Ce: Fe-P's, respectively). According to these results, bimetallic oxyhydroxides have a high potential for their application in the arsenic adsorption from water.

Regarding the adsorption capacity of both materials and according to the OH groups density, Ce: Fe-P's shows a greater arsenic adsorption capacity (179.8 mg g⁻¹) compared to ZrOx-FeOx (62.7 mg g⁻¹) being this approximately three times greater. The high arsenic adsorption capacity of Ce: Fe-P's can be attributed to its morphology and the high active groups density that it presents in its crystalline structure. On the other hand, the kinetics shown that the arsenic adsorption on Ce: Fe-P's is much faster than that on ZrOx-CeOx. The Ce:Fe-P's reaches equilibrium in the first minute, while the ZrOx-CeOx requires 40 minutes, which is attributed to the porous structure of the material and the availability of the active sites where the adsorption process is completed. It is important to mention that when the adsorption takes seconds, it is electrostatic adsorption. Therefore, the arsenic adsorption on the adsorbent materials is carried out by ligand exchange, that is, by specific adsorption.

Studies have been carried out where Ce-Fe bimetallic oxide particles have been synthesized by various synthesis methods. Wen et al., 2015 [380] synthesized magnetic mesoporous Ce-Fe bimetallic oxides with an adsorption capacity of 103 mg g⁻¹. Wen et al, 2020 [381] manufactured micelles of mesoporous Ce-Fe bimetallic oxides. Ce-Fe calcined at 350 °C showed an arsenic adsorption capacity of approximately 150 mg g⁻¹ at an equilibrium concentration of 3 mg L⁻¹. However, in both works the Ce-Fe adsorbent materials required more than 10 minutes to reach equilibrium according to the adsorption kinetics. Table 7.1 shows a comparative table of the work carried out with the bimetallic oxyhydroxides studied in chapters II and III of this research. Where it can be observed the high advantages of both the simple method used in the production of materials, as well as the high efficiency of the materials in removing arsenic from water, mainly the bimetallic oxyhydroxide Ce:Fe-P's. Although it is observed that the adsorption capacity is similar to other materials, it is important to consider the material dose and the arsenic concentration used to achieve the maximum capacity. A highly efficient material must be able to remove arsenic and/or fluorides even at low concentrations.

An important aspect to consider in the application of bimetallic oxyhydroxides in continuous systems for the contaminants remove, is how these materials will be used. It has been reported that metal oxides can anchor on the activated carbon surface due to its high oxygenated groups content within its structure. The oxyhydroxide of Ce:Fe-P's was anchored on the activated carbon surface (F400), due to that presented a high arsenic adsorption capacity. The synthesis of Ce: Fe-P's was carried out by the microwave-assisted hydrothermal method. In this case, the activated carbon was contacted with the bimetallic solution for 2 h at 25 °C and 120 rpm, to guarantee the ions diffusion in the carbon porous structure, and they were synthesized at 110 °C for 30 min. The synthesis method of this material proved to be adequate to achieve a good oxyhydroxides distribution.

Table 7.1. Ce-Fe and Zr-Fe bimetallic oxides for the removal of Arsenic

Ref.	Composition	Bimetallic	Adsorption capacity, mg/g	Ce, mg/L	pH/ temperature	Morfology	Synthesis method
Yu Zhang, et al., 2003	----	Ce-Fe	70.4		5.0/20 °C	-----	Precipitation
Basu y Ghosh, et al., 2013	Fe ₂ O ₃ y CeO ₂	Ce-Fe	2.1	4.5	7.0/30 °C	Agglomerate with irregular shape	Precipitation and drying at 100 °C
Bo Chen, et al., 2013	α-Fe ₂ O ₃ y CeO ₂	Ce-Fe-CTAB*	91.74	17	5.5/25 °C	Circulars	Thermostatic oven assisted precipitation and calcination at 80 - 400 °C) for 4 to 12.
Uttam Kumar Sahu, et al., 2016	FeO ₂ y CeO ₂ ,	Ce-Fe	32	30	3.0/25°C	Circular and aggregates	Autoclave-assisted precipitation at 180 °C for 5h
Zhipan Wen, et al., 2018	α-FeOOH	Ce-Fe	164.94	50	6.0/25 °C	Three-dimensional (3D) hierarchical flower spheres	Solvothermal with glycerol assisted by autoclave
Zongming Ren, et al., 2011	Ferrihidrita	Zr-Fe	46.1	15	7.0/25 °C	Rough and porous structure	Precipitation and drying at 65 °C
Saif Ali Chaudhry, et al., 2017	Ferrihidrita	IZBOCS	45.05	400	27 °C	Irregular and circular structure	Impregnation and calcination at 300 °C
Xiaomin Dou, et al., 2018	γ-FeOOH y (Zr(OH) ₄ ·nH ₂ O)	Fe-Zr	75	---	---	Amorphous structure	Co-precipitation
E. Vences-Alvarez y J. R. Rangel-Mendez	Ce ₂ (SO ₄) ₃ (H ₂ O) ₅ y FeOOH	Ce:Fe-P's	179.78/120	3/0.035	7.0 a 25 °C	Flat shape with flowers	Hydrothermal synthesis assisted by microwave oven at 110 °C for 30 minutes
	FeOOH y ZrO ₂	ZrO _x -FeO _x	62.72	5	^a 7.0 a 25 °C	Flat cube shapes and agglomerated particles.	

*CTAB = Cetyltrimethylammonium bromide surfactant

The design of experiments showed that the molar ratio of Ce: Fe of 5:1 anchored on the activated carbon surface obtained the highest adsorption capacity. The characterization indicated that the AC-Ce:Fe has a acicular particles morphology, characteristic of goethite with a particle size of 20 nm. The area of activated carbon decreased from 978 to 870 m² g⁻¹ when it was modified with the cerium-iron metallic solution, having a greater effect on the micropores. The reduction of micropores was 24% with respect to pristine carbon, which indicates the existence of particles with a size smaller than 2 nm capable of obstructing the micropores (Figure 4.3b). On the other hand, the chemical characterization indicated the absence of cerium on the activated carbon surface. The acid digestion showed that the AC-Ce:Fe has 3.62% w of Fe being this 1.6 times higher with respect to the carbon modified only with Fe. In addition, 0.63% w of Ce was observed on the carbon modified with Ce:Fe. The presence of Ce³⁺ in the modification of activated carbon can contribute to the morphology and size of the iron particles.

The AC-Ce:Fe showed an arsenic adsorption capacity of 5.6 mg g⁻¹, this being 32 times lower with respect to the adsorption capacity obtained with the Ce:Fe oxyhydroxide particles (179.8 mg g⁻¹). This can be attributed to the presence of Ce and that the OH groups of the bimetallic oxide are more available compared to AC-Ce:Fe. According to the adsorption kinetics, Ce:Fe-P's requires one minute to reach equilibrium, while AC-Ce:Fe requires 5 hours to remove 90% of the initial arsenic concentration. On the other hand, activated carbon modified with cerium (AC-Ce) showed an arsenic adsorption capacity of 8.52 mg g⁻¹ (Figure 4.9), which is attributed to the particle size smaller than 5 nm, which gives a greater availability of OH groups for arsenic adsorption. The exchange of ligands between the hydroxyl groups formed on the surface of cerium oxide and the arsenic species is responsible for the removal of arsenic. At high solution pH, deprotonation of hydroxyl groups produces stronger electrostatic repulsion between adsorbent and arsenic. A pH of

the solution greater than the pH_{PZC} of the AC-Ce would affect the diffusion of arsenic towards the adsorption sites in the adsorbent and finally would cause a more significant influence on the removal of As (V). The presence of both metals within the carbonaceous matrix is important since, according to the arsenic adsorption results obtained by the materials studied in this work. The union of both metals shows a synergy in terms of adsorption capacity. Iron, for example, has been widely studied and recognized for its great affinity for arsenic. Cerium has numerous advantages as an adsorbent material when it is in amorphous or hydroxylated form. CeO_2 shows a low adsorption capacity (3.5 mg g^{-1}) while cerium modified carbon showed a 2.4 times higher capacity (8.52 mg g^{-1}). Li et al., 2012 [382], showed that amorphous hydrated cerium oxide has an excellent adsorption capacity of up to 100 mg g^{-1} at an equilibrium arsenic concentration of 10 mg L^{-1} . In the case of our work, crystalline cerium oxides with an octahedral structure were obtained, which drastically reduces the formation of OH groups. However, cerium showed an affinity for arsenic. On the other hand, an advantage of having the presence of Ce (IV) in the structure of our material is that cerium causes the partial oxidation of As (III) to As (V) on the adsorbent surface. Therefore, the converted As (V) can then be more easily adsorbed [383].

On the other hand, a new carbon-based adsorbent material was synthesized for the removal of fluorides from water. In this study, the intention was to anchor Ce-Mn oxyhydroxides on the activated carbon surface. When modifying the activated carbon with the bimetallic cerium-manganese solution in the same way as with the AC-Ce:Fe, only one of the metals was anchored in the carbonaceous matrix. Recent studies have shown the effect that some cations such as Ce^{3+} and/or Mn^{2+} have on the anchoring of metallic oxyhydroxides on the activated carbon surface. The presence of Ce^{3+} or Mn^{2+} during hydrothermal hydrolysis, at a specific metal cations concentration, promotes the formation of a particular morphology. Furthermore, they can act as capping agents for particle size

control. In the case of carbon modified with cerium-manganese. It was obtained a much smaller particle size (10 to 20 nm) compared to carbon modified only with cerium (50 to 100 nm). The fluoride adsorption capacity of gAC-Ce:Mn was 8.31 mg g^{-1} , this being less than that obtained by cerium-modified carbon (gAC-Ce, 11.02 mg g^{-1}). The results show that the presence of Ce and Mn for the synthesis of AC-Ce:Fe and gAC-Ce:Mn, respectively, did not have a positive influence on the removal of arsenic and fluorides, respectively. The cerium supported in the graphitic matrix of the carbon was shown to have a high affinity and efficiency in removing arsenic and fluorides from water. Also, pH does not have a significant negative effect on fluoride adsorption capacity. This can be attributed to the fact that if it is considered that the solvated Ce^{3+} forms a non-aqueous complex with an internal sphere $\text{Ce}(\text{H}_2\text{O})_9^{3+}$ [323]. The addition of another water molecule in $\text{Ce}(\text{H}_2\text{O})_9^{3+}$ can alter the coordination of its water molecules $\text{Ce}(\text{H}_2\text{O})_{10}^{3+}$, therefore, the solvation of the species $\text{Ce}(\text{OH})_2^+$, $\text{Ce}(\text{OH})_2^+$ and $\text{Ce}(\text{OH})_3$ will form the following complexes $[\text{Ce}(\text{OH})(\text{H}_2\text{O})_8]^{2+}$, $[\text{Ce}(\text{OH})_2(\text{H}_2\text{O})_7]^+$ and $[\text{Ce}(\text{OH})_3(\text{H}_2\text{O})_6]$, respectively with an coordination number of up to 10 [323].

Furthermore, the adsorption capacity of gAC-Ce could be studied in the presence of both contaminants (As and F^-). The results showed that the arsenic and fluoride adsorption capacity of gAC-Ce was 15.8 and 16.65 mg g^{-1} , respectively, while for gAC-Ce:Mn it showed an arsenic and fluoride adsorption capacity of 8.2 and 11 mg g^{-1} , respectively. Therefore, it can be concluded that the presence of Mn does not have a positive effect on the adsorption capacity of both pollutants (As and F^-) on gAC-Ce:Mn.

Exploring another type of adsorbent, it was found that when activated carbon is modified with a lanthanum-zirconium bimetallic solution (Ac-LaZr), it has a fluoride adsorption capacity (10.7 mg g^{-1}) greater than that obtained by gAC-Ce:Mn (8.31 mg g^{-1}).

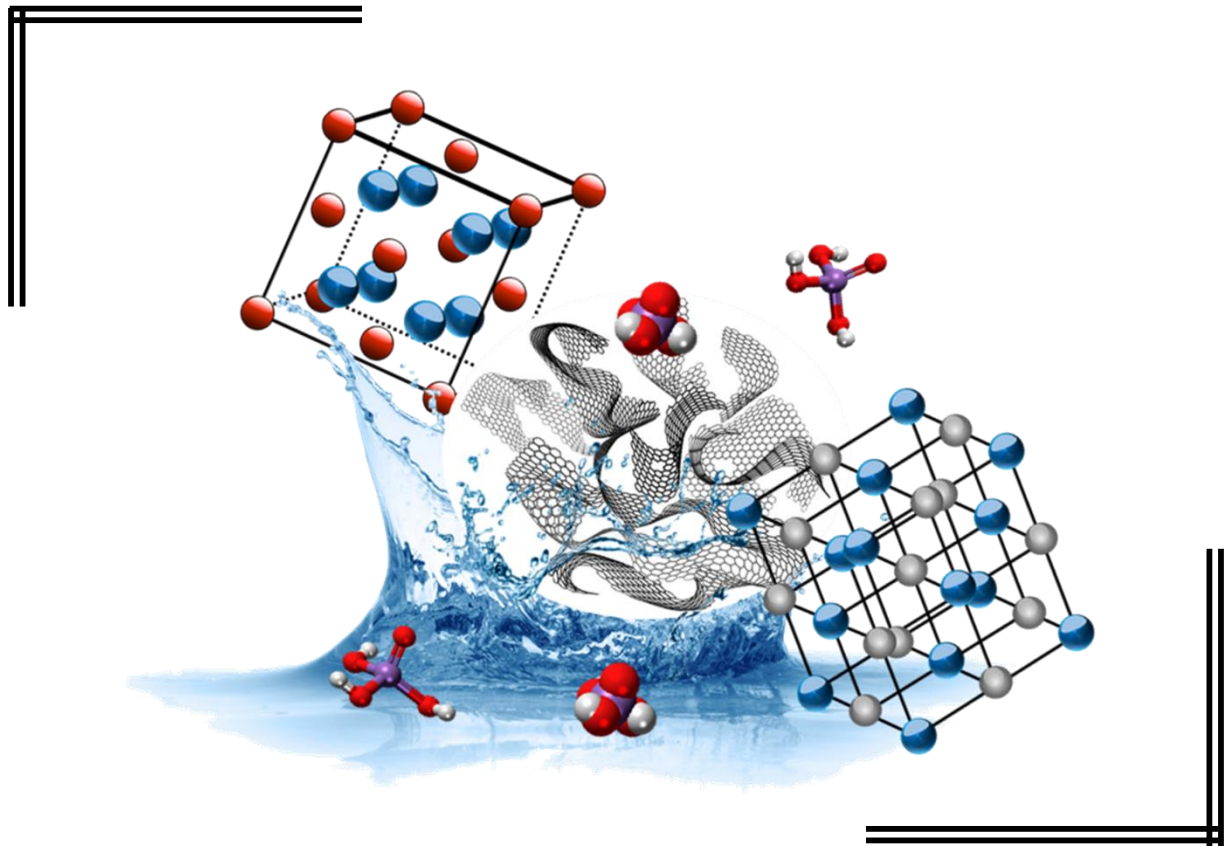
Ac-LaZr was shown to be an adsorbent material with a high potential for the removal of arsenic and fluorides with an adsorption capacity greater than that of materials above-mentioned. This can be attributed to an increase in the positive sites of the material (0.45 mmol g^{-1}) and pH_{PZC} , with respect to AC-Ce:Fe and gAC-Ce:Mn. Ac-LaZr exhibits a highly fine agglomerated particle morphology. On the other hand, the EDS showed the absence of lanthanum on the activated carbon surface. However, the monoclinic and tetragonal presence of zirconium gives the material high potential for application in packed bed columns. The adsorption columns showed a breaking point for fluoride and arsenic of 0.15 and 2.5 L of treated volume, respectively. The saturation point was at 0.3 and 3 L of treated volume for arsenic and fluorides, respectively (Figure 6.9). The Fluoride and arsenic adsorption capacities obtained in the commune were 38 and $270 \text{ } \mu\text{g g}^{-1}$, respectively. The adsorbent material, Ac-LaZr has proven to be a widely effective material for the removal of arsenic and fluorides. This high adsorption capacity of the material (Ac-LaZr) is attributed to the fact that the presence of lanthanum in the synthesis process can enhance the positive charge of the Zr ions to allow a better attraction of contaminants. Because carbon modified with Zr has a low fluoride adsorption capacity (2.67 mg g^{-1}) according to the study carried out by Velzquez et al., 2014. To increase the fluoride adsorption capacity of the material synthesized by these authors, added a complexing agent such as oxalic acid.

Although the adsorption capacity of the adsorbents studied through this research were comparable to various materials tested for the removal of the same contaminants in aqueous solutions, more research is needed to design an adsorbent that can meet the standards and treatment settings of water. Finally, it is important to mention that the presence of a complexing agent or other cations in the solution to synthesis of new adsorbent materials does not guarantee an increase in the adsorption capacity. In order for both metal ions to anchor in the crystalline structure and to have a positive effect on the adsorption capacity, it

is necessary to investigate and evaluate new methods for the synthesis of bimetallic oxides in the presence of activated carbon.

CHAPTER VIII

Final Conclusions, perspectives, and scientific products



CHAPTER VIII

Final Conclusions, perspectives, and scientific products

8.1. Final Conclusions

The synthesis method used in this work has resulted in the generation of bimetallic oxides from bimetallic solutions, with a morphology with a three-dimensional (3D) hierarchy depending on the oxides mixture and an excellent selectivity to the removal of arsenic from the water. The bimetallic oxides ZrOx-FeOx and Ce: Fe-P's synthesized showed a high adsorption capacity (62.7 and 179.8 mg g⁻¹) compared to the pristine oxides that make them up. It was observed that the arsenic adsorption capacity in both adsorbent materials is not the same, this is due to the fact that some metal oxides show a higher selectivity for arsenic, as is the case with cerium. Furthermore, the morphology and crystalline structure of the material are an important factor in having excellent adsorbent materials. For the contaminants remove such as arsenic and fluoride, a material with a high OH groups density is required. It was concluded that the pH_{PZC} and the arsenic solution pH do not have a significant influence on the adsorption capacity of bimetallic oxides. However, the presence of coexisting anions affected the adsorption capacity of the ZrOx-FeOx and Ce: Fe-P's, mainly the presence of PO_4^{3-} , due to the similarity it has with As (V). The bimetallic oxides, ZrOx-FeOx and Ce: Fe-P's, have been shown to be potential candidates for the removal of arsenic from water.

However, the particle size of ZrOx-FeOx and Ce:Fe-P's limits their application in continuous systems. Due to the above, the bimetallic oxides of Ce:Fe-P's and gAc-Ce:Mn were anchored for the arsenic and fluorides adsorption, respectively, on the graphitic matrix of using the same synthesis method. The results indicated that activated carbon is an excellent candidate for use as a support for oxides, due to its high density of acid groups on its surface. However, when synthesizing bimetallic oxides within the activated carbon structure, only one of the oxides is anchored in the oxygenated groups, while the other acts as a capping agent, regulating the particle size and morphology. Therefore, the arsenic adsorption capacity of AC-Ce:Fe (5.6 mg g^{-1}) is 32 times lower compared to Ce:Fe-P's. The fluoride adsorption capacity of gAc-Ce: Mn (8.31 mg g^{-1}) is 16.8 times lower compared to Ce:Mn-4 h (140 mg g^{-1}) reported in the literature. However, AC-Ce:Fe and gAc-Ce:Mn are adsorbent materials with a high adsorption capacity. Comparing the As (V) and F⁻ adsorption capacity of various materials of bimetallic oxides anchored on the activated carbon surface, it was observed that Ac-LaZr was one of the materials with the best adsorption capacity. Ac-LaZr showed high selectivity for both As (V) and F⁻ (3.4 and 11 mg g^{-1} , respectively), at low concentrations. The Ac-LaZr was applied in packed bed columns, where a higher selectivity was observed for As (V) followed by F⁻. The breakdown curve showed that due to a higher fluorides concentration, it presented a breakdown and saturation point at 0.5 and 0.3 L of treated volume, respectively. On the other hand, the arsenic breakdown curve showed a breakdown and saturation point at 2.5 and 3.0 L of treated volume. Ac-LaZr, showed a continuous fluoride and arsenic adsorption capacity of 38 and $270 \text{ } \mu\text{g g}^{-1}$.

Finally, metallic, and bimetallic oxides show to be adsorbent materials with a high potential for the removal of pollutants from water. However, it is important to study the anchoring of these materials on various supports, in order to find the support that allows to preserve at least 60% of the adsorption capacity of metallic and bimetallic oxides.

8.2. Perspectives

Arsenic and fluoride contamination is a subject that has been studied for decades due to the serious effect that these contaminants have on human health. In order to reduce the concentration of arsenic and fluorides within the maximum permissible limits by governmental regulations such as WHO, EPA and NOM-MEX, various adsorbent materials have been investigated. In this research work, bimetallic oxides synthesized by Microwave-assisted hydrothermal synthesis were synthesized and studied. The oxides produced in this doctoral thesis managed to exceed the adsorption capacity reported in the literature (Chapter I and II). However, once the activated carbon was modified with the bimetallic solutions, only one of the oxides was anchored. Therefore, in future works it is necessary to evaluate different methods to achieve bimetallic oxide anchoring.

Another important point to consider is to delve into the anchoring mechanisms of oxyhydroxides on the surface of activated carbon. According to the studies carried out in this thesis, oxygenated groups play an important role in the anchoring of metallic oxyhydroxides. The oxyhydroxides use as nucleation center the oxygens of the oxygenated groups of activated carbon such as carboxylic and phenolic. However, to know in greater detail which of the oxygenated groups tends to bind more easily to metal ions, the X-Ray Absorption spectroscopy techniques as Extended X-Ray Absorption Fine Structure (EXAFS) and X-ray should be considered. Absorption Near Edge Structure (XANES). These techniques. The results of these techniques would help to further support the anchoring mechanisms of oxyhydroxides on the surface of activated carbon.

Evaluate the effect of organic matter and temperature on the adsorption capacity of bimetallic oxides and carbons modified with bimetallic solutions. The effect of organic matter

and coexisting anions should be considered in packed bed columns. In addition, to further evaluate the effect of phosphates on the adsorption capacity of adsorbent materials.

On the other hand, study the anchoring of bimetallic oxides in polymeric supports and natural adsorbent materials in batch and continuous systems. Finally, carry out a pretreatment to activated carbon to increase the acid groups and thus achieve a greater anchoring of oxyhydroxides and a higher density of OH groups. The main reason why a carbon pretreatment must be carried out is to achieve an excellent oxyhydroxide distribution on the carbonaceous matrix.

8.3. Scientific Products

8.3.1. List of publications

Vences-Alvarez, E., Flores-Arciniega, J.L., Flores-Zuñiga, H., Rangel-Mendez, J.R. (2019). Fluoride removal from water by ceramic oxides from cerium and manganese solutions. *Journal of Molecular Liquids*, 286, 110880

Vences-Alvarez, E., Lopez-Valdivieso, A., Cházaro-Ruíz, L.F., Flores-Zuñiga, H., Rangel-Mendez, J.R. (2020). Enhanced arsenic removal from water by a bimetallic material ZrOx-FeOx with high OH density. *Environmental Science and Pollution Research*, 27, 33362–33372

Esmeralda Vences-Alvarez, Cesar Nieto-Delgado, Jose Rene Rangel-Méndez (2020). Chapter 3. Metal Oxyhydroxide Composites for Halogens and Metalloid Removal. *Green Adsorbents to Remove Metals, Dyes and Boron from Polluted Water*. Environ. Chemistry f. Sustainable World, 49, ISBN: 978-3-030-47399-0.

Vences-Alvarez, E., Cházaro-Ruíz, Rangel-Mendez, J.R. (2022). New bimetallic adsorbent material base dan cerium-iron nanoparticles highly selective and affine for arsenic(V). Chosphere, 297,134177.

L.E. Ríos-Saldaña, F. Perez-Rodríguez, **E. Vences Alvarez**, C. Nieto-Delgado, Rangel-Mendez, J.R. (2022). Synthesis af a granular composite base on polyvinyl alcohol-Fe:Ce bimetallic oxide particles for the selective adsorption of As(V) from water. Journal of Water Process Engineering, 48, 102621.

J.R. Rangel Méndez, **E. Vences Alvarez**, F. Perez-Rodríguez, L.E. Ríos-Saldaña. Compuestos bimetálicos basado en Cerio y Fierro y composito polimérico para la remoción de contaminantes del agua. IPICYT. Patente: MX/a/2019/010551.

8.3.2. Attendance to conferences

Nationals:

Carbon Science & Technology in The Fight Against COVID-19. The American Carbon Society. Virtual Conference, 2020.

Oxihidróxidos de La-Zr soportados sobre carbón activado para su aplicación en columnas de lecho empacado para remover As(V) y fluoruros del agua. 3er. Congreso de la Asociación Mexicana de Carbono (AMEXCARB 2019) San Luis Potosí, México, 2019.

Anclaje de oxihidróxidos bimetálicos sobre matrices gráficas para su aplicación en la remoción de arsénico y fluoruros del agua. 3er. Congreso de la Asociación Mexicana de Carbono (AMEXCARB 2019). San Luis Potosí, México, 2019.

VII Congreso Interdisciplinario de Posgrados. San Luis Potosí, México, 2018

Efecto de la sustitución de agua de pozo por agua residual tratada en la capacidad de adsorción de oro en carbón activado. 2do Congreso de la AMEXCarb 2017. San Luis Potosí, México, 2017.

Columnas de lecho empacado (GAC) para la remoción de colorantes del agua. XIV Semana Nacional de Ciencia y Tecnología San Luis Potosí, México, 2017.

V Congreso Interdisciplinario de Posgrado (CONIP). San Luis Potosí, México, 2016

Remoción de fluoruros del agua mediante un adsorbente híbrido: Carbón activado-Lantano. 1er. Congreso de la Asociación Mexicana de Carbono (AMEXCARB 2015). San Luis Potosí, México, 2015.

Internationals:

Materiales híbridos nanoestructurados y multifuncionales como electrodos para celdas solares. Cuarto Taller Latinoamericano del Materiales de Carbono (TLMC4), San Luis Potosí, México, 2021.

Oxihidróxidos bimetálicos anclados en matrices grafiticas para remover arsénico y fluoruros del agua en reactores batch y en continuo. Cuarto Taller Latinoamericano del Materiales de Carbono (TLMC4), San Luis Potosí, México, 2021.

Effect of arsenic on the fluoride removal by a hybrid adsorbent Ce:Mn-carbon. XVI Jornadas Científicas de Instituto Universitario de Materiales. Alicante, España, 2020

Effect of arsenic on the fluoride removal by a hybrid adsorbent Ce:Mn-carbon. 8th International Conference on Carbon for Energy Storage and Environment Protection (CESEP'19). Alicante, España, 2019

Hydrothermal synthesis of a hybrid adsorbent Ce:Mn-Carbon for fluoride removal from water. The World Conference on Carbon (Carbon2019). Lexington, Kentucky, United States, 2019

Material híbrido basado en oxihidróxidos bimetálicos (Ce:Fe)-GAC con capacidad elevada para remover As(V) en agua. Tercer Taller Latinoamericano de Materiales de Carbono (TLMC3). Mención Honorífica. Bogotá, Colombia, 2018.

Novel hybrid material adsorbent based on bimetal oxyhydroxides (Fe:Ce)-GAC for superior As(v) removal. The World Conference on Carbon (Carbon2018). Madrid, España, 2018.

References

- [1] J.C. Soares, A.C. Soares, P.A.R. Pereira, V. da C. Rodrigues, F.M. Shimizu, M.E. Melendez, C.S. Neto, A.L. Carvalho, F.L. Leite, S.A.S. Machado, O.N. Oliveira, Adsorption according to the Langmuir–Freundlich model is the detection mechanism of the antigen p53 for early diagnosis of cancer, *Phys. Chem. Chem. Phys.* 18 (2016) 8412–8418. <https://doi.org/10.1039/C5CP07121F>.
- [2] C. Cárdenas-López, G. Camargo, L. Giraldo, J.C. Moreno-Piraján, Design of an adsorbent employing activated carbon fiber to remove lead, *Eclética Química.* 32 (2007) 61–71. <https://doi.org/10.1590/S0100-46702007000300009>.
- [3] University of Cambridge, DoITPoMS - TLP Library Fuel Cells, *Fuel Cells.* (2019). <https://www.doitpoms.ac.uk/tlplib/fuel-cells/printall.php> (accessed May 13, 2019).
- [4] J.-P. Jolivet, *Metal Oxide Chemistry and Synthesis: From Solution to Solid State*, Edición: 1, Wiley, Chichester ; New York, 2000.
- [5] B.K. Mandal, K.T. Suzuki, Arsenic round the world: a review, *Talanta.* 58 (2002) 201–235. [https://doi.org/10.1016/S0039-9140\(02\)00268-0](https://doi.org/10.1016/S0039-9140(02)00268-0).
- [6] C. Trois, A. Cibati, South African sands as an alternative to zero valent iron for arsenic removal from an industrial effluent: Batch experiments, *Journal of Environmental Chemical Engineering.* 3 (2015) 488–498. <https://doi.org/10.1016/j.jece.2014.12.019>.
- [7] D. Mohan, C.U. Pittman, Arsenic removal from water/wastewater using adsorbents—A critical review, *Journal of Hazardous Materials.* 142 (2007) 1–53. <https://doi.org/10.1016/j.jhazmat.2007.01.006>.
- [8] P.K. DenBesten, Biological mechanisms of dental fluorosis relevant to the use of fluoride supplements, *Community Dent Oral Epidemiol.* 27 (1999) 41–47. <https://doi.org/10.1111/j.1600-0528.1999.tb01990.x>.

- [9] H. Guo, D. Stüben, Z. Berner, Arsenic removal from water using natural iron mineral–quartz sand columns, *Science of The Total Environment*. 377 (2007) 142–151. <https://doi.org/10.1016/j.scitotenv.2007.02.001>.
- [10] G. Ungureanu, S. Santos, R. Boaventura, C. Botelho, Arsenic and antimony in water and wastewater: Overview of removal techniques with special reference to latest advances in adsorption, *Journal of Environmental Management*. 151 (2015) 326–342. <https://doi.org/10.1016/j.jenvman.2014.12.051>.
- [11] T.S.Y. Choong, T.G. Chuah, Y. Robiah, F.L. Gregory Koay, I. Azni, Arsenic toxicity, health hazards and removal techniques from water: an overview, *Desalination*. 217 (2007) 139–166. <https://doi.org/10.1016/j.desal.2007.01.015>.
- [12] E.O. Kartinen, C.J. Martin, An overview of arsenic removal processes, *Desalination*. 103 (1995) 79–88. [https://doi.org/10.1016/0011-9164\(95\)00089-5](https://doi.org/10.1016/0011-9164(95)00089-5).
- [13] M.J. DeMarco, A.K. SenGupta, J.E. Greenleaf, Arsenic removal using a polymeric/inorganic hybrid sorbent, *Water Research*. 37 (2003) 164–176. [https://doi.org/10.1016/S0043-1354\(02\)00238-5](https://doi.org/10.1016/S0043-1354(02)00238-5).
- [14] X. Meng, G.P. Korfiatis, C. Christodoulatos, S. Bang, Treatment of arsenic in Bangladesh well water using a household co-precipitation and filtration system, *Water Research*. 35 (2001) 2805–2810. [https://doi.org/10.1016/S0043-1354\(01\)00007-0](https://doi.org/10.1016/S0043-1354(01)00007-0).
- [15] A.H. Khan, S.B. Rasul, A.K.M. Munir, M. Habibuddowla, M. Alauddin, S.S. Newaz, A. Hussam, Appraisal of a simple arsenic removal method for ground water of Bangladesh, *Journal of Environmental Science and Health, Part A*. 35 (2000) 1021–1041. <https://doi.org/10.1080/10934520009377018>.
- [16] S. Sarkar, L.M. Blaney, A. Gupta, D. Ghosh, A.K. SenGupta, Arsenic Removal from Groundwater and Its Safe Containment in a Rural Environment: Validation of a Sustainable Approach, *Environ. Sci. Technol.* 42 (2008) 4268–4273. <https://doi.org/10.1021/es702556t>.

- [17] M. Gallegos-García, K. Ramírez-Muñiz, S. Song, Arsenic Removal from Water by Adsorption Using Iron Oxide Minerals as Adsorbents: A Review, *Mineral Processing and Extractive Metallurgy Review*. 33 (2012) 301–315. <https://doi.org/10.1080/08827508.2011.584219>.
- [18] K.B. Payne, T.M. Abdel-Fattah, Adsorption of Arsenate and Arsenite by Iron-Treated Activated Carbon and Zeolites: Effects of pH, Temperature, and Ionic Strength, *Journal of Environmental Science and Health, Part A*. 40 (2005) 723–749. <https://doi.org/10.1081/ESE-200048254>.
- [19] D.B. Singh, G. Prasad, D.C. Rupainwar, Adsorption technique for the treatment of As(V)-rich effluents, *Colloids and Surfaces A: Physicochemical and Engineering Aspects*. 111 (1996) 49–56. [https://doi.org/10.1016/0927-7757\(95\)03468-4](https://doi.org/10.1016/0927-7757(95)03468-4).
- [20] J.A. Arcibar-Orozco, D.-B. Josue, J.C. Rios-Hurtado, J.R. Rangel-Mendez, Influence of iron content, surface area and charge distribution in the arsenic removal by activated carbons, *Chemical Engineering Journal*. 249 (2014) 201–209. <https://doi.org/10.1016/j.cej.2014.03.096>.
- [21] L.H. Velazquez-Jimenez, R.H. Hurt, J. Matos, J.R. Rangel-Mendez, Zirconium–Carbon Hybrid Sorbent for Removal of Fluoride from Water: Oxalic Acid Mediated Zr(IV) Assembly and Adsorption Mechanism, *Environ. Sci. Technol.* 48 (2014) 1166–1174. <https://doi.org/10.1021/es403929b>.
- [22] S. Mandal, T. Padhi, R.K. Patel, Studies on the removal of arsenic (III) from water by a novel hybrid material, *Journal of Hazardous Materials*. 192 (2011) 899–908. <https://doi.org/10.1016/j.jhazmat.2011.05.099>.
- [23] J.S. Yamani, S.M. Miller, M.L. Spaulding, J.B. Zimmerman, Enhanced arsenic removal using mixed metal oxide impregnated chitosan beads, *Water Research*. 46 (2012) 4427–4434. <https://doi.org/10.1016/j.watres.2012.06.004>.

- [24] W. Xu, J. Wang, L. Wang, G. Sheng, J. Liu, H. Yu, X.-J. Huang, Enhanced arsenic removal from water by hierarchically porous CeO₂-ZrO₂ nanospheres: Role of surface- and structure-dependent properties, *Journal of Hazardous Materials*. 260 (2013) 498–507. <https://doi.org/10.1016/j.jhazmat.2013.06.010>.
- [25] S.C. Peters, J.D. Blum, The source and transport of arsenic in a bedrock aquifer, New Hampshire, USA, *Applied Geochemistry*. 18 (2003) 1773–1787. [https://doi.org/10.1016/S0883-2927\(03\)00109-4](https://doi.org/10.1016/S0883-2927(03)00109-4).
- [26] V. Saxena, S. Ahmed, Dissolution of fluoride in groundwater: a water-rock interaction study, *Env Geol*. 40 (2001) 1084–1087. <https://doi.org/10.1007/s002540100290>.
- [27] J.F. Paulino, R. Neumann, J.C. Afonso, J.F. Paulino, R. Neumann, J.C. Afonso, Evaluation of cryolite from pitinga (Amazonas-Brazil) as a source of hydrogen fluoride, *Química Nova*. 39 (2016) 496–501. <https://doi.org/10.5935/0100-4042.20160049>.
- [28] C.F. Harvey, C.H. Swartz, A.B.M. Badruzzaman, N. Keon-Blute, W. Yu, M.A. Ali, J. Jay, R. Beckie, V. Niedan, D. Brabander, P.M. Oates, K.N. Ashfaque, S. Islam, H.F. Hemond, M.F. Ahmed, Arsenic Mobility and Groundwater Extraction in Bangladesh, *Science*. 298 (2002) 1602–1606. <https://doi.org/10.1126/science.1076978>.
- [29] D.K. Nordstrom, Worldwide Occurrences of Arsenic in Ground Water, *Science*. 296 (2002) 2143–2145. <https://doi.org/10.1126/science.1072375>.
- [30] R. Nickson, J. McArthur, W. Burgess, K.M. Ahmed, P. Ravenscroft, M. Rahman, Arsenic poisoning of Bangladesh groundwater, *Nature*. 395 (1998) 338–338. <https://doi.org/10.1038/26387>.
- [31] A.H. Smith, E.O. Lingas, M. Rahman, Contamination of drinking-water by arsenic in Bangladesh : a public health emergency, *Bolletín of the WHO*. (2000) 1093–1103.
- [32] U.K. Chowdhury, B.K. Biswas, T.R. Chowdhury, G. Samanta, B.K. Mandal, G.C. Basu, C.R. Chanda, D. Lodh, K.C. Saha, S.K. Mukherjee, S. Roy, S. Kabir, Q.

- Quamruzzaman, D. Chakraborti, Groundwater arsenic contamination in Bangladesh and West Bengal, India., *Environ Health Perspect.* 108 (2000) 393–397.
- [33] H.T. Hanh, K.-W. Kim, S. Bang, N.M. Hoa, Community exposure to arsenic in the Mekong river delta, Southern Vietnam, *J. Environ. Monit.* 13 (2011) 2025–2032. <https://doi.org/10.1039/C1EM10037H>.
- [34] V.N. Bashkin, K. Wongyai, Environmental fluxes of arsenic from lignite mining and power generation in northern Thailand, *Env Geol.* 41 (2002) 883–888. <https://doi.org/10.1007/s002540100404>.
- [35] T.S. Singh, K.K. Pant, Equilibrium, kinetics and thermodynamic studies for adsorption of As(III) on activated alumina, *Separation and Purification Technology.* 36 (2004) 139–147. [https://doi.org/10.1016/S1383-5866\(03\)00209-0](https://doi.org/10.1016/S1383-5866(03)00209-0).
- [36] S. Kundu, A.K. Gupta, Analysis and modeling of fixed bed column operations on As(V) removal by adsorption onto iron oxide-coated cement (IOCC), *Journal of Colloid and Interface Science.* 290 (2005) 52–60. <https://doi.org/10.1016/j.jcis.2005.04.006>.
- [37] S. Song, A. Lopez-Valdivieso, D.J. Hernandez-Campos, C. Peng, M.G. Monroy-Fernandez, I. Razo-Soto, Arsenic removal from high-arsenic water by enhanced coagulation with ferric ions and coarse calcite, *Water Research.* 40 (2006) 364–372. <https://doi.org/10.1016/j.watres.2005.09.046>.
- [38] S. Song, M. Gallegos-Garcia, Chapter 11 - Arsenic Removal from Water by the Coagulation Process, in: M. Fanun (Ed.), *The Role of Colloidal Systems in Environmental Protection*, Elsevier, Amsterdam, 2014: pp. 261–277. <https://doi.org/10.1016/B978-0-444-63283-8.00011-9>.
- [39] R.Y. Ning, Arsenic removal by reverse osmosis, *Desalination.* 143 (2002) 237–241. [https://doi.org/10.1016/S0011-9164\(02\)00262-X](https://doi.org/10.1016/S0011-9164(02)00262-X).

- [40] A. Abejón, A. Garea, A. Irabien, Arsenic removal from drinking water by reverse osmosis: Minimization of costs and energy consumption, *Separation and Purification Technology*. 144 (2015) 46–53. <https://doi.org/10.1016/j.seppur.2015.02.017>.
- [41] M.-C. Shih, An overview of arsenic removal by pressure-driven membrane processes, *Desalination*. 172 (2005) 85–97. <https://doi.org/10.1016/j.desal.2004.07.031>.
- [42] D. Pokhrel, T. Viraraghavan, Arsenic removal from an aqueous solution by a modified fungal biomass, *Water Research*. 40 (2006) 549–552. <https://doi.org/10.1016/j.watres.2005.11.040>.
- [43] J.C. Crittenden, Montgomery Watson Harza (Firm), *Water treatment principles and design*, J. Wiley, Hoboken, N.J., 2005.
- [44] Y.S. Ho, G. McKay, Sorption of dyes and copper ions onto biosorbents, *Process Biochemistry*. 38 (2003) 1047–1061. [https://doi.org/10.1016/S0032-9592\(02\)00239-X](https://doi.org/10.1016/S0032-9592(02)00239-X).
- [45] A.S. Franca, L.S. Oliveira, A.A. Nunes, C.C.O. Alves, Microwave assisted thermal treatment of defective coffee beans press cake for the production of adsorbents, *Bioresource Technology*. 101 (2010) 1068–1074. <https://doi.org/10.1016/j.biortech.2009.08.102>.
- [46] M. Doğan, H. Abak, M. Alkan, Biosorption of Methylene Blue from Aqueous Solutions by Hazelnut Shells: Equilibrium, Parameters and Isotherms, *Water Air Soil Pollut.* 192 (2008) 141–153. <https://doi.org/10.1007/s11270-008-9641-z>.
- [47] Md.T. Uddin, Md.A. Islam, S. Mahmud, Md. Rukanuzzaman, Adsorptive removal of methylene blue by tea waste, *Journal of Hazardous Materials*. 164 (2009) 53–60. <https://doi.org/10.1016/j.jhazmat.2008.07.131>.
- [48] Wade, *Química Organica Volumen 2*, n.d.
- [49] W.J. Thomas, B.D. Crittenden, *Adsorption Technology & Design*, n.d.

- [50] D. Dzombak, F.M.M. Morel, Adsorption of Inorganic Pollutants in Aquatic Systems, in: 1987. [https://doi.org/10.1061/\(ASCE\)0733-9429\(1987\)113:4\(430\)](https://doi.org/10.1061/(ASCE)0733-9429(1987)113:4(430)).
- [51] M.T. Beck, Chemistry of the outer-sphere complexes, *Coordination Chemistry Reviews*. 3 (1968) 91–115. [https://doi.org/10.1016/S0010-8545\(00\)80106-X](https://doi.org/10.1016/S0010-8545(00)80106-X).
- [52] J.C. Crittenden, R.R. Trussell, D.W. Hand, K.J. Howe, G. Tchobanoglous, *Mwh's Water Treatment: Principles and Design, Third*, MWH, 2012.
- [53] R.M. Cornell, U. Schwertmann, *The Iron Oxides: Structure, Properties, Reactions, Occurrences and Uses*, John Wiley & Sons, 2006.
- [54] W. Stumm, The Inner-Sphere Surface Complex, in: *Aquatic Chemistry*, American Chemical Society, 1995: pp. 1–32. <https://doi.org/10.1021/ba-1995-0244.ch001>.
- [55] J.-P. Jolivet, *Metal Oxide Chemistry and Synthesis: From Solution to Solid State*, n.d.
- [56] R. Burt, G. Birkett, X.S. Zhao, A review of molecular modelling of electric double layer capacitors, *Phys. Chem. Chem. Phys.* 16 (2014) 6519–6538. <https://doi.org/10.1039/C3CP55186E>.
- [57] A.E. Westwell, E.W. Anacker, Adsorption of Cetylpyridinium Chloride on Glass, *J. Phys. Chem.* 63 (1959) 1022–1024. <https://doi.org/10.1021/j150576a610>.
- [58] R.C. Bansal, M. Goyal, *Activated Carbon Adsorption*, CRC Press, 2005. <https://doi.org/10.1201/9781420028812>.
- [59] B. Likozar, D. Senica, A. Pavko, Comparison of adsorption equilibrium and kinetic models for a case study of pharmaceutical active ingredient adsorption from fermentation broths: parameter determination, simulation, sensitivity analysis and optimization, *Brazilian Journal of Chemical Engineering*. 29 (2012) 635–652. <https://doi.org/10.1590/S0104-66322012000300020>.
- [60] R.B. Garcia-Reyes, J.R. Rangel-Mendez, Adsorption kinetics of chromium(III) ions on agro-waste materials, *Bioresource Technology*. 101 (2010) 8099–8108. <https://doi.org/10.1016/j.biortech.2010.06.020>.

- [61] N. Ammavasi, R. Mariappan, Enhanced removal of hazardous fluoride from drinking water by using a smart material: Magnetic iron oxide fabricated layered double hydroxide/cellulose composite, *Journal of Environmental Chemical Engineering*. 6 (2018) 5645–5654. <https://doi.org/10.1016/j.jece.2018.08.071>.
- [62] T.K. Das, T.S. Sakthivel, A. Jeyaranjan, S. Seal, A.N. Bezbaruah, Ultra-high arsenic adsorption by graphene oxide iron nanohybrid: Removal mechanisms and potential applications, *Chemosphere*. 253 (2020) 126702. <https://doi.org/10.1016/j.chemosphere.2020.126702>.
- [63] M. Kumar, A.M. Isloor, T. Somasekhara Rao, A.F. Ismail, R. Farnood, P.M.G. Nambissan, Removal of toxic arsenic from aqueous media using polyphenylsulfone/cellulose acetate hollow fiber membranes containing zirconium oxide, *Chemical Engineering Journal*. 393 (2020) 124367. <https://doi.org/10.1016/j.cej.2020.124367>.
- [64] Y. Gan, X. Wang, L. Zhang, B. Wu, G. Zhang, S. Zhang, Coagulation removal of fluoride by zirconium tetrachloride: Performance evaluation and mechanism analysis, *Chemosphere*. 218 (2019) 860–868. <https://doi.org/10.1016/j.chemosphere.2018.11.192>.
- [65] L.P. Lingamdinne, J.R. Koduru, Y.-Y. Chang, S.-H. Kang, J.-K. Yang, Facile synthesis of flowered mesoporous graphene oxide-lanthanum fluoride nanocomposite for adsorptive removal of arsenic, *Journal of Molecular Liquids*. 279 (2019) 32–42. <https://doi.org/10.1016/j.molliq.2019.01.103>.
- [66] S. Sahu, L. Mallik, S. Pahi, B. Barik, U.K. Sahu, M. Sillanpää, R.K. Patel, Facile synthesis of poly o-toluidine modified lanthanum phosphate nanocomposite as a superior adsorbent for selective fluoride removal: A mechanistic and kinetic study, *Chemosphere*. 252 (2020) 126551. <https://doi.org/10.1016/j.chemosphere.2020.126551>.

- [67] R. Li, Q. Li, S. Gao, J.K. Shang, Exceptional arsenic adsorption performance of hydrous cerium oxide nanoparticles: Part A. Adsorption capacity and mechanism, *Chemical Engineering Journal*. 185–186 (2012) 127–135. <https://doi.org/10.1016/j.cej.2012.01.061>.
- [68] H. Deng, X. Yu, Adsorption of fluoride, arsenate and phosphate in aqueous solution by cerium impregnated fibrous protein, *Chemical Engineering Journal*. 184 (2012) 205–212. <https://doi.org/10.1016/j.cej.2012.01.031>.
- [69] T. Mishra, D.K. Mahato, A comparative study on enhanced arsenic(V) and arsenic(III) removal by iron oxide and manganese oxide pillared clays from ground water, *Journal of Environmental Chemical Engineering*. 4 (2016) 1224–1230. <https://doi.org/10.1016/j.jece.2016.01.022>.
- [70] A.V. Vitela-Rodriguez, J.R. Rangel-Mendez, Arsenic removal by modified activated carbons with iron hydro(oxide) nanoparticles, *Journal of Environmental Management*. 114 (2013) 225–231. <https://doi.org/10.1016/j.jenvman.2012.10.004>.
- [71] Z. Wen, J. Lu, Y. Zhang, G. Cheng, S. Huang, J. Chen, R. Xu, Y. Ming, Y. Wang, R. Chen, Facile inverse micelle fabrication of magnetic ordered mesoporous iron cerium bimetal oxides with excellent performance for arsenic removal from water, *Journal of Hazardous Materials*. 383 (2020) 121172. <https://doi.org/10.1016/j.jhazmat.2019.121172>.
- [72] E. Vences-Alvarez, J.L. Flores-Arciniega, H. Flores-Zuñiga, J.R. Rangel-Mendez, Fluoride removal from water by ceramic oxides from cerium and manganese solutions, *Journal of Molecular Liquids*. 286 (2019) 110880. <https://doi.org/10.1016/j.molliq.2019.110880>.
- [73] H. Marsh, F.R. Reinoso, *Activated Carbon*, Elsevier Science, 2006.

- [74] T.J. Bandoz, C.O. Ania, Chapter 4 Surface chemistry of activated carbons and its characterization, in: T.J. Bandoz (Ed.), *Interface Science and Technology*, Elsevier, 2006: pp. 159–229. [https://doi.org/10.1016/S1573-4285\(06\)80013-X](https://doi.org/10.1016/S1573-4285(06)80013-X).
- [75] M.M. Dubinin, The Potential Theory of Adsorption of Gases and Vapors for Adsorbents with Energetically Nonuniform Surfaces., *Chem. Rev.* 60 (1960) 235–241. <https://doi.org/10.1021/cr60204a006>.
- [76] B.D. Zdravkov, J.J. Čermák, M. Šefara, J. Janků, Pore classification in the characterization of porous materials: A perspective, *Cent.Eur.j.Chem.* 5 (2007) 385–395. <https://doi.org/10.2478/s11532-007-0017-9>.
- [77] D.R. Askeland, W.J. Wright, *Ciencia E Ingeniería de Los Materiales*, CENGAGE Learning, 2016.
- [78] C.B. Carter, M.G. Norton, *Ceramic Materials: Science and Engineering*, 2nd ed., Springer-Verlag, New York, 2013. <https://doi.org/10.1007/978-1-4614-3523-5>.
- [79] K. Hristovski, A. Baumgardner, P. Westerhoff, Selecting metal oxide nanomaterials for arsenic removal in fixed bed columns: From nanopowders to aggregated nanoparticle media, *Journal of Hazardous Materials.* 147 (2007) 265–274. <https://doi.org/10.1016/j.jhazmat.2007.01.017>.
- [80] E. Vences-Alvarez, L.H. Velazquez-Jimenez, L.F. Chazaro-Ruiz, P.E. Diaz-Flores, J.R. Rangel-Mendez, Fluoride removal in water by a hybrid adsorbent lanthanum–carbon, *Journal of Colloid and Interface Science.* 455 (2015) 194–202. <https://doi.org/10.1016/j.jcis.2015.05.048>.
- [81] S.M. Maliyekkal, A.K. Sharma, L. Philip, Manganese-oxide-coated alumina: A promising sorbent for defluoridation of water, *Water Research.* 40 (2006) 3497–3506. <https://doi.org/10.1016/j.watres.2006.08.007>.

- [82] V. Tomar, D. Kumar, A critical study on efficiency of different materials for fluoride removal from aqueous media, *Chemistry Central Journal*. 7 (2013) 51. <https://doi.org/10.1186/1752-153X-7-51>.
- [83] A. Bhatnagar, E. Kumar, M. Sillanpää, Fluoride removal from water by adsorption—A review, *Chemical Engineering Journal*. 171 (2011) 811–840. <https://doi.org/10.1016/j.cej.2011.05.028>.
- [84] B. Chen, Z. Zhu, Y. Guo, Y. Qiu, J. Zhao, Facile synthesis of mesoporous Ce–Fe bimetal oxide and its enhanced adsorption of arsenate from aqueous solutions, *Journal of Colloid and Interface Science*. 398 (2013) 142–151. <https://doi.org/10.1016/j.jcis.2013.02.004>.
- [85] H. Liu, S. Deng, Z. Li, G. Yu, J. Huang, Preparation of Al–Ce hybrid adsorbent and its application for defluoridation of drinking water, *Journal of Hazardous Materials*. 179 (2010) 424–430. <https://doi.org/10.1016/j.jhazmat.2010.03.021>.
- [86] C.M. Babu, R. Vinodh, B. Sundaravel, A. Abidov, M.M. Peng, W.S. Cha, H.-T. Jang, Characterization of reduced graphene oxide supported mesoporous Fe₂O₃/TiO₂ nanoparticles and adsorption of As(III) and As(V) from potable water, *Journal of the Taiwan Institute of Chemical Engineers*. 62 (2016) 199–208. <https://doi.org/10.1016/j.jtice.2016.02.005>.
- [87] J. Zhu, S.A. Baig, T. Sheng, Z. Lou, Z. Wang, X. Xu, Fe₃O₄ and MnO₂ assembled on honeycomb briquette cinders (HBC) for arsenic removal from aqueous solutions, *Journal of Hazardous Materials*. 286 (2015) 220–228. <https://doi.org/10.1016/j.jhazmat.2015.01.004>.
- [88] G. Zhang, Z. Ren, X. Zhang, J. Chen, Nanostructured iron(III)-copper(II) binary oxide: A novel adsorbent for enhanced arsenic removal from aqueous solutions, *Water Research*. 47 (2013) 4022–4031. <https://doi.org/10.1016/j.watres.2012.11.059>.

- [89] T. Basu, U.C. Ghosh, Nano-structured iron(III)–cerium(IV) mixed oxide: Synthesis, characterization and arsenic sorption kinetics in the presence of co-existing ions aiming to apply for high arsenic groundwater treatment, *Applied Surface Science*. 283 (2013) 471–481. <https://doi.org/10.1016/j.apsusc.2013.06.132>.
- [90] W. Xu, J. Wang, L. Wang, G. Sheng, J. Liu, H. Yu, X.-J. Huang, Enhanced arsenic removal from water by hierarchically porous CeO₂–ZrO₂ nanospheres: Role of surface- and structure-dependent properties, *Journal of Hazardous Materials*. 260 (2013) 498–507. <https://doi.org/10.1016/j.jhazmat.2013.06.010>.
- [91] K. Wu, T. Liu, W. Xue, X. Wang, Arsenic(III) oxidation/adsorption behaviors on a new bimetal adsorbent of Mn-oxide-doped Al oxide, *Chemical Engineering Journal*. 192 (2012) 343–349. <https://doi.org/10.1016/j.cej.2012.03.058>.
- [92] Z. Ren, G. Zhang, J. Paul Chen, Adsorptive removal of arsenic from water by an iron–zirconium binary oxide adsorbent, *Journal of Colloid and Interface Science*. 358 (2011) 230–237. <https://doi.org/10.1016/j.jcis.2011.01.013>.
- [93] S. Deng, Z. Li, J. Huang, G. Yu, Preparation, characterization and application of a Ce–Ti oxide adsorbent for enhanced removal of arsenate from water, *Journal of Hazardous Materials*. 179 (2010) 1014–1021. <https://doi.org/10.1016/j.jhazmat.2010.03.106>.
- [94] S. Deng, Z. Li, J. Huang, G. Yu, Preparation, characterization and application of a Ce–Ti oxide adsorbent for enhanced removal of arsenate from water, *Journal of Hazardous Materials*. 179 (2010) 1014–1021. <https://doi.org/10.1016/j.jhazmat.2010.03.106>.
- [95] T. Zhang, Q. Li, H. Xiao, H. Lu, Y. Zhou, Synthesis of Li–Al Layered Double Hydroxides (LDHs) for Efficient Fluoride Removal, *Ind. Eng. Chem. Res.* 51 (2012) 11490–11498. <https://doi.org/10.1021/ie300863x>.

- [96] D. Tang, G. Zhang, Efficient removal of fluoride by hierarchical Ce–Fe bimetal oxides adsorbent: Thermodynamics, kinetics and mechanism, *Chemical Engineering Journal*. 283 (2016) 721–729. <https://doi.org/10.1016/j.cej.2015.08.019>.
- [97] A. Ghosh, S. Chakrabarti, K. Biswas, U.C. Ghosh, Agglomerated nanoparticles of hydrous Ce(IV)+Zr(IV) mixed oxide: Preparation, characterization and physicochemical aspects on fluoride adsorption, *Applied Surface Science*. 307 (2014) 665–676. <https://doi.org/10.1016/j.apsusc.2014.04.095>.
- [98] S. Deng, H. Liu, W. Zhou, J. Huang, G. Yu, Mn–Ce oxide as a high-capacity adsorbent for fluoride removal from water, *Journal of Hazardous Materials*. 186 (2011) 1360–1366. <https://doi.org/10.1016/j.jhazmat.2010.12.024>.
- [99] X. Zhao, J. Wang, F. Wu, T. Wang, Y. Cai, Y. Shi, G. Jiang, Removal of fluoride from aqueous media by Fe₃O₄@Al(OH)₃ magnetic nanoparticles, *Journal of Hazardous Materials*. 173 (2010) 102–109. <https://doi.org/10.1016/j.jhazmat.2009.08.054>.
- [100] X. Zhao, J. Wang, F. Wu, T. Wang, Y. Cai, Y. Shi, G. Jiang, Removal of fluoride from aqueous media by Fe₃O₄@Al(OH)₃ magnetic nanoparticles, *Journal of Hazardous Materials*. 173 (2010) 102–109. <https://doi.org/10.1016/j.jhazmat.2009.08.054>.
- [101] K. Biswas, D. Bandhoyapadhyay, U.C. Ghosh, Adsorption kinetics of fluoride on iron(III)-zirconium(IV) hybrid oxide, *Adsorption*. 13 (2007) 83–94. <https://doi.org/10.1007/s10450-007-9000-1>.
- [102] A.M. Cooper, K.D. Hristovski, T. Möller, P. Westerhoff, P. Sylvester, The effect of carbon type on arsenic and trichloroethylene removal capabilities of iron (hydr)oxide nanoparticle-impregnated granulated activated carbons, *Journal of Hazardous Materials*. 183 (2010) 381–388. <https://doi.org/10.1016/j.jhazmat.2010.07.036>.
- [103] G. Muñiz, V. Fierro, A. Celzard, G. Furdin, G. Gonzalez-Sánchez, M.L. Ballinas, Synthesis, characterization and performance in arsenic removal of iron-doped activated carbons prepared by impregnation with Fe(III) and Fe(II), *Journal of*

- Hazardous Materials. 165 (2009) 893–902.
<https://doi.org/10.1016/j.jhazmat.2008.10.074>.
- [104] R. Sandoval, A.M. Cooper, K. Aymar, A. Jain, K. Hristovski, Removal of arsenic and methylene blue from water by granular activated carbon media impregnated with zirconium dioxide nanoparticles, *Journal of Hazardous Materials*. 193 (2011) 296–303. <https://doi.org/10.1016/j.jhazmat.2011.07.061>.
- [105] Y. Li, Q. Du, J. Wang, T. Liu, J. Sun, Y. Wang, Z. Wang, Y. Xia, L. Xia, Defluoridation from aqueous solution by manganese oxide coated graphene oxide, *Journal of Fluorine Chemistry*. 148 (2013) 67–73.
<https://doi.org/10.1016/j.jfluchem.2013.01.028>.
- [106] E. Tchomgui-Kamga, V. Alonzo, C.P. Nanseu-Njiki, N. Audebrand, E. Ngameni, A. Darchen, Preparation and characterization of charcoals that contain dispersed aluminum oxide as adsorbents for removal of fluoride from drinking water, *Carbon*. 48 (2010) 333–343. <https://doi.org/10.1016/j.carbon.2009.09.034>.
- [107] C.Y. Yin, M.K. Aroua, W.M.A.W. Daud, Review of modifications of activated carbon for enhancing contaminant uptakes from aqueous solutions, *Separation and Purification Technology*. 52 (2007) 403–415.
<https://doi.org/10.1016/j.seppur.2006.06.009>.
- [108] M. Hua, S. Zhang, B. Pan, W. Zhang, L. Lv, Q. Zhang, Heavy metal removal from water/wastewater by nanosized metal oxides: A review, *Journal of Hazardous Materials*. 211–212 (2012) 317–331. <https://doi.org/10.1016/j.jhazmat.2011.10.016>.
- [109] E. Deliyanni, T.J. Bandoz, Importance of carbon surface chemistry in development of iron–carbon composite adsorbents for arsenate removal, *Journal of Hazardous Materials*. 186 (2011) 667–674. <https://doi.org/10.1016/j.jhazmat.2010.11.055>.
- [110] V. Fierro, G. Muñoz, G. Gonzalez-Sánchez, M.L. Ballinas, A. Celzard, Arsenic removal by iron-doped activated carbons prepared by ferric chloride forced hydrolysis, *Journal*

- of Hazardous Materials. 168 (2009) 430–437.
<https://doi.org/10.1016/j.jhazmat.2009.02.055>.
- [111] C.P. Huang, L.M. Vane, Enhancing As^{5+} Removal by a Fe^{2+} -Treated Activated Carbon, Research Journal of the Water Pollution Control Federation. 61 (1989) 1596–1603.
- [112] P. Mondal, C. Balomajumder, B. Mohanty, A laboratory study for the treatment of arsenic, iron, and manganese bearing ground water using Fe^{3+} impregnated activated carbon: Effects of shaking time, pH and temperature, Journal of Hazardous Materials. 144 (2007) 420–426. <https://doi.org/10.1016/j.jhazmat.2006.10.078>.
- [113] W. Chen, R. Parette, J. Zou, F.S. Cannon, B.A. Dempsey, Arsenic removal by iron-modified activated carbon, Water Res. 41 (2007) 1851–1858.
<https://doi.org/10.1016/j.watres.2007.01.052>.
- [114] G. Ghanizadeh, M. Ehrampoush, M. Ghaneian, Application of iron impregnated activated carbon for removal of arsenic from water, Journal of Environmental Health Science & Engineering. 7 (2010) 145–156.
- [115] M.C. Román-Martínez, D. Cazorla-Amorós, A. Linares-Solano, C.S.-M. De Lecea, H. Yamashita, M. Anpo, Metal-support interaction in Pt/C catalysts. Influence of the support surface chemistry and the metal precursor, Carbon. 33 (1995) 3–13.
[https://doi.org/10.1016/0008-6223\(94\)00096-I](https://doi.org/10.1016/0008-6223(94)00096-I).
- [116] M.E. Sigrist, L. Brusa, H.R. Beldomenico, L. Dosso, O.M. Tsendra, M.B. González, C.L. Pieck, C.R. Vera, Influence of the iron content on the arsenic adsorption capacity of Fe/GAC adsorbents, Journal of Environmental Chemical Engineering. 2 (2014) 927–934. <https://doi.org/10.1016/j.jece.2014.02.013>.
- [117] M. Yoshimura, K.-S. Han, W. Suchanek, ‘Soft solution processing’ in situ fabrication of morphology-controlled advanced ceramic materials in low temperature solutions

- without firing, *Bull Mater Sci.* 22 (1999) 193–199.
<https://doi.org/10.1007/BF02749919>.
- [118] M. Yoshimura, K. Byrappa, Hydrothermal processing of materials: past, present and future, *J Mater Sci.* 43 (2008) 2085–2103. <https://doi.org/10.1007/s10853-007-1853-x>.
- [119] S. Komarneni, Nanophase materials by hydrothermal, microwave-hydrothermal and microwave-solvothermal methods, *Current Science.* 85 (2003) 1730–1734.
- [120] J.O. Eckert, C.C. Hung-Houston, B.L. Gersten, M.M. Lencka, R.E. Riman, Kinetics and Mechanisms of Hydrothermal Synthesis of Barium Titanate, *Journal of the American Ceramic Society.* 79 (1996) 2929–2939. <https://doi.org/10.1111/j.1151-2916.1996.tb08728.x>.
- [121] W.L. Suchanek, R.E. Riman, Hydrothermal Synthesis of Advanced Ceramic Powders, *Advances in Science and Technology.* 45 (2006) 184–193.
<https://doi.org/10.4028/www.scientific.net/AST.45.184>.
- [122] X. Li, C. Ni, C. Yao, Z. Chen, Development of attapulgite/Ce_{1-x}Zr_xO₂ nanocomposite as catalyst for the degradation of methylene blue, *Applied Catalysis B: Environmental.* 117–118 (2012) 118–124. <https://doi.org/10.1016/j.apcatb.2012.01.008>.
- [123] B.K. Biswas, J. Inoue, K. Inoue, K.N. Ghimire, H. Harada, K. Ohto, H. Kawakita, Adsorptive removal of As(V) and As(III) from water by a Zr(IV)-loaded orange waste gel, *Journal of Hazardous Materials.* 154 (2008) 1066–1074.
<https://doi.org/10.1016/j.jhazmat.2007.11.030>.
- [124] L. Chen, K. Zhang, J. He, X.-G. Cai, W. Xu, J.-H. Liu, Performance and mechanism of hierarchically porous Ce–Zr oxide nanospheres encapsulated calcium alginate beads for fluoride removal from water, *RSC Adv.* 6 (2016) 36296–36306.
<https://doi.org/10.1039/C6RA01337F>.

- [125] S.-W. Cao, Y.-J. Zhu, Iron oxide hollow spheres: Microwave–hydrothermal ionic liquid preparation, formation mechanism, crystal phase and morphology control and properties, *Acta Materialia*. 57 (2009) 2154–2165. <https://doi.org/10.1016/j.actamat.2009.01.009>.
- [126] S.R. Dhage, Y.B. Kholam, H.S. Potdar, S.B. Deshpande, P.P. Bakare, S.R. Sainkar, S.K. Date, Effect of variation of molar ratio (pH) on the crystallization of iron oxide phases in microwave hydrothermal synthesis, *Materials Letters*. 57 (2002) 457–462. [https://doi.org/10.1016/S0167-577X\(02\)00811-X](https://doi.org/10.1016/S0167-577X(02)00811-X).
- [127] A. Yürüm, Z.Ö. Kocabaş-Ataklı, M. Sezen, R. Semiat, Y. Yürüm, Fast deposition of porous iron oxide on activated carbon by microwave heating and arsenic (V) removal from water, *Chemical Engineering Journal*. 242 (2014) 321–332. <https://doi.org/10.1016/j.cej.2014.01.005>.
- [128] M. Berg, H.C. Tran, T.C. Nguyen, H.V. Pham, R. Schertenleib, W. Giger, Arsenic Contamination of Groundwater and Drinking Water in Vietnam: A Human Health Threat, *Environ. Sci. Technol.* 35 (2001) 2621–2626. <https://doi.org/10.1021/es010027y>.
- [129] B.K. Mandal, K.T. Suzuki, Arsenic round the world: a review, *Talanta*. 58 (2002) 201–235. [https://doi.org/10.1016/S0039-9140\(02\)00268-0](https://doi.org/10.1016/S0039-9140(02)00268-0).
- [130] P.L. Smedley, H.B. Nicolli, D.M.J. Macdonald, A.J. Barros, J.O. Tullio, Hydrogeochemistry of arsenic and other inorganic constituents in groundwaters from La Pampa, Argentina, *Applied Geochemistry*. 17 (2002) 259–284. [https://doi.org/10.1016/S0883-2927\(01\)00082-8](https://doi.org/10.1016/S0883-2927(01)00082-8).
- [131] M.F. Hossain, Arsenic contamination in Bangladesh—An overview, *Agriculture, Ecosystems & Environment*. 113 (2006) 1–16. <https://doi.org/10.1016/j.agee.2005.08.034>.

- [132] S.-H. Kim, K. Kim, K.-S. Ko, Y. Kim, K.-S. Lee, Co-contamination of arsenic and fluoride in the groundwater of unconsolidated aquifers under reducing environments, *Chemosphere*. 87 (2012) 851–856. <https://doi.org/10.1016/j.chemosphere.2012.01.025>.
- [133] S.C. Peters, J.D. Blum, The source and transport of arsenic in a bedrock aquifer, New Hampshire, USA, *Applied Geochemistry*. 18 (2003) 1773–1787. [https://doi.org/10.1016/S0883-2927\(03\)00109-4](https://doi.org/10.1016/S0883-2927(03)00109-4).
- [134] C. Jing, J. Cui, Y. Huang, A. Li, Fabrication, Characterization, and Application of a Composite Adsorbent for Simultaneous Removal of Arsenic and Fluoride, *ACS Appl. Mater. Interfaces*. 4 (2012) 714–720. <https://doi.org/10.1021/am2013322>.
- [135] M. Streat, K. Hellgardt, N.L.R. Newton, Hydrous ferric oxide as an adsorbent in water treatment: Part 2. Adsorption studies, *Process Safety and Environmental Protection*. 86 (2008) 11–20. <https://doi.org/10.1016/j.psep.2007.10.008>.
- [136] T.S.Y. Choong, T.G. Chuah, Y. Robiah, F.L. Gregory Koay, I. Azni, Arsenic toxicity, health hazards and removal techniques from water: an overview, *Desalination*. 217 (2007) 139–166. <https://doi.org/10.1016/j.desal.2007.01.015>.
- [137] C. Ferreccio, C. González, V. Milosavljevic, G. Marshall, A. Sancha, A. Smith, Lung Cancer and Arsenic Concentrations in Drinking Water in Chile, *Epidemiology*. 11 (2000) 673–679.
- [138] B. Han, T. Runnells, J. Zimbron, R. Wickramasinghe, Arsenic removal from drinking water by flocculation and microfiltration, *Desalination*. 145 (2002) 293–298. [https://doi.org/10.1016/S0011-9164\(02\)00425-3](https://doi.org/10.1016/S0011-9164(02)00425-3).
- [139] M.F. Hughes, Arsenic toxicity and potential mechanisms of action, *Toxicology Letters*. 133 (2002) 1–16. [https://doi.org/10.1016/S0378-4274\(02\)00084-X](https://doi.org/10.1016/S0378-4274(02)00084-X).
- [140] M. Kumar, A. Puri, A review of permissible limits of drinking water, *Indian J Occup Environ Med*. 16 (2012) 40–44. <https://doi.org/10.4103/0019-5278.99696>.

- [141] S.V. Jadhav, E. Bringas, G.D. Yadav, V.K. Rathod, I. Ortiz, K.V. Marathe, Arsenic and fluoride contaminated groundwaters: A review of current technologies for contaminants removal, *Journal of Environmental Management*. 162 (2015) 306–325. <https://doi.org/10.1016/j.jenvman.2015.07.020>.
- [142] E. Vences-Alvarez, L.H. Velazquez-Jimenez, L.F. Chazaro-Ruiz, P.E. Diaz-Flores, J.R. Rangel-Mendez, Fluoride removal in water by a hybrid adsorbent lanthanum–carbon, *Journal of Colloid and Interface Science*. 455 (2015) 194–202. <https://doi.org/10.1016/j.jcis.2015.05.048>.
- [143] S.A. Chaudhry, Z. Zaidi, S.I. Siddiqui, Isotherm, kinetic and thermodynamics of arsenic adsorption onto Iron-Zirconium Binary Oxide-Coated Sand (IZBOCS): Modelling and process optimization, *Journal of Molecular Liquids*. 229 (2017) 230–240. <https://doi.org/10.1016/j.molliq.2016.12.048>.
- [144] J.A. Arcibar-Orozco, D.-B. Josue, J.C. Rios-Hurtado, J.R. Rangel-Mendez, Influence of iron content, surface area and charge distribution in the arsenic removal by activated carbons, *Chemical Engineering Journal*. 249 (2014) 201–209. <https://doi.org/10.1016/j.cej.2014.03.096>.
- [145] Mu. Naushad, Inamuddin, T.A. Rangreez, Z.A. ALothman, A mercury ion selective electrode based on poly-o-toluidine Zr(IV) tungstate composite membrane, *Journal of Electroanalytical Chemistry*. 713 (2014) 125–130. <https://doi.org/10.1016/j.jelechem.2013.12.002>.
- [146] Z.A. AL-Othman, Mu. Naushad, Inamuddin, Organic–inorganic type composite cation exchanger poly-o-toluidine Zr(IV) tungstate: Preparation, physicochemical characterization and its analytical application in separation of heavy metals, *Chemical Engineering Journal*. 172 (2011) 369–375. <https://doi.org/10.1016/j.cej.2011.06.018>.
- [147] Z.A. ALothman, Inamuddin, Mu. Naushad, Recent Developments in the Synthesis, Characterization and Applications of Zirconium(IV) Based Composite Ion

- Exchangers, J Inorg Organomet Polym. 23 (2013) 257–269.
<https://doi.org/10.1007/s10904-012-9797-2>.
- [148] K. Gupta, U.C. Ghosh, Arsenic removal using hydrous nanostructure iron(III)–titanium(IV) binary mixed oxide from aqueous solution, *Journal of Hazardous Materials*. 161 (2009) 884–892. <https://doi.org/10.1016/j.jhazmat.2008.04.034>.
- [149] K. Gupta, T. Basu, U.C. Ghosh, Sorption Characteristics of Arsenic(V) for Removal from Water Using Agglomerated Nanostructure Iron(III)–Zirconium(IV) Bimetal Mixed Oxide, *J. Chem. Eng. Data*. 54 (2009) 2222–2228.
<https://doi.org/10.1021/je900282m>.
- [150] K. Biswas, K. Gupta, U.C. Ghosh, Adsorption of fluoride by hydrous iron(III)–tin(IV) bimetal mixed oxide from the aqueous solutions, *Chemical Engineering Journal*. 149 (2009) 196–206. <https://doi.org/10.1016/j.cej.2008.09.047>.
- [151] E. Vences-Alvarez, J.L. Flores-Arciniega, H. Flores-Zuñiga, J.R. Rangel-Mendez, Fluoride removal from water by ceramic oxides from cerium and manganese solutions, *Journal of Molecular Liquids*. 286 (2019) 110880.
<https://doi.org/10.1016/j.molliq.2019.110880>.
- [152] Z.A. AlOthman, A Review: Fundamental Aspects of Silicate Mesoporous Materials, *Materials*. 5 (2012) 2874–2902. <https://doi.org/10.3390/ma5122874>.
- [153] R.M. Cornell, U. Schwertmann, *The iron oxides structure, properties, reactions, occurrences, and uses*, 2nd, completely rev. and extended ed ed., Weinheim Wiley-VCH, 2003. <https://trove.nla.gov.au/work/7696568> (accessed February 7, 2019).
- [154] M. Kosmulski, The Significance of the Points of Zero Charge of Zirconium (Hydr)Oxide Reported in the Literature, *Journal of Dispersion Science and Technology*. 23 (2002) 529–538. <https://doi.org/10.1081/DIS-120014021>.

- [155] L. Deguillaume, M. Leriche, K. Desboeufs, G. Mailhot, C. George, N. Chaumerliac, Transition Metals in Atmospheric Liquid Phases: Sources, Reactivity, and Sensitive Parameters, *Chem. Rev.* 105 (2005) 3388–3431. <https://doi.org/10.1021/cr040649c>.
- [156] T.H. Yosca, J. Rittle, C.M. Krest, E.L. Onderko, A. Silakov, J.C. Calixto, R.K. Behan, M.T. Green, Iron(IV)hydroxide pKa and the Role of Thiolate Ligation in C-H Bond Activation by Cytochrome P450, *Science*. 342 (2013) 825–829. <https://doi.org/10.1126/science.1244373>.
- [157] P. Lakshmipathiraj, B.R.V. Narasimhan, S. Prabhakar, G. Bhaskar Raju, Adsorption of arsenate on synthetic goethite from aqueous solutions, *Journal of Hazardous Materials*. 136 (2006) 281–287. <https://doi.org/10.1016/j.jhazmat.2005.12.015>.
- [158] M. Barrera S, M. Chavez G, A.M. Soto E, C. Velasquez O, M.A. Garcia S, L. Olvera T, T. Rivera M, Synthesis of amorphous zirconium oxide with luminescent characteristics, MX0400318. (n.d.) 1–9.
- [159] L.H. Velazquez-Jimenez, R.H. Hurt, J. Matos, J.R. Rangel-Mendez, Zirconium–Carbon Hybrid Sorbent for Removal of Fluoride from Water: Oxalic Acid Mediated Zr(IV) Assembly and Adsorption Mechanism, *Environ. Sci. Technol.* 48 (2014) 1166–1174. <https://doi.org/10.1021/es403929b>.
- [160] K. Biswas, D. Bandhoyapadhyay, U.C. Ghosh, Adsorption kinetics of fluoride on iron(III)-zirconium(IV) hybrid oxide, *Adsorption*. 13 (2007) 83–94. <https://doi.org/10.1007/s10450-007-9000-1>.
- [161] C. Zhang, Y. Li, F. Wang, Z. Yu, J. Wei, Z. Yang, C. Ma, Z. Li, Z. Xu, G. Zeng, Performance of magnetic zirconium-iron oxide nanoparticle in the removal of phosphate from aqueous solution, *Applied Surface Science*. 396 (2017) 1783–1792. <https://doi.org/10.1016/j.apsusc.2016.11.214>.

- [162] Z. Ren, G. Zhang, J. Paul Chen, Adsorptive removal of arsenic from water by an iron–zirconium binary oxide adsorbent, *Journal of Colloid and Interface Science*. 358 (2011) 230–237. <https://doi.org/10.1016/j.jcis.2011.01.013>.
- [163] L. Rodríguez, Parámetros fisicoquímicos y concentración de flúor y arsénico en el agua de pozos de la ciudad de San Luis Potosí y zona conurbada. Alternativa de tratamiento: Adsorción de fluoruro y arsénico en la interfase Al₂O₃ activada/solución acuosa., Tesis de Maestría, Facultad de ciencias químicas, ingeniería y medicina. Universidad Autónoma de San Luis Potosí, 2006.
- [164] M.L. Pierce, C.B. Moore, Adsorption of arsenite and arsenate on amorphous iron hydroxide, *Water Research*. 16 (1982) 1247–1253. [https://doi.org/10.1016/0043-1354\(82\)90143-9](https://doi.org/10.1016/0043-1354(82)90143-9).
- [165] M. Berg, H.C. Tran, T.C. Nguyen, H.V. Pham, R. Schertenleib, W. Giger, Arsenic Contamination of Groundwater and Drinking Water in Vietnam: A Human Health Threat, *Environ. Sci. Technol.* 35 (2001) 2621–2626. <https://doi.org/10.1021/es010027y>.
- [166] B.K. Mandal, K.T. Suzuki, Arsenic round the world: a review, *Talanta*. 58 (2002) 201–235.
- [167] P.L. Smedley, H.B. Nicolli, D.M.J. Macdonald, A.J. Barros, J.O. Tullio, Hydrogeochemistry of arsenic and other inorganic constituents in groundwaters from La Pampa, Argentina, *Applied Geochemistry*. 17 (2002) 259–284. [https://doi.org/10.1016/S0883-2927\(01\)00082-8](https://doi.org/10.1016/S0883-2927(01)00082-8).
- [168] M.F. Hossain, Arsenic contamination in Bangladesh—An overview, *Agriculture, Ecosystems & Environment*. 113 (2006) 1–16. <https://doi.org/10.1016/j.agee.2005.08.034>.
- [169] S.-H. Kim, K. Kim, K.-S. Ko, Y. Kim, K.-S. Lee, Co-contamination of arsenic and fluoride in the groundwater of unconsolidated aquifers under reducing environments,

- Chemosphere. 87 (2012) 851–856.
<https://doi.org/10.1016/j.chemosphere.2012.01.025>.
- [170] C. Jing, J. Cui, Y. Huang, A. Li, Fabrication, Characterization, and Application of a Composite Adsorbent for Simultaneous Removal of Arsenic and Fluoride, *ACS Appl. Mater. Interfaces*. 4 (2012) 714–720. <https://doi.org/10.1021/am2013322>.
- [171] M. Streat, K. Hellgardt, N.L.R. Newton, Hydrous ferric oxide as an adsorbent in water treatment: Part 2. Adsorption studies, *Process Safety and Environmental Protection*. 86 (2008) 11–20. <https://doi.org/10.1016/j.psep.2007.10.008>.
- [172] G. Sriram, M. Kigga, U.T. Uthappa, R.M. Rego, V. Thendral, T. Kumeria, H.-Y. Jung, M.D. Kurkuri, Naturally available diatomite and their surface modification for the removal of hazardous dye and metal ions: A review, *Advances in Colloid and Interface Science*. 282 (2020) 102198. <https://doi.org/10.1016/j.cis.2020.102198>.
- [173] J.-Y. Chung, S.-D. Yu, Y.-S. Hong, Environmental Source of Arsenic Exposure, *J Prev Med Public Health*. 47 (2014) 253–257. <https://doi.org/10.3961/jpmph.14.036>.
- [174] O.N. Jerome, *Arsenic in the Environment, Part 1: Cycling and Characterization*, Wiley, New York, 1994.
- [175] M. Argos, T. Kalra, P.J. Rathouz, Y. Chen, B. Pierce, F. Parvez, T. Islam, A. Ahmed, M. Rakibuz-Zaman, R. Hasan, G. Sarwar, V. Slavkovich, A. van Geen, J. Graziano, H. Ahsan, Arsenic exposure from drinking water, and all-cause and chronic-disease mortalities in Bangladesh (HEALS): a prospective cohort study, *Lancet*. 376 (2010) 252–258. [https://doi.org/10.1016/S0140-6736\(10\)60481-3](https://doi.org/10.1016/S0140-6736(10)60481-3).
- [176] H. Gibb, C. Haver, D. Gaylor, S. Ramasamy, J.S. Lee, D. Lobdell, T. Wade, C. Chen, P. White, R. Sams, Utility of recent studies to assess the National Research Council 2001 estimates of cancer risk from ingested arsenic, *Environ Health Perspect*. 119 (2011) 284–290. <https://doi.org/10.1289/ehp.1002427>.

- [177] T.S.Y. Choong, T.G. Chuah, Y. Robiah, F.L. Gregory Koay, I. Azni, Arsenic toxicity, health hazards and removal techniques from water: an overview, *Desalination*. 217 (2007) 139–166. <https://doi.org/10.1016/j.desal.2007.01.015>.
- [178] C. Ferreccio, C. González, V. Milosavljevic, G. Marshall, A.M. Sancha, A.H. Smith, Lung cancer and arsenic concentrations in drinking water in Chile, *Epidemiology*. 11 (2000) 673–679. <https://doi.org/10.1097/00001648-200011000-00010>.
- [179] B. Han, T. Runnells, J. Zimbron, R. Wickramasinghe, Arsenic removal from drinking water by flocculation and microfiltration, *Desalination*. 145 (2002) 293–298. [https://doi.org/10.1016/S0011-9164\(02\)00425-3](https://doi.org/10.1016/S0011-9164(02)00425-3).
- [180] M.F. Hughes, Arsenic toxicity and potential mechanisms of action, *Toxicol. Lett.* 133 (2002) 1–16. [https://doi.org/10.1016/s0378-4274\(02\)00084-x](https://doi.org/10.1016/s0378-4274(02)00084-x).
- [181] A.T. Fisher, L. López-Carrillo, B. Gamboa-Loira, M.E. Cebrián, Standards for arsenic in drinking water: Implications for policy in Mexico, *J Public Health Policy*. 38 (2017) 395–406. <https://doi.org/10.1057/s41271-017-0087-7>.
- [182] E. Vences-Alvarez, L.H. Velazquez-Jimenez, L.F. Chazaro-Ruiz, P.E. Diaz-Flores, J.R. Rangel-Mendez, Fluoride removal in water by a hybrid adsorbent lanthanum–carbon, *Journal of Colloid and Interface Science*. 455 (2015) 194–202. <https://doi.org/10.1016/j.jcis.2015.05.048>.
- [183] J.A. Arcibar-Orozco, D.-B. Josue, J.C. Rios-Hurtado, J.R. Rangel-Mendez, Influence of iron content, surface area and charge distribution in the arsenic removal by activated carbons, *Chemical Engineering Journal*. 249 (2014) 201–209. <https://doi.org/10.1016/j.cej.2014.03.096>.
- [184] R. Li, Q. Li, S. Gao, J.K. Shang, Exceptional arsenic adsorption performance of hydrous cerium oxide nanoparticles: Part A. Adsorption capacity and mechanism, *Chemical Engineering Journal*. 185–186 (2012) 127–135. <https://doi.org/10.1016/j.cej.2012.01.061>.

- [185] A.M. Raichur, M. Jyoti Basu, Adsorption of fluoride onto mixed rare earth oxides, *Separation and Purification Technology*. 24 (2001) 121–127. [https://doi.org/10.1016/S1383-5866\(00\)00219-7](https://doi.org/10.1016/S1383-5866(00)00219-7).
- [186] H. Xiao, Z. Ai, L. Zhang, Nonaqueous Sol–Gel Synthesized Hierarchical CeO₂ Nanocrystal Microspheres as Novel Adsorbents for Wastewater Treatment, *J. Phys. Chem. C*. 113 (2009) 16625–16630. <https://doi.org/10.1021/jp9050269>.
- [187] X. Peng, Z. Luan, J. Ding, Z. Di, Y. Li, B. Tian, Ceria nanoparticles supported on carbon nanotubes for the removal of arsenate from water, *Materials Letters*. 59 (2005) 399–403. <https://doi.org/10.1016/j.matlet.2004.05.090>.
- [188] M.J. Haron, F. Ab Rahim, A.H. Abdullah, M.Z. Hussein, A. Kassim, Sorption removal of arsenic by cerium-exchanged zeolite P, *Materials Science and Engineering: B*. 149 (2008) 204–208. <https://doi.org/10.1016/j.mseb.2007.11.028>.
- [189] K. Gupta, U.C. Ghosh, Arsenic removal using hydrous nanostructure iron(III)–titanium(IV) binary mixed oxide from aqueous solution, *Journal of Hazardous Materials*. 161 (2009) 884–892. <https://doi.org/10.1016/j.jhazmat.2008.04.034>.
- [190] K. Gupta, T. Basu, U.C. Ghosh, Sorption Characteristics of Arsenic(V) for Removal from Water Using Agglomerated Nanostructure Iron(III)–Zirconium(IV) Bimetal Mixed Oxide, *J. Chem. Eng. Data*. 54 (2009) 2222–2228. <https://doi.org/10.1021/je900282m>.
- [191] K. Biswas, K. Gupta, U.C. Ghosh, Adsorption of fluoride by hydrous iron(III)–tin(IV) bimetal mixed oxide from the aqueous solutions, *Chemical Engineering Journal*. 149 (2009) 196–206. <https://doi.org/10.1016/j.cej.2008.09.047>.
- [192] T. Basu, D. Nandi, P. Sen, U.C. Ghosh, Equilibrium modeling of As(III,V) sorption in the absence/presence of some groundwater occurring ions by iron(III)–cerium(IV) oxide nanoparticle agglomerates: A mechanistic approach of surface interaction,

- Chemical Engineering Journal. 228 (2013) 665–678.
<https://doi.org/10.1016/j.cej.2013.05.037>.
- [193] B. Chen, Z. Zhu, Y. Guo, Y. Qiu, J. Zhao, Facile synthesis of mesoporous Ce–Fe bimetal oxide and its enhanced adsorption of arsenate from aqueous solutions, *Journal of Colloid and Interface Science*. 398 (2013) 142–151.
<https://doi.org/10.1016/j.jcis.2013.02.004>.
- [194] U.K. Sahu, M.K. Sahu, S.S. Mohapatra, R.K. Patel, Removal of As(V) from aqueous solution by Ce-Fe bimetal mixed oxide, *Journal of Environmental Chemical Engineering*. 4 (2016) 2892–2899. <https://doi.org/10.1016/j.jece.2016.05.041>.
- [195] Z. Wen, J. Ke, J. Xu, S. Guo, Y. Zhang, R. Chen, One-step facile hydrothermal synthesis of flowerlike Ce/Fe bimetallic oxides for efficient As(V) and Cr(VI) remediation: Performance and mechanism, *Chemical Engineering Journal*. 343 (2018) 416–426. <https://doi.org/10.1016/j.cej.2018.03.034>.
- [196] Y. Zhang, M. Yang, X. Huang, Arsenic(V) removal with a Ce(IV)-doped iron oxide adsorbent, *Chemosphere*. 51 (2003) 945–952. [https://doi.org/10.1016/S0045-6535\(02\)00850-0](https://doi.org/10.1016/S0045-6535(02)00850-0).
- [197] C.E. Flores-Chaparro, L.F.C. Ruiz, Ma.C. Alfaro-De la Torre, J.R. Rangel-Mendez, Soluble hydrocarbons uptake by porous carbonaceous adsorbents at different water ionic strength and temperature: something to consider in oil spills, *Environ Sci Pollut Res*. 23 (2016) 11014–11024. <https://doi.org/10.1007/s11356-016-6286-0>.
- [198] H. Qiu, L. Lv, B. Pan, Q. Zhang, W. Zhang, Q. Zhang, Critical review in adsorption kinetic models, *J. Zhejiang Univ. Sci. A*. 10 (2009) 716–724.
<https://doi.org/10.1631/jzus.A0820524>.
- [199] M. Gallegos-Garcia, K. Ramírez-Muñiz, S. Song, Arsenic Removal from Water by Adsorption Using Iron Oxide Minerals as Adsorbents: A Review, *Mineral Processing*

- and Extractive Metallurgy Review. 33 (2012) 301–315.
<https://doi.org/10.1080/08827508.2011.584219>.
- [200] Y. Hakuta, S. Onai, H. Terayama, T. Adschiri, K. Arai, Production of Ultra-fine Ceria Particles by Hydrothermal Synthesis Under Supercritical Conditions, *Journal of Materials Science Letters*. 17 (1998) 1211–1213.
<https://doi.org/10.1023/A:1006597828280>.
- [201] S. Yu, V.M.H. Ng, F. Wang, Z. Xiao, C. Li, L.B. Kong, W. Que, K. Zhou, Synthesis and application of iron-based nanomaterials as anodes of lithium-ion batteries and supercapacitors, *J. Mater. Chem. A*. 6 (2018) 9332–9367.
<https://doi.org/10.1039/C8TA01683F>.
- [202] F.N. Sayed, V. Polshettiwar, Facile and Sustainable Synthesis of Shaped Iron Oxide Nanoparticles: Effect of Iron Precursor Salts on the Shapes of Iron Oxides, *Scientific Reports*. 5 (2015) 9733. <https://doi.org/10.1038/srep09733>.
- [203] S.I. Siddiqui, S.A. Chaudhry, Iron oxide and its modified forms as an adsorbent for arsenic removal: A comprehensive recent advancement, *Process Safety and Environmental Protection*. 111 (2017) 592–626.
<https://doi.org/10.1016/j.psep.2017.08.009>.
- [204] C.R. Armstrong, S.A. Wood, Effect of fulvic acid on neodymium uptake by goethite, *J Colloid Interface Sci*. 387 (2012) 228–233. <https://doi.org/10.1016/j.jcis.2012.07.060>.
- [205] J. Ma, C. Zhu, J. Lu, B. Ouyang, Q. Xie, H. Liu, S. Peng, T. Chen, Kinetics analysis of interfacial electron-transfer processes in goethite suspensions systems, *Chemosphere*. 188 (2017) 667–676.
<https://doi.org/10.1016/j.chemosphere.2017.09.029>.
- [206] I.M. Ugwu, D.M. Sherman, Irreversibility of sorption of cobalt to goethite (α -FeOOH) and disparities in dissolution of aged synthetic Co-goethite, *Chemical Geology*. 467 (2017) 168–176. <https://doi.org/10.1016/j.chemgeo.2017.08.011>.

- [207] L.A. De Faria, S. Trasatti, The Point of Zero Charge of CeO₂, *Journal of Colloid and Interface Science*. 167 (1994) 352–357. <https://doi.org/10.1006/jcis.1994.1370>.
- [208] L.K. Limbach, R. Bereiter, E. Müller, R. Krebs, R. Gälli, W.J. Stark, Removal of Oxide Nanoparticles in a Model Wastewater Treatment Plant: Influence of Agglomeration and Surfactants on Clearing Efficiency, *Environ. Sci. Technol.* 42 (2008) 5828–5833. <https://doi.org/10.1021/es800091f>.
- [209] D.E. Speed, 10 - Environmental aspects of planarization processes, in: S. Babu (Ed.), *Advances in Chemical Mechanical Planarization (CMP)*, Woodhead Publishing, 2016: pp. 229–269. <https://doi.org/10.1016/B978-0-08-100165-3.00010-3>.
- [210] S. Phanichphant, A. Nakaruk, D. Channei, Photocatalytic activity of the binary composite CeO₂/SiO₂ for degradation of dye, *Applied Surface Science*. 387 (2016) 214–220. <https://doi.org/10.1016/j.apsusc.2016.06.072>.
- [211] F. Zhang, P. Wang, J. Koberstein, S. Khalid, S.-W. Chan, Cerium oxidation state in ceria nanoparticles studied with X-ray photoelectron spectroscopy and absorption near edge spectroscopy, *Surface Science*. 563 (2004) 74–82. <https://doi.org/10.1016/j.susc.2004.05.138>.
- [212] M. Baalousha, P. Le Coustumer, I. Jones, J.R. Lead, Characterisation of structural and surface speciation of representative commercially available cerium oxide nanoparticles, *Environmental Chemistry*. (2010). <https://agris.fao.org/agris-search/search.do?recordID=US201301880161> (accessed August 10, 2020).
- [213] P. Berg, M. Singer, *Dealing with Genes: The Language of Heredity*, University Science Books, 1992.
- [214] A. Sarvaramini, D. Azizi, F. Larachi, Hydroxamic acid interactions with solvated cerium hydroxides in the flotation of monazite and bastnäsité—Experiments and DFT study, *Applied Surface Science*. 387 (2016) 986–995. <https://doi.org/10.1016/j.apsusc.2016.07.044>.

- [215] P. Lakshmipathiraj, B.R.V. Narasimhan, S. Prabhakar, G. Bhaskar Raju, Adsorption of arsenate on synthetic goethite from aqueous solutions, *Journal of Hazardous Materials*. 136 (2006) 281–287. <https://doi.org/10.1016/j.jhazmat.2005.12.015>.
- [216] G. Sriram, A. Bendre, T. Altalhi, H.-Y. Jung, G. Hegde, M. Kurkuri, Surface engineering of silica based materials with Ni–Fe layered double hydroxide for the efficient removal of methyl orange: Isotherms, kinetics, mechanism and high selectivity studies, *Chemosphere*. 287 (2022) 131976. <https://doi.org/10.1016/j.chemosphere.2021.131976>.
- [217] G. Sriram, U.T. Uthappa, D. Losic, M. Kigga, H.-Y. Jung, M.D. Kurkuri, Mg–Al Layered Double Hydroxide (LDH) Modified Diatoms for Highly Efficient Removal of Congo Red from Aqueous Solution, *Applied Sciences*. 10 (2020) 2285. <https://doi.org/10.3390/app10072285>.
- [218] R.M. Cornell, U. Schwertmann, *The Iron Oxides: Structure, Properties, Reactions, Occurrences and Uses*, John Wiley & Sons, 2006.
- [219] E. Kumar, P. Selvarajan, D. Muthuraj, Synthesis and characterization of CeO₂ nanocrystals by solvothermal route, *Materials Research*. 16 (2013) 269–276. <https://doi.org/10.1590/S1516-14392013005000021>.
- [220] M. Farahmandjou, M. Zarinkamar, T.P. Firoozabadi, M. Farahmandjou, M. Zarinkamar, T.P. Firoozabadi, Synthesis of Cerium Oxide (CeO₂) nanoparticles using simple CO-precipitation method, *Revista Mexicana de Física*. 62 (2016) 496–499. http://www.scielo.org.mx/scielo.php?script=sci_abstract&pid=S0035-001X2016000500496&lng=es&nrm=iso&tlng=en.
- [221] R.M. Rego, G. Sriram, K.V. Ajeya, H.-Y. Jung, M.D. Kurkuri, M. Kigga, Cerium based UiO-66 MOF as a multipollutant adsorbent for universal water purification, *Journal of Hazardous Materials*. 416 (2021) 125941. <https://doi.org/10.1016/j.jhazmat.2021.125941>.

- [222] C. Zhang, Y. Li, F. Wang, Z. Yu, J. Wei, Z. Yang, C. Ma, Z. Li, Z. Xu, G. Zeng, Performance of magnetic zirconium-iron oxide nanoparticle in the removal of phosphate from aqueous solution, *Applied Surface Science*. 396 (2017) 1783–1792. <https://doi.org/10.1016/j.apsusc.2016.11.214>.
- [223] T. Basu, D. Nandi, P. Sen, U.C. Ghosh, Equilibrium modeling of As(III,V) sorption in the absence/presence of some groundwater occurring ions by iron(III)–cerium(IV) oxide nanoparticle agglomerates: A mechanistic approach of surface interaction, *Chemical Engineering Journal*. 228 (2013) 665–678. <https://doi.org/10.1016/j.cej.2013.05.037>.
- [224] G. Sriram, U.T. Uthappa, R.M. Rego, M. Kigga, T. Kumeria, H.-Y. Jung, M.D. Kurkuri, Ceria decorated porous diatom-xerogel as an effective adsorbent for the efficient removal of Eriochrome Black T, *Chemosphere*. 238 (2020) 124692. <https://doi.org/10.1016/j.chemosphere.2019.124692>.
- [225] H. Woo, J. Woong Kim, M. Kim, S. Park, K. Hyun Park, Au nanoparticles supported on magnetically separable Fe₂O₃–graphene oxide hybrid nanosheets for the catalytic reduction of 4-nitrophenol, *RSC Advances*. 5 (2015) 7554–7558. <https://doi.org/10.1039/C4RA13989E>.
- [226] D. Zhang, H. Fu, L. Shi, C. Pan, Q. Li, Y. Chu, W. Yu, Synthesis of CeO₂ Nanorods via Ultrasonication Assisted by Polyethylene Glycol, *Inorg. Chem*. 46 (2007) 2446–2451. <https://doi.org/10.1021/ic061697d>.
- [227] S. Phoka, P. Laokul, E. Swatsitang, V. Promarak, S. Seraphin, S. Maensiri, Synthesis, structural and optical properties of CeO₂ nanoparticles synthesized by a simple polyvinyl pyrrolidone (PVP) solution route, *Materials Chemistry and Physics*. 115 (2009) 423–428. <https://doi.org/10.1016/j.matchemphys.2008.12.031>.
- [228] R.P. Senthilkumar, V. Bhuvaneshwari, R. Ranjithkumar, S. Sathiyavimal, V. Malayaman, B. Chandarshekar, Synthesis, characterization and antibacterial activity

- of hybrid chitosan-cerium oxide nanoparticles: As a bionanomaterials, *International Journal of Biological Macromolecules*. 104 (2017) 1746–1752. <https://doi.org/10.1016/j.ijbiomac.2017.03.139>.
- [229] T. Yamashita, P. Hayes, Analysis of XPS spectra of Fe²⁺ and Fe³⁺ ions in oxide materials, *Applied Surface Science*. 254 (2008) 2441–2449. <https://doi.org/10.1016/j.apsusc.2007.09.063>.
- [230] A.P. Grosvenor, B.A. Kobe, M.C. Biesinger, N.S. McIntyre, Investigation of multiplet splitting of Fe 2p XPS spectra and bonding in iron compounds, *Surface and Interface Analysis*. 36 (2004) 1564–1574. <https://doi.org/10.1002/sia.1984>.
- [231] D. Brion, Etude par spectroscopie de photoelectrons de la degradation superficielle de FeS₂, CuFeS₂, ZnS et PbS a l'air et dans l'eau, *Applications of Surface Science*. 5 (1980) 133–152. [https://doi.org/10.1016/0378-5963\(80\)90148-8](https://doi.org/10.1016/0378-5963(80)90148-8).
- [232] Ph. de Donato, C. Mustin, R. Benoit, R. Erre, Spatial distribution of iron and sulphur species on the surface of pyrite, *Applied Surface Science*. 68 (1993) 81–93. [https://doi.org/10.1016/0169-4332\(93\)90217-Y](https://doi.org/10.1016/0169-4332(93)90217-Y).
- [233] B. Stypula, J. Stoch, The characterization of passive films on chromium electrodes by XPS, *Corrosion Science*. 36 (1994) 2159–2167. [https://doi.org/10.1016/0010-938X\(94\)90014-0](https://doi.org/10.1016/0010-938X(94)90014-0).
- [234] J.-X. Feng, S.-H. Ye, H. Xu, Y.-X. Tong, G.-R. Li, Design and Synthesis of FeOOH/CeO₂ Heterolayered Nanotube Electrocatalysts for the Oxygen Evolution Reaction, *Advanced Materials*. 28 (2016) 4698–4703. <https://doi.org/10.1002/adma.201600054>.
- [235] K. Kuntaiah, P. Sudarsanam, B.M. Reddy, A. Vinu, Nanocrystalline Ce_{1-x}Sm_xO_{2-delta} (x=0.4) solid solutions: structural characterization versus CO oxidation, *Rsc Advances*. 3 (2013) 7953–7962. <https://doi.org/10.1039/c3ra23491f>.

- [236] B.M. Reddy, A. Khan, Y. Yamada, T. Kobayashi, S. Loridant, J.-C. Volta, Raman and X-ray Photoelectron Spectroscopy Study of CeO₂-ZrO₂ and V₂O₅/CeO₂-ZrO₂ Catalysts, *Langmuir*. 19 (2003) 3025–3030. <https://doi.org/10.1021/la0208528>.
- [237] E. Bêche, P. Charvin, D. Perarnau, S. Abanades, G. Flamant, Ce 3d XPS investigation of cerium oxides and mixed cerium oxide (Ce_xTi_yO_z), *Surface and Interface Analysis*. 40 (2008) 264–267. <https://doi.org/10.1002/sia.2686>.
- [238] D.A. Dzombak, F.M. Morel, Adsorption of inorganic pollutants in aquatic systems, *Journal of Hydraulic Engineering*. 113 (1987) 430–475.
- [239] N.A. Piro, J.R. Robinson, P.J. Walsh, E.J. Schelter, The electrochemical behavior of cerium(III/IV) complexes: Thermodynamics, kinetics and applications in synthesis, *Coordination Chemistry Reviews*. 260 (2014) 21–36. <https://doi.org/10.1016/j.ccr.2013.08.034>.
- [240] X. Sun, Y. Lei, R. Zhou, B. Qu, D. Li, B. Zhang, X.C. Zeng, New phases of 3d-transition metal–cerium binary compounds: an extensive structural search, *RSC Adv*. 7 (2017) 40486–40498. <https://doi.org/10.1039/C7RA07103E>.
- [241] V.I. Ponomarenko, M.A. Porai-Koshits, E.N. Kurkutova, K. Sulaimankulov, Crystal structure of cerium(III) sulfate-2-urea-5-water Ce₂(SO₄)₃·2OC(NH₂)₂·5H₂O and the structural characteristics of the sulfates of the rare earth elements, *J Struct Chem*. 19 (1979) 733–741. <https://doi.org/10.1007/BF00752837>.
- [242] B.M. Gatehouse, A. Pring, The crystal structure of hydrogen cerium(III) sulfate hydrate, [H₃O][Ce(SO₄)₂] · H₂O, *Journal of Solid State Chemistry*. 38 (1981) 116–120. [https://doi.org/10.1016/0022-4596\(81\)90480-1](https://doi.org/10.1016/0022-4596(81)90480-1).
- [243] A. Bucci, G. Menendez Rodriguez, G. Bellachioma, C. Zuccaccia, A. Poater, L. Cavallo, A. Macchioni, An Alternative Reaction Pathway for Iridium-Catalyzed Water Oxidation Driven by Cerium Ammonium Nitrate (CAN), *ACS Catal*. 6 (2016) 4559–4563. <https://doi.org/10.1021/acscatal.6b01325>.

- [244] Z. Codolà, L. Gómez, S.T. Kleespies, L. Que Jr, M. Costas, J. Lloret-Fillol, Evidence for an oxygen evolving iron–oxo–cerium intermediate in iron-catalysed water oxidation, *Nat Commun.* 6 (2015) 5865. <https://doi.org/10.1038/ncomms6865>.
- [245] Z. Ren, G. Zhang, J. Paul Chen, Adsorptive removal of arsenic from water by an iron–zirconium binary oxide adsorbent, *Journal of Colloid and Interface Science.* 358 (2011) 230–237. <https://doi.org/10.1016/j.jcis.2011.01.013>.
- [246] C.E. Flores-Chaparro, M.C. Rodriguez-Hernandez, L.F. Chazaro-Ruiz, Ma.C. Alfaro-De la Torre, M.A. Huerta-Diaz, J.R. Rangel-Mendez, Chitosan-macroalgae biocomposites as potential adsorbents of water-soluble hydrocarbons: Organic matter and ionic strength effects, *Journal of Cleaner Production.* 197 (2018) 633–642. <https://doi.org/10.1016/j.jclepro.2018.06.200>.
- [247] U.K. Sahu, M.K. Sahu, S.S. Mohapatra, R.K. Patel, Removal of As(V) from aqueous solution by Ce-Fe bimetal mixed oxide, *Journal of Environmental Chemical Engineering.* 4 (2016) 2892–2899. <https://doi.org/10.1016/j.jece.2016.05.041>.
- [248] T. Zuyi, C. Taiwei, Points of Zero Charge and Potentiometric Titrations, *Adsorption Science & Technology.* 21 (2003) 607–616. <https://doi.org/10.1260/026361703771953622>.
- [249] National Research Council, *Arsenic in Drinking Water.*, National Academies Press, Washington, 1999. <https://www.ncbi.nlm.nih.gov/books/NBK230885/> (accessed August 19, 2021).
- [250] K. Pi, E. Markelova, P. Zhang, P.V. Cappellen, Arsenic Oxidation by Flavin-Derived Reactive Species under Oxic and Anoxic Conditions: Oxidant Formation and pH Dependence, *Environmental Science & Technology.* (2019). <https://doi.org/10.1021/acs.est.9b03188>.
- [251] J.A. Rodríguez-Romero, D.I. Mendoza-Castillo, H.E. Reynel-Ávila, D.A. de Haro-Del Rio, L.M. González-Rodríguez, A. Bonilla-Petriciolet, C.J. Duran-Valle, K.I. Camacho-

- Aguilar, Preparation of a new adsorbent for the removal of arsenic and its simulation with artificial neural network-based adsorption models, *Journal of Environmental Chemical Engineering*. 8 (2020) 103928. <https://doi.org/10.1016/j.jece.2020.103928>.
- [252] S.I. Siddiqui, S.A. Chaudhry, Iron oxide and its modified forms as an adsorbent for arsenic removal: A comprehensive recent advancement, *Process Safety and Environmental Protection*. 111 (2017) 592–626. <https://doi.org/10.1016/j.psep.2017.08.009>.
- [253] V.K. Sharma, M. Sohn, Aquatic arsenic: Toxicity, speciation, transformations, and remediation, *Environment International*. 35 (2009) 743–759. <https://doi.org/10.1016/j.envint.2009.01.005>.
- [254] World Health Organization, Arsenic, Arsenic. (2018). <https://www.who.int/news-room/fact-sheets/detail/arsenic> (accessed August 13, 2020).
- [255] D. Cortés-Arriagada, D.E. Ortega, Removal of arsenic from water using iron-doped phosphorene nanoadsorbents: A theoretical DFT study with solvent effects, *Journal of Molecular Liquids*. 307 (2020) 112958. <https://doi.org/10.1016/j.molliq.2020.112958>.
- [256] S.A. Chaudhry, T.A. Khan, I. Ali, Zirconium oxide-coated sand based batch and column adsorptive removal of arsenic from water: Isotherm, kinetic and thermodynamic studies, *Egyptian Journal of Petroleum*. 26 (2017) 553–563. <https://doi.org/10.1016/j.ejpe.2016.11.006>.
- [257] X. Yang, G. Huang, C. An, X. Chen, J. Shen, J. Yin, P. Song, Z. Xu, Y. Li, Removal of arsenic from water through ceramic filter modified by nano-CeO₂: A cost-effective approach for remote areas, *Science of The Total Environment*. (2020) 141510. <https://doi.org/10.1016/j.scitotenv.2020.141510>.

- [258] Y. Wang, H. Liu, S. Wang, X. Li, X. Wang, Y. Jia, Simultaneous removal and oxidation of arsenic from water by δ -MnO₂ modified activated carbon, *Journal of Environmental Sciences*. 94 (2020) 147–160. <https://doi.org/10.1016/j.jes.2020.03.006>.
- [259] E. Vences-Alvarez, A. Lopez-Valdivieso, L.F. Cházaro-Ruíz, H. Flores-Zuñiga, J.R. Rangel-Mendez, Enhanced arsenic removal from water by a bimetallic material ZrOx-FeOx with high OH density, *Environ Sci Pollut Res*. 27 (2020) 33362–33372. <https://doi.org/10.1007/s11356-020-09492-8>.
- [260] Z. Li, S. Deng, G. Yu, J. Huang, V.C. Lim, As(V) and As(III) removal from water by a Ce–Ti oxide adsorbent: Behavior and mechanism, *Chemical Engineering Journal*. 161 (2010) 106–113. <https://doi.org/10.1016/j.cej.2010.04.039>.
- [261] K. Gupta, S. Bhattacharya, D. Nandi, A. Dhar, A. Maity, A. Mukhopadhyay, D.J. Chattopadhyay, N.R. Ray, P. Sen, U.C. Ghosh, Arsenic(III) sorption on nanostructured cerium incorporated manganese oxide (NCMO): A physical insight into the mechanistic pathway, *Journal of Colloid and Interface Science*. 377 (2012) 269–276. <https://doi.org/10.1016/j.jcis.2012.01.066>.
- [262] V.K. Gupta, V.K. Saini, N. Jain, Adsorption of As(III) from aqueous solutions by iron oxide-coated sand, *Journal of Colloid and Interface Science*. 288 (2005) 55–60. <https://doi.org/10.1016/j.jcis.2005.02.054>.
- [263] G. Zhang, F. Liu, H. Liu, J. Qu, R. Liu, Respective Role of Fe and Mn Oxide Contents for Arsenic Sorption in Iron and Manganese Binary Oxide: An X-ray Absorption Spectroscopy Investigation, *Environ. Sci. Technol*. 48 (2014) 10316–10322. <https://doi.org/10.1021/es501527c>.
- [264] M. Zhu, G. Diao, Synthesis of Porous Fe₃O₄ Nanospheres and Its Application for the Catalytic Degradation of Xylenol Orange, *J. Phys. Chem. C*. 115 (2011) 18923–18934. <https://doi.org/10.1021/jp200418j>.

- [265] U.K. Sahu, S.S. Mahapatra, R.K. Patel, Application of Box–Behnken Design in response surface methodology for adsorptive removal of arsenic from aqueous solution using CeO₂/Fe₂O₃/graphene nanocomposite, *Materials Chemistry and Physics*. 207 (2018) 233–242. <https://doi.org/10.1016/j.matchemphys.2017.11.042>.
- [266] T. Sun, Z. Shi, X. Zhang, X. Wang, L. Zhu, Q. Lin, Efficient degradation of p-arsanilic acid with released arsenic removal by magnetic CeO₂–Fe₃O₄ nanoparticles through photo-oxidation and adsorption, *Journal of Alloys and Compounds*. 808 (2019) 151689. <https://doi.org/10.1016/j.jallcom.2019.151689>.
- [267] Y. Zhang, X. Dou, B. Zhao, M. Yang, T. Takayama, S. Kato, Removal of arsenic by a granular Fe–Ce oxide adsorbent: Fabrication conditions and performance, *Chemical Engineering Journal*. 162 (2010) 164–170. <https://doi.org/10.1016/j.cej.2010.05.021>.
- [268] U.K. Sahu, M.K. Sahu, S.S. Mohapatra, R.K. Patel, Removal of As(V) from aqueous solution by Ce-Fe bimetal mixed oxide, *Journal of Environmental Chemical Engineering*. 4 (2016) 2892–2899. <https://doi.org/10.1016/j.jece.2016.05.041>.
- [269] C. Nieto-Delgado, J. Gutiérrez-Martínez, J.R. Rangel-Méndez, Modified activated carbon with interconnected fibrils of iron-oxyhydroxides using Mn²⁺ as morphology regulator, for a superior arsenic removal from water, *Journal of Environmental Sciences*. 76 (2019) 403–414. <https://doi.org/10.1016/j.jes.2018.06.002>.
- [270] V. Sreeja, P.A. Joy, Microwave–hydrothermal synthesis of γ -Fe₂O₃ nanoparticles and their magnetic properties, *Materials Research Bulletin*. 42 (2007) 1570–1576. <https://doi.org/10.1016/j.materresbull.2006.11.014>.
- [271] A. Yürüm, Z.Ö. Kocabaş-Ataklı, M. Sezen, R. Semiat, Y. Yürüm, Fast deposition of porous iron oxide on activated carbon by microwave heating and arsenic (V) removal from water, *Chemical Engineering Journal*. 242 (2014) 321–332. <https://doi.org/10.1016/j.cej.2014.01.005>.

- [272] S. Komarneni, R. Roy, Q.H. Li, Microwave-hydrothermal synthesis of ceramic powders, *Materials Research Bulletin*. 27 (1992) 1393–1405. [https://doi.org/10.1016/0025-5408\(92\)90004-J](https://doi.org/10.1016/0025-5408(92)90004-J).
- [273] D.M.P. Mingos, The applications of microwaves in chemical syntheses, *Res Chem Intermed*. 20 (1994) 85–91. <https://doi.org/10.1163/156856794X00090>.
- [274] J.A. Arcibar-Orozco, M. Avalos-Borja, J.R. Rangel-Mendez, Effect of Phosphate on the Particle Size of Ferric Oxyhydroxides Anchored onto Activated Carbon: As(V) Removal from Water, *Environ. Sci. Technol*. 46 (2012) 9577–9583. <https://doi.org/10.1021/es204696u>.
- [275] M.D. Donohue, G.L. Aranovich, Classification of Gibbs adsorption isotherms, *Advances in Colloid and Interface Science*. 76–77 (1998) 137–152. [https://doi.org/10.1016/S0001-8686\(98\)00044-X](https://doi.org/10.1016/S0001-8686(98)00044-X).
- [276] J. Flores, A. Maubert, N. Martín, Evaluación de los intercambios iónicos en una zeolita natural mexicana para la separación de N₂-O₂ en el aire atmosférico, *Revista Mexicana de Ingeniería Química*. 5 (2006) 119–129.
- [277] Z.A. AlOthman, A Review: Fundamental Aspects of Silicate Mesoporous Materials, *Materials*. 5 (2012) 2874–2902. <https://doi.org/10.3390/ma5122874>.
- [278] C. Nieto-Delgado, J.R. Rangel-Mendez, Anchorage of iron hydro(oxide) nanoparticles onto activated carbon to remove As(V) from water, *Water Research*. 46 (2012) 2973–2982. <https://doi.org/10.1016/j.watres.2012.03.026>.
- [279] P. Lodeiro, S.M. Kwan, J.T. Perez, L.F. González, C. Gérente, Y. Andrès, G. McKay, Novel Fe loaded activated carbons with tailored properties for As(V) removal: Adsorption study correlated with carbon surface chemistry, *Chemical Engineering Journal*. 215–216 (2013) 105–112. <https://doi.org/10.1016/j.cej.2012.11.052>.
- [280] H. Marsh, F.R. Reinoso, *Activated Carbon*, Edición: 1, Elsevier Science, Amsterdam ; Boston, 2006.

- [281] W.-C. Yang, Handbook of Fluidization and Fluid-Particle Systems, CRC Press, 2003.
- [282] D.O. Cooney, Adsorption design for wastewater treatment, Lewis Publishers, Boca Raton, Fl., 1999.
- [283] R.M. Cornell, U. Schwertmann, The Iron Oxides: Structure, Properties, Reactions, Occurrences and Uses, John Wiley & Sons, 2003.
- [284] T. Yamashita, P. Hayes, Analysis of XPS spectra of Fe²⁺ and Fe³⁺ ions in oxide materials, Applied Surface Science. 254 (2008) 2441–2449. <https://doi.org/10.1016/j.apsusc.2007.09.063>.
- [285] J.F. Moulder, W.F. Stickle, P.E. Sobol, K.D. Bomben, Handbook of X-ray Photoelectron Spectroscopy, Perkin-Elmer Corporation, Physical Electronics Division. (1992) 40, 44, 80, 81, 144.
- [286] D. Brion, Etude par spectroscopie de photoelectrons de la degradation superficielle de FeS₂, CuFeS₂, ZnS et PbS a l'air et dans l'eau, Applications of Surface Science. 5 (1980) 133–152. [https://doi.org/10.1016/0378-5963\(80\)90148-8](https://doi.org/10.1016/0378-5963(80)90148-8).
- [287] Ph. de Donato, C. Mustin, R. Benoit, R. Erre, Spatial distribution of iron and sulphur species on the surface of pyrite, Applied Surface Science. 68 (1993) 81–93. [https://doi.org/10.1016/0169-4332\(93\)90217-Y](https://doi.org/10.1016/0169-4332(93)90217-Y).
- [288] B. Stypula, J. Stoch, The characterization of passive films on chromium electrodes by XPS, Corrosion Science. 36 (1994) 2159–2167. [https://doi.org/10.1016/0010-938X\(94\)90014-0](https://doi.org/10.1016/0010-938X(94)90014-0).
- [289] Y. Marcus, G. Hefter, Ion Pairing, Chem. Rev. 106 (2006) 4585–4621. <https://doi.org/10.1021/cr040087x>.
- [290] J.-P. Jolivet, Metal Oxide Chemistry and Synthesis: From Solution to Solid State, Edición: 1, Wiley, Chichester ; New York, 2000.

- [291] C. Nieto Delgado, Production of activated carbon from agave salmiana bagasse and its modification to remove arsenic from water, (2010). <https://repositorio.ipicyt.edu.mx//handle/11627/82> (accessed August 16, 2020).
- [292] S. Chaudhari, T. Banerji, P.R. Kumar, 7 - Domestic- and Community-Scale Arsenic Removal Technologies Suitable for Developing Countries, in: S. Ahuja (Ed.), *Water Reclamation and Sustainability*, Elsevier, Boston, 2014: pp. 155–182. <https://doi.org/10.1016/B978-0-12-411645-0.00007-9>.
- [293] D.G. Strawn, Review of interactions between phosphorus and arsenic in soils from four case studies, *Geochem Trans.* 19 (2018). <https://doi.org/10.1186/s12932-018-0055-6>.
- [294] UNICEF, *Water Front, Fluoride in water: An overview*, (1999). <https://www.unicef.org/wash/files/wf13e.pdf> (accessed August 17, 2020).
- [295] M.A. Ortega-Guerrero, Presencia, distribución, hidrogeoquímica y origen de arsénico, fluoruro y otros elementos traza disueltos en agua subterránea, a escala de cuenca hidrológica tributaria de Lerma-Chapala, México, *Revista mexicana de ciencias geológicas*. 26 (2009) 143–161.
- [296] L.G. Chacón, N.M. Frechero, A.O. Oropeza, E. Gaona, L.J. López, Análisis de la concentración de fluoruro en agua potable de la delegación Tláhuac, Ciudad de México, *Revista Internacional de Contaminación Ambiental*. 27 (2011) 283–289.
- [297] S.-G. Wang, Y. Ma, Y.-J. Shi, W.-X. Gong, Defluoridation performance and mechanism of nano-scale aluminum oxide hydroxide in aqueous solution, *Journal of Chemical Technology & Biotechnology*. 84 (2009) 1043–1050. <https://doi.org/10.1002/jctb.2131>.
- [298] M. Mohapatra, S. Anand, B.K. Mishra, D.E. Giles, P. Singh, Review of fluoride removal from drinking water, *Journal of Environmental Management*. 91 (2009) 67–77. <https://doi.org/10.1016/j.jenvman.2009.08.015>.

- [299] D.L. Ozsvath, Fluoride and environmental health: a review, *Rev Environ Sci Biotechnol.* 8 (2009) 59–79. <https://doi.org/10.1007/s11157-008-9136-9>.
- [300] L. Valenzuela, J. Ramírez-Hernández, J.A. Sol, J.A. Reyes, Alternativas para la Eliminación Doméstica de Fluor en el Agua de Consumo Humano, *Información Tecnológica.* 22 (2011) 23–32. <https://doi.org/10.4067/S0718-07642011000200004>.
- [301] S.S. Tripathy, A.M. Raichur, Abatement of fluoride from water using manganese dioxide-coated activated alumina, *Journal of Hazardous Materials.* 153 (2008) 1043–1051. <https://doi.org/10.1016/j.jhazmat.2007.09.100>.
- [302] Y. Ku, H.-M. Chiou, The Adsorption of Fluoride Ion from Aqueous Solution by Activated Alumina, *Water, Air, & Soil Pollution.* 133 (2002) 349–361. <https://doi.org/10.1023/A:1012929900113>.
- [303] M. Srimurali, A. Pragathi, J. Karthikeyan, A study on removal of fluorides from drinking water by adsorption onto low-cost materials, *Environmental Pollution.* 99 (1998) 285–289. [https://doi.org/10.1016/S0269-7491\(97\)00129-2](https://doi.org/10.1016/S0269-7491(97)00129-2).
- [304] C.A. Bower, J.T. Hatcher, Adsorption of fluoride by soils and minerals, *Soil Sci.; (United States).* 103:3 (1967). <https://doi.org/10.1097/00010694-196703000-00001>.
- [305] Y.-H. Li, S. Wang, X. Zhang, J. Wei, C. Xu, Z. Luan, D. Wu, Adsorption of fluoride from water by aligned carbon nanotubes, *Materials Research Bulletin.* 38 (2003) 469–476. [https://doi.org/10.1016/S0025-5408\(02\)01063-2](https://doi.org/10.1016/S0025-5408(02)01063-2).
- [306] I. Abe, S. Iwasaki, T. Tokimoto, N. Kawasaki, T. Nakamura, S. Tanada, Adsorption of fluoride ions onto carbonaceous materials, *Journal of Colloid and Interface Science.* 275 (2004) 35–39. <https://doi.org/10.1016/j.jcis.2003.12.031>.
- [307] A.M. Raichur, M. Jyoti Basu, Adsorption of fluoride onto mixed rare earth oxides, *Separation and Purification Technology.* 24 (2001) 121–127. [https://doi.org/10.1016/S1383-5866\(00\)00219-7](https://doi.org/10.1016/S1383-5866(00)00219-7).

- [308] M. Syed Junaid, T. Noor, P. Fahmida, U. T. H., A. Rafia, U. Fahim, Arsenic, Fluoride and Nitrate in Drinking Water: The Problem and its Possible Solution, *Science Alert*. (n.d.). <https://doi.org/10.3923/rjes.2007.179.184>.
- [309] R.J. Krupadam, M.S. Khan, S. Das, Adsorption of fluoride from water by surface-functionalized polyurethane foam, *Water Sci. Technol.* 62 (2010) 759–765. <https://doi.org/10.2166/wst.2010.190>.
- [310] X. Liao, B. Shi, Adsorption of Fluoride on Zirconium(IV)-Impregnated Collagen Fiber, *Environ. Sci. Technol.* 39 (2005) 4628–4632. <https://doi.org/10.1021/es0479944>.
- [311] N. Chen, Z. Zhang, C. Feng, M. Li, D. Zhu, N. Sugiura, Studies on fluoride adsorption of iron-impregnated granular ceramics from aqueous solution, *Materials Chemistry and Physics*. 125 (2011) 293–298. <https://doi.org/10.1016/j.matchemphys.2010.09.037>.
- [312] C. Janardhana, G.N. Rao, R.S. Sathish, V.S. Lakshman, Study on defluoridation of drinking water by impregnation of metal ions in activated charcoal, *Indian Journal of Chemical Technology*. 13(4) (2006) 414–416.
- [313] C. Nieto-Delgado, J. Gutiérrez-Martínez, J.R. Rangel-Méndez, Modified activated carbon with interconnected fibrils of iron-oxyhydroxides using Mn²⁺ as morphology regulator, for a superior arsenic removal from water, *Journal of Environmental Sciences*. 76 (2019) 403–414. <https://doi.org/10.1016/j.jes.2018.06.002>.
- [314] E. Vences-Alvarez, J.L. Flores-Arciniega, H. Flores-Zuñiga, J.R. Rangel-Mendez, Fluoride removal from water by ceramic oxides from cerium and manganese solutions, *Journal of Molecular Liquids*. 286 (2019) 110880. <https://doi.org/10.1016/j.molliq.2019.110880>.
- [315] S. Deng, H. Liu, W. Zhou, J. Huang, G. Yu, Mn-Ce oxide as a high-capacity adsorbent for fluoride removal from water, *J. Hazard. Mater.* 186 (2011) 1360–1366. <https://doi.org/10.1016/j.jhazmat.2010.12.024>.

- [316] L.H. Velazquez-Jimenez, R.H. Hurt, J. Matos, J.R. Rangel-Mendez, Zirconium–Carbon Hybrid Sorbent for Removal of Fluoride from Water: Oxalic Acid Mediated Zr(IV) Assembly and Adsorption Mechanism, *Environ. Sci. Technol.* 48 (2014) 1166–1174. <https://doi.org/10.1021/es403929b>.
- [317] J.-P. Jolivet, *Metal Oxide Chemistry and Synthesis: From Solution to Solid State*, Edición: 1, Wiley, Chichester ; New York, 2000.
- [318] K.D. Hristovski, P.K. Westerhoff, T. Möller, P. Sylvester, Effect of synthesis conditions on nano-iron (hydr)oxide impregnated granulated activated carbon, *Chemical Engineering Journal*. 146 (2009) 237–243. <https://doi.org/10.1016/j.cej.2008.05.040>.
- [319] G. Muñiz, V. Fierro, A. Celzard, G. Furdin, G. Gonzalez-Sánchez, M.L. Ballinas, Synthesis, characterization and performance in arsenic removal of iron-doped activated carbons prepared by impregnation with Fe(III) and Fe(II), *Journal of Hazardous Materials*. 165 (2009) 893–902. <https://doi.org/10.1016/j.jhazmat.2008.10.074>.
- [320] X. Yan, E. Michael, S. Komarneni, J.R. Brownson, Z.-F. Yan, Microwave-hydrothermal/solvothermal synthesis of kesterite, an emerging photovoltaic material, *Ceramics International*. 40 (2014) 1985–1992. <https://doi.org/10.1016/j.ceramint.2013.07.108>.
- [321] Z. Yan, J. Wang, R. Zou, L. Liu, Z. Zhang, X. Wang, Hydrothermal Synthesis of CeO₂ Nanoparticles on Activated Carbon with Enhanced Desulfurization Activity, *Energy Fuels*. 26 (2012) 5879–5886. <https://doi.org/10.1021/ef301085w>.
- [322] H. Marsh, F.R. Reinoso, *Activated Carbon*, Edición: 1, Elsevier Science, 2006.
- [323] A. Sarvaramini, D. Azizi, F. Larachi, Hydroxamic acid interactions with solvated cerium hydroxides in the flotation of monazite and bastnäsité—Experiments and DFT study, *Applied Surface Science*. 387 (2016) 986–995. <https://doi.org/10.1016/j.apsusc.2016.07.044>.

- [324] H.J. Amezquita-Garcia, E. Razo-Flores, F.J. Cervantes, J.R. Rangel-Mendez, Anchorage of anthraquinone molecules onto activated carbon fibers to enhance the reduction of 4-nitrophenol, *Journal of Chemical Technology & Biotechnology*. 90 (2015) 1685–1691. <https://doi.org/10.1002/jctb.4478>.
- [325] L.H. Velazquez-Jimenez, A. Pavlick, J.R. Rangel-Mendez, Chemical characterization of raw and treated agave bagasse and its potential as adsorbent of metal cations from water, *Industrial Crops and Products*. 43 (2013) 200–206. <https://doi.org/10.1016/j.indcrop.2012.06.049>.
- [326] E. Vences-Alvarez, L.H. Velazquez-Jimenez, L.F. Chazaro-Ruiz, P.E. Diaz-Flores, J.R. Rangel-Mendez, Fluoride removal in water by a hybrid adsorbent lanthanum–carbon, *Journal of Colloid and Interface Science*. 455 (2015) 194–202. <https://doi.org/10.1016/j.jcis.2015.05.048>.
- [327] G. Socrates, *Infrared and Raman Characteristic Group Frequencies: Tables and Charts*, Edición: 3 Sub, John Wiley & Sons Inc, Chichester ; New York, 2001.
- [328] M.M. Ali, H.S. Mahdi, A. Parveen, A. Azam, Optical properties of cerium oxide (CeO₂) nanoparticles synthesized by hydroxide mediated method, *AIP Conference Proceedings*. 1953 (2018) 030044. <https://doi.org/10.1063/1.5032379>.
- [329] D.O. Cooney, *Adsorption Design for Wastewater Treatment*, CRC Press, 1998.
- [330] C.R. O'Connor, J.A. Boscoboinik, M. Karatok, M.A. van Spronsen, Carbon monoxide, CO(g), by high-resolution near-ambient-pressure x-ray photoelectron spectroscopy, *Surface Science Spectra*. 27 (2020) 014002. <https://doi.org/10.1116/1.5131166>.
- [331] Z. Wang, R. Wei, X. Liu, Fabrication of selectively functionalized-graphene reinforced copper phthalocyanine nanocomposites with low dielectric loss and high dielectric constant, *AIP Conference Proceedings*. 1794 (2017) 020036. <https://doi.org/10.1063/1.4971918>.

- [332] E. Bêche, P. Charvin, D. Perarnau, S. Abanades, G. Flamant, Ce 3d XPS investigation of cerium oxides and mixed cerium oxide (CexTiyOz), *Surface and Interface Analysis*. 40 (2008) 264–267. <https://doi.org/10.1002/sia.2686>.
- [333] K. Kuntaiah, P. Sudarsanam, B.M. Reddy, A. Vinu, Nanocrystalline Ce_{1-x}Sm_xO_{2-δ} (x = 0.4) solid solutions: structural characterization versus CO oxidation, *RSC Adv*. 3 (2013) 7953–7962. <https://doi.org/10.1039/C3RA23491F>.
- [334] B.M. Reddy, A. Khan, Y. Yamada, T. Kobayashi, S. Loridant, J.-C. Volta, Raman and X-ray Photoelectron Spectroscopy Study of CeO₂-ZrO₂ and V₂O₅/CeO₂-ZrO₂ Catalysts, *Langmuir*. 19 (2003) 3025–3030. <https://doi.org/10.1021/la0208528>.
- [335] T. Yamashita, P. Hayes, Analysis of XPS spectra of Fe²⁺ and Fe³⁺ ions in oxide materials, *Applied Surface Science*. 254 (2008) 2441–2449. <https://doi.org/10.1016/j.apsusc.2007.09.063>.
- [336] A.P. Grosvenor, B.A. Kobe, M.C. Biesinger, N.S. McIntyre, Investigation of multiplet splitting of Fe 2p XPS spectra and bonding in iron compounds, *Surface and Interface Analysis*. 36 (2004) 1564–1574. <https://doi.org/10.1002/sia.1984>.
- [337] D. Brion, Etude par spectroscopie de photoelectrons de la degradation superficielle de FeS₂, CuFeS₂, ZnS et PbS a l'air et dans l'eau, *Applications of Surface Science*. 5 (1980) 133–152. [https://doi.org/10.1016/0378-5963\(80\)90148-8](https://doi.org/10.1016/0378-5963(80)90148-8).
- [338] Ph. de Donato, C. Mustin, R. Benoit, R. Erre, Spatial distribution of iron and sulphur species on the surface of pyrite, *Applied Surface Science*. 68 (1993) 81–93. [https://doi.org/10.1016/0169-4332\(93\)90217-Y](https://doi.org/10.1016/0169-4332(93)90217-Y).
- [339] B. Stypula, J. Stoch, The characterization of passive films on chromium electrodes by XPS, *Corrosion Science*. 36 (1994) 2159–2167. [https://doi.org/10.1016/0010-938X\(94\)90014-0](https://doi.org/10.1016/0010-938X(94)90014-0).

- [340] Y. Marcus, G. Hefter, Standard Partial Molar Volumes of Electrolytes and Ions in Nonaqueous Solvents, *Chem. Rev.* 104 (2004) 3405–3452. <https://doi.org/10.1021/cr030047d>.
- [341] R. Koner, I. Goldberg, A unique two-dimensional coordination network of 1-benzofuran-2,3-dicarboxylate with lanthanum(III) obtained by solvothermal synthesis, *Acta Crystallogr C.* 65 (2009) m149-151. <https://doi.org/10.1107/S0108270109007161>.
- [342] R. Koner, I. Goldberg, Two- and three-dimensional hydrated coordination polymers of diaqualanthanum(3+) ions with 2-hydroxypropanedioate, oxalate and acetate anions as bridging ligands, *Acta Crystallogr C.* 65 (2009) m160-164. <https://doi.org/10.1107/S0108270109008798>.
- [343] W.-J. Di, S.-M. Lan, Q. Zhang, Y.-X. Liang, Poly[[tetra- $\mu(3)$ -acetato-hexa- $\mu(2)$ -acetato-diaqua- $\mu(2)$ -oxalato-tetra-lanthanum(III)] dihydrate], *Acta Crystallogr Sect E Struct Rep Online.* 67 (2011) m1436-1437. <https://doi.org/10.1107/S1600536811038037>.
- [344] G.B. Ayer, V.V. Klepov, K.A. Pace, H.-C. zur Loye, Quaternary cerium(IV) containing fluorides exhibiting Ce₃F₁₆ sheets and Ce₆F₃₀ frameworks, *Dalton Trans.* 49 (2020) 5898–5905. <https://doi.org/10.1039/D0DT00616E>.
- [345] G. Alagumuthu, M. Rajan, Equilibrium and kinetics of adsorption of fluoride onto zirconium impregnated cashew nut shell carbon, *Chemical Engineering Journal.* 158 (2010) 451–457. <https://doi.org/10.1016/j.cej.2010.01.017>.
- [346] P. Lodeiro, S.M. Kwan, J.T. Perez, L.F. González, C. Gérente, Y. Andrès, G. McKay, Novel Fe loaded activated carbons with tailored properties for As(V) removal: Adsorption study correlated with carbon surface chemistry, *Chemical Engineering Journal.* 215–216 (2013) 105–112. <https://doi.org/10.1016/j.cej.2012.11.052>.

- [347] T. Hiemstra, W.H. van Riemsdijk, A surface structural model for ferrihydrite I: Sites related to primary charge, molar mass, and mass density, *Geochimica et Cosmochimica Acta*. 73 (2009) 4423–4436. <https://doi.org/10.1016/j.gca.2009.04.032>.
- [348] L. Chen, B.-Y. He, S. He, T.-J. Wang, C.-L. Su, Y. Jin, Fe—Ti oxide nano-adsorbent synthesized by co-precipitation for fluoride removal from drinking water and its adsorption mechanism, *Powder Technology*. 227 (2012) 3–8. <https://doi.org/10.1016/j.powtec.2011.11.030>.
- [349] S.A. Chaudhry, Z. Zaidi, S.I. Siddiqui, Isotherm, kinetic and thermodynamics of arsenic adsorption onto Iron-Zirconium Binary Oxide-Coated Sand (IZBOCS): Modelling and process optimization, *Journal of Molecular Liquids*. 229 (2017) 230–240. <https://doi.org/10.1016/j.molliq.2016.12.048>.
- [350] A. Ghosh, S. Chakrabarti, K. Biswas, U.C. Ghosh, Agglomerated nanoparticles of hydrous Ce(IV)+Zr(IV) mixed oxide: Preparation, characterization and physicochemical aspects on fluoride adsorption, *Applied Surface Science*. 307 (2014) 665–676. <https://doi.org/10.1016/j.apsusc.2014.04.095>.
- [351] Z. Wen, J. Ke, J. Xu, S. Guo, Y. Zhang, R. Chen, One-step facile hydrothermal synthesis of flowerlike Ce/Fe bimetallic oxides for efficient As(V) and Cr(VI) remediation: Performance and mechanism, *Chemical Engineering Journal*. 343 (2018) 416–426. <https://doi.org/10.1016/j.cej.2018.03.034>.
- [352] R. Chitrakar, S. Tezuka, A. Sonoda, K. Sakane, K. Ooi, T. Hirotsu, Selective adsorption of phosphate from seawater and wastewater by amorphous zirconium hydroxide, *Journal of Colloid and Interface Science*. 297 (2006) 426–433. <https://doi.org/10.1016/j.jcis.2005.11.011>.
- [353] G.C. Velazquez-Peña, M.T. Olgúin-Gutiérrez, M.J. Solache-Ríos, C. Fall, Significance of FeZr-modified natural zeolite networks on fluoride removal, *Journal of*

- Fluorine Chemistry. 202 (2017) 41–53.
<https://doi.org/10.1016/j.jfluchem.2017.09.004>.
- [354] S.SD. Elanchezhiyan, S. Muthu Prabhu, Y. Kim, C.M. Park, Lanthanum-substituted bimetallic magnetic materials assembled carboxylate-rich graphene oxide nanohybrids as highly efficient adsorbent for perfluorooctanoic acid adsorption from aqueous solutions, *Applied Surface Science*. 509 (2020) 144716.
<https://doi.org/10.1016/j.apsusc.2019.144716>.
- [355] D. Zhao, Y. Yu, C. Wang, J.P. Chen, Zirconium/PVA modified flat-sheet PVDF membrane as a cost-effective adsorptive and filtration material: A case study on decontamination of organic arsenic in aqueous solutions, *Journal of Colloid and Interface Science*. 477 (2016) 191–200. <https://doi.org/10.1016/j.jcis.2016.04.043>.
- [356] K.D. Hristovski, P.K. Westerhoff, J.C. Crittenden, L.W. Olson, Arsenate Removal by Nanostructured ZrO₂ Spheres, *Environ. Sci. Technol.* 42 (2008) 3786–3790.
<https://doi.org/10.1021/es702952p>.
- [357] S.M. Prabhu, P. Koilraj, K. Sasaki, Synthesis of sucrose-derived porous carbon-doped Zr_xLa_{1-x}OOH materials and their superior performance for the simultaneous immobilization of arsenite and fluoride from binary systems, *Chemical Engineering Journal*. 325 (2017) 1–13. <https://doi.org/10.1016/j.cej.2017.05.052>.
- [358] H. Cui, Q. Li, S. Gao, J.K. Shang, Strong adsorption of arsenic species by amorphous zirconium oxide nanoparticles, *Journal of Industrial and Engineering Chemistry*. 18 (2012) 1418–1427. <https://doi.org/10.1016/j.jiec.2012.01.045>.
- [359] L. Mu, Stability and Toxicity of Cerium Oxide Nanoparticles in Water-Soil-Plant Systems, All Dissertations. (2019).
https://tigerprints.clemson.edu/all_dissertations/2487.

- [360] S. Dudek, D. Kołodyńska, Enhanced Arsenic(V) Removal on an Iron-Based Sorbent Modified by Lanthanum(III), *Materials* (Basel). 13 (2020). <https://doi.org/10.3390/ma13112553>.
- [361] A. Vincent, T.M. Inerbaev, S. Babu, A.S. Karakoti, W.T. Self, A.E. Masunov, S. Seal, Tuning Hydrated Nanocerium Surfaces: Experimental/Theoretical Investigations of Ion Exchange and Implications in Organic and Inorganic Interactions, *Langmuir*. 26 (2010) 7188–7198. <https://doi.org/10.1021/la904285g>.
- [362] M. Kosmulski, The Significance of the Points of Zero Charge of Zirconium (Hydr)Oxide Reported in the Literature, *Journal of Dispersion Science and Technology*. 23 (2002) 529–538. <https://doi.org/10.1081/DIS-120014021>.
- [363] S. Muhammad, S.T. Hussain, M. Waseem, A. Naeem, J. Hussain, M. Tariq Jan, Surface charge properties of zirconium dioxide, *Iranian Journal of Science and Technology (Sciences)*. 36 (2012) 481–486. <https://doi.org/10.22099/ijsts.2012.2110>.
- [364] J.H. Adair, E. Suvaci, J. Sindel, *Surface and Colloid Chemistry*, in: K.H.J. Buschow, R.W. Cahn, M.C. Flemings, B. Ilschner, E.J. Kramer, S. Mahajan, P. Veysière (Eds.), *Encyclopedia of Materials: Science and Technology*, Elsevier, Oxford, 2001: pp. 1–10. <https://doi.org/10.1016/B0-08-043152-6/01622-3>.
- [365] R.M. Cornell, U. Schwertmann, *The Iron Oxides: Structure, Properties, Reactions, Occurrences and Uses*, Weinheim, 2003.
- [366] X. Dou, D. Mohan, C.U. Pittman, S. Yang, Remediating fluoride from water using hydrous zirconium oxide, *Chemical Engineering Journal*. 198–199 (2012) 236–245. <https://doi.org/10.1016/j.cej.2012.05.084>.
- [367] K. Pandi, D. Lee, J. Choi, Facile synthesis of zirconium-organic frameworks@biomass-derived porous graphitic nanocomposites: Arsenic adsorption performance and mechanism, *Journal of Molecular Liquids*. 314 (2020) 113552. <https://doi.org/10.1016/j.molliq.2020.113552>.

- [368] D. Sarkar, D. Mohapatra, S. Ray, S. Bhattacharyya, S. Adak, N. Mitra, Synthesis and characterization of sol-gel derived ZrO₂ doped Al₂O₃ nanopowder, *Ceramics International*. 33 (2007) 1275–1282. <https://doi.org/10.1016/j.ceramint.2006.05.002>.
- [369] G.Y. Guo, Y.L. Chen, New zirconium hydroxide, *Journal of Materials Science*. 39 (2004) 4039–4043. <https://doi.org/10.1023/B:JMSC.0000031491.78154.cb>.
- [370] G.V. Jere, M.T. Santhamma, IR and laser raman studies on peroxo fluoro species of zirconium, *Inorganica Chimica Acta*. 24 (1977) 57–61. [https://doi.org/10.1016/S0020-1693\(00\)93851-9](https://doi.org/10.1016/S0020-1693(00)93851-9).
- [371] D.-W. Cho, B.-H. Jeon, Y. Jeong, I.-H. Nam, U.-K. Choi, R. Kumar, H. Song, Synthesis of hydrous zirconium oxide-impregnated chitosan beads and their application for removal of fluoride and lead, *Applied Surface Science*. 372 (2016) 13–19. <https://doi.org/10.1016/j.apsusc.2016.03.068>.
- [372] F. Qunbo, W. Fuchi, Z. Huiling, Z. Feng, Study of ZrO₂ phase structure and electronic properties, *Molecular Simulation*. 34 (2008) 1099–1103. <https://doi.org/10.1080/08927020802101759>.
- [373] V.-J.L. Halla, H. Hurt Robert, M. Juan, R.-M.J. Rene, Zirconium-carbon hybrid sorbent for removal of fluoride from water: oxalic acid mediated Zr(IV) assembly and adsorption mechanism, *Environ Sci Technol*. 48 (2014) 1166–1174. <https://doi.org/10.1021/es403929b>.
- [374] Y. Zhang, Y. Qian, W. Li, X. Gao, B. Pan, Fluoride uptake by three lanthanum based nanomaterials: Behavior and mechanism dependent upon lanthanum species, *Science of The Total Environment*. 683 (2019) 609–616. <https://doi.org/10.1016/j.scitotenv.2019.05.185>.
- [375] L. Xu, J. Wang, Magnetic Nanoscaled Fe₃O₄/CeO₂ Composite as an Efficient Fenton-Like Heterogeneous Catalyst for Degradation of 4-Chlorophenol, *Environ. Sci. Technol*. 46 (2012) 10145–10153. <https://doi.org/10.1021/es300303f>.

- [376] C.L. Fausey, I. Zucker, E. Shaulsky, J.B. Zimmerman, M. Elimelech, Removal of arsenic with reduced graphene oxide-TiO₂-enabled nanofibrous mats, *Chemical Engineering Journal*. 375 (2019) 122040. <https://doi.org/10.1016/j.cej.2019.122040>.
- [377] M. Yu, J. Jia, X. Liu, J. Cui, B. Xi, X. He, X. Mao, p-Arsanilic acid degradation and arsenic immobilization by a disilicate-assisted iron/aluminum electrolysis process, *Chemical Engineering Journal*. 368 (2019) 428–437. <https://doi.org/10.1016/j.cej.2019.02.159>.
- [378] U.C. Ghosh, D. Bandyopadhyay, B. Manna, M. Mandal, Hydrous Iron(III)-Tin(IV) Binary Mixed Oxide: Arsenic Adsorption Behaviour from Aqueous Solution, *Water Quality Research Journal*. 41 (2006) 198–209. <https://doi.org/10.2166/wqrj.2006.023>.
- [379] Y. Zhang, M. Yang, X. Huang, Arsenic(V) removal with a Ce(IV)-doped iron oxide adsorbent, *Chemosphere*. 51 (2003) 945–952. [https://doi.org/10.1016/S0045-6535\(02\)00850-0](https://doi.org/10.1016/S0045-6535(02)00850-0).
- [380] Z. Wen, Y. Zhang, C. Dai, Z. Sun, Nanocasted synthesis of magnetic mesoporous iron cerium bimetal oxides (MMIC) as an efficient heterogeneous Fenton-like catalyst for oxidation of arsenite, *Journal of Hazardous Materials*. 287 (2015) 225–233. <https://doi.org/10.1016/j.jhazmat.2015.01.065>.
- [381] Z. Wen, J. Lu, Y. Zhang, G. Cheng, S. Huang, J. Chen, R. Xu, Y. Ming, Y. Wang, R. Chen, Facile inverse micelle fabrication of magnetic ordered mesoporous iron cerium bimetal oxides with excellent performance for arsenic removal from water, *Journal of Hazardous Materials*. 383 (2020) 121172. <https://doi.org/10.1016/j.jhazmat.2019.121172>.
- [382] R. Li, Q. Li, S. Gao, J.K. Shang, Exceptional arsenic adsorption performance of hydrous cerium oxide nanoparticles: Part A. Adsorption capacity and mechanism, *Chemical Engineering Journal*. 185–186 (2012) 127–135. <https://doi.org/10.1016/j.cej.2012.01.061>.

- [383] Y. Yu, C. Zhang, L. Yang, J. Paul Chen, Cerium oxide modified activated carbon as an efficient and effective adsorbent for rapid uptake of arsenate and arsenite: Material development and study of performance and mechanisms, *Chemical Engineering Journal*. 315 (2017) 630–638. <https://doi.org/10.1016/j.cej.2016.09.068>.

ANNEXES

A-1. Mechanism of formation of metallic oxyhydroxides (Ce, and Fe) on the activated carbon surface: Speciation diagrams of the species Ce and Fe.

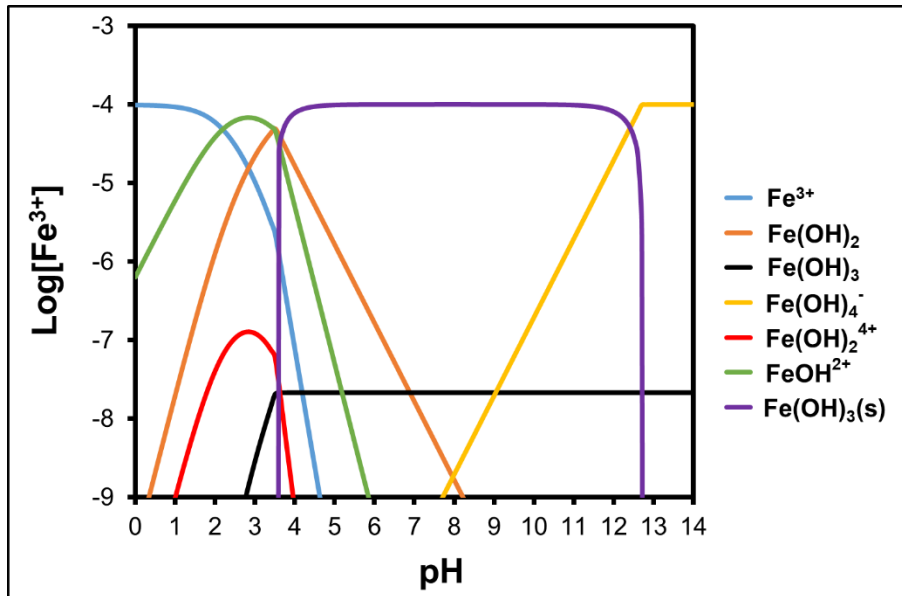


Figure A-1.1. Speciation diagrams of Fe (III).

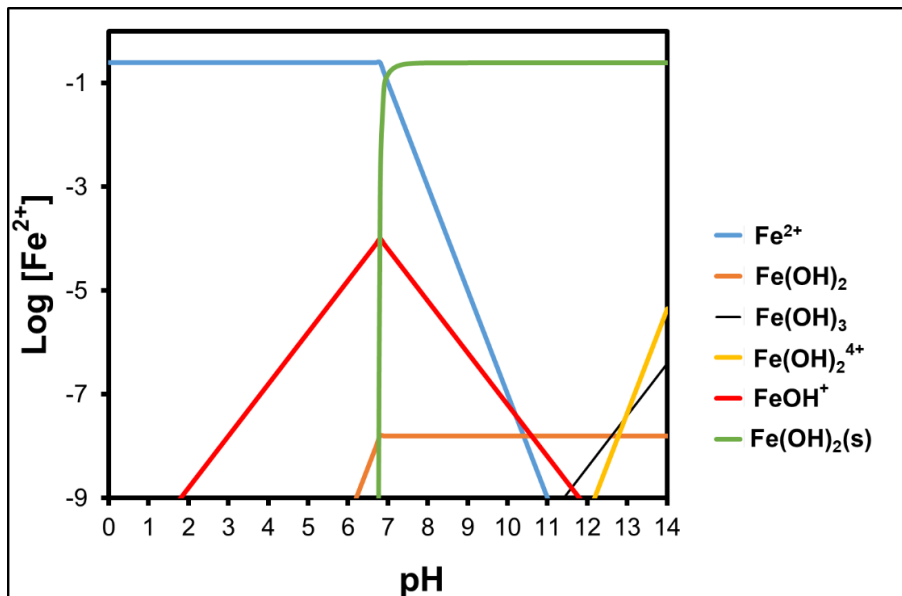


Figure A-1.2. Speciation diagrams of Fe (II).

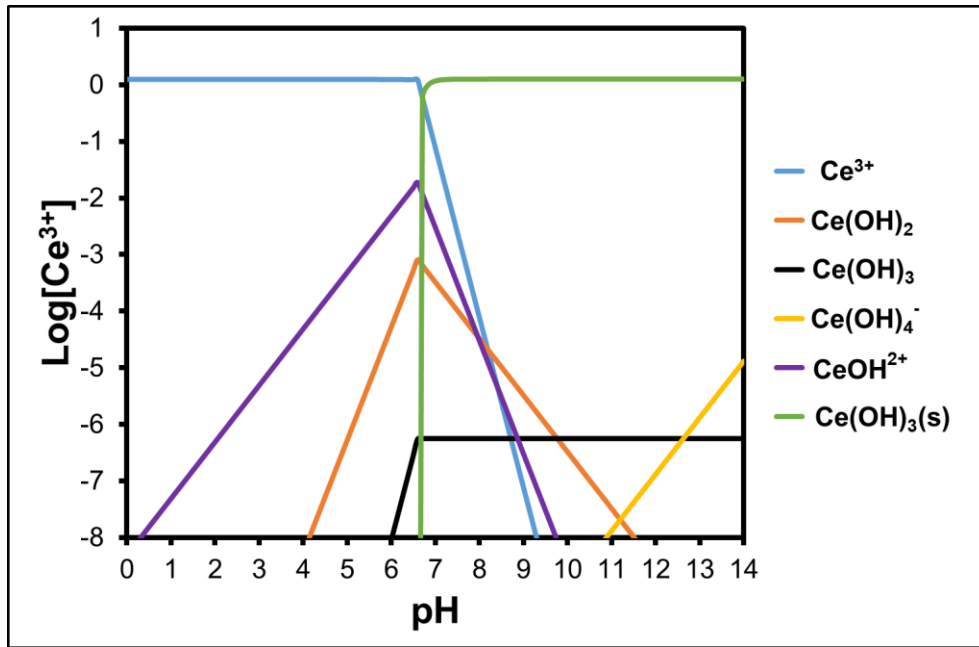


Figure A-1.3. Speciation diagrams of Ce (III).

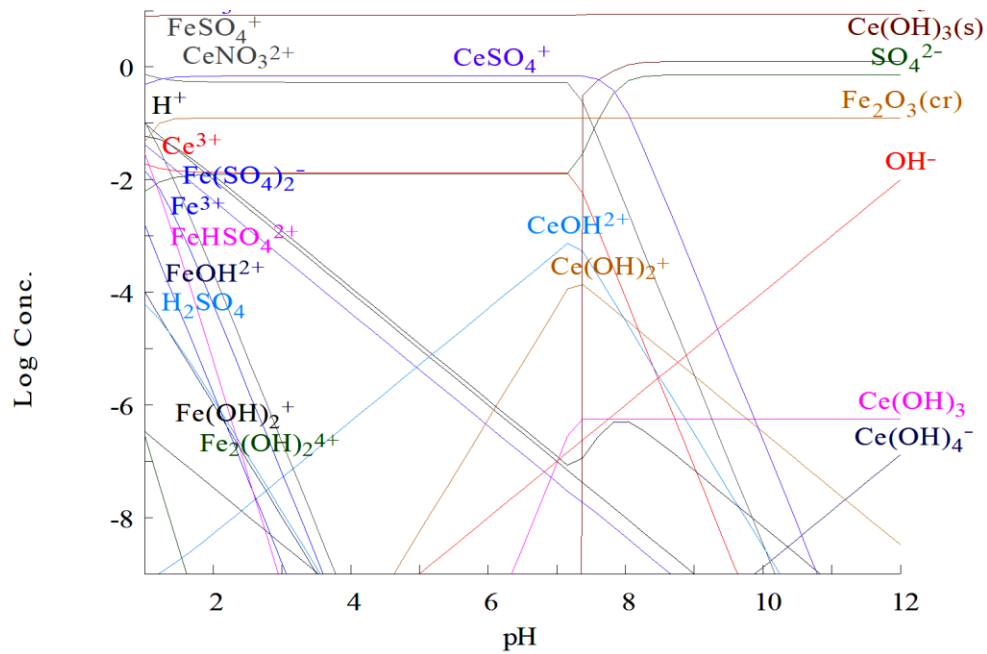


Figure A-1.4. Speciation diagrams of Fe (III), Fe (II), Ce (III), SO_4^{2-} and N^+ .

ANNEXES

A-2: Mechanism of formation of Ce and Mn oxyhydroxides on the activated carbon surface: Speciation diagrams of the species Ce and Mn.

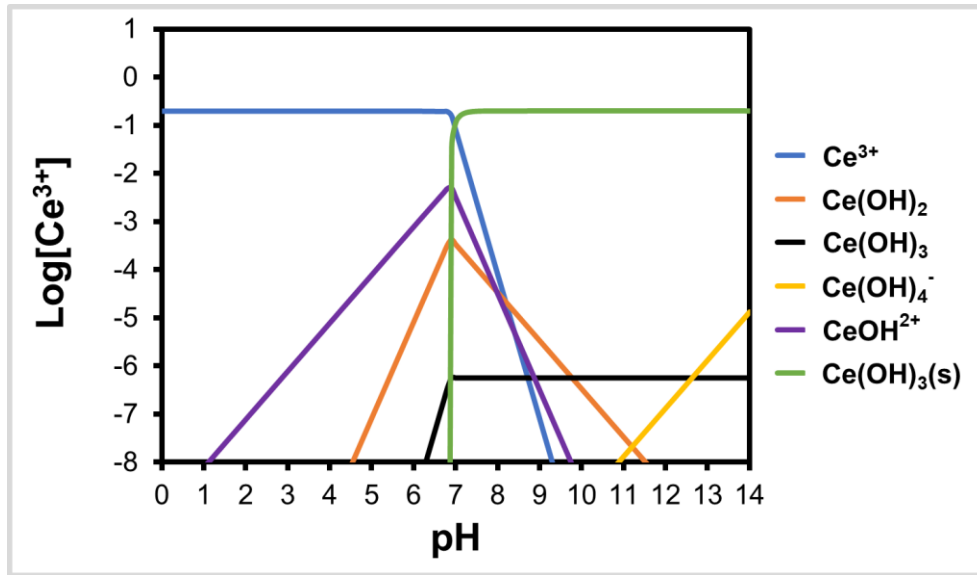


Figure A-2.1. Speciation diagrams of Ce (III).

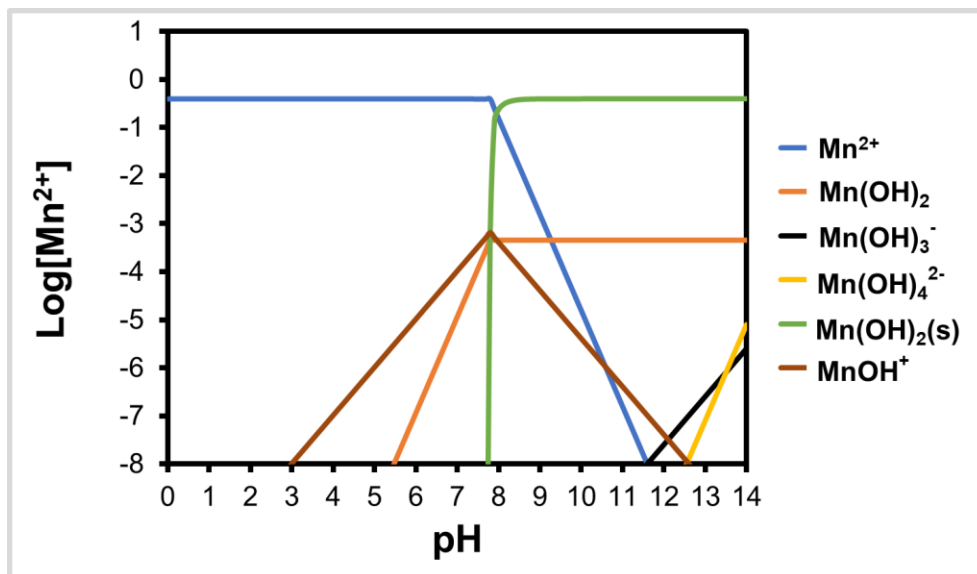


Figure A-2.2. Speciation diagrams of Mn (II).